The background of the entire page is a close-up, low-angle photograph of several parallel, blue, corrugated tubes. The tubes are arranged diagonally from the top-left towards the bottom-right. The lighting is bright, creating a strong sense of depth and highlighting the texture of the corrugations. The tubes are set against a light, almost white background.

Direct frequency comb spectroscopy in the vacuum ultraviolet

Roel Th. Zinkstok

**Direct frequency comb spectroscopy
in the vacuum ultraviolet**



Nederlandse Organisatie voor Wetenschappelijk Onderzoek



vrije Universiteit amsterdam 1535

The work described in this thesis was performed as part of a research program of the Netherlands Organization for Scientific Research (NWO) and was carried out at the Laser Centre of the Vrije Universiteit, De Boelelaan 1081, 1081 HV Amsterdam.

Copyright ©2007 Roel Th. Zinkstok, Amsterdam, the Netherlands.

Printed by PrintPartners Ipskamp BV, Enschede

ISBN 978-90-9022619-4

VRIJE UNIVERSITEIT

**Direct frequency comb spectroscopy
in the vacuum ultraviolet**

ACADEMISCH PROEFSCHRIFT

ter verkrijging van de graad Doctor aan
de Vrije Universiteit Amsterdam,
op gezag van de rector magnificus
prof.dr. L.M. Bouter,
in het openbaar te verdedigen
ten overstaan van de promotiecommissie
van de faculteit der Exacte Wetenschappen
op woensdag 19 maart 2008 om 15.45 uur
in de aula van de universiteit,
De Boelelaan 1105

door

Roelof Theodoor Zinkstok

geboren te Utrecht

promotor: prof.dr. W. Hogervorst
copromotor: dr. K.S.E. Eikema

*Die Vernunft muß mit ihren Prinzipien, nach denen allein übereinkommende
Erscheinungen für Gesetze gelten können, in einer Hand, und mit dem
Experiment, das sie nach jenen ausdachte, in der anderen, an die Natur gehen,
zwar um von ihr belehrt zu werden, aber nicht in der Qualität eines Schülers, der
sich alles vorsagen läßt, was der Lehrer will, sondern eines bestellten Richters, der
die Zeugen nötigt, auf die Fragen zu antworten, die er ihnen vorlegt.*

Immanuel Kant

Contents

- 1 Introduction 1**
 - 1.1 Time and frequency measurement 1
 - 1.2 Laser spectroscopy 2
 - 1.3 The frequency comb laser 3
 - 1.4 Metrology in the VUV and precision tests of QED 5
 - 1.5 Direct frequency comb excitation 7
 - 1.6 Harmonic generation and phase coherence 10
 - 1.7 Thesis outline 12

- 2 Preliminaries: from waves to combs 15**
 - 2.1 Waves and pulses in vacuum 15
 - 2.2 Gaussian pulses 16
 - 2.3 Waves and pulses in linear media 17
 - 2.4 Dispersion in linear media 20
 - 2.5 The carrier-envelope phase 22
 - 2.6 Pulse trains 23
 - 2.7 Propagation in non-linear media: the non-linear index of refraction 27
 - 2.8 Harmonic generation 29

- 3 Spectroscopy with frequency combs 35**
 - 3.1 Frequency combs 35
 - 3.2 Traditional frequency comb spectroscopy 39
 - 3.3 Direct excitation with frequency comb pulses 41

CONTENTS

- 3.4 Analytical model for excitation with phase-locked pulse trains 43
- 3.5 Numerical model of excitation with phase-locked pulse trains 48
- 3.6 Numerical results 50
- 3.7 Potential pitfalls of coherent pulsed excitation 58

- 4 Laser system and vacuum setup 75**
 - 4.1 Femtosecond oscillator with full comb control 76
 - 4.2 Pulse-picking Pockels cell 81
 - 4.3 Non-saturating Ti:sapphire amplifier for pulse sequences 82
 - 4.4 Interferometer for phase measurements 85
 - 4.5 Frequency conversion 89
 - 4.6 Vacuum setup and ion detection 89

- 5 Control and precise measurement of carrier-envelope phase dynamics 95**
 - 5.1 Introduction 95
 - 5.2 Carrier-envelope phase control 96
 - 5.3 Setup and methods for phase stabilization and measurement 97
 - 5.4 Real-time measurements of carrier-envelope phase stability 99
 - 5.5 Effects of the feedback loop 101
 - 5.6 Influence of the pump laser on ϕ_{ce} 103
 - 5.7 Long-term phase coherence of ϕ_{ce} and compressor stability 107
 - 5.8 Conclusions 112

- 6 Deep-ultraviolet quantum-interference metrology with ultrashort laser pulses 113**
 - 6.1 Introduction 113
 - 6.2 Principle of the experiment 114
 - 6.3 Setup 116
 - 6.4 Doppler shift 118
 - 6.5 Interference signals from pulse trains 119
 - 6.6 Isotope shift measurements 121
 - 6.7 Systematic shifts 122
 - 6.8 Absolute frequency measurements 123
 - 6.9 Outlook 124

- 7 Frequency comb laser spectroscopy in the vacuum ultraviolet region 125**
 - 7.1 Coherent pulsed excitation in the VUV 125
 - 7.2 Design of the experiment 126

- 7.3 Third-harmonic generation 128
- 7.4 Lifetime measurement 129
- 7.5 Isotope shift measurements 129
- 7.6 Pulse train signals 131
- 7.7 Pulse pair signals 133
- 7.8 Procedure for absolute frequency measurements with pulse pairs 136
- 7.9 Conclusions 138

8 A source of 2 terawatt, 2.7 cycle laser pulses based on non-collinear optical parametric chirped-pulse amplification 141

- 8.1 Introduction 141
- 8.2 Principles of NOPCPA 142
- 8.3 Ultra-broadband two-terawatt NOPCPA system 144
- 8.4 Spectral phase shaping and few-cycle pulse compression 148
- 8.5 Pulse contrast measurements 151
- 8.6 Conclusions and outlook 156

Bibliography 159

List of publications 183

Summary 185

Samenvatting 191

Dankwoord 197

Introduction

The work described in this thesis is concerned with the development and demonstration of a new method for performing highly accurate absolute frequency metrology in the extreme and vacuum ultraviolet (200-30 nm), and possibly at even shorter wavelengths. This chapter aims at providing a background to this work, and describes the two major fields that may benefit from such a metrological method: time and frequency metrology on the one hand, and precision tests of fundamental physical theories on the other.

1.1 Time and frequency measurement

For centuries, people have measured time intervals by using the most accurate oscillation available to divide time in little chunks equal to the period of that particular oscillation. Counting the number of these chunks is all it takes to track time. The precision of the measurement depends on the period of the oscillation used, or its inverse, the frequency. Over the centuries many different periodic phenomena have been employed, and in the course of that development the standard of time has improved tremendously: starting from the earth's orbit around the Sun and its rotation around its axis (with a periods of 365.24 days and 24 hours, respectively), it evolved via the pendulum (1583, period ~ 1 s) and the quartz oscillator (1918, period $\sim 10^{-5}$ s) to the oscillation of a microwave transition in a cesium atom (1955, period $\sim 10^{-10}$ s). This last frequency has become of special importance, as in 1967 the second was redefined to comprise exactly 9 192 631 770 oscillations of this cesium-133 transition [1]. At present, the cesium clock

is the official primary frequency standard, to which all other frequency measurements must be referenced.

In fact, as no other quantity in nature can be measured as accurately as a frequency, many metrological experiments on other quantities depend on the conversion of the quantity of interest to a frequency. Length metrology is a clear example: the speed of light was defined to be 299 792 458 m/s in 1983 [2], and therefore a measurement of length is just a measurement of the time needed for light to travel that distance. Over the years, frequency metrology has become a very active yet challenging line of research. For a long time electronic standards dominated this field, but since it became possible to perform measurements on atomic systems that were accurate enough for metrological applications, precision spectroscopy at microwave and optical frequencies supplanted electronic standards. A crucial step in this development was the invention of the laser.

1.2 Laser spectroscopy

Soon after the first ideas to extend the maser principle to optical frequencies had been published by Schawlow and Townes in 1958 [3], the race to build the first laser started [4]. The first to succeed was Theodore Maiman, who built a pulsed ruby laser in 1960 [5]. Not much later, Ali Javan and coworkers demonstrated continuous laser operation in a helium-neon gas mixture [6]; since then, many more laser types have been developed all across the optical spectrum.

A first requirement for a laser to be useful for metrological applications is frequency stabilization of its narrow linewidth output. Many techniques to accomplish this have been developed over the years, such as the use of the Lamb dip [7, 8] for intra-cavity stabilization of the laser frequency [9] and saturation spectroscopy [10] on molecular transitions, e.g. in iodine. External Fabry-Perot cavities (etalons) are used as well, since a laser can be locked to a stabilized etalon using one of many cavity locking techniques like the Hänsch-Couillaud [11] or Drever-Hall [12] techniques. In modern high-resolution spectroscopy these locking schemes are used routinely.

Using such highly stabilized, narrow-band lasers it became possible to perform spectroscopy on a wide variety of systems. However, in order to measure absolute transition frequencies the laser frequency must be compared to a primary frequency standard, the cesium clock, which operates at a radio frequency of 9.2 GHz. Consequently, there is a gap to be bridged between the optical and RF domain. The first experiments to do this employed large and extremely complicated frequency chains using many auxiliary lasers, transfer oscillators and phase-locked loops. Examples are the measurement of

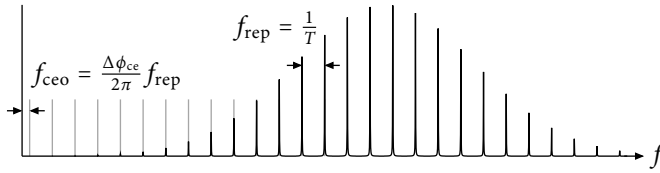


Figure 1.1: The spectrum of a frequency comb laser. The mode spacing is given by the repetition rate of the pulses f_{rep} while the offset of the comb from zero frequency is given by the carrier-envelope offset frequency f_{ceo} .

the 88 THz transition in CH_4 [13], the I_2 -stabilized He-Ne transition at 473 THz [14] and, more recently, a phase-coherent comparison between a cesium standard and the 455 THz inter-combination transition in ^{40}Ca [15].

The concept of frequency dividers [16] constituted a major improvement, as they offer a simple method to cut optical frequency gaps in half. Successive application of this method can reduce the frequency difference to a level where electronic counting becomes possible. This was applied for example to the measurement of the 1S-2S transition in hydrogen at 2466 THz [17], the $5s\ ^2\text{S}_{1/2} \rightarrow 4d\ ^2\text{D}_{3/2}$ transition at 445 THz in $^{88}\text{Sr}^+$ [18], and the 2S-12D transition in hydrogen and deuterium at 799 THz [19]. A technique capable of similar division of optical frequency differences has been demonstrated with phase-locked parametric oscillators [20]. Around the same time DeVoe and coworkers demonstrated another approach, measuring the mode spacing of a high-finesse cavity over a large range, which in effect provided them with a comb of 150 frequencies spanning a range of about 50 THz [21]. Lasers having widely differing frequencies could be referenced to the same cavity, and the frequency gap between them is then the sum of the appropriate of mode spacings.

The next step in the simplification of these optical-to-RF frequency comparisons was the invention of the electro-optic comb by Kourogi [22, 23]. In such a device, a large number of Phase-locked sidebands are generated from a single-mode laser with an electro-optic crystal inside a resonant cavity. The resulting comb can be a few THz wide, and it was put to good use in several experiments [24, 25].

1.3 The frequency comb laser

The major breakthrough in this area, however, came with the introduction of the optical frequency comb laser in 1998 [26–28] and the development of a completely self-

referenced comb shortly thereafter [29, 30]. It was recognized that a Kerr-lens mode-locked pulsed titanium:sapphire (Ti:sapphire) laser [31] emits a spectrum of closely spaced modes which are controlled by only two parameters: the repetition frequency of the laser f_{rep} , which determines the mode spacing, and the carrier-envelope offset frequency f_{ceo} , which determines the offset of the entire (extrapolated) comb from zero frequency (see figure 1.1). Both these quantities are RF frequencies. Any frequency in the comb can be expressed as

$$f_n = f_{\text{ceo}} + n f_{\text{rep}} \quad (1.1)$$

Control of f_{rep} was nothing new, but the technique for stabilization of f_{ceo} using an f - $2f$ -interferometer [29, 30] was a revolutionary step. The combined action of these two locking schemes produced a comb of up to a million precisely controlled optical frequencies spanning hundreds of THz, which could be directly referenced to an RF standard via f_{rep} and f_{ceo} . This comb structure can act as a frequency ruler, to which an unknown optical frequency can be compared. Usually, this unknown frequency stems from a stabilized narrow-band cw laser, which is used at the same time to probe a transition. From the known f_{rep} and f_{ceo} and the measured beat frequency, the unknown frequency can be determined modulo f_{rep} . This ambiguity must be resolved using a coarse frequency measurement with e.g. a wave meter.

This spectroscopic application of the frequency comb laser was an immediate success. The first measurements on e.g. the cesium D_1 line [26], reached an accuracy of about one part in 10^{10} , but already in the same year, an accuracy of 10^{-14} (40 Hz) was demonstrated on the hydrogen 1S-2S transition [32]. Other experiments, in which different frequency combs were compared to each other, showed that in general the uncertainty of the frequency comb approach was less than 5×10^{-16} [30]. The accuracy is ultimately limited by the stability of the RF source used, as for the optical modes its intensity noise is multiplied by the square of the mode number n in equation 1.1 [33]. When instead the frequency comb is locked directly to a highly stable optical cavity, much better results can be achieved, as in this case the reference frequency is in the optical domain as well. Measurements using frequency combs referenced to such an optical cavity indeed demonstrated improved stability [34, 35], and the most recent experiments have brought the uncertainty even further down to 8×10^{-20} [36].

It is no surprise that nowadays frequency comb lasers are operated in many metrology and spectroscopy laboratories. Especially the turn-key fiber comb lasers that have become available recently provide a simple tool for metrology [37], and with the commercially available rubidium frequency standards an accuracy of 10^{-12} can be achieved routinely; the use of a commercial cesium clock will improve this by a factor of ten.

The stunning performance of the frequency comb laser has spurred the research in pursuit of suitable atomic clock transitions at ever higher frequencies reaching into the optical domain, which might one day replace the cesium primary standard. Recent examples are the strontium ion at NPL [38], the mercury ion at NIST [39], the strontium lattice clock in Paris [40], the indium ion at MPQ [41] and the $^{27}\text{Al}^+$ clock transition at NIST [42, 43]. The best of these measurements reaches an accuracy of about 10^{-16} .

Extrapolating this development, it does not seem far-fetched to envision atomic or ionic clocks that operate at ultraviolet (UV) or even vacuum ultraviolet (VUV, 200-100 nm) and extreme ultraviolet (XUV, 100-30 nm) wavelengths. Performing high-resolution spectroscopy, however, becomes increasingly challenging with increasing frequency, and translating the accuracy that frequency combs deliver in the infrared and visible regions of the spectrum to these ultra-high frequencies is not a straightforward task. Nonetheless, the work presented in this thesis provides a method for performing frequency comb spectroscopy in the VUV and XUV spectral regions, and thus may further the development of VUV atomic clocks.

1.4 Metrology in the VUV and precision tests of QED

The development of extremely high frequency atomic clocks, as described in the previous section, is not the only line of research that might benefit from the method for frequency comb spectroscopy in the VUV that is presented in this thesis. Given the amazing progress of spectroscopic measurements made in the last century, increasingly accurate tests of the fundamental theories of atomic structure can be performed. This development becomes even more interesting with the availability of high precision at high frequencies.

The theory of atomic structure has developed from the elementary Schrödinger theory, capable of explaining the gross electronic structure, to the Dirac theory that clarified fine structure [44, 45]. Then the experiments by Lamb and Retherford in 1947 showed that, contrary to the predictions of the Dirac theory, the $2^2S_{1/2}$ and $2^2P_{1/2}$ levels in hydrogen were not degenerate [46, 47]. This discovery incited the development of quantum electrodynamics (QED), a theory that has since been tested to breath-taking precision.

Of course, the predictions from this theory are most accurate for the simplest atoms and ions, such as hydrogen and helium, and the hydrogen-like ions. In the calculations for such systems, the energy of the atomic levels is usually expressed as the sum of three terms. The first of these is the energy derived from the Dirac theory, while the second term describes the relativistic corrections due to the proton recoil up to order $(Z\alpha)^2$

(Z is the proton number and α is the fine structure constant) which are responsible for the fine structure. The last term includes all higher-order corrections, and is usually termed the Lamb shift. These QED corrections are conventionally treated in a double series expansion in Z and α , of which the leading orders correspond to the self-energy and the electron vacuum polarization [48].

The first two contributions to the level energy (the Dirac term and the relativistic corrections) have been calculated to such a precision that they can be considered exact for simple atomic systems like hydrogen and helium. The calculation of the QED terms is less precise, as it is hampered not so much by the understanding of the theory, but by the precision of the physical constants involved, most notably the proton mean square charge radius and the Rydberg constant. The value for the former has been heavily debated, as different and contradicting values were measured, see e.g. [48]. However, careful analysis of the data has explained the differences [49]; still, a more precise determination is badly needed, and hopefully the muonic hydrogen experiment at PSI will yield better results [50].

All in all, the calculations of the Lamb shift in the hydrogen ground state have reached an accuracy of about 30 kHz [51]. If the proton charge radius were known exactly, the calculations would be at least an order of magnitude more precise. For helium, the most precise theoretical prediction to date is for the ionization energy of the ground state, which has been calculated with an accuracy of 36 MHz [52].

In order to check these theoretical predicted energies, extremely precise measurements are needed of simple atomic and ionic systems. Such measurements of the Lamb shift have been performed for many systems, most notably for hydrogen and helium, the simplest atoms. In hydrogen the most accurate experimental result to date has been reported by Schwob et al. in 1999. They determined the Lamb shift for the ground state by comparing measurements on several transitions using two-photon Doppler-free spectroscopy. The resulting value has an accuracy of 2.7×10^{-6} [17, 19, 24, 53, 54], slightly better than the theoretical accuracy. The measured and calculated values are in fair agreement. For helium however, the two most accurate measurements of the Lamb shift disagree by more than three standard deviations [55, 56]. The measurement performed by Eikema et al. [56] is the most precise, with an accuracy of 45 MHz, and these results agree with theory [52].

Apart from such direct comparisons of predicted and measured transition frequencies, there are other interesting avenues of research to follow. For example, the high accuracy of the measured data can be used to deduce values for the proton charge radius or the Rydberg constant if the QED calculations themselves are considered to be

exact [57, 58]. Another possibility is to perform spectroscopy on hydrogen and hydrogen-like ions, such as He^+ and Li^{2+} . Such measurements will give insight into the influence of the nuclear size on the level energies of the atom and will allow the testing of theoretical predictions of nuclear radii. Furthermore, it has been proposed that some or all of the fundamental constants might slowly vary in time [59, 60]. The precision offered by frequency comb spectroscopy allows one to look for such variations by repeating the measurement in time. In the course of a few years, such experiments have put strict limits on the variability of e.g. the fine structure constant [61, 62].

From these considerations it is clear that highly precise tests of QED can be performed by comparing the results from theoretical calculations with accurate spectroscopic data of simple atomic and ionic systems. However, for all of these systems, the ground state is separated from the first excited state by a large energy gap. In hydrogen, the $1S$ - $2S$ transition needs 2×243 nm, for the $1s^2 \ ^1S$ to $1s2s \ ^1S$ in neutral helium this already changes to 2×120 nm, while for singly ionized helium one needs 2×61 nm to excite the $1s$ - $2s$ transition. Such wavelengths pose a serious challenge for experiments on these transitions, since the generation of narrow-band laser light is hard already in the deep-UV, gets seriously difficult in the VUV [63] and is almost impossible at higher frequencies. For example, the best helium ground state Lamb shift measurement was performed by exciting the $1s \ ^1S \rightarrow 2p \ ^1P$ transition at 58 nm with a 250 MHz linewidth laser system [56], which came close to the limits of nanosecond VUV laser technology. It is therefore not to be expected that a substantial improvement of the experimental resolution in the VUV or XUV can be achieved in this way.

1.5 Direct frequency comb excitation

As an alternative to precision spectroscopy with narrow-band cw radiation, phase-locked pulses can be used to excite the atoms under study. This method is similar to the method of separated oscillatory fields proposed sixty years ago by Ramsey for spectroscopy on molecular or atomic beams [64, 65]. In his method (schematically depicted in figure 1.2), atoms fly through two spatially separated regions in which phase-locked oscillating fields are present that are resonant with a transition between two quantum states of the atom. The field in the first region excites a coherent superposition of the two states, which continues to oscillate when the atom flies through the field-free region. The oscillation frequency of the superposition of states in this field-free region is just the eigenfrequency that connects the two states. When the atom enters the second region, the field there interacts with the superposition of states. As the field is phase-locked to the field in the

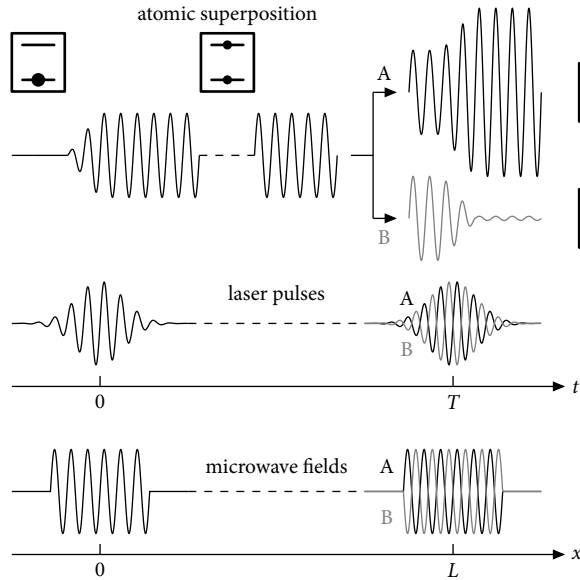


Figure 1.2: The principle of Ramsey spectroscopy in the spatially separated fields configuration (bottom) and the temporally separated fields configuration (middle). A two-level atom in the ground state interacting with the first field will be transformed into a superposition of the ground and excited states, which evolves with a frequency proportional to the energy difference between the states. The interaction with the second field can either enhance (A) or diminish (B) the excited state population, depending on the phase difference between the second field and the atomic superposition.

first region, its contribution to the coherent superposition can interfere with that of the first field. Depending on the phase difference between the superposition and the second field, excitation can be either enhanced or suppressed. For such an experiment, a distinct response versus excitation field frequency can be recorded, which shows a narrow resonance peak with several sidebands. This technique has found widespread use for radio-frequency (microwave) transitions of e.g. present-day cesium fountain clocks.

Ramsey's technique was quickly applied in the optical domain using spatially separated laser beams [66]. More interestingly, the step was made from spatially separated fields to temporally separated fields, that is, to pulses; picture 1.2 shows this approach as

well. In such experiments, nanosecond phase-locked pulses are generated from a single pulse using a delay line or a cavity, and Doppler-free excitation is realized by placing the sample near a mirror, such that a standing wave is generated in the sample [67–70]. Although the bandwidth of the pulses used would suggest that a high resolution is not possible, the phase coherence between the pulses allows a resolution significantly better than the bandwidth of the individual pulses. This was certainly the case for the mode-locked lasers that became available in the seventies. Eckstein et al. used such a laser in Doppler-free experiments where the sample was situated at such a distance from a mirror, that reflected pulses met with the next pulse in the sample [71]. Although no absolute frequency measurements could be performed, stabilization of the mode structure was sufficient to observe linewidths of a few MHz, making accurate relative frequency measurements possible. Using the same method on rubidium atoms in a magneto-optical trap, Snadden and coworkers were able to measure spectra with a linewidth down to 450 kHz [72]. For these optical experiments, the mode structure of the lasers used invites us to interpret the method from a frequency perspective: when laser mode N is resonant with the two-photon transition, the combination of modes $N - 1$ and $N + 1$ will also be resonant. In fact, all modes $N - i$ will combine resonantly with corresponding modes $N + i$, resulting in a high excitation rate. When the transition is exactly halfway between two modes, again excitation by symmetric mode pairs occurs. In between these situations, the modes do not add up to a resonant combination, so the atoms are not excited. In the case of single photon transitions, there is no such collective enhancement of the excitation, and resonance only occurs when a single mode coincides with the transition frequency.

This interpretation makes it immediately clear that the recorded frequency spectra are periodic, as the same conditions appear when the mode spectrum of the laser is scanned over the mode spacing (or half the mode spacing for two-photon transitions). The whole spectrum of the studied atom that lies within the bandwidth of the laser is wrapped to this small frequency range. In case a small bandwidth is used, like in the experiments described above, this is not a big problem, as only one or a few transitions are excited. However, when broadband lasers are used, this is of greater concern as the spectra become increasingly complex.

After the experiment of Eckstein, which came close to the theoretical limits of the method, no new developments took place until the advent of frequency comb lasers. First, it was demonstrated in 1997 by Bellini et al. that the experiments from the seventies using ns and ps pulses could be performed just as well with fs pulses. Bellini used pulses from a mode-locked Ti:sapphire laser that were split into two copies in a delay line to

probe cesium atoms [73]. Although not presenting any revolutionary new insights, this experiment triggered the idea of using a frequency comb for Ramsey-like excitation. The precisely known mode frequencies of these lasers make it possible to extract absolute frequencies from the measured data. After a proposal paper for direct frequency comb excitation of rubidium [74] and several papers detailing the theoretical framework of multi-pathway interference with direct excitation [75–77], the first demonstration of this method was presented in 2004 by Marian et al. [78], which was extended in a later paper [79]. In their experiments, absolute frequency measurements of one- and two-photon transitions in the infrared were performed on cold rubidium atoms, and extensive modelling showed good agreement with the measured data. This approach was subsequently adopted to perform metrology on a variety of atomic species, e.g. cesium [80, 81] and calcium [82, 83], which clearly showed the versatility of direct frequency comb spectroscopy (DFCS) in the infrared and red parts of the spectrum.

The method of DFCS has several advantages. First of all, there is no need for a cw laser at the transition wavelength. In the infrared and red part of the spectrum, this is not a great advantage, but it does open the door to applications at higher frequencies. Furthermore, the AC Stark shift of the atomic levels in DFCS is proportional to the average intensity of the laser, and not to the peak intensity: the levels are only shifted during the short time in which the atoms interact with the pulses. During the much longer time between the pulses, the levels do not shift, so the total Stark shift is equivalent to that induced by a cw laser of the same average power [80, 84]. Another benefit is the wide bandwidth of the ultrashort pulses used, which makes it possible to cover a broad spectrum with only one laser. Of course, the downside is that many transitions will be excited at the same time, making the experimental spectra rather complicated because of the wrapping effect mentioned earlier. For this reason, it can be necessary to select only a small part of the comb spectrum. Finally, the high peak power of the ultrashort pulses facilitates the up-conversion to higher frequencies through frequency doubling in crystals or harmonic generation in gases. However, for the generation of VUV radiation the power of the pulses directly generated from a frequency comb oscillator is not enough, and some form of amplification or enhancement will still be needed.

1.6 Harmonic generation and phase coherence

As said, to enter the realm of XUV or VUV frequencies with DFCS, harmonic generation of the comb pulses is required. The process of optical harmonic generation was discovered shortly after the laser had been introduced. Franken et al. observed radiation at exactly

twice the frequency of their laser when they sent its light through a quartz crystal [85]. Soon other crystals were shown to exhibit similar properties in different frequency mixing schemes [86, 87]. These observations are explained by considering the nonlinear polarization induced in the medium by intense laser fields, which in turn causes radiation to be emitted at sum or difference frequencies of the input frequencies [88, 89]. In order to compensate for the phase mismatch that accumulates in longer crystals due to dispersion, birefringent crystals were adopted, in which interaction lengths of several millimeters and longer can be achieved. Such nonlinear birefringent crystals can be used to generate intense UV radiation down to about 200 nm, as radiation at shorter wavelengths is absorbed in the crystal.

For the production of higher frequencies, harmonic generation has to be performed in gases. Similar to frequency mixing in crystals, the nonlinear polarization induced by the driving field in a gas cell or jet causes radiation at harmonics of the fundamental frequency to be emitted. The first observations of third harmonic generation [90] and higher harmonics [91] up to a few orders were still well explained with such a perturbative approach, which predicts a fast decline in intensity with increasing order. In later experiments at higher driving field intensity, above 10^{13} W/cm², harmonics as high as the 33rd order were detected [92, 93], demonstrating that this decline does not continue. Instead there is a range of harmonics for which the intensity stays roughly constant, commonly called the plateau. These observations were explained in a semi-classical picture in which harmonic generation is visualized in three steps: tunneling ionization, acceleration of the liberated electron in the driving laser field, and collisional recombination of the electron with its parent ion accompanied by harmonic radiation [94]. This intuitive picture was soon justified by Lewenstein et al. who presented a full quantum mechanical treatment of the problem [95]. Experimentally it was seen that the plateau harmonics can extend to extremely high frequencies: in recent years, the use of high-power ultrashort pulses (10 fs, 10^{16} W/cm²) from Ti:sapphire laser systems has made it possible to produce soft x-rays up to 1 keV (1.2 nm) [96].

It is therefore clear that short pulses can be up-converted to frequencies that far exceed the spectral regions to which high resolution spectroscopy currently is confined. Performing DFCS with harmonically up-converted pulses brings the accuracy of frequency combs into the VUV, XUV and possibly even the soft x-ray regions. However, the up-conversion process should not compromise the phase coherence of the comb pulses. For up-conversion in crystals, several processes can affect the phase of the generated radiation. Not only self-phase modulation in the crystal, but also the nonlinear process itself is capable of introducing an intensity-dependent phase shift, which translates

amplitude noise into phase noise [97–100]. As these effects become significant only for quite high powers, they are usually negligible for cw lasers. However, it can become problematic for ultrashort, high-intensity laser pulses [101].

When gases are used, even more processes come to play a role. Ionization of the medium changes the index of refraction, mostly due to the creation of free electrons. Fluctuations in the medium density or the driving field intensity will then lead to phase fluctuations in the generated field. Furthermore, as can be seen from the three-step model for high-harmonic generation, the phase of the harmonics is influenced by the field that the electron experiences during its trajectory in the driving field [95, 102–104]. Fluctuations in the driving laser field will cause phase variations in the generated radiation.

Several experiments have been reported in which the temporal [102, 105], spatial [106] and spectral [107–109] coherence of harmonic generation was investigated by interference of harmonics generated in separate locations in a gas jet. The results showed that the harmonic radiation was still highly coherent. However, in all these experiments the separate harmonic sources were driven by pulses that were generated from a single fundamental pulse in a Michelson interferometer of a birefringent crystal. Therefore, the effects of driving laser intensity fluctuations, the most likely cause of phase shifts, could not be measured. Only Bellini performed some measurements of the coherence time of the harmonics (approximately equal to the inverse of the phase of the harmonics), and concluded that especially for the short-electron-trajectory harmonics, there is indeed an intensity dependence of the harmonic phase [102]. As such, we cannot conclude that frequency comb pulses can be up-converted without sacrificing phase coherence.

Recently, an alternate approach for UV-XUV frequency comb generation was demonstrated separately by Gohle [110] and Jones [111]. Both used an external enhancement cavity to boost the power of the comb pulses, and positioned a gas jet at the focus of the cavity. They succeeded in generating harmonics up to the 7th [111] and the 15th [110] order. However, phase coherence of the harmonic comb was demonstrated only for the third harmonic at 266 nm by a comparison with third harmonic radiation produced in crystals. Therefore the question of phase coherence at shorter wavelengths remains.

1.7 Thesis outline

This thesis describes the realization of absolute frequency metrology and spectroscopy in the VUV using amplified and up-converted frequency comb pulses. It demonstrates that the phase coherence of the comb is preserved, and that DFCS can be performed

with only a few phase-coherent pulses. Furthermore, a new approach is proposed which replaces the Ti:sapphire amplifier used in the experiments with an amplifier based on optical parametric chirped pulse amplification. The latter technique offers the prospect of highly phase-stable amplification of frequency comb pulses, alleviating the difficulties associated with the phase shifts induced by the Ti:sapphire amplifier. The combination of these techniques is expected to allow highly precise frequency comb metrology on simple atomic systems like helium, facilitating stringent testing of QED. At the same time, DFCS is thought to be a promising approach for the development of atomic clocks operating at VUV and XUV wavelengths.

In the following chapters a comprehensive description is given of the concepts, practical implementation and experimental results of frequency comb metrology at VUV frequencies. Chapter 2 starts out explaining short pulses and their propagation characteristics, as well as other concepts relevant to the experiments described in the rest of this thesis. The next chapter continues with a more practical treatment of the various spectroscopic applications of the frequency comb laser, followed by a detailed modelling, both analytically and numerically, of the interaction between phase-locked pulses and simple two-level atoms. These simulations demonstrate the capabilities of DFCS, as well as its limitations. The latter are discussed in more detail, in order to evaluate the various aspects of the method that might be challenging. Chapter 4 deals with the experimental system that was developed to realize DFCS in the VUV. All elements of the frequency comb, amplifier and atomic beam setup are presented here together with some characterization and calibration measurements of the various parts. The subsequent chapter discusses several experiments that were carried out to quantify the performance of the frequency comb control. Thorough measurements of carrier-envelope phase dynamics over a wide range of time scales are reported and the influence of the pump laser and of environmental disturbances is evaluated. In chapter 6 the first demonstration of absolute and relative frequency metrology in the deep-UV is demonstrated on a two-photon transition in krypton at 2×212.5 nm. Measurements of the isotope shifts were performed with an uncertainty down to 150 kHz and a measurement of the absolute transition frequency with an uncertainty of 3.5 MHz was achieved, which constitutes an improvement by an order of magnitude over earlier spectroscopic experiments in this wavelength region using ns pulses. It is demonstrated in chapter 7 that this method can be pushed even further, reaching VUV wavelengths. The 125 nm resonance in xenon is excited with pulse trains of varying lengths and pulse pairs with varying delays. The required wavelength is produced by frequency doubling in a crystal and frequency tripling in a gas. Apart from relative frequency measurements, an enquiry into the

INTRODUCTION

effects of the harmonic generation process on the phase coherence of the VUV pulses is performed. The results demonstrate the preservation of phase coherence over a wide range of driving intensities and gas pressures, Finally, chapter 8 reports on a different subject, the realization of a 2 TW, 7.6 fs laser system based on non-collinear optical parametric chirped pulse amplification. The system described here will be used in future DFCS experiments to replace the Ti:sapphire amplifier that was employed in the experiments of chapters 6 and 7. With such an amplifier, DFCS at XUV wavelengths will be performed on helium in the near future.

Preliminaries: from waves to combs

The work described in this thesis hinges on the generation, control and application of ultrashort laser pulses. In this chapter the basic principles of short pulses and their spectral composition, the propagation of such pulses through linear and non-linear media, the creation of pulse trains, and the basics of several non-linear interactions which are relevant to ultrashort optics and spectroscopy will be discussed. The concepts introduced in this chapter are used throughout this thesis.

2.1 Waves and pulses in vacuum

The propagation of electromagnetic fields through vacuum is governed by a wave equation derived from the Maxwell equations. Considering only the electric part of the wave, and restricting the propagation to the z -direction, this equation is

$$\frac{\partial^2}{\partial z^2} E(z, t) - \mu_0 \epsilon_0 \frac{\partial^2}{\partial t^2} E(z, t) = 0. \quad (2.1)$$

The general solution of this equation consists of plane waves, propagating with a velocity $1/\sqrt{\mu_0 \epsilon_0} = c$, the speed of light. These can be written as

$$E(z, t) = A e^{i(kz - \omega t)} + B e^{-i(kz + \omega t)}. \quad (2.2)$$

The waves oscillate at an angular frequency ω , and have a wave vector $k = 2\pi/\lambda = \omega/c$ where λ is the wavelength. The first exponential describes waves propagating in the positive z -direction, whereas the second exponential describes those propagating in

the opposite direction. As the wave equation 2.1 is linear, any superposition of plane waves is also a solution. Discarding the waves propagating in the negative z -direction for simplicity, such a wave packet is written as

$$E(z, t) = \int_{-\infty}^{\infty} \mathcal{E}(\omega) e^{i(kz - \omega t)} d\omega = \int_{-\infty}^{\infty} E(z, \omega) e^{-i\omega t} d\omega, \quad (2.3)$$

which shows that the time and frequency descriptions of the electric field are related by a Fourier transform. Here $\mathcal{E}(\omega)$ gives the amplitude of the spectral components that make up the wave packet. When this function is clearly peaked around a central frequency ω_1 , and has a width that is relatively small compared to ω_1 , it makes sense to expand $\mathcal{E}(\omega)$ around this central frequency. $\mathcal{E}(\omega)$ then becomes $\mathcal{E}(\omega - \omega_1) e^{-i\omega_1 t}$, and 2.3 transforms into

$$\begin{aligned} E(z, t) &= \int_{-\infty}^{\infty} \mathcal{E}(\omega - \omega_1) e^{-i\omega_1 t} e^{i(kz - \omega t)} d\omega \\ &= e^{i(kz - \omega_1 t)} \int_{-\infty}^{\infty} \mathcal{E}(\omega - \omega_1) e^{-i\omega t} d\omega \\ &= \mathcal{E}(z, t) e^{i(kz - \omega_1 t)}. \end{aligned} \quad (2.4)$$

Now the electric field is described by a carrier wave oscillating at a frequency ω_1 modulated by an envelope function $\mathcal{E}(z, t)$. Again, this temporal envelope function is related to the amplitude function in frequency space $\mathcal{E}(z, \omega)$ by a simple Fourier transform.

2.2 Gaussian pulses

As an example, consider a Gaussian pulse, such as the one shown in figure 2.1: the envelope function is then given by

$$\mathcal{E}_{\text{Gauss}}(z, t) = \mathcal{E}_0 e^{-2 \ln(2) (t/\tau_p)^2}, \quad (2.5)$$

where \mathcal{E}_0 is the amplitude and τ_p the full width at half maximum (FWHM) duration of the intensity envelope. The spectrum corresponding to this temporal shape can be retrieved by Fourier transformation:

$$\begin{aligned} \mathcal{E}_{\text{Gauss}}(z, \omega) &= \frac{1}{2\pi} \int_{-\infty}^{\infty} \mathcal{E}_0 e^{-2 \ln(2) (t/\tau_p)^2} e^{i\omega t} dt \\ &= \mathcal{E}_0 \frac{\sqrt{\pi} \tau_p}{\sqrt{2 \ln(2)}} \exp\left(-\frac{\omega^2 \tau_p^2}{8 \ln(2)}\right). \end{aligned} \quad (2.6)$$

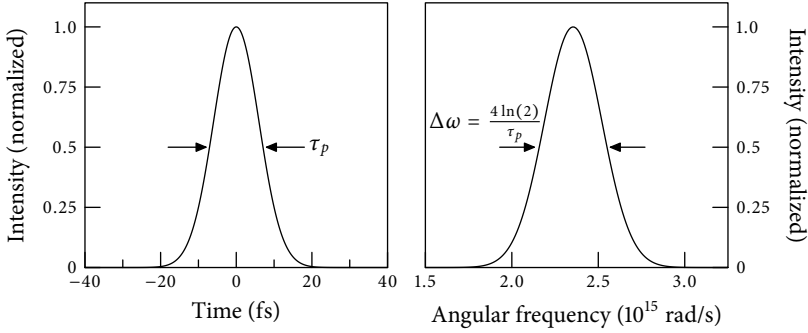


Figure 2.1: Left: the temporal field profile of a 10 fs (intensity FWHM), transform-limited Gaussian pulse. Right: the corresponding frequency spectrum, Gaussian as well, with a width $\Delta\omega$ of $4 \ln(2)/\tau_p \approx 280 \times 10^{12}$ rad/s.

So the spectrum is Gaussian as well, with a FWHM in intensity of $4 \ln(2)/\tau_p$, as shown in the right panel of figure 2.1. In this case without dispersion, the product of the spectral width $\Delta\omega$ and the pulse duration, called the time-bandwidth product, is constant:

$$\Delta\omega\tau_p = 2\pi c_B. \quad (2.7)$$

Here c_B depends on the pulse shape; for a Gaussian pulse, it is $2 \ln(2)/\pi \approx 0.441$. The equality in equation 2.7 is only a limiting case: the pulse is said to be transform-limited. When dispersion is present, the time-bandwidth product is larger, as will be shown in the next section.

An important conclusion from equation 2.7 is that the shorter a pulse is, the broader its spectrum must be. In general, this holds for any wave packet and its spectrum: the spectral width is inversely proportional to the wave packet's duration in time.

2.3 Waves and pulses in linear media

When an electric field propagates through a medium, the wave equation 2.1 must be augmented with a term describing the polarization induced by the field. The wave equation now becomes

$$\frac{\partial^2}{\partial z^2} E(z, t) - \mu_0 \epsilon_0 \frac{\partial^2}{\partial t^2} E(z, t) = \mu_0 \frac{\partial^2}{\partial t^2} P(z, t). \quad (2.8)$$

The polarization $P(z, t)$ represents the response of the medium to the field. Assuming that the polarization varies linearly with the field, and using the electric susceptibility χ_e of the medium, it can be written as

$$P(z, t) = \epsilon_0 \int_{-\infty}^{\infty} \chi_e(t) E(z, t - t') dt'. \quad (2.9)$$

When the medium response is assumed to be instantaneous, the polarization can be simplified to $P(z, t) = \epsilon_0 \chi_e E(z, t)$, as the time dependence in 2.9 is a simple δ -function in this case. In general, χ_e is a tensor to allow different polarizabilities along different axes in the medium, where each polarization component can depend on any of the applied field components. However, for the discussion in this paragraph, an isotropic medium is assumed.

In order to facilitate the extension to wave packets later on, the wave equation 2.8 is transformed to the frequency domain:

$$\frac{\partial^2}{\partial z^2} E(z, \omega) + \mu_0 \epsilon_0 \omega^2 (1 + \chi_e(\omega)) E(z, \omega) = 0. \quad (2.10)$$

The general solution to this modified wave equation again consists of plane waves,

$$E(z, t) = A e^{i(k(\omega)z - \omega t)} + B e^{-i(k(\omega)z + \omega t)}, \quad (2.11)$$

but now the wave vector $k(\omega)$ has become a frequency-dependent quantity:

$$k^2(\omega) = \mu_0 \epsilon_0 \omega^2 (1 + \chi_e(\omega)) = \frac{\omega^2}{c^2} (1 + \chi_e(\omega)). \quad (2.12)$$

Keeping in mind that in general $\chi_e(\omega)$ is a complex quantity, and again discarding the waves propagating in the negative z -direction, the solutions can be written as

$$E(z, t) = A e^{-\alpha(\omega)z} e^{i(\omega z n(\omega)/c - \omega t)}, \quad (2.13)$$

where $n(\omega) = \text{Re}\sqrt{1 + \chi_e(\omega)}$ is the index of refraction of the medium, and $\alpha(\omega) = \text{Im}\sqrt{1 + \chi_e(\omega)}$ is the absorption coefficient for the electric wave in the medium. In the presence of a resonance in the medium, the absorption will display a Lorentzian frequency dependence, and the index of refraction will follow a dispersive curve, as shown in figure 2.2. Thus the wave travels through the medium with a frequency-dependent velocity $c/n(\omega)$, and while propagating through the medium, it experiences attenuation (or amplification, in the case of media that exhibit population inversion).

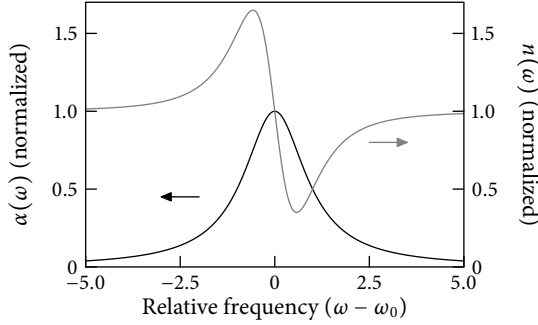


Figure 2.2: The absorption coefficient $\alpha(\omega) = \text{Im}\sqrt{1 + \chi_e(\omega)}$ and the index of refraction $n(\omega) = \text{Re}\sqrt{1 + \chi_e(\omega)}$ versus frequency in the vicinity of a resonance.

Next, we consider again the propagation of a superposition of waves. Inserting the wave packet $\mathcal{E}(z, \omega)e^{i(k_0 z - \omega_1 t)}$ into the wave equation and expanding all derivatives while taking out the carrier wave yields a wave equation for the envelope function:

$$\frac{\partial^2}{\partial z^2} \mathcal{E}(z, \omega) + 2ik_0 \frac{\partial}{\partial z} \mathcal{E}(z, \omega) - k_0^2 \mathcal{E}(z, \omega) + \mu_0 \epsilon_0 \omega_1^2 (1 + \chi_e(\omega)) \mathcal{E}(z, \omega) = 0. \quad (2.14)$$

This second-order differential equation can be simplified when the envelope function varies sufficiently slowly compared to the carrier wave. Then the first term in 2.14 can be neglected compared to the second term,

$$\frac{\partial^2}{\partial z^2} \mathcal{E}(z, \omega) \ll 2ik_0 \frac{\partial}{\partial z} \mathcal{E}(z, \omega), \quad (2.15)$$

which is known as the slowly-varying envelope approximation (SVEA). Although this approximation might seem inappropriate for pulses shorter than about 1 ps, the results obtained using this approximation can in general be applied reasonably well even for pulses lasting only a few cycles of the carrier wave. In the SVEA, the envelope wave equation 2.14 can be simplified to

$$\frac{\partial}{\partial z} \mathcal{E}(z, \omega) - i \frac{1}{2k_0} (k^2(\omega) - k_0^2) \mathcal{E}(z, \omega) = 0. \quad (2.16)$$

As a final step, $k(\omega)$ is expanded around the carrier frequency ω_1 ,

$$\begin{aligned} k(\omega) &= k_0 + \left. \frac{dk}{d\omega} \right|_{\omega_1} (\omega - \omega_1) + \frac{1}{2} \left. \frac{d^2 k}{d\omega^2} \right|_{\omega_1} (\omega - \omega_1)^2 + \dots \\ &= k_0 + k'(\omega - \omega_1) + k''(\omega - \omega_1)^2 + \dots, \end{aligned} \quad (2.17)$$

and it is assumed that $k(\omega) - k_o$ is small, so that $k^2(\omega) - k_o^2$ can be approximated by

$$\begin{aligned} k^2(\omega) - k_o^2 &= (k(\omega) + k_o)(k(\omega) - k_o) \\ &\approx 2k_o(k_o + k'(\omega - \omega_l) + k''(\omega - \omega_l)^2 + \dots - k_o) \\ &= 2k_o \left(\sum_{n=1}^{\infty} \frac{1}{n!} \frac{d^n k}{d\omega^n} \Big|_{\omega_l} (\omega - \omega_l)^n \right). \end{aligned} \quad (2.18)$$

The wave equation now reduces to:

$$\frac{\partial}{\partial z} \mathcal{E}(z, \omega) - i \left(\sum_{n=1}^{\infty} \frac{1}{n!} \frac{d^n k}{d\omega^n} \Big|_{\omega_l} (\omega - \omega_l)^n \right), \quad (2.19)$$

which can be Fourier-transformed back to the time domain, yielding

$$\frac{\partial}{\partial z} \mathcal{E}(z, t) - \sum_{n=1}^{\infty} \frac{i^{n+1}}{n!} \frac{d^n k}{d\omega^n} \Big|_{\omega_l} \frac{\partial^n}{\partial t^n} \mathcal{E}(z, t) = 0. \quad (2.20)$$

If only the terms up to second order are kept, we have

$$\frac{\partial}{\partial z} \mathcal{E}(z, t) + k' \frac{\partial}{\partial t} \mathcal{E}(z, t) - \frac{1}{2} k'' \frac{\partial^2}{\partial t^2} \mathcal{E}(z, t) = 0. \quad (2.21)$$

This equation describes the propagation of a pulse envelope through a linear medium, taking into account the dispersion up to second order. When higher-order dispersion becomes significant, the appropriate higher-order terms as given in 2.20 can be included.

2.4 Dispersion in linear media

To gain some more insight in the propagation of pulses in a dispersive medium, we turn again to the Gaussian pulse. Starting from the frequency domain wave equation 2.10, it is seen that the general solution for the envelope can be written as $\mathcal{E}(z, \omega) = \mathcal{E}(o, \omega) e^{ik(\omega)z}$. Using the Gaussian spectral envelope $\mathcal{E}_o e^{-2 \ln(2)(\omega/\Delta\omega)^2}$, with an intensity FWHM of $\Delta\omega$, and inserting the lowest-order terms of the expansion of $k(\omega)$ into the general solution, we get

$$\mathcal{E}(z, \omega) = \mathcal{E}_o \exp \left(-ik_o z - ik' z (\omega - \omega_l) - \left[\frac{2 \ln(2)}{\Delta\omega^2} + ik'' z \right] (\omega - \omega_l)^2 \right). \quad (2.22)$$

Transforming this to the time domain, we find

$$\begin{aligned} \mathcal{E}(z, t) &\propto \mathcal{E}_o \exp \left(-i\omega_l \left(t - \frac{z}{v_\phi} \right) - \frac{\Delta\omega^2}{8 \ln(2) + 2ik'' z \Delta\omega^2} \left(t - \frac{z}{v_g} \right)^2 \right) \\ &= \mathcal{E}_c(t, z) \exp \left(\frac{2 \ln(2) \Delta\omega^2 - \frac{1}{2} ik'' z \Delta\omega^4}{16 \ln^2(2) + (k'' z \Delta\omega^2)^2} \left(t - \frac{z}{v_g} \right)^2 \right). \end{aligned} \quad (2.23)$$

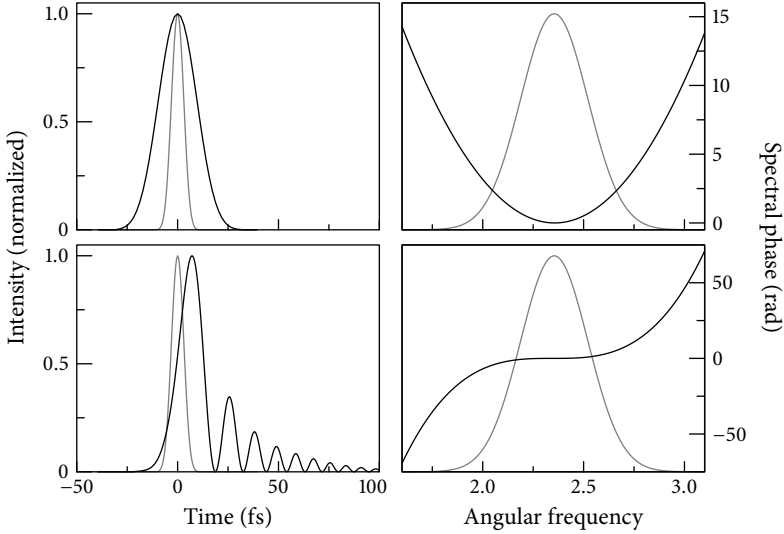


Figure 2.3: The effect of quadratic (top panels) and cubic (bottom panels) dispersion on the temporal pulse shape of a 7 fs transform-limited Gaussian input pulse. On the left, the input pulse is shown in gray and the dispersed pulse in black, while on the right the spectral phase is shown in black with the Gaussian spectrum in gray. A quadratic spectral phase broadens the pulse in time, while a cubic phase also gives rise to a train of post-pulses.

This field is composed of a carrier wave at ω_l , travelling at a phase velocity $v_\phi = \omega/k|_{\omega_l}$, and an envelope that is still Gaussian, travelling at the group velocity $v_g = d\omega/dk|_{\omega_l} = 1/k'$. However, the pulse envelope now depends on k'' , as can be seen from the real part of equation 2.23. The width has become

$$\tau_p(z) = \sqrt{\frac{16 \ln^2(2) + (k''z\Delta\omega^2)^2}{\Delta\omega^2}} = \tau_p(0) \sqrt{1 + \frac{(2k''z \ln(2))^2}{\tau_p(0)^4}}. \quad (2.24)$$

First-order dispersion, described by k' and characterized by a linear spectral phase, only shifts the envelope of the pulse in time, as can be seen from the $(t - z/v_g)^2 = (t - k'z)^2$ term in 2.23. In contrast, second-order dispersion, described by k'' and characterized by a quadratic spectral phase, tends to broaden the pulse in time. This is also shown in figure 2.3, where a transform-limited 7 fs input pulse is approximately tripled in length after experiencing a group velocity dispersion of only 30 fs². In such cases, the time-bandwidth product (equation 2.7) increases with increasing second-order dispersion.

For a Gaussian pulse, we obtain

$$\Delta\omega\tau_p = \sqrt{16 \ln^2(2) + (k''z\Delta\omega^2)^2}. \quad (2.25)$$

For such a dispersed pulse, the instantaneous frequency of the pulse (which is the time derivative of the phase) is not constant anymore, but varies linearly in time: the pulse is said to be *chirped*.

Higher-order dispersion introduces other pulse distortions. Third-order dispersion for example, originating from the next term in the expansion of the wave vector k , introduces a strong temporal asymmetry in addition to pulse broadening. This is clearly seen in the lower part of figure 2.3 as a train of post-pulses. The inclusion of even higher-order terms causes similar pulse broadening and substructures like pre- and post-pulses. In general, the broader the bandwidth of a pulse, the more higher-order terms need to be taken into account for a satisfactory description of its propagation.

2.5 The carrier-envelope phase

When considering ultrashort pulses that last only a few cycles of the electromagnetic field, an important parameter is the phase between the carrier wave and the envelope of the pulse, which is indicated in figure 2.4. Many aspects of the interaction between ultrashort pulses and matter, for example in high harmonic generation, depend on this parameter, which is called the carrier-envelope phase ϕ_{ce} . Therefore, it is necessary to include it in the mathematical description. To this end, the propagation of a wave packet through a medium is analyzed. The z -dependence of the plane-wave solutions to equation 2.8 is given by $e^{ik(\omega)z}$, and using the Fourier relation the total field of the wave

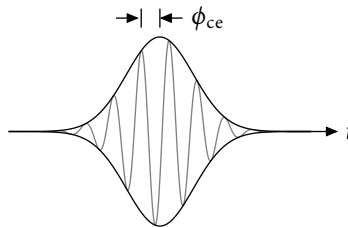


Figure 2.4: The carrier-envelope phase ϕ_{ce} of a pulse is the phase between the envelope of the pulse (indicated in black) and the underlying carrier wave (indicated in gray).

packet can be written as

$$E(t, z) = \int_{-\infty}^{\infty} E(\omega) e^{ik(\omega)z} e^{-i\omega t} d\omega. \quad (2.26)$$

Writing $E(\omega)$ as the inverse Fourier transform of $E(\tau)$, this expression becomes

$$E(t, z) = \int_{-\infty}^{\infty} \frac{1}{2\pi} \int_{-\infty}^{\infty} E(\tau) e^{i\omega\tau} d\tau e^{ik(\omega)z} e^{-i\omega t} d\omega. \quad (2.27)$$

Using the propagator function

$$G(t - \tau) = \frac{1}{2\pi} \int_{-\infty}^{\infty} e^{i(\omega(t-\tau) - k(\omega)z)} d\omega, \quad (2.28)$$

the field can be written as

$$E(t, z) = \int_{-\infty}^{\infty} E(\tau) G(t - \tau, z) d\tau. \quad (2.29)$$

In this way, the propagation of the field through a medium is easily described through the $k(\omega)z$ term in the propagator. Using the expansion of $k(\omega)$ from equation 2.17 and the definitions of the phase and group velocities, the field after propagating through a length z is given by

$$\begin{aligned} E(t, z) &= \frac{1}{2\pi} \exp\left(i\left(\omega_l \frac{dk}{d\omega} - k_l\right)z\right) \int_{-\infty}^{\infty} \int_{-\infty}^{\infty} E(\tau) \exp\left(i\omega\left(t - \tau - \frac{z}{v_g}\right)\right) d\omega d\tau \\ &= \exp\left(i\omega_l\left(\frac{1}{v_g} - \frac{1}{v_\phi}\right)z\right) \int_{-\infty}^{\infty} E(\tau) \delta\left(t - \tau - \frac{z}{v_g}\right) d\tau \\ &= \exp\left(i\omega_l\left(\frac{1}{v_g} - \frac{1}{v_\phi}\right)z\right) E\left(t - \frac{z}{v_g}\right). \end{aligned} \quad (2.30)$$

The pulse field has acquired an extra phase $\omega_l\left(\frac{1}{v_g} - \frac{1}{v_\phi}\right)z$ depending on the difference between the group and phase velocities in the medium. The carrier wave travelling at v_ϕ slips underneath the envelope travelling at v_g , so the carrier-envelope phase ϕ_{ce} is continuously changing when the pulse travels through a dispersive medium. As said, this quantity turns out to be of great importance for the generation and control of ultrashort pulses, as will be discussed later on.

2.6 Pulse trains

After this discussion of single pulses and their propagation through a medium, we now turn to the description of multiple pulses. In particular, consider a train of N similar

short pulses that are spaced evenly in time. If the field of a single pulse is given by $E_{\text{single}}(t)$, the electric field of the pulse train can be written as

$$E(t) = \sum_{n=0}^{N-1} E_{\text{single}}(t - nT), \quad (2.31)$$

where T is the time delay between individual pulses. Fourier transforming this expression, keeping in mind that the Fourier transform of the n^{th} pulse acquires a phase $-n\omega T$ (that is, $\mathcal{F}(E(t - nT)) = \exp(-in\omega T)\mathcal{F}(E(t))$), we derive:

$$\begin{aligned} E_{\text{train}}(\omega) &= E_{\text{single}}(\omega) \sum_{n=0}^{N-1} e^{-in\omega T} \\ &= E_{\text{single}}(\omega) \frac{1 - e^{-iN\omega T}}{1 - e^{-i\omega T}}. \end{aligned} \quad (2.32)$$

As the intensity is proportional to the square of the field, we obtain

$$\begin{aligned} I_{\text{train}}(\omega) &= \frac{1 - \cos(N\omega T)}{(1 - \cos(\omega T))} I_{\text{single}}(\omega) \\ &= \frac{\sin^2(N\omega T/2)}{\sin^2(\omega T/2)} I_{\text{single}}(\omega). \end{aligned} \quad (2.33)$$

This expression shows that the spectrum of a pulse train has the overall shape of the single pulse spectrum $I_{\text{single}}(\omega)$, but with a modulated amplitude. This modulation becomes more and more pronounced when more pulses are added to the sequence, as is shown in figure 2.5. For only two pulses, the modulating function is just $4 \cos^2(\omega T/2)$, a simple cosine modulation with a period of $1/T$. When the pulse train grows longer, the peaks narrow down, while their period remains constant. In the limit of an infinite pulse train, we obtain:

$$\begin{aligned} I_{\text{train},\infty}(\omega) &= \lim_{N \rightarrow \infty} \frac{\sin^2(N\omega T/2)}{N \sin^2(\omega T/2)} I_{\text{single}}(\omega) \\ &= I_{\text{single}}(\omega) \sum_{n=0}^{\infty} \delta(\omega T - 2\pi n), \end{aligned} \quad (2.34)$$

a sequence of infinitely narrow spikes separated by the pulse repetition frequency $\omega_{\text{rep}} = 2\pi/T$. From this comb-like structure the term *frequency comb* is derived. It is important that all the frequency components of the comb be locked in phase if they are to form a train of short pulses. When such pulses are to be generated, the usual method

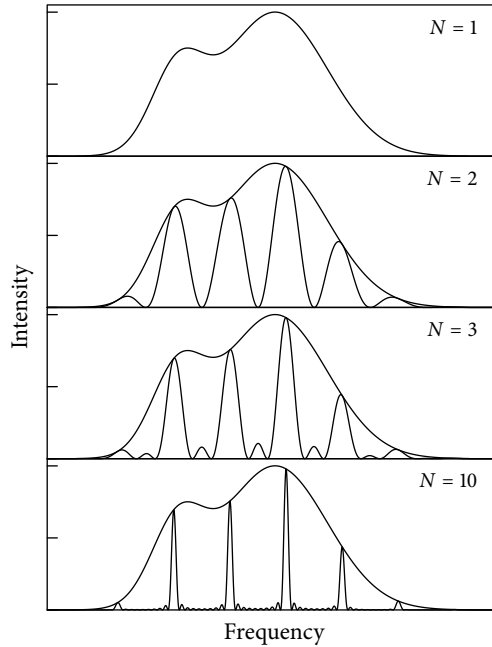


Figure 2.5: The spectrum of pulse trains with an increasing number of pulses N . For $N = 1$, this is simply the single-pulse spectrum, which has been repeated in the other panels for comparison. When more pulses are added, the spectrum more and more resembles a regular mode structure. The individual graphs are normalized to the maximum intensity.

is to generate a large number of discrete frequency components and to phase-lock them together, a process called *mode-locking*.

When the effects of dispersion are included as well, the slip between the carrier wave and the envelope needs to be incorporated. An extra phase factor of $n\phi_{ce}$ is added to the field in equation 2.32, yielding

$$I_{\text{train},\infty}(\omega) = I_{\text{single}}(\omega) \sum_{n=0}^{\infty} \delta(\omega T - \phi_{ce} - 2\pi n) \quad (2.35)$$

for the infinite pulse train spectrum. The frequencies in the comb are no longer an exact multiple of the repetition frequency, but are shifted over ϕ_{ce}/T . Now we can write the

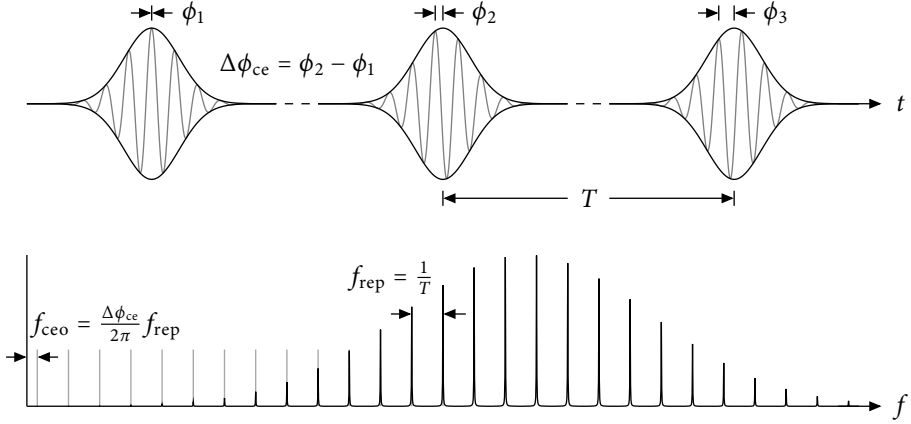


Figure 2.6: The relation between the time domain and frequency domain picture of a frequency comb, parametrized by f_{rep} and f_{ceo} .

frequency of the n^{th} comb mode as

$$\omega_n = \frac{\phi_{\text{ce}} + 2\pi n}{T} = \omega_{\text{ceo}} + n\omega_{\text{rep}}, \quad (2.36)$$

where the carrier-envelope offset frequency ω_{ceo} and the pulse repetition frequency ω_{rep} are introduced. Expressed as normal frequencies, the corresponding parameters are defined as f_{ceo} and f_{rep} . Expression 2.36 demonstrates the usefulness of the frequency comb principle: with only two parameters, f_{rep} and f_{ceo} or T and ϕ_{ce} , all the frequencies of the comb can be controlled. Fixing these two by locking them to a stable reference results in a comb of frequencies that are fixed with virtually the same precision as the reference.

The intimate relation between the time domain picture and the frequency domain picture of a frequency comb is summarized in figure 2.6, where a few pulses out of an infinite train are shown, with a carrier-envelope phase slip of $2\pi/3$. The corresponding frequency spectrum shows the mode structure, the period of which is inversely related to the pulse time delay, and the offset frequency of which is proportional to the carrier-envelope phase slip $\Delta\phi_{\text{ce}} = \phi_2 - \phi_1$.

2.7 Propagation in non-linear media: the non-linear index of refraction

The assumption made in section 2.3 that the polarization of the medium varies linearly with the electric field is not generally valid: especially at high field strengths, a non-linear polarization will be induced. The polarization can be written as

$$\mathbf{P} = \epsilon_0 \left[\chi^{(1)} \mathbf{E} + \chi^{(2)} \mathbf{E} \mathbf{E} + \chi^{(3)} \mathbf{E} \mathbf{E} \mathbf{E} + \dots \right], \quad (2.37)$$

where $\chi^{(j)}$ is the j th order susceptibility, a tensor of rank $j + 1$. Many optical effects can be related to the different orders of this expansion; however, in this section we will focus on the non-linear index of refraction only, a third-order effect.

The first-order susceptibility $\chi^{(1)} = \chi_e$ is the linear susceptibility discussed before, which relates to the index of refraction n and the absorption α of the medium. The second-order susceptibility describes effects that depend on the square of the field strength, such as second harmonic generation and parametric interactions; it is non-zero only for media without inversion symmetry. The third-order term gives rise to effects such as third-harmonic generation, four-wave mixing, non-linear refraction, etcetera. To include its effect in the wave equation, we assume that the non-linear response of the medium is instantaneous (therefore neglecting effects like the Raman effect, which is a time-delayed response of the medium). The third-order polarization can then be written $P_{NL}(z, t) = \epsilon_0 \epsilon_{NL} E(z, t)$, where $\epsilon_{NL} = \frac{3}{4} \chi^{(3)} |E(z, t)|^2$ is the non-linear part of the permittivity. In this expression, the polarization oscillating at the third harmonic has been neglected. Inserting this term into equation 2.8 and following the same manipulations as used in section 2.3, the result is

$$2i\kappa_0 \frac{\partial}{\partial z} \mathcal{E}(z, \omega) + (\kappa^2(\omega) - \kappa_0^2) \mathcal{E}(z, \omega) = 0, \quad (2.38)$$

an equation exactly like 2.16, but now with a different propagation constant $\kappa^2(\omega) = \frac{\omega^2}{c^2} \epsilon(\omega) = \frac{\omega^2}{c^2} (1 + \chi_e + \frac{3}{4} \chi^{(3)} |E|^2)$. Using the non-linear index of refraction $\tilde{n} = n + n_2 |\mathcal{E}|^2$ and absorption coefficient $\tilde{\alpha} = \alpha + \alpha_2 |\mathcal{E}|^2$, the permittivity can be written

$$\epsilon(\omega) = \left(\tilde{n} + \frac{i\tilde{\alpha}}{2\kappa_0} \right)^2. \quad (2.39)$$

When the non-linear absorption is discarded, and $n_2 |\mathcal{E}|^2 + i\alpha/(2\kappa_0)$ is renamed as Δn , this simplifies to

$$\epsilon(\omega) = (n + \Delta n)^2 \approx n + 2n\Delta n. \quad (2.40)$$

Treating the effect of Δn as a small perturbation, the change of the propagation constant is small as well. Hence it can be written as $\kappa + \Delta\kappa$, with $\Delta\kappa = \kappa_0 \Delta n$. Furthermore, similar

to equation 2.18, $\kappa^2(\omega) - \kappa_0^2$ is approximated by $2\kappa_0(\kappa(\omega) - \kappa_0)$. Equation 2.38 now reads

$$\frac{\partial}{\partial z} \mathcal{E}(z, \omega) - i(\kappa(\omega) + \Delta\kappa - \kappa_0) \mathcal{E}(z, \omega) = 0. \quad (2.41)$$

Again expanding $\kappa(\omega)$ around the carrier frequency and Fourier transforming to the time domain, we arrive at

$$\frac{\partial}{\partial z} \mathcal{E}(z, t) + \kappa' \frac{\partial}{\partial t} \mathcal{E}(z, t) + \frac{i}{2} \kappa'' \frac{\partial^2}{\partial t^2} \mathcal{E}(z, t) = i \frac{\omega_1 n_2}{c} |\mathcal{E}|^2 \mathcal{E}(z, t) - \frac{\alpha}{2} \mathcal{E}(z, t). \quad (2.42)$$

This equation is known as the *non-linear Schrödinger equation*, and it incorporates the effects of absorption, first- and second-order dispersion and the non-linear index of refraction. Although many assumptions are made in its derivation, which limits its application to pulses longer than about a picosecond, still many propagation effects are at least qualitatively described by this equation.

Two of the effects that result from the non-linear index of refraction warrant some special attention, namely self-phase modulation (SPM) and self-focusing. To start with the latter, it is seen that for any beam with a non-uniform intensity profile, the intensity-dependent index of refraction $\tilde{n} = n + n_2 |\mathcal{E}|^2$ will lead to a variation of the index of refraction over the transverse beam profile. Thus for a Gaussian beam, the index of refraction will be higher on axis, which effectively creates a lens that focuses the beam during propagation. This effect can be the cause of optical damage, but also of filament formation, when self-focusing is balanced by diffraction.

Self-phase modulation is another consequence of the non-linear index of refraction. To study its effects, we inspect the non-linear Schrödinger equation without dispersion and absorption, leaving only

$$\frac{\partial}{\partial z} \mathcal{E}(z, t) = \frac{i\omega_1 n_2}{c} |\mathcal{E}(z, t)|^2 \mathcal{E}(z, t). \quad (2.43)$$

This equation is easily integrated, yielding

$$\mathcal{E}(z, t) = \mathcal{E}(0, t) e^{i\omega_1 n_2 |\mathcal{E}(z, t)|^2 z / c}. \quad (2.44)$$

The envelope of the pulse propagates undistorted through the medium, but a phase factor $\delta\phi = \omega_1 n_2 |\mathcal{E}(z, t)|^2 z / c$ is added, growing with distance and proportional to the intensity of the field. Since the instantaneous frequency of the pulse is the time derivative of the phase, a field varying in time will result in a frequency chirp added to the pulse:

$$\delta\omega = -\frac{d\phi_{NL}}{dt} = -\frac{\omega_1 n_2 z}{c} \frac{d}{dt} |\mathcal{E}(z, t)|^2. \quad (2.45)$$

Thus for positive n_2 , in the leading edge of the pulse the frequency is decreased as $d|\mathcal{E}|^2/dt > 0$ there, while in the trailing edge the frequency is increased. The pulse will therefore acquire extra frequency components during propagation, and an approximately linear frequency chirp over the central part of the pulse. Using proper phase compensation techniques, it is possible to recompress such a spectrally broadened pulse. Similar approaches are commonly used to obtain few-cycle pulses from high-power laser systems that do not have a sufficiently wide gain bandwidth, see e.g. [112].

2.8 Harmonic generation

The higher-order polarization terms can also be the source of radiation oscillating at different frequencies than the driving radiation, in various frequency mixing schemes. Harmonic generation is such a process, where a single-frequency input field is converted to a field with a frequency that is an exact multiple of the driving frequency.

For second-harmonic generation, we consider the interaction of a fundamental field $E_1(z, t) = E_1(z)e^{-i(\omega_1 t - k_1 z)}$ and a harmonic field $E_2(z, t) = E_2(z)e^{-i(\omega_2 t - k_2 z)}$ where $\omega_2 = 2\omega_1$. The corresponding polarization terms are given by

$$\begin{aligned} P_1(z, t) &= \frac{1}{2}\epsilon_0\chi^{(2)}(-\omega_1; 2\omega_1, -\omega_1)E_2(z, t)E_1^*(z, t) \\ P_2(z, t) &= \frac{1}{2}\epsilon_0\chi^{(2)}(-2\omega_1; \omega_1, \omega_1)E_1(z, t)E_1(z, t). \end{aligned} \quad (2.46)$$

Inserting these into equation 2.8, two coupled equations can be derived for the amplitudes of the waves $E_1(z)$ and $E_2(z)$:

$$\begin{aligned} \frac{\partial E_1(z)}{\partial z} &= -\frac{i\omega_1\chi^{(2)}}{2cn_1}E_2E_1^*e^{-i\Delta kz} \\ \frac{\partial E_2(z)}{\partial z} &= -\frac{i\omega_2\chi^{(2)}}{4cn_2}E_1E_1e^{i\Delta kz}, \end{aligned} \quad (2.47)$$

where the n_i denote the refractive index at the corresponding frequencies and $\Delta k = 2k_1 - k_2$ is the phase mismatch. From these equations it follows that a second-harmonic field will be generated even when it is initially zero, while backconversion to the fundamental can occur when there is enough power in the second-harmonic field. To make the equations more useful for the discussion of short pulses, the fields are expressed with an

explicit amplitude and phase term, i.e. $E_1(z) = \rho_1 e^{i\phi_1}$ and $E_2(z) = \rho_2 e^{i\phi_2}$ (see e.g. [88]):

$$\begin{aligned}
 \frac{\partial \rho_1}{\partial z} &= -\frac{\omega_1 \chi^{(2)}}{2cn_1} \rho_1 \rho_2 \sin \theta \\
 \frac{\partial \rho_2}{\partial z} &= \frac{\omega_2 \chi^{(2)}}{4cn_2} \rho_1^2 \sin \theta \\
 \frac{\partial \phi_1}{\partial z} &= -\frac{\omega_1 \chi^{(2)}}{2cn_1} \rho_2 \cos \theta \\
 \frac{\partial \phi_2}{\partial z} &= -\frac{\omega_2 \chi^{(2)}}{4cn_2} \frac{\rho_1^2}{\rho_2} \cos \theta,
 \end{aligned} \tag{2.48}$$

with $\theta = 2\phi_1 - \phi_2 + \Delta kz$. Integration of these equations yields the evolution of the amplitude and the phase of the fundamental and harmonic waves.

Third-harmonic generation depends on the third-order non-linear susceptibility $\chi^{(3)}$, through which a fundamental field E_1 creates a polarization in the medium given by

$$P(3\omega) = \frac{1}{4} \chi^{(3)}(-3\omega; \omega, \omega, \omega) E(\omega) E(\omega) E(\omega). \tag{2.49}$$

The coupled amplitude equations for third-harmonic generation with focused Gaussian beams were solved by Bjorklund [113]. According to his treatment, the power of the harmonic radiation can be expressed as:

$$P(3\omega) \propto \chi^{(3)} P^3(\omega) F(b\Delta k, \frac{b}{L}, \frac{f}{L}), \tag{2.50}$$

where the phase-matching integral F is given by

$$F(b\Delta k, \frac{b}{L}, \frac{f}{L}) = \left| \int_{-\xi}^{\xi} \frac{\exp(-ib\Delta k \xi'/2)}{(1 + i\xi')^2} d\xi' \right|. \tag{2.51}$$

In these expressions, b is the confocal parameter of the beam, L the length of the medium, f the focus position and $\xi = \frac{2(z-f)}{b}$ the normalized coordinate. The phase-matching integral includes all geometric effects that influence the harmonic generation, and is a direct measure of the efficiency of the process.

One of the effects influencing the phase matching between the fundamental and harmonic radiation is the Gouy phase which a focused Gaussian beam acquires as it propagates through the focus, proportional to $\tan^{-1} \xi$. As the fundamental and the harmonic radiation have different focusing properties, they will acquire a different Gouy

phase; in addition, the Gouy phase is proportional to the harmonic order. Thus the generation of harmonics is arrested and even reversed when the waves travel through the focus. However, this effect can be compensated in a medium that provides a negative phase mismatch: in the optimum case, where $b\Delta k = -2$, the phase due to the medium dispersion balances the Gouy phase. Thus, for third-harmonic generation, one usually looks for a medium that shows a negative phase mismatch in the spectral region of interest. When such a medium is not available, third-harmonic generation is still possible if the focus of the fundamental beam is positioned on the boundary of the medium, such that cancellation of the amplitude over the focus is suppressed.

2.8.1 High-harmonic generation: the three-step model

For low-order harmonics generated by moderately intense laser fields up to 10^{13} W/cm² in a gaseous atomic medium, the perturbative approach used in the previous paragraph for third-harmonic generation describes the observations quite well: with increasing harmonic order, the intensity of the radiation drops rapidly. However, when the driving laser field has a higher intensity this approach breaks down, and for an adequate description of the generation of higher harmonics a different theoretical framework is called for. The observation of very high harmonics with an almost constant intensity up to a steep cut-off, the so-called plateau harmonics [92, 93], was a clear indication of the shortcomings of the perturbative theory. To explain such observations, Corkum and Kulander proposed a simple semi-classical theory of high harmonic generation [94, 114] for intense driving fields. In this view, the generation of harmonics is a three-step process, depicted schematically in figure 2.7, where a single atom in the medium is shown. First, the driving laser field tilts the Coulomb potential of the atom such that an electron can tunnel out, creating an ionic core and a free electron. In the next step, the motion of this free electron in the strong driving laser field is treated classically. The electron is accelerated by the field and driven away from its parent ion. As the field reverses sign, the electron is slowed down and accelerated back towards the ionic core. In the final step, the electron can collide with the core; if recombination occurs, a short burst of X-rays is emitted. The energy of the X-rays will be the sum of the ionization potential of the atoms I_p and the kinetic energy gained by the electron in the driving field. The latter of these contributions depends on the time the electron was liberated, as can be seen in figure 2.8. The model predicts a value of $I_p + 3.17U_p$, where $U_p = e^2 E_0^2 / 4\omega^2 m_e$ is the ponderomotive energy for an electron of mass m_e in a field with amplitude E_0 and a frequency ω . This corresponds very well with the experimentally observed cut-off

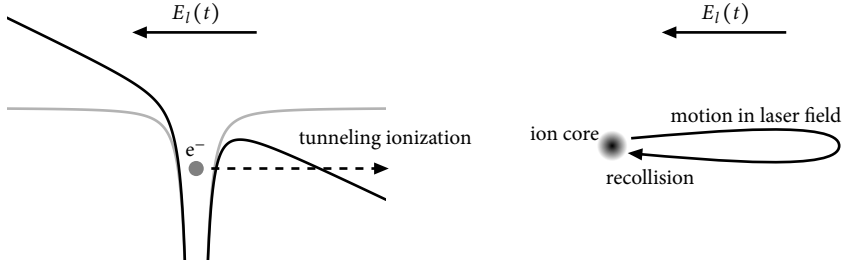


Figure 2.7: The three-step model of high-harmonic generation in an atomic gaseous medium. Left: the driving laser field $E_l(t)$ tilts the Coulomb potential of an atom such that the electron can tunnel out. Right: the liberated electron is accelerated in the driving laser field, which directs the electron back to the ionic core when it reverses sign. Upon recollision, a short burst of X-rays is emitted.

energy of the plateau harmonics. These harmonics of the highest energy can be produced only by electrons that tunneled out of the atom at the most favorable moment during the fundamental field cycle. Lower energy harmonics originate from electrons that were set free at other times, and as can be seen from figure 2.8, for each harmonic energy there are two electron trajectories that contribute most, a longer and a shorter one. The harmonics produced from these different trajectories have a very different dependence of their phase on the driving laser intensity, as well as a different spatial distribution: the short trajectory harmonics tend to be less chirped and spatially better collimated than those resulting from the long trajectories.

The semi-classical model, although it is the subject of critique [115], is confirmed by the full quantum mechanical theory developed by Lewenstein et al. [95]. In this approach the phase of the generated harmonics can be derived from the classical action of the electron moving in the driving laser field. This quantity depends on the classical momentum of the electron \mathbf{p} and on the time of ionization t_0 and recombination t_1 :

$$S(\mathbf{p}, t_0, t_1) = \int_{t_0}^{t_1} \left(\frac{(\mathbf{p} - \mathbf{A}(t))^2}{2m_e} + I_p \right) dt, \quad (2.52)$$

where \mathbf{A} is the vector potential of the laser field. The phase of the q^{th} harmonic is then given by [116, 117]

$$\phi_q = -\frac{S(\mathbf{p}, t_0, t_1)}{\hbar} + q\omega t_1. \quad (2.53)$$

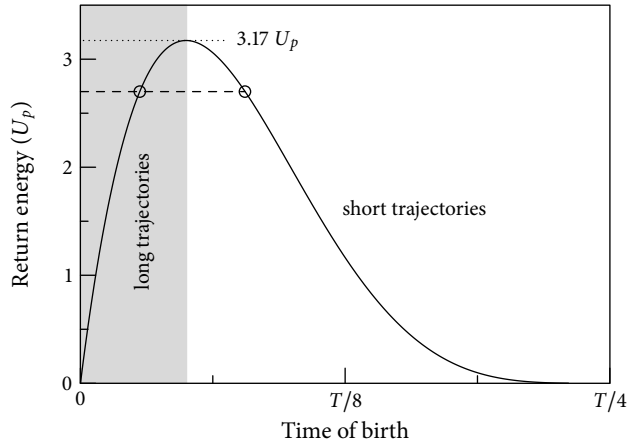


Figure 2.8: The return energy of a liberated electron as a function of the release time of the electron. The maximum return energy is about 3.17 times the ponderomotive energy of the electron in the field. The dashed line indicates a return energy lower than this cut-off energy: here two different trajectories can be identified, indicated by the circles. These are termed the short and long trajectories, and the resulting harmonics have very different characteristics (see text).

Thus the phase depends on the trajectory in the field taken by the electron, and hence it is different for the long and short trajectories. Although for both trajectories the phase shows a roughly linear dependence on the driving laser ponderomotive energy, the short trajectory phase has a much smaller slope than that of the long ones, the difference being a factor of about five to ten [116, 117]. Recent direct measurements of the atomic dipole phase confirm this behavior [104, 118].

Spectroscopy with frequency combs

The invention of the frequency comb has revolutionized the field of precision spectroscopy by providing an accurate optical frequency ruler over an extremely wide bandwidth covering the near-infrared and visible spectrum. In this chapter, the major principles and techniques that have been developed to put this versatile tool to use are presented. First the traditional methods of performing spectroscopy with frequency combs are introduced. Then the idea of direct excitation with comb pulses is detailed, including an analytic description of the process and a detailed numerical study of excitation with phase-locked pulse trains. Finally, a thorough survey is given of possible problems connected to this method of frequency comb spectroscopy, including systematic effects such as phase shifts caused by pulse picking, amplification and harmonic generation, and Doppler and Stark shifts.

3.1 Frequency combs

The generation of short optical pulses of 100 fs and longer using Kerr-lens mode-locked lasers has become a matter of routine in the last decade. Even laser systems emitting pulses that last only a few oscillations of the electromagnetic field (shorter than 10 fs) are commercially available these days. The most common source of short pulses is the Kerr-lens mode-locked Ti:sapphire laser. In this section its operation and the methods used to control its output in the form of a frequency comb will be described.

3.1.1 Ultrashort pulse generation: mode-locked lasers

Short pulses require a broad frequency spectrum, so for ultrashort pulse generation a broadband gain medium is necessary. Many types of laser media exist, based on dyes, doped fibers and doped crystals such as chromium-doped forsterite, titanium-doped sapphire, neodymium-doped YAG or YLF and many more. Of these materials, Ti:sapphire is the most versatile, and it allows the generation of the shortest pulses. Known as a laser medium since 1986 [119], it was first used for a Kerr-lens mode-locked laser in 1991 [31]. Ti:sapphire has an extremely wide gain profile, stretching from about 600 nm to well over 1050 nm, with a single-pass FWHM bandwidth of about 200 nm. At a central wavelength of about 780 nm, this corresponds to a Fourier limit slightly above 4 fs, or less than two cycles of the electro-magnetic field. Not all of this bandwidth will be available in a laser cavity, where gain narrowing decreases the spectral width substantially. However, this can be counteracted by self-phase modulation (SPM) in the laser crystal, where usually the cavity mode is focused to a very small waist. As the sapphire host material has a high damage threshold, it tolerates a high power density, so the generated SPM in Ti:sapphire can largely compensate the gain narrowing. This makes Ti:sapphire very well suited for use in ultrashort pulse lasers.

But given a medium that can sustain and amplify a wide bandwidth, a cavity is needed as well to build a laser. Such a cavity will allow only those frequencies to oscillate which fit the length of the cavity. Therefore, instead of the smooth bandwidth that can be generated by the medium alone (see the top panel of figure 3.1), a laser cavity will generate a broad spectrum of discrete modes, spaced by the inverse of the cavity's round-trip time (see the middle panel of figure 3.1). In the case of a linear cavity of length L , the mode frequencies are given by

$$f_q = \frac{qc}{2L}. \quad (3.1)$$

These modes form the basis for a pulse train, as described in the previous chapter: the mode spacing, equal to the repetition frequency, is $c/2L$, so the pulse separation in time will be $2L/c$, equivalent to the time it takes for the pulse to make one round-trip in the cavity. All modes within the gain bandwidth of the medium can oscillate simultaneously, provided that the gain is high enough to overcome the net round-trip cavity loss and self- and cross-saturation effects for that mode [120]. But this does not automatically result in a nice pulse train, as in general the output of the laser depends on the phase relation between the modes. The output shown in the middle panel of figure 3.1 is the result of randomly phased modes. Creating order in this chaos of many independently

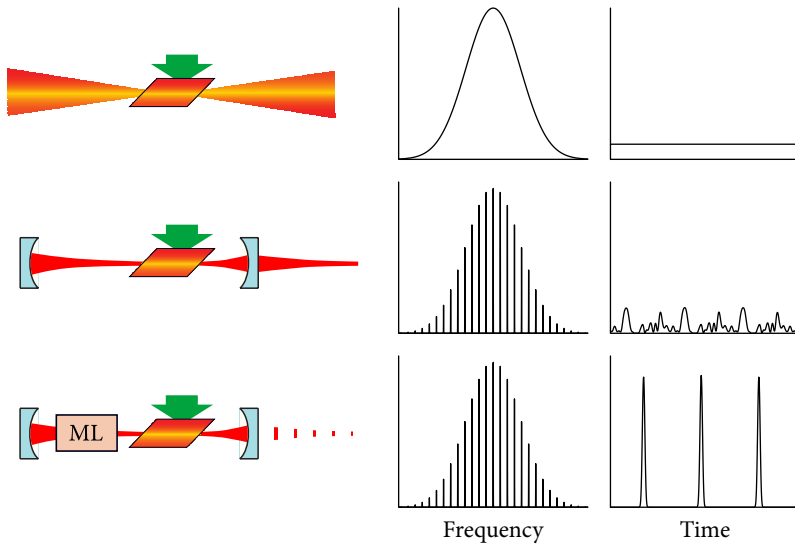


Figure 3.1: The basic ingredients of a mode-locked laser. Top panel: the broadband gain medium yields a continuous output with a broad and smooth spectrum. Middle: when placed inside a laser cavity, only the cavity modes are amplified, but as they all have random phases the output is erratic. Bottom: a mode-locking device (e.g. Kerr lens mode-locking) will allow all modes to oscillate in phase, thus producing short pulses in time.

oscillating modes is done by fixing the phase relation between them such that at specific times all modes interfere constructively to form a short pulse. This is referred to as *mode-locking*, and the result can be seen in the bottom panel of the figure. Several ways of mode-locking are possible, among which active mode-locking using an intra-cavity device that modulates the gain, saturable absorbers that favor relatively high intensity pulses while at the same time producing self-steepening of the pulses, and Kerr-lens mode-locking. The last method is based on the Kerr effect, according to which the non-linear index of refraction of the laser medium causes self-focusing of a beam when it has a higher intensity at its center than at its edges. High intensity pulses circulating in the cavity will be focused tighter in the medium, and will thus be in a different cavity mode than lower intensity pulses. When the cavity is set up such that the low-intensity modes suffer more losses (for instance using apertures, or by pumping only a very small region of the gain medium), the high intensity pulses are enhanced and will eventually

dominate. Since the most intense pulses are ultrashort pulses, this process automatically takes care of mode-locking. Mode-locking can be initiated by gently hitting one of the cavity mirrors, which starts a disturbance that quickly develops into a short pulse.

Still, the dispersion in the cavity due to the gain medium, the output coupler, the mirrors, the air path and other cavity elements can cause the modes to run out of phase. Therefore, intra-cavity dispersion compensation is needed to ensure continuous mode-locking. This can be achieved for example by employing angular dispersive elements such as prisms or gratings in the cavity, but more elegantly by using double-chirped mirrors [121, 122]. These mirrors consist of a stack of many dielectric layers with a varying thickness and varying index of refraction. The layer structure can be tailored such that different frequencies reflect at different depths in the stack, thus creating a frequency-dependent path length. Using matching sets of mirrors, the dispersion of a cavity can be compensated over a bandwidth of several hundreds of nanometers, allowing the generation of extremely short pulses.

3.1.2 Complete control of the electric field

The spectrum of such a short-pulse laser is a set of discrete frequencies, spaced by f_{rep} and offset from zero by f_{ceo} , as discussed in chapter 2. In the time domain, it corresponds to an infinite pulse train with a time $T = 1/f_{\text{rep}}$ between consecutive pulses, and a carrier-envelope phase slip of $\Delta\phi_{\text{ce}} = 2\pi f_{\text{ceo}}/f_{\text{rep}}$. The entire frequency comb can be controlled by manipulating only these two parameters f_{rep} and f_{ceo} , and when they are fixed, the electric field of the pulses is completely determined, apart from the *absolute* carrier-envelope phase ϕ_{ce} . Stabilization of f_{rep} can be easily done by detecting the pulse train with a photodiode, and filtering out f_{rep} or one of its harmonics. This signal can be mixed with that from a stable reference generator which is phase-locked to some absolute frequency standard, such as an atomic clock. The repetition rate can then be controlled by providing feedback on the cavity length, via e.g. a mirror mounted on a piezo-electric crystal. Depending on the frequency standard, f_{rep} can be stabilized to more than 13 digits over a timescale of several seconds.

Stabilizing f_{ceo} requires more effort, as the measurement of this parameter is much more complicated. The frequencies in a comb are given by $f_n = f_{\text{ceo}} + n f_{\text{rep}}$, so the offset frequency is the lowest frequency in the comb, which is in the RF domain. However, there is no light available at these frequencies, so it is impossible to measure f_{ceo} directly. But thanks to a clever technique developed by Hänsch in 1999, called f - $2f$ -interferometry [29, 30, 123], it can be measured using a non-linear interferometer. This technique uses

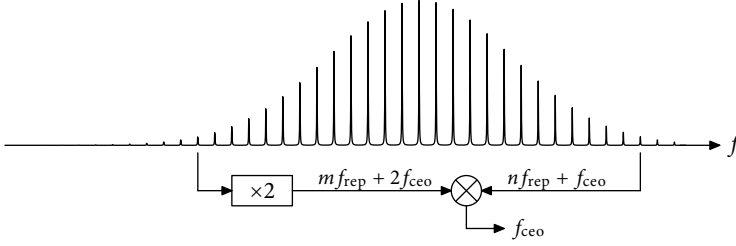


Figure 3.2: The principle of the f - $2f$ -interferometer. The low-frequency side of the comb is frequency doubled and compared with the high-frequency side: f_{ceo} is the lowest mixing product. The repetition rate f_{rep} can be directly measured from the comb light.

the second harmonic of the comb, of which the mode frequencies are given by

$$f_{n,\text{SHG}} = 2(f_{\text{ceo}} + n f_{\text{rep}}) = 2f_{\text{ceo}} + m f_{\text{rep}}. \quad (3.2)$$

When the red part of the comb spectrum is frequency doubled, and the spectrum itself is broad enough so that on the blue side there is still power in the frequency range of this doubled light, then both can be brought together on a photodiode to form beatnotes with a frequency spectrum given by (see figure 3.2):

$$f_{\text{beat}} = (2f_{\text{ceo}} + m f_{\text{rep}}) \pm (f_{\text{ceo}} + n f_{\text{rep}}) = \pm f_{\text{ceo}} + (m - n) f_{\text{rep}}. \quad (3.3)$$

Of these, the lowest detectable frequency is the offset frequency f_{ceo} . After detection and electronic filtering, the signal can be compared to a reference frequency and used for feedback. Changing the dispersion in the cavity using a pair of wedges already gives coarse control over the ratio of the group and phase velocities in the cavity and thus over ϕ_{ce} , while slightly modulating the pump power by way of an acousto-optic modulator in the pump beam [30] gives the fast control needed for an electronic feedback loop. With this method $\Delta\phi_{\text{ce}}$ has been stabilized with a residual jitter better than 100 mrad (see chapter 5 and [124–126]). The use of a monolithic ϕ_{ce} detection scheme as presented by Fuji et al. can even improve the ϕ_{ce} stability by a factor of about five [127].

3.2 Traditional frequency comb spectroscopy

The comb of precisely determined frequencies which results when f_{rep} and f_{ceo} of a mode-locked laser are locked to a reference can act as a frequency ruler, with which

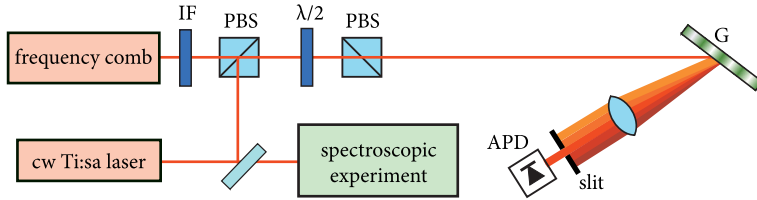


Figure 3.3: The setup used for absolute frequency calibration of a cw laser with a frequency comb. PBS: polarizing beam splitter cube, IF: interference filter, G: grating, APD: avalanche photodiode.

the frequency of a narrow-band cw laser can be measured. This is a powerful tool when performing for example a spectroscopic experiment, where a cw laser is used to excite a transition in an ensemble of atoms or molecules. To obtain an absolute frequency calibration, a beatnote is generated between the light emitted by the narrow-band cw laser and the light of the frequency comb. The setup for this is similar to that shown in figure 3.3, which was used in an experiment to perform spectroscopy on magnesium [128]. For this experiment, a cw Ti:sapphire laser (Coherent 899) was used to seed a Ti:sapphire multi-pass amplifier, whose output is converted to 202.5 nm, the wavelength needed for the experiment. A small part of the light from the cw Ti:sapphire laser is combined with the comb laser light on a beamsplitter. The comb light is filtered, to cut away the irrelevant parts of the comb laser spectrum, which would only add noise to the beat signal. Subsequently, further spectral selection is obtained by dispersing the light on a grating, after which only a narrow bandwidth around the frequency of the cw laser light is detected with an avalanche photo diode. The lowest frequency in the signal is the beat frequency f_{beat} between the cw light and the nearest comb mode, which can be filtered out and counted with a frequency counter. In figure 3.4, an example of such a beat signal is shown.

From the values of f_{rep} and f_{ceo} , derived from a rubidium-GPS frequency reference, and the measured value of f_{beat} , the absolute frequency of the transition can be determined simply from $f_{\text{ceo}} + n f_{\text{rep}} \pm f_{\text{beat}}$, provided it is known already with sufficient accuracy to be able to tell the number n of the mode with which the cw frequency is beating and to resolve the sign ambiguity. In the magnesium experiment, a fractional accuracy of about 10^{-8} was realized for f_{beat} . The determination of the absolute frequency is mainly limited by the jitter and linewidth of the cw laser, and by the residual comb jitter of about 1 MHz at the optical frequencies (RMS ≈ 300 kHz). Improvements can be made by locking the cw laser and the comb each to a stabilized high-finesse reference

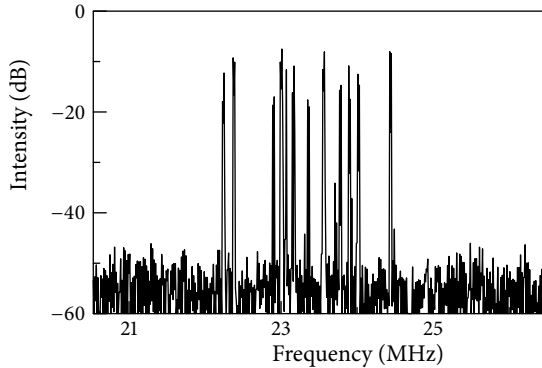


Figure 3.4: A beat note between the light of a frequency comb laser and the light from a cw Ti:sapphire oscillator used for high-resolution spectroscopy on magnesium. The frequency jitter of the beatnote is mostly due to the jitter of the cw Ti:sapphire laser during the scan of the spectrum analyzer. Sweep time: 8 ms/MHz, resolution bandwidth: 12 kHz, video bandwidth: 12 kHz.

cavity [129]. For even higher accuracy, the comb laser can be referenced to a cesium (fountain) clock; in such cases, an absolute accuracy of about 10^{-15} can be achieved, with a 10^{-16} reproducibility. This has been demonstrated on a variety of atomic and ionic systems, like the strontium ion at NPL [38], the mercury ion at NIST [39], the strontium lattice clock in Paris [40], the hydrogen atom at MPQ [130] and the $^{27}\text{Al}^+$ clock transition at NIST [43].

3.3 Direct excitation with frequency comb pulses

Although the method described in the previous section has produced results that show an unprecedented level of accuracy, it cannot be applied to just any interesting transition. First, the method requires an ultra-stable narrow-band cw laser to perform the actual spectroscopy. In the infrared, visible and ultraviolet regions, such lasers can be constructed without too many problems; in the deep-UV, this is difficult, and in the vacuum ultraviolet and beyond, this is an arduous endeavor [131] if not downright impossible. At the same time, the cw frequency must fall within the range of the frequency comb. Often some frequency mixing scheme for the cw laser can be employed to fulfill this demand, and also the comb itself can be broadened in a photonic crystal fiber, as no accuracy is sacrificed in the broadening process [132, 133]. However, at deep-UV

and shorter wavelengths, these demands are practically impossible to meet, so other techniques are needed.

A very good candidate is the direct excitation of atoms with phase-locked pulses, similar to Ramsey's method of separated oscillatory fields in the microwave region [64, 65, 134]. Here atoms move through a region where a resonant microwave field excites an atomic transition, creating a coherent superposition of the ground and excited states. Thus prepared, the atoms then travel some time without any field present, while the superposition of states evolves with a frequency proportional to the energy difference between them. Then the atoms pass through another (in atomic fountain configurations, the same) microwave region, where the field is phase-locked to the first field. The excitation contributions of the two excitation regions will interfere if the coherence survives the free flight time. Depending on the phase difference between the second field and the atomic superposition, the excited state amplitude is either enhanced or diminished. From this interference effect, the transition frequency can be determined with a very high accuracy, depending on the field-free flight time; this is the underlying principle of the cesium atomic clock, which is commercially available and is found in many metrology labs around the world. An improved version of this Ramsey-type clock is the cesium fountain clock, where a laser-cooled sample of cesium atoms is launched upward, passing through a microwave cavity, and falling back through the same cavity under the influence of gravity [135]. In such a configuration, a much longer field-free flight time in between the excitation zones can be achieved.

In the optical domain this technique can be used as well, with spatially separated standing wave laser fields produced by a single cw laser [66]. However, when the atoms are sufficiently slow, phase-locked pulses can be used to apply fields separated in time rather than in space to interrogate the atoms [67, 69–71]. Frequency combs readily supply the phase-locked pulses that are needed, and several of such experiments have been performed in recent years [72, 73, 78, 81–83]. It is this approach to Ramsey's method that can be employed for frequency comb metrology in the vuv, as the pulses from a frequency comb laser can be up-converted to the required frequency range after amplification or enhancement of the pulse's peak power. Provided that amplification and frequency conversion do not compromise the phase coherence of the pulses, the precision that frequency combs deliver in the infrared can be transported to vuv and shorter wavelengths.

The experiments in this thesis follow this idea, and demonstrate the power and potential of this approach for frequency comb metrology in the vuv. In chapters 6 and 7 experiments will be described that show the preservation of phase coherence in

the pulse trains during amplification and up-conversion, and the realization of high resolution frequency comb spectroscopy in the VUV. In this chapter, the methods are explored from a theoretical perspective. A detailed description of the excitation of atoms by coherent pulse trains will be given, as well as an overview of the limitations and potential pitfalls of the proposed methods.

3.4 Analytical model for excitation with phase-locked pulse trains

To gain insight into the method of coherent pulsed excitation, a theoretical model of the interaction between an atomic system and a train of phase-locked pulses must be used. As a first simplification, it will be assumed that the atom is a two-level system: the VUV ground state transitions probed in the experiments are very well described by such a simple model.

The atom is represented by a state vector $|\psi\rangle = c_1(t)|1\rangle + c_2(t)|2\rangle$, and finding expressions for the evolution of the coefficients c_i under the action of pulsed excitation will be the goal of this section. Matrices for the interaction with each single pulse, and a matrix for the field-free evolution of the atom in between the pulses will be constructed, so that the state of an atom initially in state $|\psi_0\rangle$, after the n th pulse can be written as

$$|\psi_n\rangle = \mathcal{M}_{\text{pulse}, n} \cdot \mathcal{M}_{\text{free}} \cdot \mathcal{M}_{\text{pulse}, n-1} \dots \mathcal{M}_{\text{free}} \cdot \mathcal{M}_{\text{pulse}, 1} |\psi_0\rangle. \quad (3.4)$$

The matrix for interaction with a single pulse $\mathcal{M}_{\text{pulse}}$ is derived starting from the Schrödinger equation,

$$i\hbar \frac{\partial}{\partial t} |\psi\rangle = H |\psi\rangle = (H_0 + H_{\text{int}}) |\psi\rangle. \quad (3.5)$$

The Hamiltonian of the free atom H_0 can be written

$$H_0 = \frac{\hbar}{2} \omega_{\text{atom}} (|2\rangle\langle 2| - |1\rangle\langle 1|), \quad (3.6)$$

where $\omega_{\text{atom}} = (E_2 - E_1)/\hbar$ is the transition frequency, with E_i the energy of the states. The zero point of energy is taken to be halfway between the two levels; spontaneous emission is not taken into account. The dipole interaction Hamiltonian H_{int} of the atom and the field $\mathbf{E}(z, t) = \mathcal{E}e^{-i\omega_1 t} + c.c.$ is given by

$$\begin{aligned} H_{\text{int}} &= -\mathbf{d}_{21} \cdot \mathbf{E} \\ &= -(\mathbf{d}_{21}|2\rangle\langle 1| + \mathbf{d}_{21}^*|1\rangle\langle 2|) \cdot (\mathcal{E}e^{-i\omega_1 t} + \mathcal{E}^*e^{i\omega_1 t}) \\ &= -\hbar(\Omega e^{-i\omega_1 t} + \tilde{\Omega}e^{i\omega_1 t})|2\rangle\langle 1| - \hbar(\tilde{\Omega}^*e^{-i\omega_1 t} + \Omega^*e^{i\omega_1 t})|1\rangle\langle 2|, \end{aligned} \quad (3.7)$$

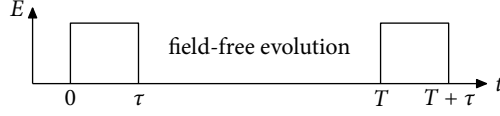


Figure 3.5: The excitation field used in the analytic model. Two square pulses of duration τ and separation T are used to excite the two-level atom.

where \mathbf{d}_{21} is the dipole moment connecting state $|1\rangle$ and $|2\rangle$, $\Omega = \mathbf{d}_{21} \cdot \mathcal{E}/\hbar$ is the so-called Rabi frequency, and $\tilde{\Omega} = \mathbf{d}_{21} \cdot \mathcal{E}^*/\hbar$. The total Hamiltonian is then given by

$$H_{\text{total}} = \hbar \begin{pmatrix} \omega_{\text{atom}}/2 & -\Omega e^{-i\omega_l t} - \tilde{\Omega} e^{i\omega_l t} \\ -\tilde{\Omega}^* e^{-i\omega_l t} - \Omega^* e^{i\omega_l t} & -\omega_{\text{atom}}/2 \end{pmatrix}. \quad (3.8)$$

The time dependence in the Hamiltonian can be removed by transforming to the Schrödinger picture, where the new state $|\tilde{\psi}\rangle$ is the transformed state $|\psi\rangle = \mathcal{U}|\tilde{\psi}\rangle$. \mathcal{U} is a unitary transformation describing rotation at the field frequency ω_l :

$$\mathcal{U} = \begin{pmatrix} e^{-i\omega_l t/2} & 0 \\ 0 & e^{i\omega_l t/2} \end{pmatrix}. \quad (3.9)$$

The Hamiltonian must be transformed as well: by inserting $|\psi\rangle = \mathcal{U}|\tilde{\psi}\rangle$ into the Schrödinger equation 3.5 and multiplying the resulting equation with \mathcal{U}^\dagger , the transformed Hamiltonian is expressed as

$$\begin{aligned} \tilde{H} &= -i\hbar\mathcal{U}^\dagger\dot{\mathcal{U}} + \mathcal{U}^\dagger H \mathcal{U} \\ &= \hbar \begin{pmatrix} -(\omega_l - \omega_{\text{atom}})/2 & -\Omega - \tilde{\Omega} e^{i2\omega_l t} \\ -\tilde{\Omega}^* e^{-i2\omega_l t} - \Omega^* & (\omega_l - \omega_{\text{atom}})/2 \end{pmatrix} \end{aligned} \quad (3.10)$$

The terms oscillating at $2\omega_l$ will average out on a timescale relevant to the interaction, so they are neglected: this approximation is known as the rotating wave approximation (see e.g. [136]). Writing $\Delta = \omega_l - \omega_{\text{atom}}$, the time-independent Hamiltonian now reads

$$\tilde{H} = \begin{pmatrix} -\hbar\Delta/2 & -\hbar\Omega \\ -\hbar\Omega^* & \hbar\Delta/2 \end{pmatrix}. \quad (3.11)$$

If the pulsed field interacting with the atom is assumed to have a square shape with a duration τ (see figure 3.5), integration of the Schrödinger equation is straightforward, yielding

$$|\psi(t)\rangle = e^{-i\tilde{H}\tau/\hbar}|\psi_0\rangle. \quad (3.12)$$

Writing the right hand side with the exponentiated operator as

$$e^{i\mathbf{w}\cdot\boldsymbol{\sigma}\tau}|\psi_0\rangle, \quad (3.13)$$

with $\sigma_x = \begin{pmatrix} 0 & 1 \\ 1 & 0 \end{pmatrix}$, $\sigma_y = \begin{pmatrix} 0 & -i \\ i & 0 \end{pmatrix}$ and $\sigma_z = \begin{pmatrix} 1 & 0 \\ 0 & -1 \end{pmatrix}$, while $\mathbf{w} = (\text{Re}(\Omega), -\text{Im}(\Omega), \Delta/2)$, it can be cast in a more illuminating form (see [137]) using

$$e^{i\mathbf{w}\cdot\boldsymbol{\sigma}\tau} = \cos(|\mathbf{w}|\tau) \mathbf{1} + i \frac{\mathbf{w}\cdot\boldsymbol{\sigma}}{|\mathbf{w}|} \sin(|\mathbf{w}|\tau), \quad (3.14)$$

where $\mathbf{1}$ is the unit matrix. Using this relation, the matrix $\mathcal{M}_{\text{pulse}}$ describing the interaction of a pulse with the two-level atom becomes:

$$\mathcal{M}_{\text{pulse}} = \begin{pmatrix} \cos(w\tau) + i \frac{\Delta}{2w} \sin(w\tau) & i \frac{\Omega}{w} \sin(w\tau) \\ i \frac{\Omega^*}{w} \sin(w\tau) & \cos(w\tau) - i \frac{\Delta}{2w} \sin(w\tau) \end{pmatrix}, \quad (3.15)$$

where $w = |\mathbf{w}| = \sqrt{|\Omega|^2 + (\Delta/2)^2}$. The excitation probability after the interaction of a single pulse with the atom can now be written as

$$|\psi_{\text{single}}\rangle = \mathcal{M}_{\text{pulse}}|\psi_0\rangle. \quad (3.16)$$

Assuming the atom to be initially in the ground state, we obtain for the state amplitudes

$$\begin{aligned} c_{1,\text{single}} &= \langle 1|\psi_{\text{single}}\rangle = \cos(w\tau) - i \frac{\Delta}{2w} \sin(w\tau) \\ c_{2,\text{single}} &= \langle 2|\psi_{\text{single}}\rangle = i \frac{\Omega}{w} \sin(w\tau). \end{aligned} \quad (3.17)$$

The amplitudes of the states display the familiar Rabi oscillations with a temporal period determined by the Rabi flopping frequency w . In the limit of low power, $\Omega \ll \Delta$ and the flopping frequency w is approximately equal to $\Delta/2$; the excited state population then reduces to

$$|c_{2,\text{single}}|^2 = 4 \left(\frac{\Omega}{\Delta} \right)^2 \sin^2 \left(\frac{\tau\Delta}{2} \right). \quad (3.18)$$

To calculate the effect of a coherent pulse pair, the matrix for the field-free evolution of the atom during a time $T - \tau$ is needed as well (see figure 3.5). As spontaneous decay of the upper state is not included in the model, the pulse matrix can be used, but with Ω set to zero:

$$\mathcal{M}_{\text{free}} = \begin{pmatrix} e^{i(T-\tau)\Delta/2} & 0 \\ 0 & e^{-i(T-\tau)\Delta/2} \end{pmatrix}. \quad (3.19)$$

Furthermore, in order to describe the second pulse, the pulse matrix needs to be modified, as the field now has changed to $E(t - T)$, and as it might have acquired an extra phase ϕ , for example the carrier-envelope phase. This can be accounted for by rotating the state vector back using the unitary transformation \mathcal{U} defined above, and then rotating it to the new frame using a second unitary transformation \mathcal{U}_2^\dagger , defined by

$$\mathcal{U}_2 = \begin{pmatrix} e^{-i(\omega_l(t-T)+\phi)/2} & 0 \\ 0 & e^{i(\omega_l(t-T)+\phi)/2} \end{pmatrix}. \quad (3.20)$$

Then the effective rotation is

$$\mathcal{U}_2^\dagger \mathcal{U} = \begin{pmatrix} e^{-i(\omega_l T + \phi)/2} & 0 \\ 0 & e^{i(\omega_l T + \phi)/2} \end{pmatrix}. \quad (3.21)$$

Now all ingredients are ready to calculate the effects of two pulses interacting with a two-level atom. Taking the atom to be initially in the ground state, we have

$$|\psi\rangle = \mathcal{M}_{\text{pulse}} \mathcal{U}_2^\dagger \mathcal{U} \mathcal{M}_{\text{free}} \mathcal{M}_{\text{pulse}} |1\rangle. \quad (3.22)$$

Carrying out the algebra, this yields for the amplitude of the upper level:

$$c_{2,\text{pair}} = \langle 2|\psi\rangle = i \frac{2\Omega}{w} \sin(w\tau) \left[\cos(w\tau) \cos\left(\frac{\omega_{\text{atom}} T + \phi + \Delta\tau}{2}\right) + \frac{i\Delta}{2w} \sin(w\tau) \sin\left(\frac{\omega_{\text{atom}} T + \phi + \Delta\tau}{2}\right) \right]. \quad (3.23)$$

In the prefactor of this expression, the single pulse excitation amplitude $c_{2,\text{single}}$ of equation 3.17 can be recognized. Rewriting the trigonometric functions in the rest of the expression, the excited state amplitude becomes

$$c_{2,\text{pair}} = i \frac{2c_{2,\text{single}}}{w} \left[\cos\left(\frac{\omega_{\text{atom}} T + \phi}{2}\right) \left(w \cos(w\tau) \cos\left(\frac{\tau\Delta}{2}\right) + \frac{\Delta}{2} \sin(w\tau) \sin\left(\frac{\tau\Delta}{2}\right) \right) - \sin\left(\frac{\omega_{\text{atom}} T + \phi}{2}\right) \left(w \cos(w\tau) \sin\left(\frac{\tau\Delta}{2}\right) - \frac{\Delta}{2} \sin(w\tau) \cos\left(\frac{\tau\Delta}{2}\right) \right) \right]. \quad (3.24)$$

Again assuming low power, w is approximated by $\Delta/2$, and 3.24 reduces to

$$c_{2,\text{pair}} = 2c_{2,\text{single}} \cos\left(\frac{\omega_{\text{atom}} T + \phi}{2}\right). \quad (3.25)$$

The population in the upper level is then given by

$$|c_{2,\text{pair}}|^2 = 4|c_{2,\text{single}}|^2 \cos^2\left(\frac{\omega_{\text{atom}} T + \phi}{2}\right). \quad (3.26)$$

It is seen that this quantity is an oscillating function, the period of which is determined by the time delay between the pulses $T = 1/f_{\text{rep}}$ and by the transition frequency ω_{atom} . The Rabi frequency and the detuning only affect the amplitude of the signal through $c_{2,\text{single}}$. Therefore, if the comb laser's f_{rep} is varied (changing T), the upper state population will be modulated with a period inversely proportional to f_{rep} . The same thing occurs when f_{ceo} and thus ϕ_{ce} of the comb is varied. This is the result of quantum interference between the population amplitudes excited by both pulses, which depends on the phase difference between the field and the freely evolving atomic state vector.

The discussion can be continued for more pulses, but of course the algebra gets more and more elaborate. However, a general expression can be derived for the upper state population after the interaction with N pulses $|c_{2,N}|^2$:

$$|c_{2,N}|^2 = N^2 |c_{2,\text{single}}|^2 \left| \sum_{n=0}^N e^{in(\omega_1 T + \phi)} \right|^2. \quad (3.27)$$

This expression is very similar to the expression describing the spectrum of a pulse train, given in equations 2.32 and 2.33. The same spectral shape is seen here: adding more pulses makes the resonance structures in the excited state population signal increasingly narrow. In the limit of an infinite pulse train, the interference structure is just the comb-like spectrum. Of course, this only holds when there is no radiative decay, meaning that the linewidth of the transition is negligible compared to the width of the comb modes. Otherwise, the resonance width will be limited by the linewidth of the transition.

An important feature of coherent pulsed excitation is the fact that the bandwidth of the individual pulses only determines the amplitude of the interference signals of equations 3.26 and 3.27. In these expressions, the bandwidth is hidden in $c_{2,\text{single}}$, which contains the Rabi frequency Ω and thus the field envelope. This means that although the bandwidth of these pulses can be large, it will not limit the resolution of the quantum interference signal. For a two-pulse experiment, the measured resonance width is half the inverse of the pulse delay T , while the bandwidth of the pulses is equal to the inverse of their duration τ_p . The resonance width therefore is a factor $0.5 T/\tau_p$ smaller than the bandwidth; taking typical numbers ($T \approx 10$ ns, $\tau_p \approx 1$ ps), this is a factor of 5000. Thus coherent pulsed excitation can indeed be used for high resolution spectroscopy.

3.4.1 Frequency domain picture

The excitation process can be understood in the frequency domain as well. Fourier-transforming a pulse pair in time to the frequency domain, it is seen that its spectrum

is modulated sinusoidally (see figure 2.5). When any of the peaks of the pulse pair spectrum coincides with the frequency of the transition that is probed, the atom will be excited. Changing the time delay between the pulses is equivalent to tuning the spacing frequency f_{rep} . Since the pulse pair spectrum is in the optical domain, where the n of equation 2.36 is rather high, in the order of 10^6 , a change of f_{rep} means foremost a linear shift of all modes in the spectrum. At the same time, of course, the spacing of the modes is changed, but this change is a factor of 10^6 less than the shift in position. Thus the modulated spectrum of the pulses is shifted along the resonance, and provided that the transition linewidth is less than f_{rep} , the excitation follows the modal spectral shape of the pulse train.

3.5 Numerical model of excitation with phase-locked pulse trains

To investigate the method of coherent pulsed excitation more closely, and to be able to say more about the effect of several important experimental parameters, a numerical model is needed. For this model, we use the same approach as employed by Felinto et al. [75–77]. We consider again the two-level atom with the wave function $|\psi(t)\rangle = c_1(t)|1\rangle + c_2(t)|2\rangle$. $|1\rangle$ and $|2\rangle$ are the stationary states of the atom, which have an energy E_1 and E_2 , respectively. This wave function is inserted into the Schrödinger equation 3.5, yielding

$$\frac{\partial c_1(t)}{\partial t}|1\rangle + \frac{\partial c_2(t)}{\partial t}|2\rangle = \frac{1}{i\hbar} [c_1(t)H|1\rangle + c_2(t)H|2\rangle]. \quad (3.28)$$

Now an equation can be derived for the time evolution of the coefficients $c_i(t)$ by multiplying 3.28 on the left by $\langle i|$:

$$\frac{\partial c_i(t)}{\partial t} = \frac{1}{i\hbar} \sum_j \langle i|H|j\rangle c_j(t). \quad (3.29)$$

For a more general description that includes the effects of coherent accumulation, the atomic density matrix ρ is employed, which is defined as follows:

$$\begin{aligned} \rho_{11} &= |c_1|^2 = N_1/N & \rho_{12} &= c_1 c_2^* \\ \rho_{21} &= c_2 c_1^* & \rho_{22} &= |c_2|^2 = N_2/N, \end{aligned} \quad (3.30)$$

where N_1 and N_2 are the number of atoms in state $|1\rangle$ and $|2\rangle$, respectively, and N is the total number of atoms. The diagonal elements are real and satisfy

$$\rho_{11} + \rho_{22} = 1, \quad (3.31)$$

as the system is closed. From the definition of the density matrix elements it is seen that the time evolution of the matrix elements can be written as

$$\frac{\partial \rho_{mn}}{\partial t} = \frac{\partial c_m}{\partial t} c_n^* + c_m \frac{\partial c_n^*}{\partial t}. \quad (3.32)$$

Using the time evolution of the c_i of equation 3.29, one obtains

$$\begin{aligned} \frac{\partial \rho_{mn}}{\partial t} &= \frac{1}{i\hbar} \sum_k \langle m|H|k\rangle c_k(t) c_n^*(t) - \frac{1}{i\hbar} \sum_k \langle k|H|n\rangle c_k^*(t) c_m(t) \\ &= \frac{1}{i\hbar} \sum_k [\langle m|H|k\rangle \rho_{kn} - \rho_{mk} \langle k|H|n\rangle]. \end{aligned} \quad (3.33)$$

This result is known as the Liouville equation, usually written as

$$\frac{\partial \rho}{\partial t} = \frac{1}{i\hbar} [H, \rho]. \quad (3.34)$$

To describe the interaction of the two-level atom with a radiation field, the rotating-wave approximation Hamiltonian of the previous section, equation 3.11, is used again. However, in order to include the effects of e.g. a varying carrier-envelope phase, an extra phase factor $e^{i\phi}$ is added to the external field. The Hamiltonian is then rotated back using the inverse transformation of equation 3.10:

$$\begin{aligned} H &= i\hbar \dot{\mathcal{U}} \mathcal{U}^\dagger + \mathcal{U} \tilde{H} \mathcal{U}^\dagger \\ &= \hbar \begin{pmatrix} \omega_{\text{atom}}/2 & \Omega e^{-i(\omega_l t + \phi)} \\ \Omega^* e^{i(\omega_l t + \phi)} & -\omega_{\text{atom}}/2 \end{pmatrix}. \end{aligned} \quad (3.35)$$

As the description so far does not include radiative decay, the Liouville equation is augmented with a phenomenological relaxation term, expressed as

$$-\Gamma = -\frac{\gamma}{2} (|2\rangle\langle 2| \rho + \rho |2\rangle\langle 2| - |2\rangle\langle 1| \rho |1\rangle\langle 1|), \quad (3.36)$$

with γ designating the decay rate of the upper state population; the total Liouville equation now becomes

$$\frac{\partial \rho}{\partial t} = \frac{1}{i\hbar} [H, \rho] - \Gamma. \quad (3.37)$$

By writing out all components of this matrix equation, the following set of equations is obtained:

$$\dot{\rho}_{11} = \gamma\rho_{22} - i\Omega e^{-i(\omega_l t + \phi)}\rho_{12} + i\Omega^* e^{i(\omega_l t + \phi)}\rho_{21} \quad (3.38a)$$

$$\dot{\rho}_{22} = -\gamma\rho_{22} + i\Omega e^{-i(\omega_l t + \phi)}\rho_{12} - i\Omega^* e^{i(\omega_l t + \phi)}\rho_{21} \quad (3.38b)$$

$$\dot{\rho}_{21} = -i\Omega e^{-i(\omega_l t + \phi)}(\rho_{22} - \rho_{11}) - (\gamma/2 + i\omega_{\text{atom}})\rho_{21} \quad (3.38c)$$

$$\dot{\rho}_{12} = i\Omega^* e^{i(\omega_l t + \phi)}(\rho_{22} - \rho_{11}) - (\gamma/2 - i\omega_{\text{atom}})\rho_{12}. \quad (3.38d)$$

These equations are the optical Bloch equations. The time dependence of these equations can be removed by introducing the new variables

$$\begin{aligned} \tilde{\rho}_{11} &= \rho_{11} & \tilde{\rho}_{12} &= \rho_{12} e^{-i(\omega_l t + \phi)} \\ \tilde{\rho}_{21} &= \rho_{21} e^{i(\omega_l t + \phi)} & \tilde{\rho}_{22} &= \rho_{22}. \end{aligned} \quad (3.39)$$

Introducing these into equations 3.38 and eliminating $\tilde{\rho}_{11}$ from the equations, we arrive at the following set of equations:

$$\dot{\tilde{\rho}}_{11} = \gamma\tilde{\rho}_{22} + i\Omega^* \tilde{\rho}_{21} - i\Omega \tilde{\rho}_{12} \quad (3.40a)$$

$$\dot{\tilde{\rho}}_{22} = -\gamma\tilde{\rho}_{22} - i\Omega^* \tilde{\rho}_{21} + i\Omega \tilde{\rho}_{12} \quad (3.40b)$$

$$\dot{\tilde{\rho}}_{21} = -i\Omega(2\tilde{\rho}_{22} - 1) - (\gamma/2 - i\Delta)\tilde{\rho}_{21} \quad (3.40c)$$

$$\dot{\tilde{\rho}}_{12} = i\Omega^*(2\tilde{\rho}_{22} - 1) - (\gamma/2 + i\Delta)\tilde{\rho}_{12}, \quad (3.40d)$$

where $\Delta = \omega_l - \omega_{\text{atom}} + \dot{\phi}$ is the generalized detuning between the electric field and the atomic transition, including a possible time-dependent phase shift.

3.6 Numerical results

The equations 3.40 need to be solved for the case of an electric field consisting of pulse trains, as described in section 2.6. Thus we write

$$\begin{aligned} E_{\text{train}} &= \sum_{n=0}^{n=N} E(t - nT) e^{in\Delta\Psi} \\ &= \left[\sum_{n=0}^N \mathcal{E}(t - nT) e^{in\phi_{\text{ce}}} \right] e^{i\omega_l t} \\ &= \mathcal{E}_{\text{train}}(t) e^{i\omega_l t}, \end{aligned} \quad (3.41)$$

incorporating the carrier-envelope phase shift ϕ_{ce} in the slowly varying envelope function $\mathcal{E}_{\text{train}}$ and setting $\dot{\phi} = 0$.

The Bloch equations are integrated using a fourth-order Runge-Kutta algorithm with variable stepsize [138]. As a model atomic system, the $5p^6 \ ^1S_0 \rightarrow 5p^5 \ (^2P_{3/2}) \ 5d[1/2]_1$ transition at 2.398×10^{15} Hz (125 nm) in xenon was chosen, the transition that is excited in the experiments of chapter 7. The decay rate γ for this transition is $\gamma = \frac{1}{58.9} \text{ ns}^{-1}$ (see chapter 7), while the transition dipole moment \mathbf{d}_{21} is estimated using the following approximate relation [139]:

$$\begin{aligned} \mathbf{d}_{21} &= \sqrt{A_{21} \frac{3\epsilon_0 \hbar c^3}{2\omega_{\text{atom}}^3}} \\ &= 9.86 \times 10^{-31}, \end{aligned} \quad (3.42)$$

where $A_{21} = 1.4 \times 10^7$ has been used [140]. The electric field is a train of 1 ps long Gaussian pulses with a varying number of pulses. To match the conditions of the experiment described in chapter 7, the delay between the pulses is chosen to be 13.3 ns, while the amplitude of the pulses is taken to be 6.1×10^3 V/m, equivalent to a 50 fJ, 1 ps pulse. The resulting excited state population ρ_{22} as a function of time is shown in figure 3.6 for irradiation with pulse trains of varying lengths and with $\phi_{\text{ce}} = 0$. As the lifetime of the upper state is larger than the time between the pulses, the coherence survives long enough for the contributions of consecutive pulses to interfere. In this case, the second

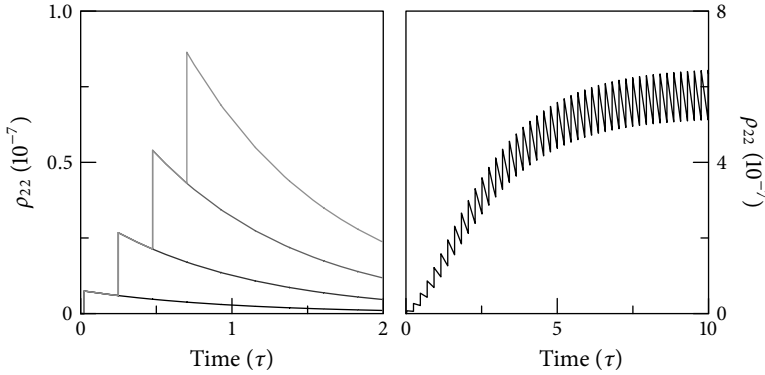


Figure 3.6: The excited state population ρ_{22} over time, when a varying number of phase-locked and time-delayed pulses hit the two-level atom. Left panel: a detailed view of the excitation due to 1 (black) to 4 (lightest gray) pulses. Right panel: the excitation due to a continuing pulse train on a longer timescale. Time is expressed in units of the upper state lifetime τ , while the delay between the pulses in this case is about 0.22τ .

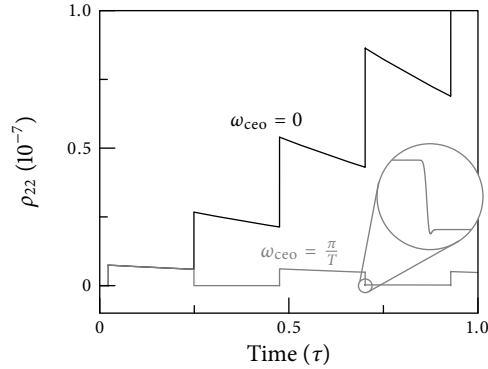


Figure 3.7: The excited state population over time for $\omega_{\text{ceo}} = 0$ (black curve), and for ω_{ceo} equal to half the mode spacing (gray curve). The time is expressed in multiples of the upper state lifetime τ . The circular inset shows that the cancellation in the second case is not exact, due to excited state population decay during the time between the equally intense pulses.

pulse is in phase with the atomic superposition and the excited state population will be enhanced, as can be seen in figure 3.6. Subsequent pulses that are in phase will continue to build up the excited state population, until there is a balance between radiative decay and excitation. This can be seen in the right panel of figure 3.6, where the effect of a long sequence of identical pulses is shown. To control the excitation, several parameters can be varied. For instance, the entire comb mode spectrum can be shifted by adjusting ω_{ceo} . Recall that only when a comb mode is resonant with the transition, the excitation contributions of the pulses will add constructively. As shifting the spectrum moves the comb modes one by one in and out of resonance, the excitation will be modulated. When the spectrum is tuned such that ω_{atom} falls exactly halfway between two comb modes, the pulses annihilate the coherence excited by the previous pulses. This effect is shown in figure 3.7, where the excited state population is plotted against time for $\omega_{\text{ceo}} = 0$ and $\omega_{\text{ceo}} = \pi/T$. The annihilation is not perfect, due to the decay of the upper level: as the second pulse area is equal to that of the first, it contains more energy than needed to deplete the upper state completely.

The interference is demonstrated more clearly by tracking ρ_{22} directly after the interaction of a pulse train with the atom while varying ω_{ceo} continuously, as portrayed in figure 3.8. A pulse train of only one pulse long naturally shows a constant signal versus detuning, as its spectrum is an unmodulated Gaussian one (see equation 2.33). However,

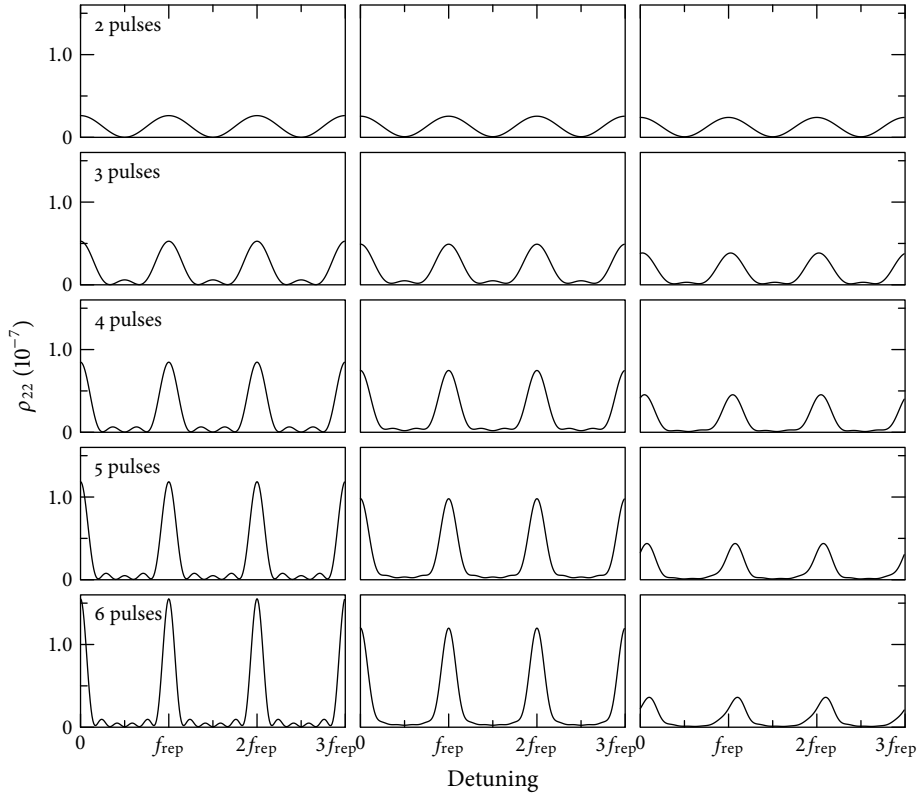


Figure 3.8: The excited state population versus detuning, probed 1 ns after excitation with 2 to 6 phase-locked pulses, separated by $T = 13.33$ ns, or $f_{\text{rep}} = 75$ MHz. The left panels show the signals without Doppler broadening taken into account, while in the middle panels the effect of a 10 MHz Doppler width is included. On the right, random phases (0, 150, 10, 50, 30 and 20 mrad respectively) are used for each pulse to simulate phase distortions due to e.g. amplification or upconversion, as well as a 10 MHz Doppler width.

two pulses have a sinusoidally modulated spectrum, which, when tuned over the atomic resonance, yields a simple sinusoidally varying spectrum, shown in the upper left panel of figure 3.8. As more and more pulses are added, the peak structures in the signal narrow down; the period of the signal, which is equal to the inverse of the time delay T between the pulses, remains constant. Similar signals can be obtained by scanning ω_{rep} instead of ω_{ceo} . This translates all frequency components in the comb almost linearly, similar to scanning ω_{ceo} .

To bring the simulations closer to the experimental conditions, several parameters have been added to the simulation: lifetime effects, Doppler broadening, chirp effects and the occurrence of unwanted phase shifts have all been considered. This yields interesting insights in the applicability and limitations of the method of quantum interference spectroscopy.

First, the lifetime of the excited state is an important factor in the interference process: only when it is of the order of the time delay between the pulses or longer, a significant population amplitude will be left in the upper state when the next pulse comes around, so that interference can take place. In figure 3.9 it can be seen what happens when the lifetime varies from infinity to much shorter than the pulse delay. The interference maxima increase quadratically with the number of pulses for an infinite lifetime, at least when the excitation fraction is small enough to ensure that no saturation occurs. When the lifetime decreases, the maxima progressively decrease. With a lifetime five times larger than the pulse delay, the maxima grow more or less linearly with the number of pulses, and with an even shorter lifetime the trend becomes sub-linear. For short lifetimes, little excitation amplitude is built up, which quickly saturates.

If the atoms are not at rest, the atomic resonance will become Doppler broadened, as different velocity classes are resonant at different detunings. This effect will reduce the contrast of the interference pattern when the Doppler width is larger than, or comparable to, the width of the resonances in the interference signal. This can be included in the model by replacing ω_{atom} by $\omega_{\text{atom}} - \mathbf{k}_l \cdot \mathbf{v}$, where \mathbf{k}_l is the laser wave vector and \mathbf{v} the velocity of the atoms. Effectively, the signal is then convolved with the Doppler profile of the transition; the results can be seen in the middle part of figure 3.8, where a Doppler profile with a width of 10 MHz was used, comparable to the Doppler width that can be obtained in a highly collimated atomic beam (see also chapter 4). The small structure in between the main resonances is washed out, and the resonances themselves are not narrower than the Doppler width. When the Doppler width is of the same order of magnitude as the fringe period, then the contrast of the fringes deteriorates quickly.

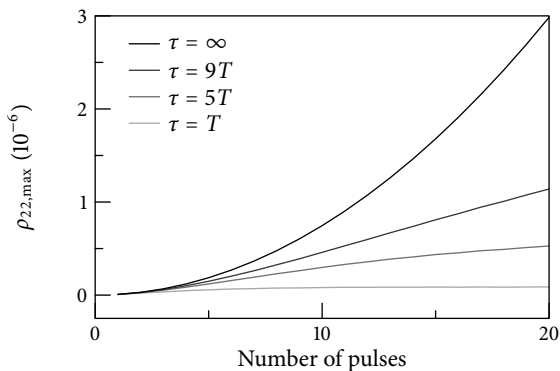


Figure 3.9: The interference maxima peak height as a function of the number of pulses in the train for various excited state lifetimes τ . Though rising quadratically for infinite lifetime, the trend becomes sub-linear for lifetimes of the order of the pulse delay (13 ns).

Another point of concern is the effect of uncontrolled phase shifts between the pulses. When an experiment requires amplification or frequency conversion, or even both, this can give rise to phase shifts that are hard to measure and control. To see the effects of such phase shifts, the signal due to a pulse train with realistic phase shifts between the pulses (of the order of 0.1 rad) has been calculated, and is shown in the rightmost panels of figure 3.8. It is clear that the positions of the resonances are shifted, and that the shape of the resonances is distorted. This problem has to be dealt with carefully in spectroscopic measurements, as unknown phase shifts cause a deviation of the measured transition frequency with respect to the true frequency.

Next, the effect of chirp in the pulses on the excitation needs to be considered. In normal pulsed spectroscopy, be it nanosecond or shorter pulses, a changing carrier frequency during a pulse will result in a measured value for the resonance frequency that is shifted from the actual value [56, 98]. In the case of direct excitation with phase-locked pulses, this would mean a shift of the interference pattern. However, as chirp is just a shift of the temporal phase over the pulse, it should be of no consequence when all pulses in the excitation pulse train have exactly the same chirp. Then the situation is similar to a train of pulses where each pulse is given the same phase shift: as the interference pattern is only sensitive to phase *differences*, no shift of the pattern (and hence of the measured resonance frequency) will occur. This has been confirmed by adding different amounts of quadratic chirp to only one pulse of a pulse pair and to both, as shown in

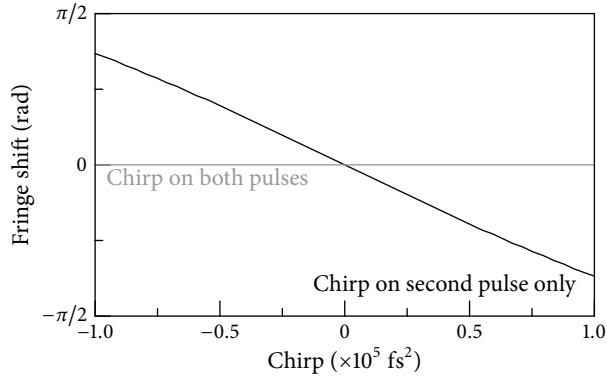


Figure 3.10: The shift of the interference pattern as a function of chirp for: a) a chirp only on the second pulse; b) the same chirp on both pulses. It is clear that a reproducible chirp does not affect the interference pattern.

figure 3.10. In the latter case, no shift is observed, while in the former case phase shifts approaching a quarter of a cycle are observed for a chirp of $1 \times 10^5 \text{ fs}^2$.

The use of longer pulse trains yields an increase in resolution, provided that the pulses do not acquire unknown phase shifts. But an increase in resolution can also be achieved without the need for more pulses. The period of the interference signal is determined by the inverse of the pulse period T , so increasing T yields narrower resonances. This can be seen in figure 3.11, where the delay is increased in steps of $T \approx 13.3 \text{ ns}$. Because the upper level has a finite lifetime, its population will decrease significantly during the time between the pulses. This decay is responsible for the diminished contrast of the interference signal as the pulse delay increases. However, as long as there is a recognizable oscillation, the many resonances that can be recorded still allow for an accurate determination of the transition frequency.

It is interesting to note that the resolution of the pulse pair approach is in principle not limited by the natural linewidth, which is the case when exciting with pulse trains. In the former case, the period of the interference signal depends only on the delay between the pulses, which can be increased almost indefinitely. Of course, the signal amplitude and contrast rapidly diminish when the delay is increased beyond the lifetime of the upper state, as is shown in the right panel of figure 3.12, for the case of zero Doppler broadening. Depending on the signal-to-noise ratio, it is possible to obtain a resolution that is significantly better than the natural linewidth, especially when the ensemble of

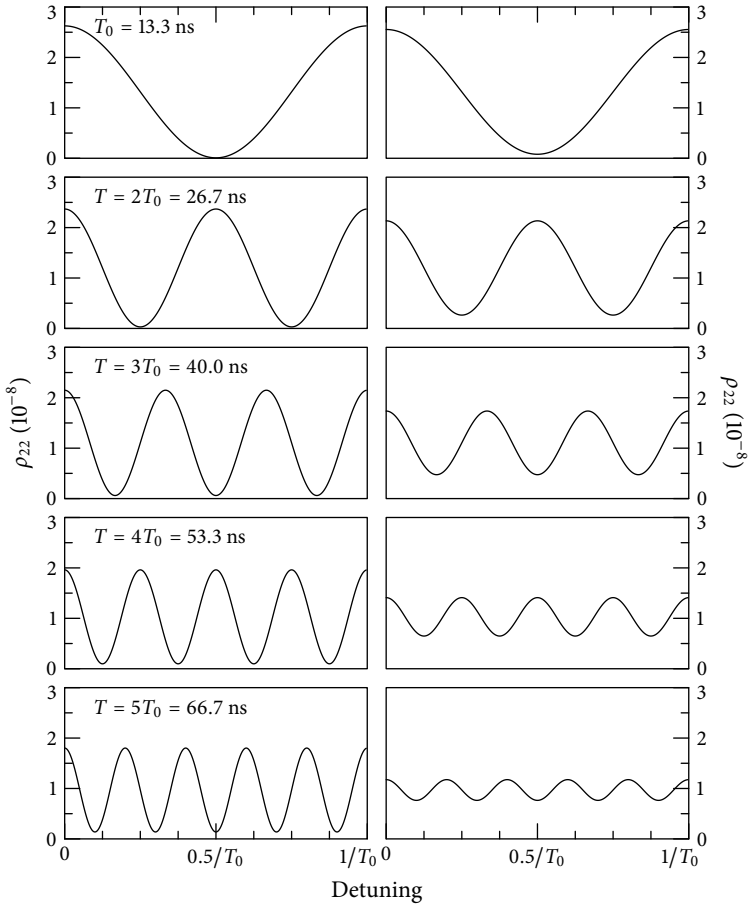


Figure 3.11: The excited state population versus detuning after excitation with pulse pairs that have different delays (13.3 ns - 66.7 ns). The left panels show the signals without Doppler broadening taken into account, while on the right the effect of a 10 MHz Doppler width is included.

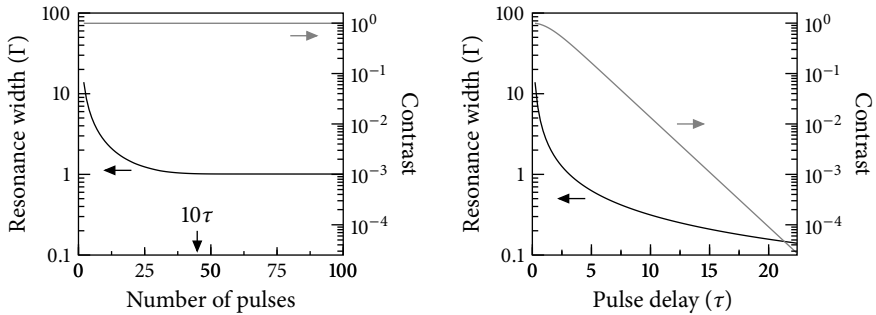


Figure 3.12: The resonance width (black line) and the contrast (gray line) for excitation with pulse trains (left) and for excitation with pulse pairs (right). The resonance width is expressed in multiples of the natural linewidth of the transition $\Gamma = 1/\tau$, while the delay is expressed in multiples of the lifetime of the upper state τ . In the left panel, 10τ has been indicated as well to compare the timescales: in fact both panels have the same time span. No Doppler broadening was taken into account.

atoms is cooled. Naturally, the best results are obtained for long-living transitions. When pulse trains are used, the resonance width does not drop below the natural linewidth of the transition, as is shown in the left panel of figure 3.12. This is counterbalanced by the fact that in this case the contrast is very high and independent of the length of the pulse train.

3.7 Potential pitfalls of coherent pulsed excitation

The results of the previous section indicate that direct excitation of atoms with phase-locked pulse trains or pairs is a powerful approach to high-resolution spectroscopy. This is especially true for spectroscopy at xuv and shorter wavelengths, as the high peak power of short pulses facilitates relatively easy frequency upconversion. However, before it is put to use, a number of pitfalls need to be investigated with respect to this method. The most important of these is the question whether the amplification and frequency conversion of phase-locked pulses disrupts the vital phase relationship between the pulses: any induced unknown phase shift will directly lead to an error in the determination of the transition frequency. Other effects that have to be considered are the Doppler shift and broadening of the transition, and a possible AC Stark shift induced by

relatively powerful pulses. The discussion will be guided by the experimental parameters corresponding to the experiments described later in this thesis (see chapters 6 and 7).

3.7.1 Doppler shift and broadening

In general, the atoms under investigation are moving during the interaction with the laser field. Therefore, the transition frequencies of the atoms will be shifted in comparison to those of atoms in rest. Assuming energy and momentum conservation during the interaction, the energy of the absorbed photon to second order in v/c is [141]

$$\hbar\omega = \hbar\omega_{\text{atom}} + \hbar\mathbf{v} \cdot \mathbf{k} + \frac{(\hbar\omega)^2}{2m_0c^2} - \hbar\omega_{\text{atom}} \frac{v^2}{2c^2}, \quad (3.43)$$

where ω is the angular frequency of the laser field, \mathbf{v} the velocity of the atoms, \mathbf{k} the wave vector of the field and m_0 the rest mass of the atom. The second term on the right is the linear Doppler shift, the third the recoil shift and the fourth term the quadratic or relativistic Doppler shift.

Considering first only the linear Doppler shift, the deviation of the absorbed frequency f from the actual transition frequency f_{atom} is

$$\delta f_{\text{Doppler}} = \frac{\mathbf{k} \cdot \mathbf{v}}{2\pi} = \frac{v}{\lambda} \cos \alpha = f \frac{v}{c} \cos \alpha, \quad (3.44)$$

where α is the angle between the direction of the wave vector of the light field and the atoms. The Maxwellian velocity distribution of thermal atoms therefore yields a Gaussian frequency spread for an ensemble, and thus a broadened Gaussian lineshape. Cooling of the atoms under investigation or the use of highly collimated beams combined with a perpendicular excitation geometry can greatly reduce the line broadening due to the Doppler effect; the latter technique is used in the experiments described in this thesis. When skimming the beam using two apertures of size d and D separated by a distance l , the maximum opening angle of the apertures is

$$\alpha \approx (d + D)/l, \quad (3.45)$$

and the Doppler width will be multiplied by a factor of $\sin \alpha$. For apertures of 0.25 mm separated by 170 mm, as used in the experiments of this thesis, the Doppler width for the 125 nm line in xenon at room temperature is approximately 10 MHz, as opposed to the 2.4 GHz Doppler width for a non-collimated beam. When the atomic beam is produced in a supersonic expansion, the narrower speed distribution yields a narrower Doppler width as well.

For the quantum interferometry to be successful, the Doppler width must be kept well below the period of the interference signal. With the 75 MHz period in our experiments, a 10 MHz Doppler width is sufficient to obtain a high-quality signal, as can be seen in figure 3.8. However, there is still the problem of a possible Doppler *shift*: if the laser beam and the atomic beam are not exactly perpendicular, the Doppler width will remain the same but the measured resonance frequency will be shifted. As it is hard to realize a truly perpendicular geometry, the simplest solution is to excite the atoms first with the laser pulses coming from one side, and subsequently with pulses coming from the exact opposite direction. These consecutive measurements have an equal Doppler shift, but in the opposite direction: the true resonance frequency is then the average of the frequencies measured from either side. This approach transfers the problem from a perpendicularity problem to one concerning parallelism, which is much easier to check: the opposite beams can easily be made to propagate with an angle smaller than 1 mrad between them. This was applied in the krypton experiments described in chapter 6, yielding a residual Doppler shift error of about 1.8 MHz. To improve on this, one could even use Sagnac interferometry to align the counter-propagating beams [142].

Of course, as the quantum interference signal is periodic, the angle between the laser beams and the atomic beam should not be so large as to make the shift between the signals measured from either side larger than about a quarter of the period. If the shift becomes larger, it will be unclear which resonance to use to determine the shift. Again taking the krypton case as an example, this means that the beams should be perpendicular within about 0.5° . Even if that is not feasible, there is still another option: a measurement of isotope shifts, which is a relative measurement, can give an estimate of the Doppler shift that is accurate enough to be able to determine the actual resonance position. This approach has been applied in the krypton experiments.

In the case of a two-photon transition, it seems natural to largely circumvent all Doppler-related problems by performing two-photon Doppler-free spectroscopy using colliding pulses [80, 143–145]. However, the short pulses used here have a large bandwidth, and a single pulse is capable of exciting a Doppler-shifted two-photon transition on its own, without the need for a counter-propagating pulse. Therefore, it is hard to recognize the true Doppler-free signal in this case. And even if that signal is found, any imbalance in signal strength of the counter-propagating beams will cause the signal to be shifted away from the true resonance position. Thus separate excitation from opposite sides, although not capable of delivering Doppler-free signals, is less prone to errors.

The other terms that appear in equation 3.43, although they are much smaller in magnitude than the first-order Doppler shift, are still significant. The second-order (quadratic) Doppler shift,

$$\delta f_{\text{quad. Doppler}} = -\frac{f_{\text{atom}} v^2}{2 c^2}, \quad (3.46)$$

is mainly important for low-mass species and high transition frequencies. It is a consequence of the time dilation in the frame of the moving atoms as observed in the laboratory frame. For the excitation of the 125 nm transition in xenon atoms that move at a speed of 305 m/s, it can be calculated to be about -1.2 kHz.

The recoil shift, given by the third term of 3.43,

$$\delta f_{\text{recoil}} = \frac{hf^2}{2m_0c^2}, \quad (3.47)$$

is due to the momentum transferred to the atom by the absorption of a photon. It is only important at optical and higher frequencies, where the photon momentum becomes high enough compared to the atomic rest mass. Still, even for atoms as heavy as xenon it remains relatively small, being only 97 kHz for the 125 nm excitation of xenon.

3.7.2 AC Stark shift

When an atom is exposed to an external static electric field, the position of the electronic energy levels will depend on the applied field. This is called the Stark effect. Using second-order perturbation theory, the Stark shift of a level can be expressed as

$$\Delta E_m = \sum_n \frac{|\langle m|\mathbf{d}|n\rangle|^2}{E_m - E_n} E^2, \quad (3.48)$$

where the summation runs over all other states that are coupled to the perturbed level by a dipole moment. For a two-level system perturbed by a non-resonant oscillating electric field, the energies of both levels will shift according to (see e.g. [146])

$$\Delta E = \pm \frac{\mathbf{d}_{21}^2 E_0^2}{2} \frac{\omega_{\text{atom}}}{\omega_{\text{atom}}^2 - \omega_l^2}, \quad (3.49)$$

where ω_{atom} is the unperturbed transition frequency, \mathbf{d}_{21} the dipole matrix element connecting the two levels and E_0 the field amplitude. The positive shift holds for the upper state, while the negative shift applies to the lower state. Thus the transition

frequency that is measured in the presence of such a field is shifted from the field-free value, an effect that is referred to as the AC Stark effect. In the quantum interference scheme, the field is only present during the short pulses. The atoms evolve freely during the time between the pulses, so the measured Stark shift, which is the average shift during the whole interaction, is much less than the peak Stark shift that occurs during the pulses. In fact, as the Stark shift is linear with the light intensity, it is proportional to the average power of the pulse train interacting with the atoms, and not to the peak power of the pulses. For two-photon transitions, this holds as well [80, 84]: of course, the two-level assumption is then less likely to be valid, as levels halfway the two states can have a large contribution as well.

The relatively broad spectrum of the pulses used for the quantum interference excitation scheme requires that the Stark shift contributions of all frequency components are integrated over the spectrum. As the field components with frequencies higher than the transition frequency and those with frequencies that are lower push the resonance frequency in opposite directions, most of the shifts cancel. At the same time, the Stark shift is inversely dependent on the detuning from the transition frequency, so the largest contributions are due to only a limited range of frequencies. As the power in this range is quite low, and the difference in power between the frequencies above and those below the resonance is even lower, the Stark shift due to such a pulse is rather small, and can usually be neglected. This is confirmed by the measurements of the power dependence in our experiments (see chapters 6 and 7): for both single-photon and two-photon transitions, the fields are too weak to introduce a significant shift within the measurement accuracy.

3.7.3 Phase shifts due to pulse picking, amplification and harmonic generation

The method of quantum interference spectroscopy is based on the fact that the pulses have a fixed and known phase relation. It is therefore of utmost importance that this phase relation is maintained, whatever happens to the pulses during their trip from the oscillator to the interaction region. However, in our experiment, the pulses encounter a Pockels cell, a non-saturation amplifier and several stages of frequency conversion. These devices need to be characterized with respect to their influence on the phase coherence of the pulses. If they are found to alter the pulse-to-pulse phase, it will be necessary to measure these changes during any spectroscopic measurements, in order to correct the measurements for these shifts. In the next chapter, the interferometric technique that we employed for this purpose will be discussed.

Pockels cell In our experiments, pulses are selected from the oscillator pulse train using a Pockels cell. Such a device works on the principle of birefringence induced by an external electric field. The optical axis of the uni-axial crystal potassium dideuterium phosphate (KD^*P) is aligned parallel to the propagation direction of the incoming laser beam, and two ring electrodes around the end faces of the crystal are used to apply a voltage along the optical axis. Due to this applied field, the index of refraction ellipsoid of the medium is changed along the directions perpendicular to the optical axis, making the crystal biaxially birefringent. The retardation accumulated by the laser beam is directly proportional to the applied field. At a specific voltage, a retardation of π is achieved, rotating the polarization of the incoming beam over 90° : this voltage is called the half-wave voltage $V_{\lambda/2}$. A polarizer then selects only the rotated polarization state, thus giving the opportunity to switch pulses traveling through the Pockels cell with a pulsed electric field applied to the Pockels cell crystal.

As the Pockels cell operates by imparting phase shifts onto the different polarization components of the laser pulses, and as these shifts are proportional to the applied field, in general a phase shift can be induced between two pulses that experience slightly different retardation due to a slightly different instantaneous voltage applied to the Pockels cell. To quantify this, consider a Pockels cell on which a horizontally polarized laser field is incident. The electric field can be written

$$\begin{pmatrix} E_x \\ E_y \end{pmatrix} = E_o \begin{pmatrix} \sin(\omega_1 t) \\ 0 \end{pmatrix}, \quad (3.50)$$

where x and y are the horizontal and vertical directions. The Pockels cell crystal is oriented with its slow (x') and fast (y') axes at 45° with respect to the x and y axes, so the field components on which the Pockels cell acts are

$$\begin{pmatrix} E_{x'} \\ E_{y'} \end{pmatrix} = \frac{E_o}{\sqrt{2}} \begin{pmatrix} \sin(\omega_1 t) \\ \sin(\omega_1 t) \end{pmatrix}. \quad (3.51)$$

The Pockels cell adds to both components a voltage-dependent phase shift, which for a $\bar{4}2$ -class crystal like KD^*P is $\phi_i = \pm \pi n_o^3 r_{63} V / \lambda$ (see e.g. paragraph 7.2.1 of [147]), where n_o is the ordinary refractive index of the material, r_{63} is one of the linear electro-optic tensor elements, V is the voltage applied to the Pockels cell and λ is the wavelength of the light. It is fortunate that the phase shifts in both polarization components depend on the same tensor element r_{63} , but have opposite signs, as will be clear later on. Introducing

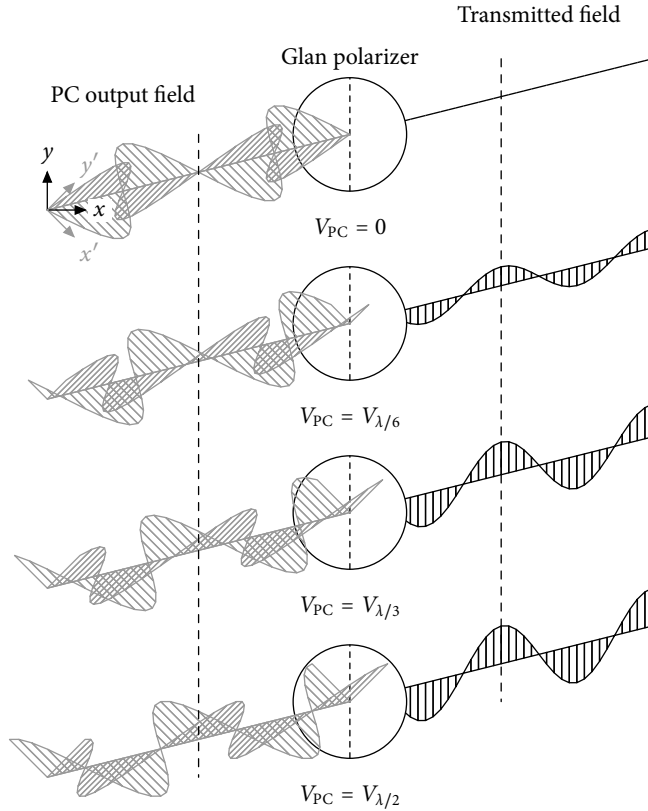


Figure 3.13: Schematic diagram of the pulse picking process. The Pockels cell output light field (gray) is shown decomposed along the voltage-induced ordinary and extraordinary axes of the Pockels cell, x' and y' ; the Glan polarizer selects the vertical component along y . As the Pockels cell imparts equal but opposite phase shifts to both polarization components $E_{x'}$ and $E_{y'}$, the phase of the field after the Glan polarizer is independent of the retardation: only the amplitude is affected.

the phase shifts into the field expression yields

$$\begin{pmatrix} E_{x'} \\ E_{y'} \end{pmatrix} = \frac{E_o}{\sqrt{2}} \begin{pmatrix} \sin(\omega_1 t + \phi_1) \\ \sin(\omega_1 t + \phi_2) \end{pmatrix}. \quad (3.52)$$

Projected back on the original x and y axes, the field transmitted by the vertical polarizer after the Pockels cell can be written

$$\begin{pmatrix} E_x \\ E_y \end{pmatrix} = \begin{pmatrix} 0 \\ E_{x'} - E_{y'} \end{pmatrix} = E_o \begin{pmatrix} 0 \\ \sin(\omega_1 t)(\cos \phi_1 - \cos \phi_2) + \cos(\omega_1 t)(\sin \phi_1 - \sin \phi_2) \end{pmatrix}. \quad (3.53)$$

The vertical component is then equal to

$$E_y = A \sin(\omega_1 t + \Phi), \quad (3.54)$$

with $A = \sqrt{(\cos \phi_1 - \cos \phi_2)^2 + (\sin \phi_1 - \sin \phi_2)^2}$ and $\Phi = \arctan\left(\frac{\sin \phi_1 - \sin \phi_2}{\cos \phi_1 - \cos \phi_2}\right)$. With the appropriate trigonometric manipulations, this expression can be reduced to

$$\begin{aligned} E_y &= E_o \sqrt{2 - 2 \cos(\phi_1 - \phi_2)} \sin(\omega_1 t + \frac{1}{2}(\phi_1 + \phi_2) - \pi/2) \\ &= E_o \sqrt{2 - 2 \cos(2\pi n_o^3 r_{63} V/\lambda)} \sin(\omega_1 t - \pi/2). \end{aligned} \quad (3.55)$$

Here it becomes clear why it is so fortunate that the voltage-dependent phase shifts of both polarization components are proportional to the same electro-optic tensor element: the sum $\phi_1 + \phi_2$ now cancels, leaving no voltage-dependent phase shift on the output field. The amplitude of course is a function of the Pockels cell voltage, as expected. This situation is illustrated in figure 3.13, where the transmitted field is shown for several Pockels cell voltage values. From this discussion, it is clear that for a Pockels cell no phase shifts are expected in the transmitted field. However, measurements are needed in the experimental situation to corroborate these findings.

Multipass amplifier Several effects can cause phase shifts during amplification of the laser pulses, of which the most important are self-phase modulation, refractive index changes resulting from a changing population inversion, and heating due to phonons produced in the relaxation to the upper and from the lower laser level. The self-phase modulation is the result of the high intensities reached with the relatively short pulses

focused inside the Ti:sapphire, as discussed in the previous chapter. A pulse of intensity I will acquire a phase shift

$$\phi_{\text{spm}} = \frac{\omega_l n_2 L I}{\epsilon_0 c^2}. \quad (3.56)$$

Here ω_l is again the center frequency of the pulse spectrum, n_2 is the non-linear index of refraction, and L is the length of the non-linear medium that is traversed.

Next, the phase shift for a light wave traveling through a medium of length L consisting of two-level atoms has two main contributions:

$$\phi = \phi_{\text{free space}} + \phi_{\text{pop}} = \frac{\omega_l L}{c} + \frac{\omega_l L}{2c} \text{Re}(\chi_e(\omega_l)). \quad (3.57)$$

The first part is simply the free space propagation constant, while the second part is the population-dependent phase related to the presence of resonances in the medium, yielding a dispersive frequency dependence. For the case of Ti:sapphire, two resonant structures play a role: the absorption in the visible and ultraviolet regions, and the lasing transition in the infrared. The former gives rise to normal dispersion, decaying with increasing wavelength over the near-infrared region; the latter is centered around the peak of the gain curve at 800 nm, and thus adds a dispersive shape over the entire infrared gain bandwidth of the medium when the upper and lower laser level have different occupation numbers. In a four-level medium like Ti:sapphire, the laser levels are either empty, or there is an inverted population: in the former case, the second term of 3.57 will be zero, whereas in the latter case the extra phase shift is a linear function of the population inversion. As the population inversion experienced by the individual pulses may be different, the pulses may acquire a different phase.

Finally, both the index of refraction and the length of the amplifier medium are a function of the temperature of the medium. The ions in the medium that are excited to the pump band lose energy by emitting phonons during the transfer from the pump band to the upper laser level and the same happens during the transfer from the lower laser level to the ground state. Therefore, the temperature of the medium depends on the population dynamics of the ions. When the first pulse is amplified, the stimulated decay of population to the lower laser level will produce a burst of heat as these ions decay to the ground state. As the heat is deposited right in the seed beam path, the second pulse will experience a slightly warmer medium, which again translates into a phase shift between the pulses.

In order to shed more light on these aspects, a numerical model has been constructed to describe the phase evolution due to inversion, self-phase modulation and heating in a Ti:sapphire amplifier. The amplifier used in the experiments described in this thesis is

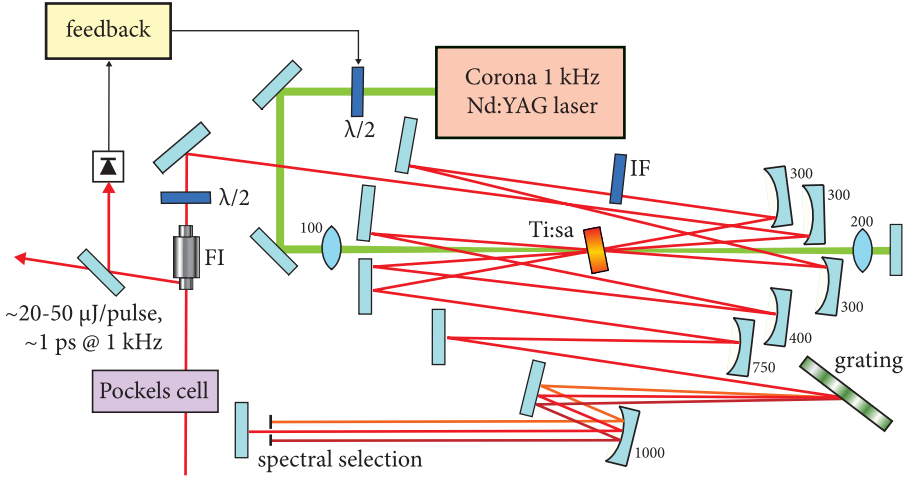


Figure 3.14: The multi-pass amplifier used in the experiments. The model described in this section is based on this setup. Radii of curvature and focal lengths are indicated in the figure in units of mm.

shown in figure 3.14; all setup parameters for the model are taken from this setup, which is described in more detail in chapter 4. The model consists of simple rate equations for the four-level amplifier medium and the pump and seed fields. The amplifier is divided into thin slices, and for each slice these rate equations are integrated in time. Using the simplified level scheme shown in figure 3.15, these can be written (see e.g. [120]):

$$\begin{aligned}
 \frac{dn_o}{dt} &= \gamma_{1o}n_1 + \gamma_{3o}n_3 + \frac{\sigma_p}{\hbar\omega_p}I_p(n_3 - n_o) \\
 \frac{dn_1}{dt} &= \gamma_{21}n_2 - \gamma_{1o}n_1 + \frac{\sigma_s}{\hbar\omega_s}I_s(n_2 - n_1) \\
 \frac{dn_2}{dt} &= \gamma_{32}n_3 - \gamma_{21}n_2 - \frac{\sigma_s}{\hbar\omega_s}I_s(n_2 - n_1) \\
 \frac{dn_3}{dt} &= -\gamma_{3o}n_3 - \gamma_{32}n_3 - \frac{\sigma_p}{\hbar\omega_p}I_p(n_3 - n_o) \\
 \frac{dI_s}{dt} &= \frac{\sigma_s I_s n_{\text{ions}} \Delta l}{\delta t} (n_2 - n_1),
 \end{aligned} \tag{3.58}$$

where the γ 's are the spontaneous decay rates, the n_i 's are the population fractions (level 1 and 2 being the laser levels), I_p and I_s are the instantaneous pump and seed intensities

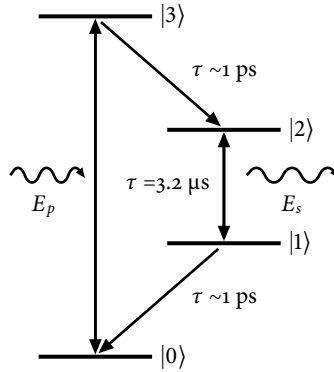


Figure 3.15: Simplified level scheme of titanium-doped sapphire. In the model, only the excitation and decay pathways as indicated in this diagram are considered. The medium is pumped by E_p and the seed field E_s is amplified.

respectively, σ_p and σ_s are the stimulated cross sections for the pump and seed, n_{ions} is the total number of titanium ions per unit volume, Δl is the crystal slice length and δt the length of the time step used. The equations are integrated in time using the measured 110 ns long pulse profile of the pump laser used in our experiments, and two Gaussian seed pulses that traverse the crystal six times. The losses due to mirrors, gratings and spectral filters in the amplifier are all taken into account. At each point in time, the seed intensity and population inversion at the peak of the seed pulses is used to calculate the cumulative phase shifts for each pulse.

The gain properties as derived from the amplifier model are very similar to what is observed experimentally. When the delay between the pump and seed pulses is varied, both seed pulses display a gain curve that reflects the population inversion, shown in figure 3.16. However, as the small signal gain is exponentially dependent on the inversion, it rises and falls much more steeply. Furthermore, it is seen that the second pulse clearly has a lower gain, indicating that some saturation is already present, even though the stored energy is about ten times the extracted energy. The peak gain is around 30 to 40 thousand for both pulses, yielding an output pulse energy of about 15 $\mu\text{J}/\text{pulse}$. The pulse intensity ratio changes with pump-seed timing, as the seed pulses are about 13 ns apart and experience a different gain.

The phase shifts accumulated by the pulses as calculated from the model are rather similar to what has been observed in the experiments. As an example, the phase shifts

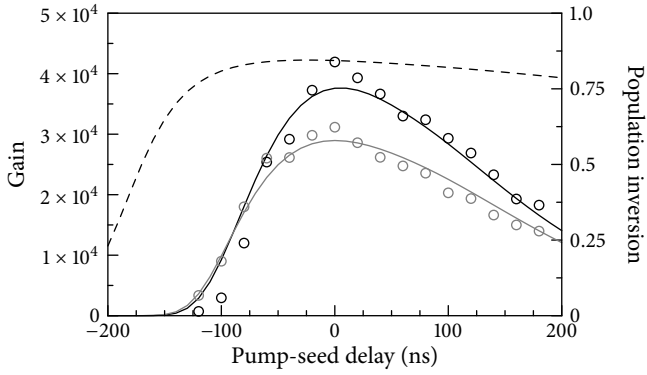


Figure 3.16: The gain of both pulses in an amplified pulse pair versus the pump-seed delay. The first pulse is indicated in black, the second pulse in gray. The solid lines are the results from the simulation, the circles show the pulse gain as measured with the real amplifier shown in figure 3.14.

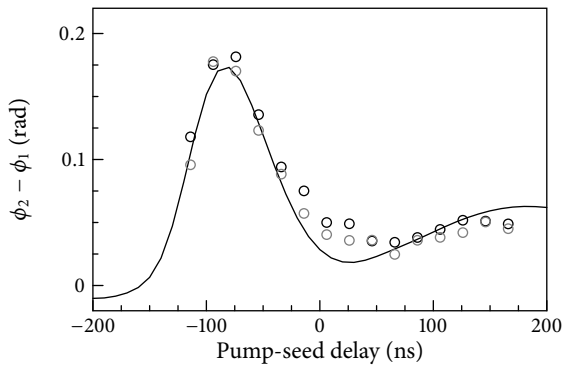


Figure 3.17: The phase difference acquired by an amplified pulse pair versus the pump-seed delay. The solid black line is the result from the simulation, the black and gray circles indicate two separate measurements of the phase shifts introduced by the real amplifier (for the measurement method, see chapter 4).

versus pump-seed timing are shown in figure 3.17. The prominent peak that occurs on the leading edge of the gain curve is due to self-phase modulation, which is mostly compensated for at later times by the phase shift due to heating. The population-dependent phase shift only makes a small contribution. All in all, the phase dynamics of the amplifier can be explained reasonably well by the relatively simple model presented here. It is seen that the phase shifts can be as high as 200 mrad, which immediately makes clear that these shifts must be measured carefully if metrology is to be performed with such amplified pulse pairs. This will be discussed in more detail in chapter 4.

Frequency conversion The final possible cause of phase distortions to be discussed is the frequency conversion process. The experiments in this thesis employ harmonic generation in crystals as well as in gaseous media, and both processes may affect the phase coherence of the pulses.

First we consider frequency doubling in the crystals. By integrating the coupled amplitude equations written with explicit amplitude and phase terms (equations 2.48), the phase evolution of the generated harmonic radiation can be calculated. This was done using the SNLO program [99]. The phase mismatch Δk is one of the most important parameters for this calculation: its magnitude has been estimated to be less than 0.2 mm^{-1} using the maximum observed reduction in SHG efficiency. As the experiments performed in this thesis involved multiple stages of frequency conversion, the observed ion signal is a sensitive probe for the SHG intensity. The phase acquired by the second-harmonic radiation has been calculated using our own experimental parameters for various fundamental pulse energies, showing a linear increase over the range of 1 to 20 μJ input pulses (see figure 3.18). The slope of about 5 mrad per μJ is sufficiently low for the relative intensity jitter of the seed pulses to be as high as 10% without inducing significant shifts. The actual relative intensity jitter is much lower.

Next, in the case of third-harmonic generation in gasses, several effects may influence the phase of the generated harmonics. First, we shall consider self-phase modulation in the generating medium. An estimate for the value of n_2 for oxygen at a driving wavelength of 375 nm, as used in chapter 7, can be made by interpolating the data from [148] ($5 \times 10^{-23} \text{ m}^2/\text{W}$ at 800 nm), [149] and [150] ($9.7 \times 10^{-23} \text{ m}^2/\text{W}$ at 515 nm), and [151] ($30 \times 10^{-23} \text{ m}^2/\text{W}$ at 248 nm), yielding $\sim 12 \times 10^{-23} \text{ m}^2/\text{W}$ at 375 nm. Integrating the phase shift given in equation 2.44 over the medium length using this value, together with the experimental parameters of chapter 7, the size of the phase shift can be estimated to be about 250 mrad for a 10 μJ pulse. For a relative intensity jitter between two pulses

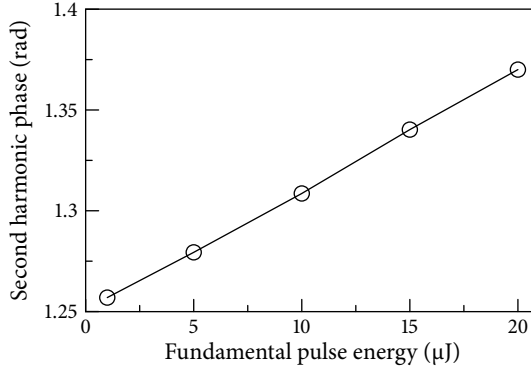


Figure 3.18: The calculated phase acquired by the generated second-harmonic wave as a function of fundamental pulse energy.

of a few percent, the phase jitter is of the order of 10 mrad, or about 60 kHz for the fundamental. For the harmonic radiation, this is amplified by a factor equal to the harmonic order. The resulting 180 kHz is too small to be detected in our experiments.

Furthermore, because of the high intensities involved, harmonic generation in a gas is usually accompanied by ionization, forming a plasma. The index of refraction as a result of the free electrons n_{free} depends on the free electron density $N_e(z, t)$ according to [152]

$$n_{\text{free}}(\omega) = \sqrt{1 - \left(\frac{\omega_p(z, t)}{\omega}\right)^2}, \quad (3.59)$$

with $\omega_p^2 = e^2 N_e(z, t) / m_e \epsilon_0$ being the plasma frequency. As the ionization happens during the pulse, a phase shift will accumulate over the interaction region, given by

$$\phi(t) = -\frac{q\omega}{c} \int_0^L n_{\text{free}} dz, \quad (3.60)$$

where q is the harmonic order. The ionization degree of the medium can be determined by extrapolating the data given in figure 4 of [153] for ionization of oxygen with 405 nm pulses to the pressure and peak power in our experiment. This results in a free electron density at the end of the pulse, N_e , of about $5 \times 10^{13} \text{ cm}^{-3}$, and with 5×10^{18} atoms per cubic cm present at 0.2 bar and 293 K, the ionization fraction is then estimated to be only about 10^{-5} . At these free electron densities, the plasma frequency is much lower than the laser frequency, and assuming a homogeneous medium, the maximum phase

shift that is accumulated in the third harmonic can thus be estimated to be about

$$\delta\phi = \frac{qe^2 N_e L}{2m_e \epsilon_0 \omega c}. \quad (3.61)$$

Inserting the numbers for our experimental conditions, it is seen that this phase shift is of the order of 1 mrad. But since quantum interference spectroscopy is only sensitive to phase differences between the pulses, only the change in N_e from pulse to pulse is significant, which is at most equal to the stated number. The worst-case shift of the order of a mrad is well below our detection limit, so the ionization-induced phase shifts are of no concern in the present experiments.

For high-harmonic generation, according to the three-step model (see section 2.8.1), the phase of the harmonics is influenced by the classical action of the electron moving in the driving laser field. However, the driving field intensity used in the experiment of chapter 7 (of the order of 10^{12} W/cm²) is much too low to induce any phase shift, as can be expected for low-order harmonic generation.

Finally, there is the single atom effect originating from the time-dependent electric dipole phase induced by the non-adiabatic change of the driving field within an optical cycle, as described by e.g. [103]. However, this is an effect that plays a significant role only when the pulse duration is below about 30 fs. When using ps pulses, as done in the experiments of this thesis, the change in field strength from one cycle to the next is so small that it can be considered adiabatic. Hence this effect is not capable of disturbing the phase coherence of the generated harmonic pulses used for the experiments.

3.7.4 Measurement ambiguity

The last item on the list of potential pitfalls is somewhat special, as it is not limiting the precision of the method per se, but nevertheless imposes a strict prerequisite on a frequency measurement, be it absolute or relative. It is a direct consequence of the inherent ambiguity of the interference signals that are recorded in a typical measurement run: these are an almost endless repetition of the same basic resonance shape. One of the resonances in the recorded signal corresponds to the actual resonance that is probed, but from the signal itself it is not clear which one it is. Even though the width of the resonances can be impressively narrow, the best one can do is to quote a large set of possible values, which are spaced by the period of the interference signal. For relative frequency measurements, this is a problem as well: in the simple case of zero difference, two identical signals are recorded, but the same signals are recorded when the frequencies differ by exactly the mode spacing. Without prior knowledge, it is quite

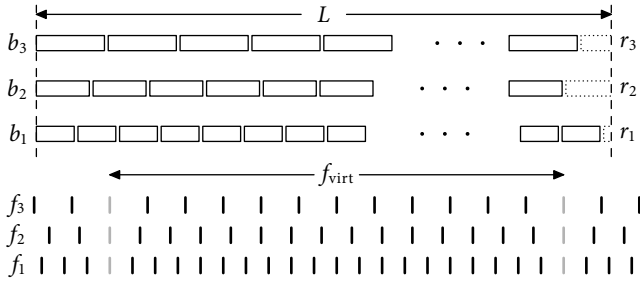


Figure 3.19: The Chinese remainder theorem. Above: measuring length L with three yardsticks of different length b_1 , b_2 and b_3 . Trying to bridge L with an integer number n_i times b_i leaves a remainder r_i : from the b_i and the r_i , L can be retrieved. Below: measuring a frequency with three different pulse delays, or repetition rates f_1 , f_2 and f_3 . Quantum interference measurements in the three situations give three sets of possible frequencies: the combination of the three gives a coincidence that occurs much less often, every f_{virt} . This longer period makes it possible to pinpoint the right frequency with less demands on the initial knowledge of the unknown frequency.

a challenge to determine how many modes the two signals are shifted with respect to each other, and in which direction.

The problem is easily solved when the absolute or relative frequency to be determined is already known in advance with an accuracy better than at least half the mode spacing. In this case, by comparing the coarse value to the measured set of possible frequencies, it will be possible to identify the correct center mode. In practice, however, an initial accuracy better than about a third of the mode spacing is needed for sufficient confidence.

Another approach that relaxes this constraint uses two or more different mode spacings, i.e. pulse delays. This approach is an optical implementation of the ancient Chinese remainder theorem, which was already known in the third century AD, and is now widely used in length and frequency metrology. To explain it, consider the measurement of an unknown, large distance L , as shown in figure 3.19. Several yardsticks of different lengths b_i are used, and for each yardstick only the remainder of L is measured, called r_i . The distance L can now be expressed as $L = n_i b_i + r_i$ for each i . Defining $b = \prod_i b_i$, the theorem states that if no yardstick is an exact multiple of any

other yardstick, L can be found from (see [154]):

$$L = \sum_i \frac{u_i b}{b_i} r_i \pmod{b}, \quad (3.62)$$

where u_i is determined from the constraint $b/b_i = 1 \pmod{b_i}$. In other words, the quantity b acts as a larger virtual yardstick, making it much easier to determine the total length L . Using the same technique for our method of frequency metrology, the pulse delays used, or rather the mode spacings f_i , create a virtual mode spacing f_{virt} , equal to the least common multiple of the f_i , see the lower panel of figure 3.19. To find an unknown frequency, it is compared with all f_i : the large value of f_{virt} makes it possible to use a relatively crude initial value to pinpoint the exact frequency. Of course this approach needs a careful choice of pulse delays: taken too far apart, the virtual mode spacing will be not much larger than the largest in the set, and taken too close together, it becomes very hard to distinguish the sets from one another.

Laser system and vacuum setup

The experiments described in this thesis require an elaborate setup, consisting of several important parts as shown in figure 4.1. Phase-locked pulses are generated with a Kerr-lens mode-locked laser with full comb control. Next, pulse pairs or trains are selected from the frequency comb output in a pulse selection setup. The pulses are subsequently amplified in a multi-pass titanium:sapphire amplifier. For the production of deep-UV to VUV pulses, one or more stages of frequency up-conversion are needed, such as doubling crystals or a gas cell for harmonic generation. Finally, the interaction of the comb pulses with the atoms under study takes place in an evacuated atomic beam apparatus fitted with appropriate detectors and acquisition electronics. In this chapter, the construction and operation of all these objects will be described in detail. Furthermore, to establish the phase shifts accumulated in the multi-pass amplifier, experiments using a linear interferometer setup have been performed, which is discussed as well.

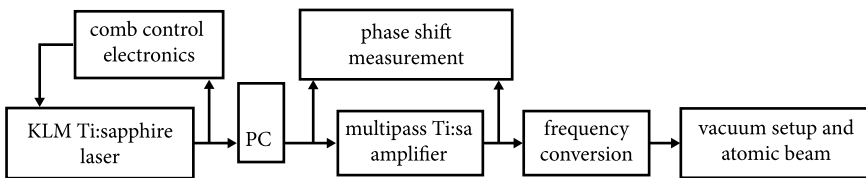


Figure 4.1: Overview of the experimental setup.

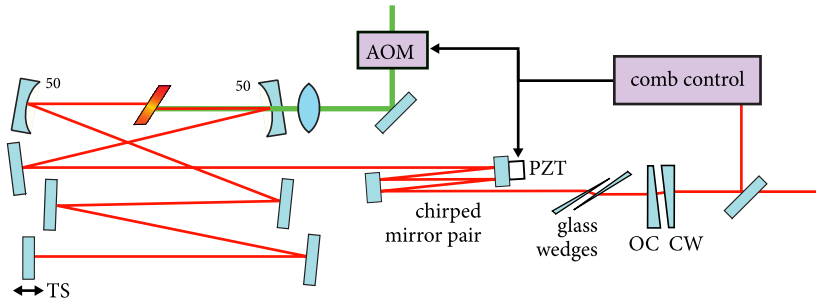


Figure 4.2: Layout of the Ti:sapphire oscillator. TS: translation stage, OC: output coupler, CW: compensation wedge, PZT: piezo transducer, AOM: acousto-optic modulator. The small numbers are radii of curvature in mm.

4.1 Femtosecond oscillator with full comb control

The heart of the laser system is a Femtolaser Femtosource Scientific Pro Kerr-lens mode-locked laser that delivers ≈ 11 fs, 8 nJ pulses at a repetition rate of 75 MHz; it is schematically drawn in figure 4.2. It consists of a 2 m long linear cavity folded into its enclosure by seven plane chirped mirrors, two curved mirrors and a 90% reflective wedged output coupler. Inside the cavity, at the waist halfway between the curved mirrors, a 2 mm thick Ti:sapphire crystal is inserted. The laser is pumped by 5 W of 532 nm continuous wave laser light from a Coherent Verdi X. The chirped mirrors ensure that the dispersion in the cavity is minimized between about 680 and 950 nm, while a pair of fused silica wedges (1° , 1–2 mm thickness), inserted in the cavity at Brewster's angle, are used for fine tuning of the cavity's dispersion. When mode-locking, the laser emits about 600 mW of power in a spectrum ranging from 670–980 nm.

For frequency comb operation, the mode structure of the spectrum needs to be phase-locked to a reference. In our case, this reference is a Rb atomic clock (Stanford Research PRS-10) that is linked to a GPS satellite receiver (Trimble Acutime 2000) with a feedback response time of 10 000 s. The Allan variance of the 10 MHz clock signal from the reference is smaller than 1×10^{-11} at a 10 s gate time, dropping below 1×10^{-12} around a gate time of an hour, but increasing rapidly at longer gate times. The GPS signal at 1 pulse per second is more stable than the clock signal at these timescales, so the long-term stability of the clock is improved by phase-locking it to the GPS.

The repetition rate f_{rep} of the oscillator is locked in a dual-frequency locking scheme. The fundamental of f_{rep} (75 MHz) is detected with a photodiode, filtered out and mixed

down with the fifth harmonic of the signal from a 15 MHz RF generator that is phase-locked to the atomic clock. The resulting difference frequency is low-pass filtered and sent to the locking electronics. At the same time, the 140th harmonic of f_{rep} at ~ 10.5 GHz is detected with a fast photodiode (EOT ET4000), mixed down with the signal from a low-phase-noise RF generator (Agilent E 8241A), filtered and directed to the locking electronics as well. There a potentiometer is used to switch gradually from the first harmonic to the 140th harmonic loop, and the selected signal is fed to a PI controller (Toptica). Its feedback signal is amplified to a range of 0–100 V and applied to a piezo mounted on one of the chirped cavity mirrors. As the locking range of this feedback system is not enough to compensate for the cavity length changes that occur over the course of a day due to temperature drifts, a slow feedback loop was added that drives heating resistors clamped to the laser baseplate. Using the feedback signal from the PI controller, a Schmitt trigger and a FET switch control the current through the resistors, compensating for external temperature variations. This ensures stable repetition rate locking for extended periods of time. The 10 s Allan variance of the locked repetition rate has been measured to be 2.5×10^{-12} relative to the atomic clock, which means that on average the length deviations of the the 2.0 m cavity are kept within one tenth of a Bohr radius.

The measurement and control of the carrier-envelope offset frequency f_{ceo} is more complicated. As discussed in chapter 3, the $f-2f$ technique is used to detect f_{ceo} by generating a beat note between the second harmonic of the red side of the frequency comb spectrum and the blue side, which contains nearly the same frequencies if the spectrum spans a full octave. The beat note between these two components will give a range of new frequencies:

$$f_{\text{beat}} = (2f_{\text{ceo}} + mf_{\text{rep}}) \pm (f_{\text{ceo}} + nf_{\text{rep}}) = \pm f_{\text{ceo}} + (m - n)f_{\text{rep}}. \quad (4.1)$$

The lowest frequency of the beating product is the offset frequency f_{ceo} .

In an experimental realization of this technique it is required that the comb spans at least one optical octave. Though oscillators exist that indeed generate such extremely broad spectra [126, 155, 156], this is by no means standard. The spectrum of our frequency comb laser needs external broadening to reach a full octave. This can be done using fiber nonlinearities, such as self-phase modulation, four-wave mixing or Raman scattering, which can produce the required extra frequencies. However, in a normal single mode fiber, dispersion would quickly spread out the pulses in time, decreasing their peak intensity to a value too low to induce any of these effects. Therefore, spectral broadening in normal glass fibers is limited.

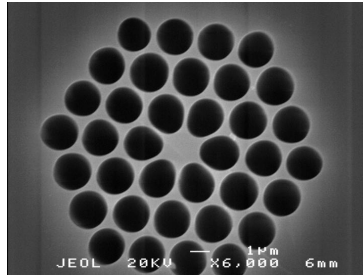


Figure 4.3: A cross section of a micro-structured fiber, showing a $1.7 \mu\text{m}$ core surrounded by air gaps to tailor the dispersion.

However, using specially designed photonic crystal fibers [157, 158], this problem can be overcome. The fibers consist of a narrow core surrounded by air gaps (see figure 4.3), such that the lowest-order mode travels partly through air. The added wave-guiding dispersion of this structure can be tailored such that it compensates the material dispersion of the fiber for a large part, thus enabling short pulses to travel through long stretches of fiber essentially undistorted. In such a fiber, the nonlinear effects can be sustained much longer, leading to highly efficient continuum generation [132, 159]. This method readily produces the required optical octave, while the phase coherence of the optical modes is not disrupted. In our setup, about 150 mW of comb light is focused into a ~ 6 cm long micro-structured fiber with a $1.7 \mu\text{m}$ core diameter (Crystal Fibre) using a $40\times$ microscope objective. The generated continuum spans from 460 nm to well beyond 1000 nm, as can be seen in figure 4.4.

The complete $f-2f$ interferometer setup is shown in figure 4.5. The light exiting the fiber is collected with a second microscope objective and refocused into a 1 mm BBO crystal ($\theta = 22.5^\circ$). There the spectrum around 960 nm is frequency-doubled to 480 nm. This light is re-collimated with a lens, and the fundamental light is separated from the doubled light with a polarizing beam splitter cube (PBC). Both beams are reflected back through the PBC, and the overlapping beams are picked off with a mirror. A common polarization is selected with a $\lambda/2$ plate and another PBC, after which the light is sent through a 480 nm interference filter onto an avalanche photo diode (Analog Modules 712A-4). This detects the beat frequency between the fundamental and the second harmonic at f_{ceo} , together with all the other frequencies of equation 4.1 that fall within the detector bandwidth (100 MHz). The signal from the detector is shown in figure 4.6, where the largest amplitude sine wave is the beat frequency f_{ceo} at 15 MHz,

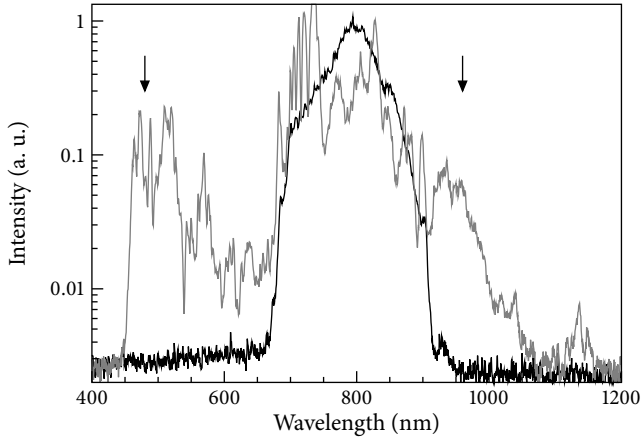


Figure 4.4: The spectral broadening observed for a 6 cm long micro-structured fiber with a core of $1.7 \mu\text{m}$. The input spectrum (black) is shown together with the supercontinuum output (gray), which is broad enough to span an optical octave (the wavelengths used for $f-2f$ locking are indicated by the arrows).

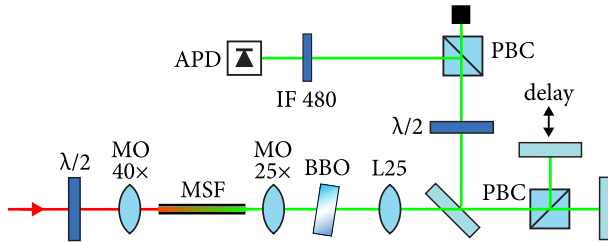


Figure 4.5: The setup for $f-2f$ interferometry. PBC: polarizing beam splitter cube, MSF: micro-structured fiber, MO: microscope objective, L25: 25 cm focal length lens, APD: avalanche photodiode, IF: interference filter.

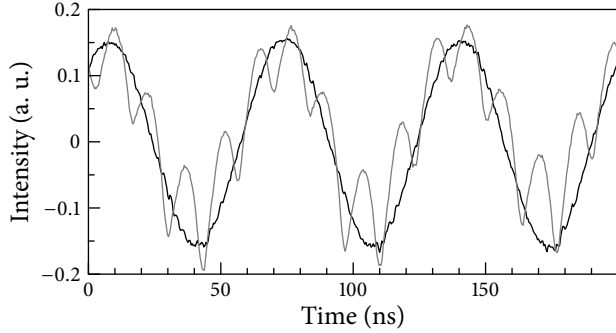


Figure 4.6: The beat signal at f_{ceo} detected by the avalanche photodiode in the $f-2f$ interferometer before (gray) and after (black) low-pass filtering.

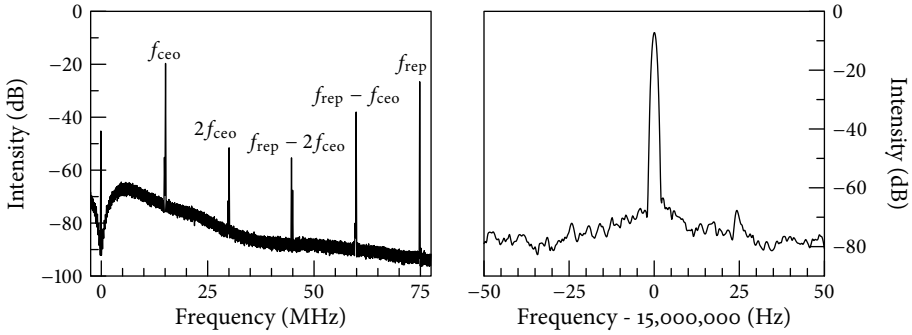


Figure 4.7: The beat signal detected by the avalanche photodiode and an RF spectrum analyzer. On the 80 MHz wide scan (left), the components at f_{rep} and $f_{rep} - f_{ceo}$ are visible as well, together with other combinations of f_{rep} and f_{ceo} that are due to saturation effects in the detector. On the 100 Hz wide scan (right) it is seen that the signal to noise ratio exceeds 60 dB, while the observed 3 dB width of 1 Hz is limited by the spectrum analyzer.

while the lower amplitude sine wave is the repetition rate of the pulses f_{rep} at 75 MHz. After low-pass filtering, only f_{ceo} remains.

To actually control f_{ceo} in a feedback loop, an experimental control parameter is needed. As ϕ_{ce} depends on the ratio of the group and phase velocities in the laser cavity, it is possible to use the intra-cavity dispersion of e.g. the glass wedges to control the evolution of ϕ_{ce} . However, it is easier and faster to modulate the pump intensity: due to

the Kerr effect, changes in the intra-cavity peak power are translated into changes in the carrier-envelope phase [160, 161].

The feedback loop is realized using the signal from the $f-2f$ interferometer as an input: first, the signal at f_{ceo} is converted to a square wave in a fast discriminator. Then it is compared with the output of the 15 MHz generator mentioned earlier, which has been converted to a square wave as well. A digital phase detector of our own design (based on the up-and-down counting principle outlined in [162]; our design however uses two up-counters) is used to detect the frequency and phase difference between the beat note and the reference frequency. Its output is linear across the central cycle, and has a capture range of 32 cycles. The phase detector output is connected to a PI controller, the output of which is used to control the pump power to the comb laser via an acousto-optic modulator (AOM) in the beam path of the pump laser. This AOM diffracts a few percent of the pump light out of the beam, and in this way influences the intra-cavity peak power and thus ϕ_{ce} .

Using this locking scheme, f_{ceo} can be locked to the reference frequency with an RMS phase deviation of only ~ 150 mrad on a timescale of a few ms. In figure 4.7, the locked beat frequency f_{ceo} can be seen on a 100 Hz scale, displaying a 60 dB signal to noise ratio and an instrument-limited 3 dB width of 1 Hz. Together with the repetition rate control, this constitutes full control over all the modes of the frequency comb.

4.2 Pulse-picking Pockels cell

For the experiments described in this thesis, amplification of the oscillator pulses is needed. As it is very hard to amplify pulses at a repetition rate of 75 MHz, the pulse train from the oscillator cannot be used directly. Instead, the repetition rate is reduced to 1 kHz using a Pockels cell (PC). This device is based on an electro-optic crystal, which transforms the polarization of the transmitted light depending on the (high) voltage applied to the crystal (see section 3.7). When the PC is driven at a specific, wavelength dependent voltage, it will rotate the polarization of the light over 90° . This value of the voltage is called the half-wave voltage. A Glan polarizer after the PC then rejects any residual light in the perpendicular polarization. The voltage (~ 5 kV at 800 nm) can be switched in a few ns, so single pulses are selected from the oscillator pulse train when ~ 10 ns pulses are applied to the crystal. The PC is triggered by a 1 kHz signal divided down from the detected f_{rep} of the oscillator, with an adjustable delay introduced by the PC driver. When the pulse length of the high voltage pulse delivered to the PC is increased, trains of pulses can be selected. Behind the Glan polarizer, a Berek polarization rotator

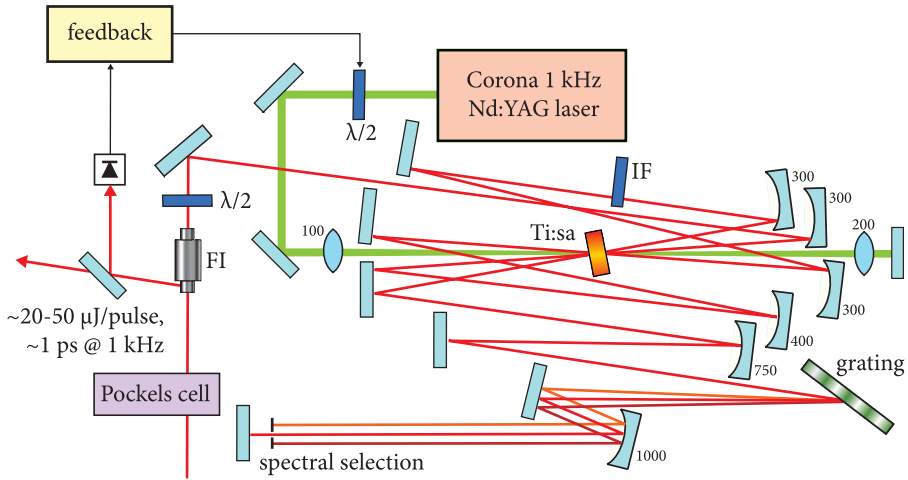


Figure 4.8: The non-saturating six pass amplifier as used for the krypton experiments of chapter 6. FI: Faraday isolator, $\lambda/2$: half-wave plate, Ti:sa: titanium:sapphire crystal, IF: interference filter. Radii of curvature and focal lengths are indicated in the figure in units of mm.

tuned to the right wavelength is used to rotate the polarization back to the horizontal plane. To prevent amplifier back-reflections from reaching the oscillator, a PBC is placed before the PC. Normally, back-reflections will arrive at the PC when it is switched off again, so the PC will not rotate their polarization back to horizontal, and they will be rejected by the PBC. Only when longer pulse trains (more than 6 pulses) are used, back-reflections can arrive at the PC when it is still switched on: this limits the maximum pulse train length. A Faraday isolator can of course resolve this problem, but the right type was not available during the krypton experiments of chapter 6.

4.3 Non-saturating Ti:sapphire amplifier for pulse sequences

Selected comb pulses are amplified in a Ti:sapphire multi-pass amplifier, which is shown in figure 4.8. Pulse trains enter the amplifier through a Faraday isolator (FI) and a half-wave plate, the combination of which rotates the polarization over 90° (45° each). At the same time, the dispersion of the heavy glass of the FI stretches the pulses in time to a duration of about 1 ps. A 5 mm long Brewster-cut Ti:sapphire crystal mounted in a water-cooled copper block is used as amplifying medium. It is pumped by a Coherent

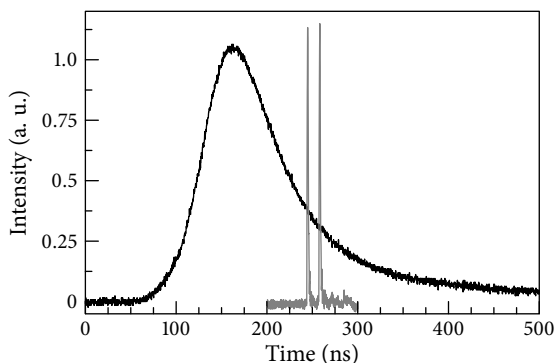


Figure 4.9: The Corona pump pulse (black) and an amplified pulse pair (gray).

Corona Nd:YAG laser, which delivers 7 mJ in a 110 ns FWHM pulse at a repetition rate of 1 kHz. The pump beam is focused into the crystal by a 100 mm focal length lens, and the transmitted pump light is reflected back through the crystal by a plane mirror and a 200 mm lens to reach a gain of about 30 at both 750 and 850 nm. The seed pulses traverse the pumped region of the crystal three times, focused at the center of the crystal on each pass by curved mirrors. After three passes, the pulses enter a $4f$ wavelength selection system consisting of a 1200 l/mm gold coated grating and a -1000 mm radius-of-curvature (ROC) curved mirror. At the Fourier plane, a narrow, adjustable slit is positioned to cut down the spectrum to a width of approximately 0.5 nm, which is necessary to ensure excitation of only a single transition in the studied atoms. Directly behind the slit a plane mirror reflects the pulses back to the grating, after which they trace the same path back through the amplifier, making an additional three passes through the crystal. The combination of the half-wave plate and the Faraday rotator leaves the polarization horizontal, thus the pulses are reflected out by the input polarizer of the FI.

By tuning the grating and the slit in the $4f$ -system, the amplified spectral region can be varied. The amplifier is designed specifically to operate in the wings of the gain bandwidth, where the wavelengths required for the experiments described in this thesis (750 nm and 850 nm) are located. As the amplifier is less efficient at 750 nm, an extra pass through the center of the crystal as well as an extra Faraday isolator before this pass is added when the setup is operated at that wavelength. The single pass gain of the amplifier is so large that it readily delivers a few mJ per pulse when tuned to the peak of the gain curve. However, since the pulses are only stretched to about a picosecond, this

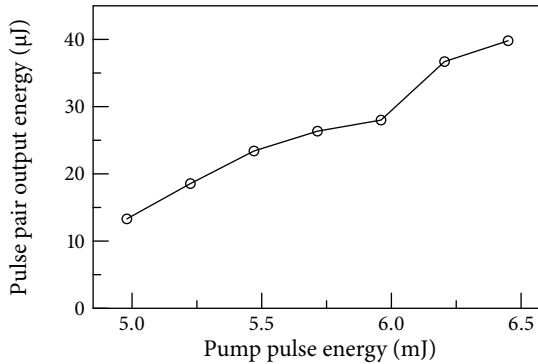


Figure 4.10: The output pulse pair energy of the multi-pass amplifier operating at 850 nm versus pump pulse energy.

would lead to destructive peak powers inside the amplifier. When tuned to the spectral wings, the gain has dropped so much that the amplifier operates in a non-saturating regime, where the pulses take out only a small part of the stored energy. This allows more than one pulse to be amplified, as the gain has not changed significantly after the first pulse. The number of pulses that can be amplified mainly depends on the length of the pump pulse: in the setup described here, it should be possible to amplify up to about 10 pulses. When amplifying pulse pairs, the output pulses (see figure 4.9) have a maximum power of about 20-30 μJ per pulse at either 750 nm or 850 nm. The amplifier performance at 850 nm is demonstrated in figure 4.10, where the pulse pair output energy is plotted against the pump power. The energy efficiency of the amplifier is about 0.6%, which is low, but understandably so, as large amounts of extracted energy are lost in the spectral filtering of the amplifier.

The major drawback of using a non-saturating amplifier is the increased sensitivity to pump power fluctuations. The Corona pump laser initially showed power fluctuations of a few percent on a timescale of tens of seconds, causing the amplifier output to vary some 40% in power. This is unacceptable, especially because the experiments include several stages of frequency conversion after the amplifier, which will only increase these fluctuations. Therefore a power stabilization feedback loop is constructed by adding a motorized half-wave plate in the pump beam. The power of the amplifier is measured with a photodiode, and a computer program uses this signal to steer a servo motor connected to a half-wave plate in the pump beam of the amplifier. The Brewster-cut

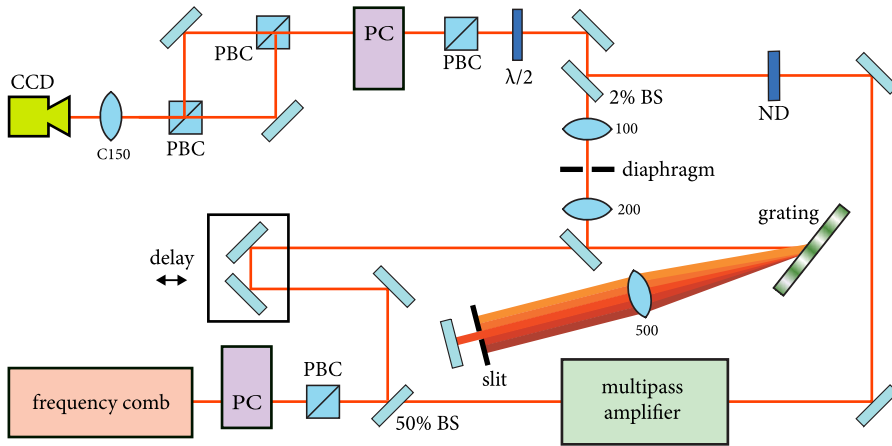


Figure 4.11: The interferometer used to measure pulse-to-pulse phase shifts induced by the amplifier. PBC: polarizing beam splitter cube, BS: beam splitter, C: cylindrical lens, ND: neutral density filter, CCD: charge-coupled device camera. The grating, the 500 mm lens and the plane mirror form a $4f$ -system with $f = 500$ mm. The numbers in the figure indicate focal lengths in mm.

crystal rejects any vertically polarized light, making it possible to modulate the output power of the amplifier. In this way, the output power can be stabilized to a maximum of about $15 \mu\text{J}$ per pulse, with a remaining jitter of less than 10%.

4.4 Interferometer for phase measurements

To assess the effect of the various parts of the setup on the pulse-to-pulse phase stability of the pulse trains, it is necessary to measure the phase shifts induced by all parts. As discussed in chapter 3, the multi-pass amplifier is likely to cause such shifts because of the different population inversion seen by different pulses and the self-phase modulation in the Ti:sapphire crystal. Also, the predicted absence of any significant Pockels-cell-induced phase shift must be checked experimentally.

The method used to measure the phase difference between two pulses is based on interferometry. The setup is shown in figure 4.11: a pulse pair is split into two replicas by a beamsplitter, after which one of the pulse pair replicas is sent through the object under study, e.g. the multi-pass amplifier. The other replica is sent through a delay line, adding the appropriate delay such that both pulse pair replicas can be overlapped again.

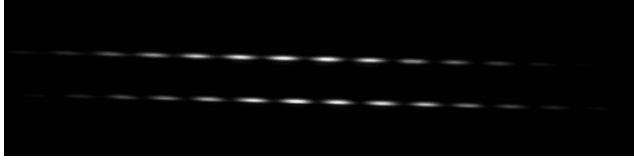


Figure 4.12: The spatial interferograms captured on a CCD camera. One interferogram corresponds to the first pulse of a pulse pair, the other to the second pulse.

The spectrum and amplitude of both replica pulse pairs are matched by attenuating the output of the amplifier and by filtering the spectrum of the delay line output. The replicas are overlapped again in space and time by a second beamsplitter, such that for both the first and the second pulse, spatial interference can be seen between the replicas. A synchronized Pockels cell, set to switch just after the first pulse's replicas have passed, imparts a 90° polarization difference between the first and second pulse replicas. These are separated on a polarizing beam splitter cube, and both are focussed by a cylindrical lens above one another on a single CCD camera, where they form spatial interference patterns. An example of a camera snapshot with both interferograms is shown in figure 4.12. The interferograms will shift with respect to each other when the phase between the pulses changes, be it through amplifier dynamics or through alignment in the projection optics. The latter cause needs to be eliminated, as it will add a spurious phase shift not related to the object under study. This is accomplished by switching the projection around: a true pulse-to-pulse phase shift will have both interference patterns swapped, as the phase is independent of the path the pulses take. An alignment phase shift will cause the switched pattern to be identical to the unswitched case, as the phase is the result of the specific path the pulse followed. The phase of each interference pattern is determined by Fourier transforming, filtering and inverse Fourier transforming the interference pattern [163]. The retrieved spectral phase is averaged over the central part of the spectrum. The phase difference between the two simultaneously recorded interference patterns can be calculated easily. Due to the switching, the phase difference will show discontinuities over time, in a square wave fashion, as can be seen in figure 4.13. The amplitude of this square wave is twice the true phase shift between the pulses acquired in the large interferometer.

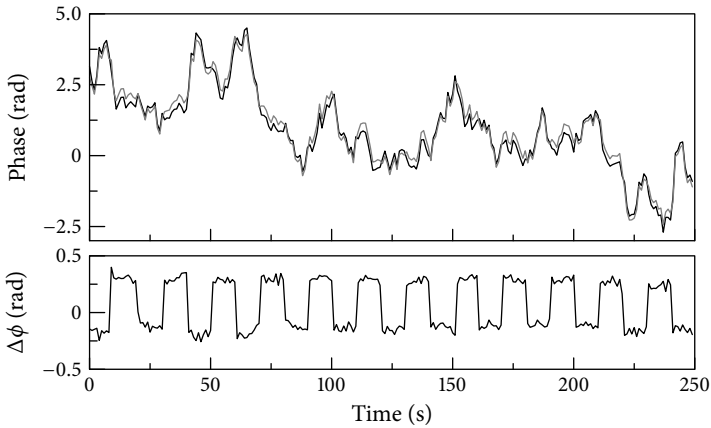


Figure 4.13: An example of an amplifier phase shift measurement. The two traces in the upper panel are the phases retrieved from the upper and the lower interferogram projected on the CCD camera. As the first and the second pulses switch position on the camera every ten seconds, the difference signal in the lower panel reveals the phase shift independent of the path followed.

4.4.1 Sensitivity check on empty interferometer

To check the sensitivity of the method, phase measurements have been performed with an empty interferometer. As is to be expected, the results indicate no detectable phase shift. To ensure the alignment insensitivity of our switching setup, the whole interferometer and the camera projection optics were re-aligned several times, again yielding no observable shifts within 20 mrad.

4.4.2 Phase shifts of the Pockels cell

The first object to be studied is the Pockels cell used for pulse picking, see section 4.2. Because it cannot be used for pulse picking during these measurements, we use an acousto-optic pulse picker to select pairs of pulses at 1 kHz. The Pockels cell itself is inserted in the test arm of the interferometer. It is timed such that only one of the pulses is rotated completely, while the other pulse falls in the flank of the Pockels cell pulse, where it sees a different voltage. In this way, it is possible to detect an interferogram for both pulses. After recombination of both arms through a polarizing beam splitter cube, a $\lambda/2$ plate and a second polarizing beam splitter cube are used to select a common polarization state. Using this setup, several measurements have been performed, which

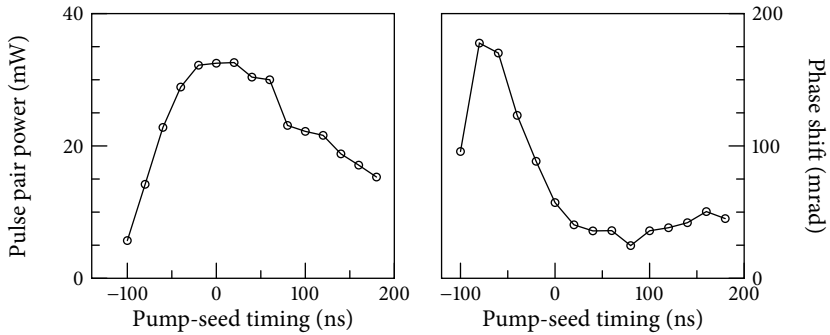


Figure 4.14: Left: the measured power, right: the measured phase shift induced by the multi-pass amplifier as a function of the pump-seed timing.

all showed phase shifts at or below the detection limit of our system. Hence it is concluded that indeed the Pockels cell is constructed and aligned such that it does not introduce a measurable phase shift on the transmitted field.

4.4.3 Phase shifts of the multi-pass amplifier

The origins of phase shifts introduced by the multi-pass amplifier were discussed in chapter 3. To measure these shifts, the reference arm of the interferometer was fitted with a $4f$ -setup similar to the one implemented in the amplifier. A telescope in the reference arm is used to match the divergences of both arms, whereas beam splitters and neutral density filters are employed in the amplifier arm to ensure equal amplitudes. To check the predictions of the numerical model presented in chapter 3, the phase shift as a function of pump-seed delay was measured: the results are shown in figure 4.14. Phase shifts up to 180 mrad are observed, displaying the general shape of a phase shift due to self phase modulation, peaking during the rising edge of the gain. Overall, there is a good agreement between the measured and the calculated amplifier-induced phase shifts (see figure 3.17). As these shifts are obviously dependent on the daily alignment and power of the amplifier, they cannot be calibrated once for all later measurements: during absolute frequency measurement as described in chapter 6, measurements of the actual amplifier phase shift must be performed in between the spectroscopic measurement runs, to allow the results to be corrected for this shift.

4.5 Frequency conversion

To perform spectroscopy in the deep ultraviolet or vacuum ultraviolet, the amplified frequency comb pulses must be upconverted. This is done in different ways for the various target wavelengths. To obtain the 212.5 nm radiation needed for the excitation of krypton (described in chapter 6), the amplifier is tuned to 850 nm, where it delivers up to 20 μJ per pulse. For frequency doubling, the output pulses are focused with a -100 mm ROC mirror into a 3 mm thick BBO crystal cut at $\theta = 30^\circ$, $\phi = 0^\circ$. The resulting 425 nm, 10 μJ pulses are then recollimated and separated from the 850 nm light using two dichroic mirrors. The pulses are frequency doubled again in a second BBO crystal (3 mm thick and cut at $\theta = 73.1^\circ$, $\phi = 0^\circ$), yielding about 2 μJ per pulse at 212.5 nm. These pulses are focused into the vacuum chamber through Brewster windows, and intersect the atomic beam perpendicularly. After several tens of ns, any excited atoms are ionized by 1.5 mJ, 100 ps pulses from a synchronized frequency-doubled Nd:YAG laser-amplifier system, that is focused into the interaction region as well.

To produce the 125 nm light used in the xenon experiments described in chapter 7, the amplifier is tuned to 750 nm. By adding a seventh pass through the center of the crystal, it is capable of producing 25 μJ per pulse. These pulses are focused into the same $\theta = 30^\circ$ BBO crystal as before, where 10 μJ pulses at 375 nm are generated. These 375 nm (UV) pulses are focused into a gas cell filled with either oxygen or acetylene, to generate the third harmonic at 125 nm. Since phase matching is not possible at this wavelength due to a positive phase-mismatch in most gases, we focus the UV pulses through a 0.1 mm pinhole, and employ differential pumping to create a sudden pressure drop across the pinhole. This provides the asymmetry necessary for third-harmonic generation, producing about 50 fJ per pulse at 125 nm. After the pinhole, the VUV radiation is collimated using a MgF_2 lens; a second differentially pumped gas cell in front of the MgF_2 lens ensures a steady gas flow away from the lens, to prevent contamination of its surface. The harmonic pulses then enter the atomic beam chamber, where they perpendicularly intersect a beam of atoms. The intensity of the VUV pulses is monitored at the opposite end of the chamber using a channel electron multiplier (Dr. Sjuts Optotechnik GmbH) behind a Lyman- α filter (Acton 122-XN).

4.6 Vacuum setup and ion detection

The actual spectroscopy is performed on an atomic beam under high vacuum conditions. An overview of the vacuum setup used is shown in figure 4.15. Two interconnected

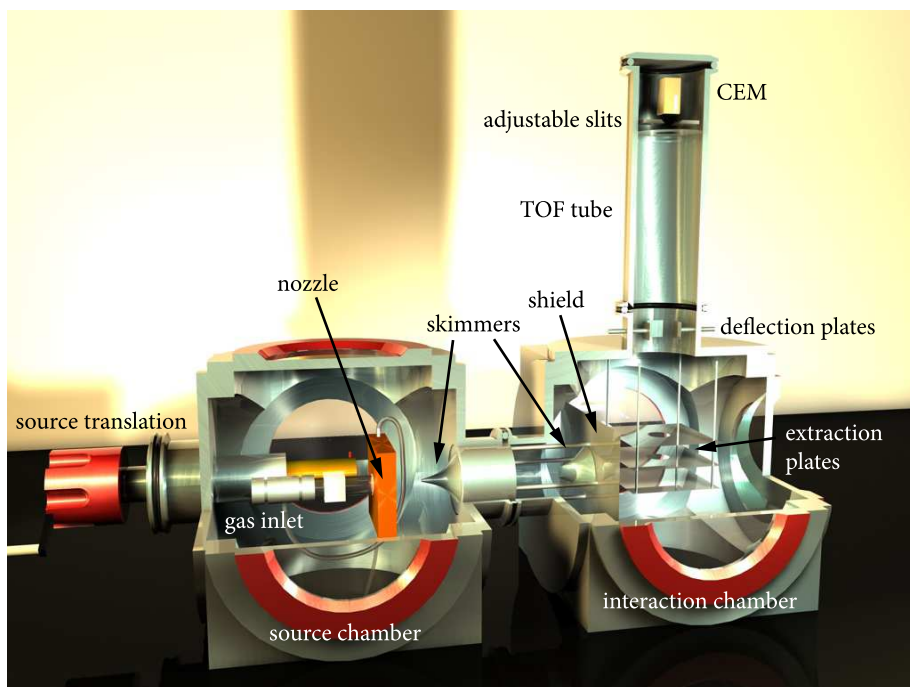


Figure 4.15: The vacuum setup used for the creation of an atomic beam and ion detection. TOF tube: time-of-flight tube; CEM: channel electron multiplier.

cubic aluminum chambers are evacuated to a pressure of about 10^{-7} mbar using two turbo molecular pumps (Pfeiffer Vacuum) with oil-free backing pumps. In the center of the first chamber, an atomic beam source is positioned, identical to the source used by Rooijackers et al. [164]. A controlled flow of gas can be let in through a needle valve, and is injected into the chamber through a 0.25 mm diameter nozzle. At the highest atomic beam intensities that were employed, the pressure in the source chamber rises to 10^{-4} mbar. The source emits about 2×10^{18} atoms $\text{sr}^{-1} \text{s}^{-1}$, with a most probable velocity at room temperature of about 380 m/s for krypton atoms and 305 m/s for xenon atoms. The atoms fly towards the second chamber, but are mostly blocked by a pair of skimmers placed along the axis running through the center of both chambers. The first one of these is positioned about 3 cm from the nozzle, and is a circular skimmer with an aperture diameter of 0.29 mm. The second skimmer has a slit geometry of 0.24 mm by

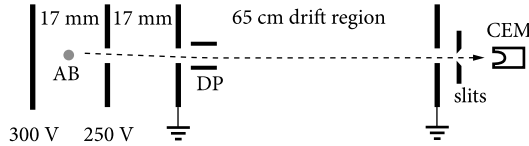


Figure 4.16: The dual-stage time-of-flight tube. AB: atomic beam, DP: deflection plates (in two dimensions perpendicular to the tube axis). The slits are also in two dimensions.

10 mm, and is positioned about 14 cm from the first one. To prevent scattered atoms from reaching the interaction region, a screen is placed around this second skimmer. The atomic beam that is selected in this way has a very narrow velocity spread in the direction perpendicular to the beam: at room temperature, the residual FWHM Doppler width is 10 MHz for the 125 nm transition in xenon, and 14 MHz for the 212.5 nm transition in krypton. The source can be translated in three perpendicular directions: for maximum beam intensity, it is aligned to the axis defined by the skimmers using the glow from a DC discharge that can be maintained through the nozzle.

4.6.1 Time-of-flight ion detection

The interaction region is situated at the lower end of a dual-stage time-of-flight tube that accelerates the ions towards the channel electron multiplier detector: a diagram of the TOF-tube is given in figure 4.16. The bottom plate is kept at a potential of 300 V, while the plate above the interaction region is held at 250 V. The two plates around the interaction region are separated by 17 mm, while a third plate 17 mm above the second, is grounded. This is followed by a field free region that extends for 65 cm, ending with a grounded fine mesh in front of a channel electron multiplier (CEM, dr. Sjuts Optotechnik GmbH). The front face of the CEM is maintained at a negative voltage of 1700 V. Ionized atoms will be accelerated towards this detector in the first two field regions. During the field-free flight, different masses can be time-focused to arrive at different times on the CEM [165]. Besides ions produced from the beam, there are also ions produced from the background gas. Therefore we use slits in two dimensions directly below the CEM to select only ions originating from the interaction region. At the same time, small deflection plates are employed in both directions at the entrance of the flight tube to direct the ions towards the CEM. In this way, the TOF setup can be tuned such that virtually no background ions reach the detector. The mass resolution of this setup, $m/\Delta m$, has been determined to be about 1000, so atomic isotopes are well resolved (see figure 4.17).

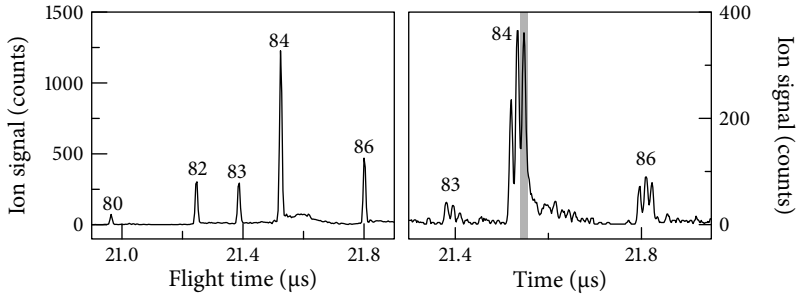


Figure 4.17: The time-of-flight spectrum of krypton ions (see chapter 6) measured with a single pulse (left), and with a pulse pair and a delayed ionization pulse (right). In the latter case, each isotope peak is split into three, with the last peak corresponding to the ions created with the ionization pulse. The shaded area indicates the counting gate used for the interference measurements.

As the UV pulses are in itself capable of ionizing the atoms, the time-of-flight spectrum for two excitation pulses and the ionization pulse shows three peaks for each isotope, as can be seen in the right panel of figure 4.17. The quantum interference signal from a single isotope is isolated from the rest by mixing the CEM signal with a square pulse of about 100 ns width in an RF mixer. The square gate pulse is generated by an arbitrary waveform generator that is synchronized to the laser pulses, and the delay of the gate can be tuned to select different isotopes. The gated signal is sent through a discriminator to convert the small signal to TTL pulses, and these are counted by an Agilent 53132A frequency counter that is configured to count the input pulses during 10 s. During a scan, a computer program scans the repetition rate of the frequency comb laser with steps of a few tens of mHz, thereby changing the delay between the pulses by 13 attoseconds per step. At each step, the ion signal from the counter is retrieved by the program, thus recording the quantum interference signal.

From the numerical simulations of chapter 3, an estimation of the expected experimental count rate can be made for the xenon experiments. Of course, this depends on the number of atoms present in the interaction region, for which we need to know the number of atoms emitted by the source as well as their velocity. Extrapolating the data from [164], who used the same source, it can be estimated that about 2×10^{18} atoms $\text{sr}^{-1} \text{s}^{-1}$ are emitted. Furthermore, to obtain the velocity, an equation from [166] for the most

probable velocity of atoms in a supersonic expansion is used,

$$\bar{v} = \sqrt{\frac{2TC_p}{m}}, \quad (4.2)$$

where T is the temperature of the atoms before the expansion, C_p is the heat capacity of the gas and m is the mass of the atoms. This yields a value of 305 m/s for xenon atoms. A similar value is obtained when the data for helium in [164] are scaled to the proper mass. Based on these values, it is seen that xenon atoms travel about 4 μm during the 13.3 ns between the pulses, which is negligible compared to the 1 mm light beam diameter. The skimmers in the setup select approximately 1×10^{-6} sr, so there are about 6.6 million atoms in the interaction region. With an excitation probability after two pulses of 0.25×10^{-7} , an estimated 0.16 atoms are excited per pulse pair. As the experiment is repeated at 1 kHz, this corresponds to a count rate of 160 counts/s, assuming a 100% detection efficiency. This value agrees very well indeed with the observed count rates.

Control and precise measurement of carrier-envelope phase dynamics

The evolution of the carrier-envelope phase ϕ_{ce} of a 10 fs Ti:sapphire laser has been traced on timescales from microseconds to seconds using various techniques. Precise locking of this phase has been achieved down to an RMS deviation of $\frac{1}{40}$ th of an optical cycle. Stability measurements were performed independently of the feedback loop, focusing on the phase jitter introduced by the feedback loop itself, by the pump laser, and by a prism compressor. It is shown that a multi-mode pump laser introduces more phase noise on ϕ_{ce} than a single-mode pump laser.

5.1 Introduction

In recent years, there has been a rapid advance in the field of ultrafast laser physics. Generation of sub-10 femtosecond pulses has become a routine task for several research groups [167–170]. This progress has led laser physics into a domain where laser pulses last only a few oscillations of the electric field [171], so that the phase between the carrier wave and the pulse envelope ϕ_{ce} becomes a significant variable. Control of ϕ_{ce} has been demonstrated with the use of an $f-2f$ nonlinear interferometer [29, 172, 173], as well as by using the phase relation between pump and signal waves in a parametric amplification scheme [174].

The influence of ϕ_{ce} has recently been demonstrated in strong field phenomena such as above threshold ionization [175] and high harmonic generation [176]. Stabilization of ϕ_{ce} has been shown to enable phase-coherent synthesis of optical pulses from separate femtosecond lasers [177, 178]. Also, the creation of isolated attosecond X-ray pulses

is predicted to greatly benefit from carrier-envelope phase control [179, 180]. Such applications make a thorough study of carrier-envelope phase locking a necessity, to provide a quantitative characterization of the various sources of phase noise involved. Such studies have been performed to some extent by several groups. Poppe et al. [181] exploited the dependence of ϕ_{ce} on the intra-cavity pulse energy to characterize phase noise of ϕ_{ce} through the measurement of pulse energy fluctuations [182]. A more detailed analysis on the pulse intensity dependence of ϕ_{ce} has been performed more recently by Holman et al. [183, 184], leading to both theoretical formulas and accurate experimental data on this subject. Furthermore, they show that there can exist a laser intensity where the first derivative $d\phi_{ce}/dI$ is zero, leading to a minimization of the carrier-envelope phase noise. Helbing et al. [161] measured the single-sideband frequency noise density of the beat note frequency between two components in the femtosecond frequency comb. Fortier et al. [124, 125] employed two $f-2f$ nonlinear interferometers to measure phase noise in ϕ_{ce} independently from the ϕ_{ce} locking loop. This also enabled them to determine the amount of phase noise added by the supercontinuum generation in a photonic fiber, which is often required to create an octave wide spectrum as input for the $f-2f$ interferometers.

In this chapter, a thorough analysis of various aspects of carrier-envelope offset locking is presented. The stability of the lock is analyzed on all time scales from microseconds to several seconds, using a fast oscilloscope, a spectrum analyzer and frequency counters. With the fast oscilloscope, the evolution of ϕ_{ce} can be tracked — for the first time to the authors' knowledge — directly and without averaging for measurement times up to 4 ms, with a bandwidth of 13 MHz. Measurements are performed using two $f-2f$ interferometers, enabling measurements that are independent of the feedback loop used to stabilize ϕ_{ce} . In addition, the phase noise added by e.g. a pulse compressor can be analyzed in this way. Effects of air flow and acoustic noise are demonstrated, and a comparison is made between pumping the mode-locked laser with a single-mode (Coherent Inc. Verdi 10) and a multi-mode (Spectra-Physics Millennia Xs) Nd:YVO₄ pump laser.

5.2 Carrier-envelope phase control

It is well known that the frequency spectrum of a femtosecond pulse train is a comb of equidistant spectral lines, of which the absolute frequencies are given by $f = nf_{\text{rep}} + f_{\text{ceo}}$ where n is an integer and f_{rep} is the pulse repetition frequency. The offset frequency

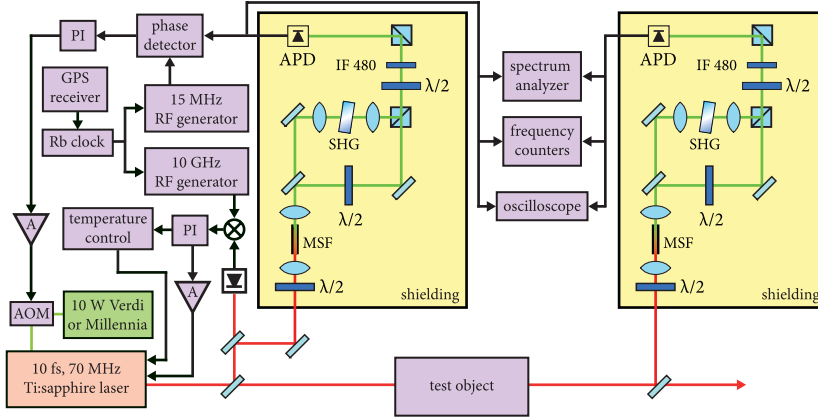


Figure 5.1: Setup for high-accuracy carrier-envelope offset stabilization and phase noise measurements. PBS = polarizing beam splitter, APD = avalanche photodiode, SHG = second harmonic generation, A: electronic amplifier, PI: proportional-integral controller, MSF: microstructure fiber, IF: interference filter, and AOM = acousto-optic modulator.

f_{ceo} is determined by [27, 123]:

$$f_{ceo} = \frac{1}{2\pi} \frac{d\phi_{ce}}{dt} = \frac{\Delta\phi_{ce}}{2\pi} f_{rep}, \quad (5.1)$$

in which $\Delta\phi_{ce}$ is the pulse-to-pulse phase shift of ϕ_{ce} , caused by differences between group and phase velocity inside the laser cavity. This implies that pulse-to-pulse phase coherence can be imposed by locking f_{rep} and f_{ceo} to a known frequency reference.

5.3 Setup and methods for phase stabilization and measurement

In figure 5.1 a schematic is given of the setup used for stabilization of ϕ_{ce} and for phase noise measurements. The femtosecond laser (FemtoSource Scientific Pro, FemtoLaser GmbH) is a Kerr-lens mode-locked Ti:sapphire oscillator equipped with chirped mirrors for intra-cavity dispersion compensation. The emitted pulse train consists of 8 nJ, 10 fs pulses with f_{rep} of 70 MHz. In all the phase stabilization experiments described here, a Verdi solid state pump laser at 532 nm has been used for pumping the Ti:sapphire laser. Only for the measurements described in section 5.6, the Verdi was replaced by a Millennia laser.

Stabilization of f_{rep} is achieved by measuring the 140th harmonic of f_{rep} at about 10 GHz with a fast photodiode, and comparing this signal with the output of a highly stable RF synthesizer (Agilent E8241A PSG-L) operating at 10 GHz. The RF synthesizer frequency is phase-locked to a commercial Rb atomic clock (Stanford Research Systems PRS10, with a 10 s Allan variance $< 1 \cdot 10^{-11}$). The resulting difference frequency forms the basis for a feedback signal, which controls the laser cavity length by way of a piezo-mounted cavity mirror. Coarse control of the cavity length is achieved by temperature stabilization of the laser baseplate. Using a second fast photodiode and a frequency counter outside the feedback loop, we have measured the stability of f_{rep} to be $2.5 \cdot 10^{-12}$ relative to the Rb clock on a 10 s averaging time.

Stabilization of f_{ceo} is achieved using the $f-2f$ nonlinear interferometer scheme [29]. The 100 nm wide (FWHM) output spectrum of the Ti:sapphire laser is spectrally broadened by supercontinuum generation in a microstructure ('holey') fiber (1.7 μm diameter core, from Crystal Fibre), after which it spans a full octave. The infrared part of the spectrum around 960 nm is frequency doubled in a 1 mm thick BBO crystal, and overlapped with the blue part of the spectrum at 480 nm. The beat note signal f_{ceo} can then be measured with an avalanche photodiode, and compared to a reference oscillator phase-locked to the Rb clock. The resulting difference signal is used to stabilize f_{ceo} by modulating the pump power to the Ti:sapphire laser with an acousto-optic modulator (AOM). The interferometer is placed inside an isolating box, to provide shielding against air flow and acoustic noise. The reference frequency to lock f_{ceo} used in these experiments is 11 MHz.

To perform measurements outside the feedback loop, a second, identical $f-2f$ interferometer has been built. This provides the means necessary to measure f_{ceo} both inside and outside of the feedback loop simultaneously. In order to trace ϕ_{ce} on different timescales, two different techniques are used. For measurement times up to 4 ms, both in-loop and out-of-loop signals are fully digitized, together with the reference oscillator signal at 11 MHz, by a fast storage oscilloscope (Tektronix TDS 7404, 4 GHz bandwidth). The instantaneous deviations in ϕ_{ce} , denoted by $\delta\phi_{\text{ce}}$, are retrieved with high resolution by computer analysis of the digitized signals by measuring the relative phase between the lock and reference phase evolution. In effect the set point phase evolution of $2\pi \times 11$ MHz is subtracted, and only deviations of ϕ_{ce} from it are registered as $\delta\phi_{\text{ce}}$. The actual value of ϕ_{ce} cannot be measured in this way, only deviations. For timescales longer than 4 ms, two synchronized interpolating frequency counters (Agilent 53132A) are used to determine the stability of f_{ceo} . In addition, a spectrum analyzer (Agilent E4440A) is used to examine the characteristics of f_{ceo} in the frequency domain.

The length of the fibers used in these experiments is 6 cm. At this length, the fiber end tip is seen to deteriorate in a few weeks at a typical in-coupled power of 25 mW. For shorter microstructure fibers the end tip has the tendency to deteriorate faster, making a 2 cm fiber unusable after less than two days of operation. We suspect that this is due to the substantial amount of blue light that is produced in the supercontinuum generation, which is possibly capable of removing oxygen atoms from the quartz crystal, thus changing the crystal structure. For longer fibers, the peak power of this blue light is lowered by group velocity dispersion, causing less damage. It is clear that for applications requiring continuous operation over longer periods of time, the use of longer fibers is beneficial.

5.4 Real-time measurements of carrier-envelope phase stability

Figure 5.2 shows a typical measurement of the evolution of the phase deviation $\delta\phi_{ce}$ recorded with the out-of-loop interferometer and the reference oscillator. This out-of-loop signal gives a true upper limit to the stability of ϕ_{ce} , as it includes phase noise added by the feedback electronics and both the in-loop and out-of-loop interferometers. One measurement lasts up to 4 ms, during which time both the in-loop and out-of-loop signals are measured, together with the signal from the reference oscillator. These three traces consist of up to 5×10^5 data points, enabling in theory the measurement of high-frequency phase noise up to 62 MHz. The actual high-frequency limit is set by the bandpass-filter used to isolate f_{ceo} , which has an upper cut-off frequency of 13 MHz. The average phase difference between the reference oscillator and the respective interferometer signals is subtracted from the measurements, as it depends on the unknown real ϕ_{ce} , but also on e.g. the arbitrary difference in length between the two arms of the $f-2f$ interferometer. The measurement in figure 5.2 shows the phase difference between the reference and the out-of-loop interferometer, having a root-mean-square (RMS) $\delta\phi_{ce}$ of 152 mrad, which is less than $\frac{1}{40}$ th of an optical cycle. This corresponds to an RMS timing jitter between carrier wave and pulse envelope of 67 attoseconds. It may be possible to improve on this value by operating the laser under conditions where $d\phi_{ce}/dI$ is zero, leading to a reduction in phase noise caused by laser power fluctuations [183, 184]. So far, we have not yet been able to find such a point of operation for our laser.

However, although the RMS phase stability is very good, the instantaneous value of $\delta\phi_{ce}$ can have a value of up to 500 mrad. It is clearly seen from figure 5.2 that there are still rapid variations in $\delta\phi_{ce}$. Fourier analysis of this signal shows that there is a

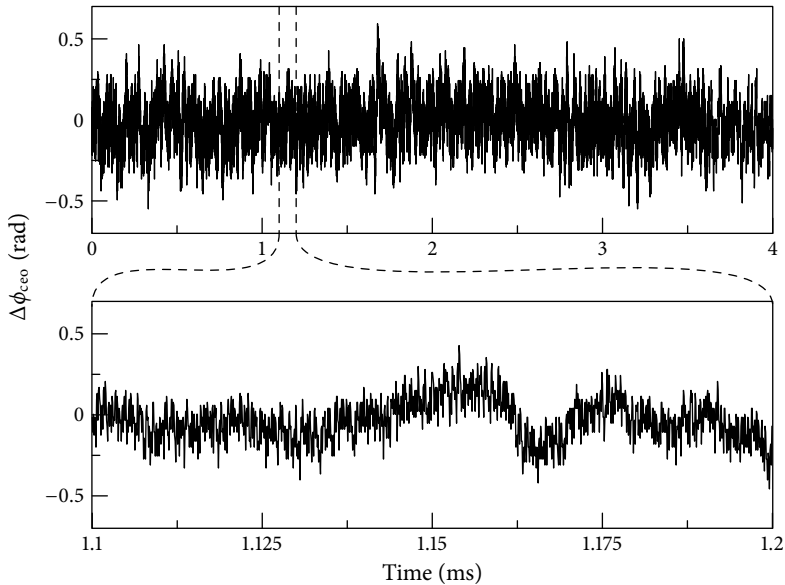


Figure 5.2: A typical oscilloscope measurement of $\delta\phi_{ce}$, with part of the trace enlarged to show rapid phase fluctuations more clearly. $\delta\phi_{ce}$ is the instantaneous deviation of ϕ_{ce} from the lock point phase evolution of $2\pi \times 11$ MHz.

significant amount of noise present: the frequency range from 10-60 kHz adds about RMS 42 mrad to the phase noise.

These observations highlight the added value of direct real-time measurements as opposed to more indirect methods that rely on the integration of noise spectra. With our method no averaging of the data occurs, and $\delta\phi_{ce}$ can be extracted directly from the measurement without any assumptions (e.g. on the relation between pulse energy and ϕ_{ce}). From the above stated difference between RMS value and maximum value of $\delta\phi_{ce}$, the danger of averaging becomes clear.

Another example of this is demonstrated by the measured traces in figure 5.3 which, in spite of the large instantaneous phase deviations that are introduced every now and then by the the locking electronics, have an RMS phase jitter of only 271 mrad. If a few pulses are selected during these 1.5 milliseconds by a pulse picker e.g. for amplification at kHz repetition rate, the chance of ending up with a ϕ_{ce} that is off by as much as 2 rad is clearly not negligible.

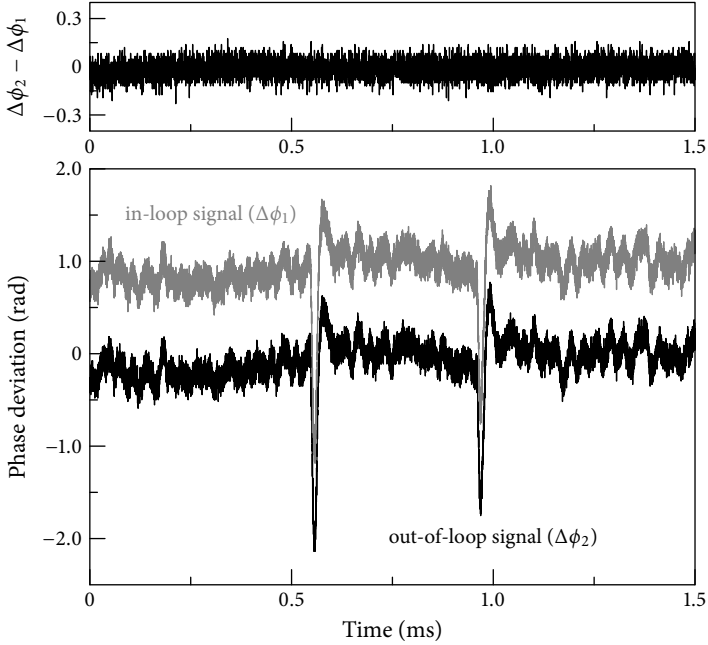


Figure 5.3: Synchronous measurement with two $f-2f$ interferometers. The top graph shows the difference between the in-loop and out-of-loop interferometer traces. The in-loop signal has been given an offset of 1 rad for clarity. The two fast excursions are introduced by the locking electronics, see text.

5.5 Effects of the feedback loop

As already stated above, the influence of the feedback loop and the $f-2f$ interferometer on the stability of ϕ_{ce} can be analyzed by running two $f-2f$ interferometers simultaneously. In addition, the influence of the continuum generation can be investigated. For this purpose it is of importance to keep in mind that small variations of the laser intensity can be converted into phase fluctuations in the microstructure fiber. We consider here only the lowest-order contribution due to the Kerr effect, i.e. the dependence of the refractive index on light intensity I , leading to $n(I) = n_o + n_2 I$ where n_o is the linear and n_2 the nonlinear index of refraction. As the pulse envelope sees a different refractive index (the group index $n_g = n + \omega dn/d\omega$) than the carrier wave at angular frequency

ω , this leads to an intensity dependent phase slip [161]

$$\delta\phi_{ce} = \frac{\omega^2 l}{c} \frac{dn_2}{d\omega} \Delta I \quad (5.2)$$

after passing through a fiber of length l , assuming higher-order dispersion to be negligible. This equation can be simplified to $\delta\phi_{ce} = C_{ap}\Delta P$, where ΔP is the laser power variation. We use 6 cm long fibers with a core diameter of 1.7 μm . From equation 5.2 we estimate $C_{ap} = 3 \times 10^2 \text{ rad/nJ}$ for our microstructure fiber. For this calculation, a (crude) value for $dn_2/d\omega$ has been derived from [185], through a linear interpolation between values of n_2 at different wavelengths.

Any phase noise generated in the microstructure fiber in the in-loop $f-2f$ interferometer will be written back on the laser ϕ_{ce} . In contrast, the out-of-loop interferometer will detect this phase noise, together with the phase noise added by the second piece of microstructure fiber. This phase noise is obviously below a 2π level (otherwise the $f-2f$ phase-locking scheme could never work with microstructure fiber), but it can still be significant [124].

Results of a 1.5 ms measurement with both interferometers are shown in figure 5.3. In this specific experiment, the settings of the locking electronics are adjusted in such a way that fast phase excursions are introduced. By way of the feedback loop this leads to a rapid modulation of the laser intensity. This intensity modulation could then in turn lead to a phase difference between the two interferometers, as only the out-of-loop measurement is capable of detecting this fiber-generated phase noise. However, if the two interferometers would operate at exactly the same power and fiber length, the phase shifts induced by the feedback loop would be identical too. Therefore the interferometers are operated using different power levels: at the in-loop $f-2f$ interferometer, 25 mW of light is coupled into the fiber, while at the out-of-loop interferometer 50 mW input power is used. Surprisingly, figure 5.3 shows no phase deviation between the interferometers. The global difference in measured $\delta\phi_{ce}$ is RMS 39 mrad, and can be seen to consist entirely of white noise. Even during the large ($> 2 \text{ rad}$) phase excursions no difference in $\delta\phi_{ce}$ is detected down to the detection limit, which is about 30 mrad. This measurement has been repeated using various intensities at the fibers, yielding similar results as shown in figure 5.3. Thus we conclude that the 6 cm long, 1.7 μm core diameter microstructure fibers used for phase-locking ϕ_{ce} do not introduce significant phase noise at the tested level of accuracy.

This is in strong contrast with the results of Fortier et al. [124], who extract a value of $C_{ap} = 3784 \text{ rad/nJ}$ from their measurements. They then measure the RMS intensity stability to be 3.16×10^{-4} , and conclude that amplitude-to-phase coupling induces 0.514 rad

of RMS phase noise on ϕ_{ce} , much higher than what is found in the present work. Of course, the exact value of C_{ap} depends on the type and length of fiber used, but a factor six difference seems to be unlikely.

Fortier et al. apply a sinusoidal modulation to the input power of the in-loop $f-2f$ interferometer, and measure the resulting deviation in f_{ceo} as a function of the modulation depth, which is given by $f_{ceo}(t) = \omega_{mod}/(2\pi)C_{ap}\Delta P \cos(\omega_{mod}t)$, where ω_{mod} is the modulation angular frequency, and ΔP is the power modulation amplitude. Applying this formula to their data shown in figure 2b in [124], where they have $\Delta P = 1.07$ mW, $\omega_{mod} = 2\pi \times 0.1$ Hz, and the maximum deviation of f_{ceo} (when the cosine is 1) is about 0.6 Hz, we obtain the value of $C_{ap} = 558$ rad/nJ. This value for C_{ap} agrees reasonably well with the estimate from equation 5.2. However, this number is off by a factor of about 2π compared to their cited value of 3784 rad/nJ. A closer look reveals this same 2π difference between two consecutive formulas in [124], leading us to conclude that their measurements are in agreement with the present work, but that their value of C_{ap} suffers from an error in calculation. Indeed, in a later paper by the same authors [186], the same experiment is described, resulting in a value for C_{ap} of 591 rad/nJ.

Using the value of $C_{ap} = 558$ rad/nJ, and the relation between $\delta\phi_{ce}$ and the intracavity pulse energy measured by Poppe et al. [181] of 0.21 rad/nJ (which we assume applicable to our case), we can calculate the expected phase difference between the interferometers resulting from the phase excursions shown in figure 5.3. For a phase excursion of 2 rad in 15 μ s, and a difference in in-coupled power of 0.35 nJ between the interferometers, this expected phase difference turns out to be about 22 mrad. This is just below the present detection limit, but clearly confirms the lower value for C_{ap} , as otherwise a clear phase difference would have been detected.

5.6 Influence of the pump laser on ϕ_{ce}

It already has been pointed out by Helbing et al. [161] and Morgner et al. [173], that beam pointing instability of the Ti:sapphire oscillator can have a detrimental effect on the stability of ϕ_{ce} . These authors address several possible sources of beam pointing instability, and estimate the magnitude of the noise added in this way. There is another possible source of phase noise which has — to our knowledge — not yet been discussed until now, namely the beam pointing instability of the pump laser. To investigate this, the pump laser that was used in the experiments described above, a single-longitudinal-mode Nd:YVO₄ laser model Verdi 10, Coherent Inc., is replaced by a multi-longitudinal-mode Nd:YVO₄ laser (Millennia Xs, Spectra Physics). The beat note obtained from

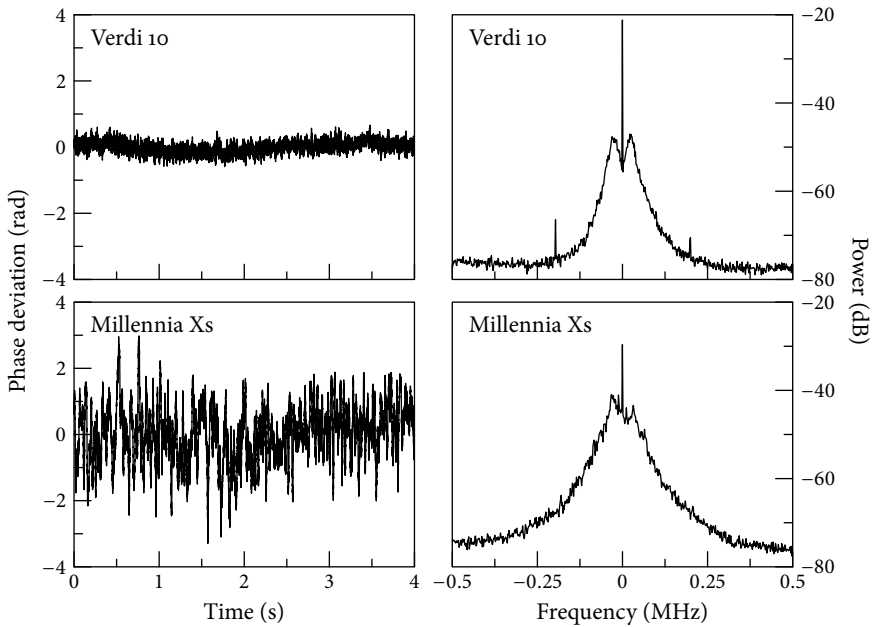


Figure 5.4: Comparison of $\delta\phi_{ce}$ when using Verdi 10 and Millennia Xs pump lasers, using a fast oscilloscope (left graphs) and a spectrum analyzer (right graphs, 1 kHz resolution bandwidth, averaged over 50 measurements). A large difference in phase stability is observed. The offset frequency f_{ceo} is locked to 11 MHz.

the $f-2f$ interferometers at f_{ceo} has the same signal-to-noise ratio as before, but can easily be seen to fluctuate much more. When using the single-mode laser, f_{ceo} stays within a 500 kHz bandwidth for minutes without active stabilization, while with the multi-mode laser f_{ceo} is seen to fluctuate over several MHz within a fraction of a second. Repeating the measurements on the stability of ϕ_{ce} with the two interferometers, striking differences are found. A comparison of the results is shown in figure 5.4, where both oscilloscope traces and spectrum analyzer traces are shown.

It can clearly be seen from the phase measurements that the high-frequency phase noise is typically a factor of six larger in the case of the multi-mode pump laser. Apart from that, from the spectrum analyzer measurements the width of f_{ceo} can be seen to be much larger in this case. When using the single-mode laser, the frequency spectrum of f_{ceo} shows a sharp spike extending 30 dB above a noise pedestal of about 200 kHz wide.

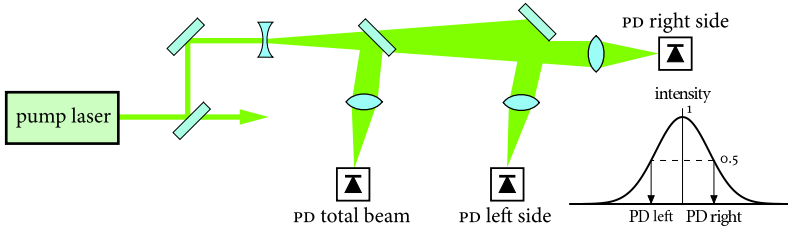


Figure 5.5: Schematic of the setup used to determine beam pointing variations of the pump laser. PD: photo diode, BS: beam splitter.

For the multi-mode laser the height of this narrow peak is only about 15 dB, while the noise pedestal is broader. It must, however, be noted that the difference in performance between the two lasers also depends on the 30 kHz bandwidth of the feedback loop, as a larger bandwidth loop may be able to correct for more of the extra phase noise. Similar spectrum analyzer measurements have been performed with a faster feedback loop (bandwidth ~ 80 -100 kHz) by Jones [187]. These measurements also demonstrate a broader noise band in the case of a multi-mode pump laser, which is not completely suppressed by the faster feedback loop.

To check whether these effects are the consequence of beam pointing variations due to mode fluctuations in the Millennium laser or because of intensity fluctuations, the setup shown in figure 5.5 is used. The laser beam is expanded by a concave lens, and two photodiodes are positioned at the sides of the beam where the light intensity is about 50% of the center value. A small reflection of the beam from a quartz wedge is focused on a third photodiode, to monitor the intensity of the entire beam. This third photodiode is connected to the spectrum analyzer, to determine the power spectral density of the intensity noise [188, 189]. These measurements have been done for the frequency intervals of 1–1000 Hz, 1–100 kHz, and 0.1–1 MHz, with resolution bandwidths of 1 Hz, 51 Hz and 1 kHz, respectively. At frequencies below 1 kHz, the Verdi is seen to outperform the Millennium by about a factor of 2 in stability. However, in the range of 1–100 kHz, almost no difference between the two lasers is observed. At frequencies above 200 kHz, the Millennium again exhibits more intensity fluctuations: we measure 70% ($\pm 16\%$) more noise in the bandwidth from 200 to 700 kHz compared to the Verdi. Phase noise induced by intensity fluctuations with frequencies below 30 kHz can be effectively suppressed by our f_{ceo} stabilization loop. As a result, only intensity noise above 30 kHz will cause a distortion of the ϕ_{ce} phase stability. From these considerations,

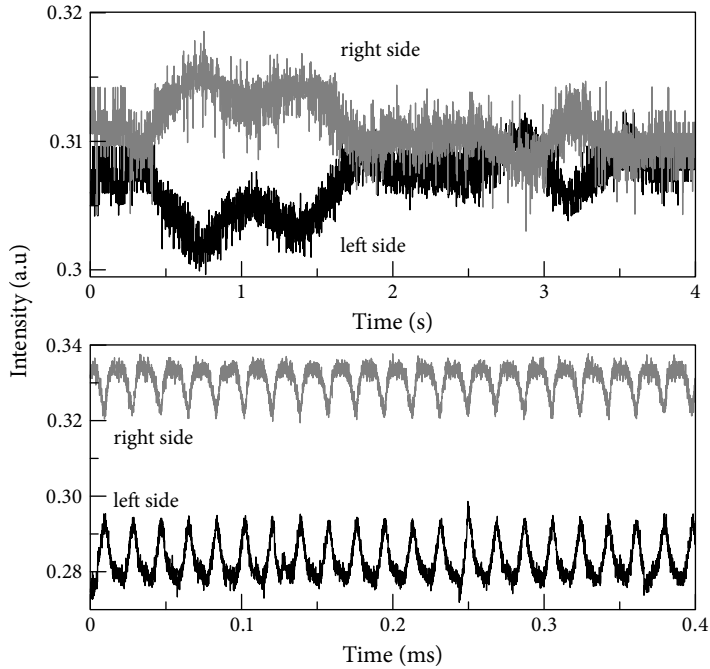


Figure 5.6: Measurements on mode fluctuations of the multi-mode pump laser. The two traces shown in each panel correspond to the signals recorded with the diode in the left and right side of the beam profile, respectively. Large beam pointing fluctuations are visible on various time scales. The bottom graph shows a fast jitter (~ 40 kHz) which occurred on some occasions (see text). The single-mode laser typically performs $4.5 \times$ better under the same conditions.

it seems that the observed difference in amplitude noise between the Millennia and the Verdi is too small to explain the large difference in phase stability of ϕ_{ce} as seen in figure 5.4.

However, measurements of the mode fluctuations of the multi-mode laser lead to much more striking results, as shown in figure 5.6. Intensity fluctuations between the left and right side of the beam can clearly be observed on all time scales from milliseconds to minutes, and can get as large as 13% of the average intensity. Sometimes a rapid (~ 40 kHz) oscillation is observed, also shown in figure 5.6. From these intensity fluctuations the jitter in the beam pointing half angle can be calculated to be $\delta\alpha = 0.1$ mrad. These measurements have been performed with two different Millennia lasers, to demon-

strate that this is really an intrinsic property of its multi-longitudinal-mode design. To strengthen the evidence even more, a Fourier analysis of the measured $\delta\phi_{ce}$ as shown in figure 5.4 also shows a pronounced peak around 40 kHz when a Millennia is used as the pump laser. In contrast, when the beam pointing stability of a Verdi laser was measured in this way, much less jitter was found. Again, the measurements have been repeated with two different Verdi lasers. On average, the beam pointing stability of the single-mode laser was found to be about 4.5 times better than the multi-mode laser on all relevant time scales.

Both the Verdi and Millennia laser design do exhibit good intensity and beam pointing properties for most applications, and easily outperform the Ar^+ laser as a pump source [190, 191]. However, use of a single-longitudinal-mode pump laser seems to be advantageous when carrier-envelope phase stabilization is required.

5.7 Long-term phase coherence of ϕ_{ce} and compressor stability

The storage capacity of the fast oscilloscope limits the measurement time to about 4 ms, before digitalization noise leads to problems in extracting the phase by computer analysis. For measurements on longer timescales, synchronized frequency counters are used. The counters are referenced to the Rb clock, while activation and read-out are computer-controlled. Timing jitter between the counters is found to be of the order of 1 μs , which is negligible for the averaging times of 1 ms and longer that are used in these measurements. A series of measurements has been performed, with counter gate times ranging from 1 ms to 5 s. On these timescales, the dominant contribution to $\delta\phi_{ce}$ is expected to come from ambient temperature fluctuations, mechanical vibrations from the building and air flow. Therefore, the optical table is mounted on air cushions to isolate the setup from ground vibrations, and the optical setup is shielded against air flow and acoustic noise.

As a criterion for the absolute frequency stability of f_{ceo} the Allan deviation σ_A is employed [192]:

$$\sigma_A = \sqrt{\frac{1}{2(M-1)} \sum_{k=1}^{M-1} (\bar{f}_{k+1} - \bar{f}_k)^2}, \quad (5.3)$$

where M is the number of consecutive measurements, and \bar{f}_k is the k^{th} frequency measurement averaged over a gate time τ :

$$\bar{f}_k = \frac{1}{\tau} \int_{t_k}^{t_k+\tau} f(t) dt. \quad (5.4)$$

Compared to the standard deviation, the Allan deviation has the advantage that long-term drifts of the average frequency are not incorporated. This leads to a more accurate reading of noise on the timescale τ under consideration. For all gate times, the Allan deviation has been calculated using 200 data points. For the 5 s gate time 100 data points were recorded consecutively.

The measurements described here have been performed with a prism-based pulse compressor as the test object in figure 5.1. The compressor is equipped with Brewster-cut fused silica prisms, and is aligned such that it compensates its own group velocity dispersion due to the quartz of the prisms of $1.8 \times 10^3 \text{ fs}^2$. This compressor is used to investigate its effect on ϕ_{ce} , as it may be an additional source of phase noise induced by a beam pointing instability of the laser [161, 173]. Similar to the f - $2f$ interferometers, the compressor is mounted inside an isolating box to minimize the effects of ambient noise and air flow. The path length from the laser through the compressor to the out-of-loop interferometer is about 4 meters.

To investigate the effects of beam pointing fluctuations on the phase stability, three different compressor geometries are used, each having a different sensitivity to these fluctuations. The first geometry is just the standard, double-pass prism compressor. In the second measurement series, this compressor is traversed in quadruple-pass, giving rise to an increase in beam pointing sensitivity by a factor of two. Finally, for the third geometry the compressor is also traversed twice, but now a retroreflector is used in between the passes. This retroreflection restores the symmetry of the compressor with respect to misalignment of e.g. the end mirror or unequal prisms, leading to a setup with a reduced sensitivity to small misalignments.

The size of a change in ϕ_{ce} as a function of the input beam pointing angle has been calculated with a ray-tracing algorithm for the various geometries, of which the results are shown in figure 5.7. In these calculations, a 0.1 mrad misalignment of the compressor end mirror is assumed, which is estimated to be a realistic upper limit. From this graph it can be seen that the various compressor geometries have very different slopes around zero angle, leading to a difference in phase stability if beam pointing fluctuations are present. Specifically, the retroreflector geometry always has a vanishing slope at zero angle, due to its insensitivity to misalignment of the end mirror.

An analytical expression for the phase delay in a double-pass prism compressor can be derived, using the 4×4 matrix formalism for dispersive optical elements introduced

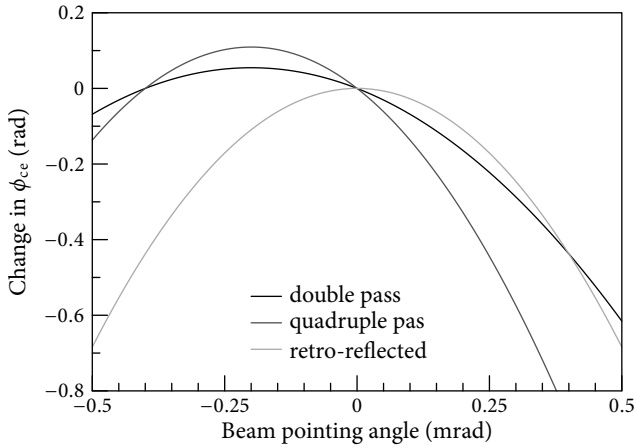


Figure 5.7: Calculations of the change in ϕ_{ce} as a function of input beam pointing angle for different prism compressor geometries, using a ray-tracing algorithm. The back mirror for retracing through the compressor has an assumed alignment error of 0.1 mrad in the optical plane.

by Kostenbauder [193]. This gives the relative phase delay $\Delta\phi$ as a function of the beam entrance angle θ_{in} and frequency ω :

$$\Delta\phi = -B\theta_{in}^2 + I_{gvd}\omega^2, \quad (5.5)$$

where B and I_{gvd} are coefficients, which depend only on the geometry of the compressor. I_{gvd} can be identified as the group velocity dispersion (GVD) parameter of the prism compressor, i.e. the amount of negative GVD introduced by the compressor.

This expression assumes a small deviation from the central ray through the compressor, which implies a not too broad spectrum. This is obviously a limitation, but the quadratic dependence on the entrance angle is supported by the ray tracing results. In addition, a linear dependence on the group velocity dispersion coefficient I_{gvd} is deduced.

This relation suggests two things: firstly, ϕ_{ce} stabilization benefits from a low compression factor. Secondly, as phase noise depends quadratically on beam pointing deviations, it can be advantageous to use a telescope to increase the beam size to reduce any angle deviations by the same amount, and therefore phase noise quadratically.

The experimental results for all three compressor types are shown in figure 5.8. The reproducibility for all measured points is about a factor of 2. From these graphs it is clear

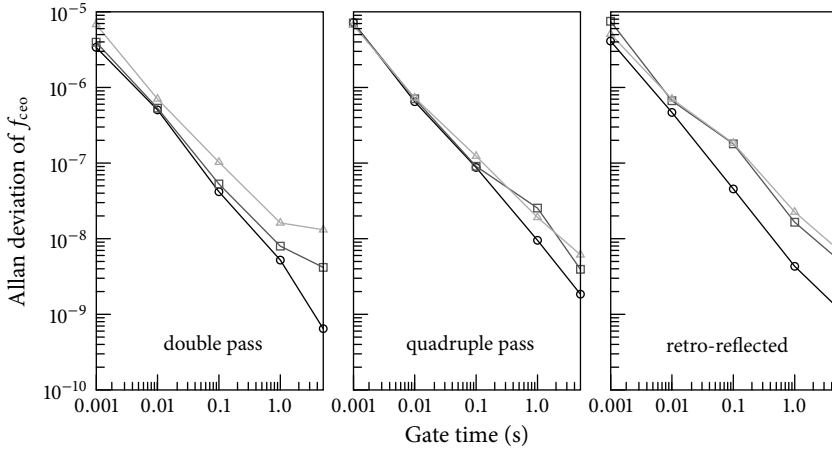


Figure 5.8: Measured Allan deviations of f_{cc0} using synchronous frequency counters, for all three compressor geometries under investigation (see text). The triangles show measurements taken with the air-conditioning and the flowboxes turned on, while the data points indicated by squares have been measured with these devices turned off. The circles show the in-loop measurements.

that no significant beam pointing related differences between the three geometries have been detected, at the resolution of the present experiment. It must be noted however, that counters were not operating at their full resolution, as the interpolation of the signals is disengaged by fast signal excursions similar to those shown in figure 5.3. After the experiments were completed, these excursions have been traced back to the phase detector used, which subsequently was replaced by a better design. For the present measurements, the absence of interpolation means that the counters have a resolution that is a 1000 times worse than specified. This explains the rather high Allan deviations measured. Indeed, with the new phase detector, the measured deviations were about three orders of magnitude better. For the oscilloscope measurements described above, the fast excursions are of no concern, as they occur not very often during the 4 ms these measurements take. Only for measurements longer than a few tens of ms, the excursions are unavoidable, as is the case for the counter measurements.

To check the phase noise at shorter timescales, the fast oscilloscope measurements were repeated with these three prism compressor setups as the test objects. Again, no significant differences between the various compressor geometries in phase noise added to $\delta\phi_{ce}$ are observed within the accuracy of the measurement. To see whether this agrees

with the simulations in figure 5.7, the beam pointing fluctuations of the Ti:sapphire laser have been measured with the setup from figure 5.5. On a timescale of seconds, a beam pointing variation of $24 \mu\text{rad}$ (half angle) is found. According to the calculated traces shown in figure 5.7 (including the end mirror misalignment), this would lead to a worst case jitter in ϕ_{ce} of 58 mrad for the quadruple-pass compressor, a value that is indeed too small to be observable in the present experiment.

To estimate the effects of noise from the surroundings on $\delta\phi_{ce}$, especially with the long optical path lengths involved in a compressor, the measurements described here have been performed with and without the air-conditioning and flow boxes turned on. Figure 5.8 shows that air flow is not a problem, as long as proper shielding is employed. In contrast, when the shielding is removed from the compressor and out-of-loop interferometer, the stability deteriorates drastically. This is clearly visible in figure 5.9, which shows a spectrum analyzer measurement of f_{ceo} with and without the shielding in place (this particular measurement is taken with a reasonable lock, the signal-to-noise ratio is a factor of two lower compared to ideal circumstances). From this figure it becomes clear that ambient noise sources can lead to over an order of magnitude more phase noise on $\delta\phi_{ce}$ at low frequencies. As the noise gets worse for longer averaging times, one can conclude that without proper isolation, low-frequency (on the Hz to sub-Hz level) noise can have a detrimental effect on the phase coherence of ϕ_{ce} .

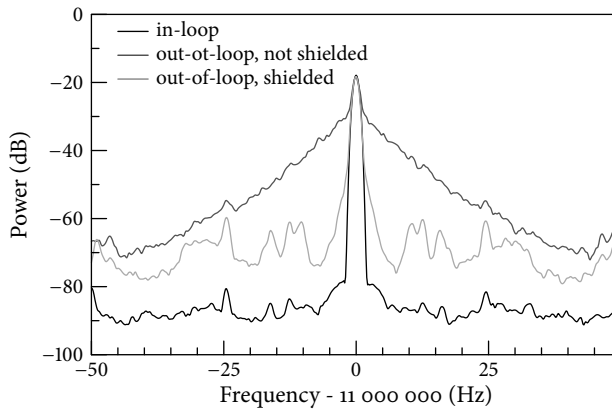


Figure 5.9: Spectrum analyzer traces of the stabilized f_{ceo} , at a resolution bandwidth of 1 Hz. The broadening due to air flow and ambient noise is easily seen. The 3 dB width of the stabilized f_{ceo} is measured to be 1 Hz, which is the detection limit of the spectrum analyzer.

From the shielded 5 s gate time measurements, the RMS frequency jitter in f_{ceo} is calculated to be 48 mHz out-of-loop (5.7 mHz in-loop). Combined with the real-time oscilloscope measurements described in section 5.4, it can be concluded that carrier-envelope phase coherence can be maintained over the 5 s measurement time (measurement limited), and that it is possible to do 100 measurements (equal to 500 seconds) consecutively without cycle slips. It must be noted that in the years after these experiments were performed, several improvements in the locking electronics and the physical setup of the $f-2f$ interferometers were made. It is now possible to keep the comb tightly locked over several hours of operation.

5.8 Conclusions

Using an $f-2f$ nonlinear interferometer, the carrier-envelope phase ϕ_{ce} of the 10 fs pulses emitted by a mode-locked Ti:sapphire oscillator has been stabilized with an RMS accuracy better than $\frac{1}{40}$ th of an optical cycle, which is equal to an RMS timing jitter of 67 attoseconds between carrier and envelope. Using a second $f-2f$ interferometer, this phase stability has been measured independently from the stabilization feedback loop (including the interferometer used for locking ϕ_{ce}). With a fast storage oscilloscope, the phase evolution of ϕ_{ce} at the full oscillator repetition rate can be traced directly without averaging for measurement times up to 4 ms. Longer timescales have been investigated using synchronized frequency counters, demonstrating carrier-envelope phase coherence over an extended period of time, provided that the setup is properly shielded against various noise sources.

The influence of the pump laser on the stability of ϕ_{ce} has been investigated, demonstrating that beam pointing fluctuations may affect the phase stability of ϕ_{ce} . A multi-longitudinal-mode pump laser is shown to induce considerably more phase noise than a single-longitudinal-mode laser.

The risk of introducing phase noise through the use of a prism-based pulse compressor has also been evaluated, using various compressor geometries. No additional noise on ϕ_{ce} could be detected, in good agreement with ray-tracing calculations.

From our measurements, we can conclude that chirped pulse amplification [194] of phase-stable pulses using prism-based stretcher-compressor setups is possible as long as the phase noise introduced by the amplifier can be kept at acceptable levels, and extreme compression ratios are avoided. Indeed, it has been shown recently that phase coherent pulse amplification is possible [176].

Deep-ultraviolet quantum-interference metrology with ultrashort laser pulses

Precision spectroscopy at ultraviolet and shorter wavelengths has been hindered by poor accessibility to that spectral region with narrow-band lasers. In this chapter, high accuracy quantum-interference metrology is demonstrated on atomic transitions using an amplified train of phase-controlled pulses from a frequency comb laser. The peak power of these pulses allows for efficient harmonic up-conversion, paving the way for extension of frequency comb metrology in atoms and ions to the extreme ultraviolet and soft-X-ray spectral regions. A proof-of-principle experiment is performed on a deep-ultraviolet (2×212.55 nanometers) two-photon transition in krypton, improving the accuracy of the absolute transition frequency and isotope shifts by more than an order of magnitude.

6.1 Introduction

In recent years, the invention of the femtosecond frequency comb laser [29, 30, 195] has brought about a revolution in metrology. A frequency comb acts as a bridge between the radio-frequency (RF) domain (typically tens of MHz) and the optical frequency domain (typically hundreds of THz). Thus in precision spectroscopy, the optical cycles of a continuous wave (cw), ultra-stable laser can be phase-locked and counted directly with respect to an absolute frequency standard such as an atomic clock [32, 196]. The resultant frequency measurements approach a precision of 1 part in 10^{15} in certain cases, offering the potential to detect possible drift in the fundamental constants [60, 61], among other quantum-mechanical applications.

6.2 Principle of the experiment

Here we perform precision metrology without the use of a cw laser. Instead, an atomic transition is excited directly with amplified and frequency-converted pulses from a femtosecond frequency comb laser. Due to quantum-interference effects in the atomic excitation process, the spectral resolution is at least six orders of magnitude higher than the optical bandwidth of the individual laser pulses.

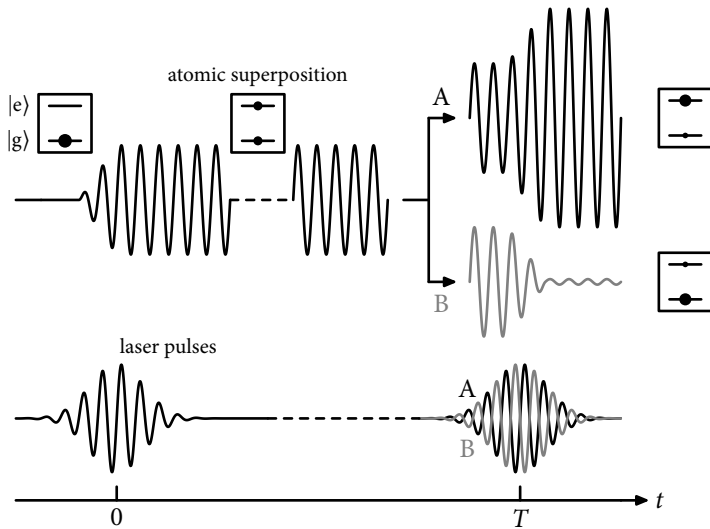


Figure 6.1: The principle of quantum-interference metrology. An atom in the ground state $|g\rangle$ is resonantly excited by a broadband laser pulse. This pulse creates a coherent superposition of the ground and excited state, with an initial phase difference between the states determined by the laser pulse. After the initial excitation, the superposition will evolve freely with a phase velocity $\omega_o = (E_e - E_g)/\hbar$, where $E_e - E_g$ is the energy difference between the states. After a time T , a second pulse with a controlled phase illuminates the atom, interfering with the atomic superposition. Depending on the phase and the time delay T , the total $|g\rangle \rightarrow |e\rangle$ excitation probability can be either enhanced (case A, black pulse) or suppressed (case B, gray pulse). By measuring the amplitude of the superposition (i.e. the population of the excited state) after the second pulse with, for example, an ionizing laser pulse, the energy difference between the states can be deduced.

The method employed is related to Ramsey's principle of separated oscillatory fields [64], which probes the phase evolution of an atom in spatially separated interaction zones. This technique is widely used in the RF domain for atomic fountain clocks [197]. By extension, in the optical domain excitation can be performed by pulses separated in time, rather than in space, to maintain phase coherence between the excitation contributions. Several experiments have been performed to investigate Ramsey-type quantum-interference fringes in the optical domain [67, 69, 70, 72, 73] and phase-stable amplification of single pulses [176]. Actual quantitative spectroscopy with phase-coherent light pulses has been limited to a few relative frequency measurements on fine and hyperfine structure of atoms [71–73] and relative and absolute measurements on rubidium [78]; absolute frequency measurements have been frustrated by an unknown phase difference between the pulses or by limited resolution.

We generate powerful laser pulses with a precise phase relationship by amplifying a selected pulse train from a frequency comb laser. This amplified frequency comb can be used to measure absolute optical frequencies directly. The significance of using amplified laser pulses is that the high peak power allows for efficient frequency up-conversion in crystals and gases. It has been demonstrated that harmonic generation in gases can preserve the coherence properties of the driving laser pulse [106, 108]. Therefore the present experiment paves the way for precision metrology with frequency combs at optical frequencies that are very difficult, or almost impossible, to reach with cw lasers, such as vacuum ultraviolet and even shorter wavelengths (e.g. X-rays). Possible applications are precision spectroscopy of hydrogen-like ions and helium to test quantum electrodynamics and nuclear size effects. The technique may also lead to more accurate atomic clocks that operate on resonances with ultra-high frequencies.

The principles of quantum-interference metrology have been discussed in detail in chapter 3. The general idea is shown once more in figure 6.1. An atom is excited by a train of N phase-locked laser pulses, all separated by a time T . Assuming a two-level system, the resulting excited state population after the pulse train can be written as (see chapter 3):

$$|b_N|^2 = \left| \sum_{n=1}^N a_n e^{i(n-1)(\omega_0 T + \varphi)} \right|^2, \quad (6.1)$$

where φ is the phase difference between subsequent laser pulses, and a_n is the excitation amplitude for the n^{th} pulse. Thus $|b_N|^2$ is a periodic function of both the pulse delay T and the phase difference φ . The resonance frequency ω_0 is encoded not just in the amplitude a_n , as with conventional spectroscopy, but also in the phase of the oscillating population signal. At the maxima of the periodic signal (when the second laser pulse

arrives in phase with the atomic superposition) the comb lines are in resonance with the transition; if the time delay and the pulse-to-pulse phase shift are known, the exact transition frequency can be derived from the position of these maxima. Because the transition frequency can now be obtained from the phase of the signal, the measurement is largely insensitive to the laser pulse spectral shape, which only influences the general signal amplitude. Therefore spectral distortions of the laser pulses, due to amplification or harmonic generation, have little influence on the measurement, provided the distortion is identical from pulse to pulse. In contrast, traditional single pulse spectroscopy is strongly affected by chirp [55, 56]. However, the periodicity of the signal with respect to T leads to an inherent ambiguity in the determination of the transition frequency. This ambiguity can be resolved if a previous measurement with an accuracy much better than the repetition frequency exists; otherwise the measurement can be repeated with different repetition rates, as shown below.

6.3 Setup

The details of the experimental setup used for this experiment have already been discussed in chapter 4. For reference, the various parts will briefly be reviewed again. The frequency comb used in our experiment is based on a mode-locked Ti:sapphire oscillator. It emits 7 nJ pulses with a bandwidth (full width at half maximum) of about 90 nm, centered at 800 nm, and with an adjustable repetition rate between 60.9 and 79 MHz. Both the repetition rate and the phase of the pulses are locked to a Global Positioning System-disciplined Rb atomic clock [29, 30, 172, 198]. An electro-optic modulator (EOM) and polarizing optics are used to select two or three consecutive pulses from the mode-locked pulse train. These pulses are amplified in a six-pass Ti:sapphire non-saturating amplifier to an energy of about 15 μ J/pulse. This in contrast to standard multi-pass amplifiers, which operate in saturated mode to reduce output power fluctuations, and can therefore amplify only one pulse. In the present experiment, the number of pulses that can be amplified is limited to three by the EOM, which has to be switched off before any back-reflections from the amplifier can reach the oscillator. Including an additional optical isolator in the setup will allow the amplification of longer pulse trains. Spectral filtering is applied in the amplifier to limit the bandwidth of the amplified pulses to <0.5 nm. This filtering reduces the complexity of the signal, as only a single transition will be excited (see below).

6.3.1 Phase measurements

As discussed in chapter 3, the amplification process gives rise to a small phase shift (~ 100 - 200 mrad) between the pulses, which is measured with a 1σ accuracy of 25 mrad ($< 1/250^{\text{th}}$ of an optical cycle) using the interferometer setup described in chapter 4. In short, these measurements are performed by placing the amplifier in one arm of a Mach-Zehnder interferometer and recording spatial interferograms on a CCD camera, from which this phase shift can be extracted. An electro-optic modulator (EOM) and polarizing optics were used to project the interference patterns for two consecutive pulses simultaneously and vertically displaced from one another on a CCD camera. The relative positions on the CCD (up or down) were alternated by switching the EOM, in order to cancel out any alignment effects. The relative phase shift to the comb laser was then determined by looking at the phase difference in both projection situations. The amplitude of this difference signal is equal to twice the phase shift due to the amplifier. In order to correct the spectroscopic measurements for these shifts, it is measured before and after each measurement run. During the measurements, no significant drift of the amplifier-induced phase has been observed.

6.3.2 Atomic beam apparatus and time-of-flight ion detection

To demonstrate the potential of high frequency quantum-interference metrology we selected the $4p^6 \rightarrow 4p^5 5p[1/2]_o$ two-photon transition in krypton at a frequency of $\omega_o/2\pi = 2821$ THz. The required wavelength of 212.55 nm for exciting this resonance was obtained by fourth-harmonic generation of the amplifier output at 850.2 nm through sequential frequency doubling in two BBO crystals. The resultant 212.55 nm pulses (1.6 μ J) were focused in a highly collimated atomic beam of krypton (figure 6.2). The excited state population was probed by a delayed 532 nm ionization pulse (1.5 mJ, 100 ps) from a Nd:YAG laser-amplifier system, and the produced ions are accelerated in a time-of-flight tube capable of resolving the various isotopes. The experiment is repeated at 1 kHz, and the number of produced ions are counted during 10 s. Then the repetition rate of the frequency comb is changed slightly, and the cycle starts again. As both the ground and excited state of this transition are $J = 0$ states, the atoms can be considered as two-level systems. In general, multiple magnetic sublevels can be present, which may complicate the signal if stray magnetic fields are not properly shielded.

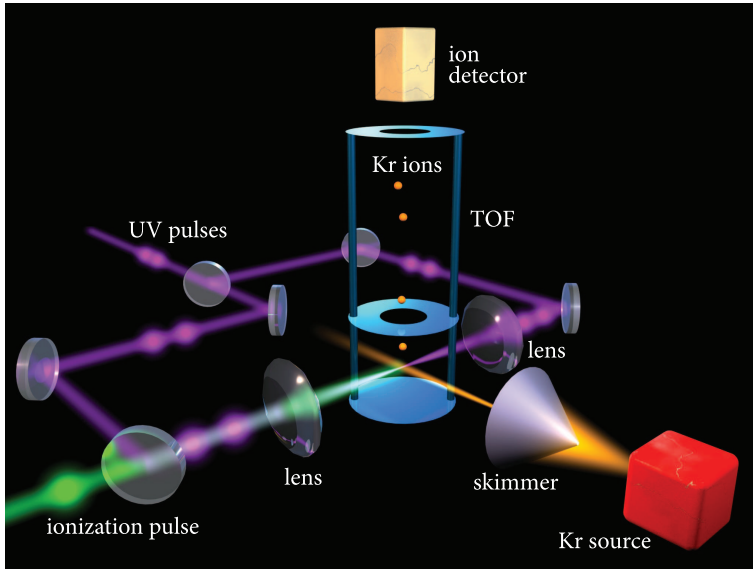


Figure 6.2: Schematic of the experimental vacuum setup. The ultraviolet pulses (1 mm beam diameter) are focused with an $f = 30$ cm lens on a collimated krypton beam (0.3 mm wide, Doppler width < 10 MHz) from both sides, crossing the beam perpendicularly. Measurements are performed with light from one side at a time. After the ultraviolet excitation, a delayed 532 nm pulse is used for ionization, and the resulting krypton ions are accelerated into a 60 cm long time-of-flight mass spectrometer by a pulsed electric field. Here the isotopes are separated in time and counted using a channel electron multiplier.

6.4 Doppler shift

The isotope shift and the absolute transition measurements described below can be influenced by a possible systematic Doppler shift as a result of non-perpendicular excitation. This shift can in principle be reduced on a two-photon transition by measuring with colliding pulses from opposite sides [143–145]. This arrangement also enhances the signal, as was seen experimentally in our setup. However, contrary to cw spectroscopy, the Doppler-free signal (photons absorbed from opposite sides) and the Doppler-shifted signal (two photons from one side) cannot be distinguished properly in the case of excitation with two ultrashort pulses, because the large bandwidth of the short pulses always contains a resonant frequency. This situation might lead to a calibration error

when there is an imbalance in signal strength from opposite sides, which would do more harm than good. Therefore all measurements were performed from two opposite sides separately, with the average taken to determine the Doppler-free signal. The total Doppler shift can only be determined modulo the repetition rate due to the mode ambiguity. However, on account of their different masses, the various isotopes show Doppler shifts that differ a few hundred kHz. From these differences in the Doppler shifts, a valuable initial estimate of about 25 MHz for the total shift Doppler shift can be derived. From the measurement of the absolute positions, one can then determine the Doppler shift to be 29 MHz for each of the counter-propagating beams.

6.5 Interference signals from pulse trains

The data depend on the number of phase-locked pulses used to excite the transition (figure 6.3). The pulse delay T was scanned by changing the comb laser repetition frequency, which is near 75 MHz. In order to scan the optical frequencies in the UV over 75 MHz (one mode spacing), f_{rep} needs to be scanned about 2.0 Hz; the delay of the pulses is then changed by 361 as. The delay steps taken during a scan are even smaller, only 12.6 as.

With a single pulse the excitation probability is constant, as no interference takes place. With two pulses a clear cosine oscillation is observed, with a contrast reaching 93%. Three pulse excitation gives the pulse-like structure predicted by equation 6.1 ($N = 3$), as well as an expected narrowing by $3/2$ compared to two pulse excitation. The solid lines are fits using equation 6.1, including an additional amplitude scaling factor to account for signal strength variations between the traces. In the three-pulse case, we took into account that the amplitude contribution of the pulses is not exactly equal, due to spontaneous emission of the 5p state (lifetime is 23 ns) and differences in energy between the three pulses. The energy ratio of the pulses in the three-pulse train was 1.0 : 0.91 : 0.6, whereas in the two-pulse excitation, the pulses energies have been kept equal to within about 5%.

To check the behavior of the interference signal, we varied the pulse-to-pulse (carrier-envelope) phase shift ϕ_{ce} . As the frequency of the comb light is quadrupled, and a two-photon transition is involved, scanning ϕ_{ce} over $1/8^{\text{th}}$ of a cycle should move the quantum-interference fringes through one complete cycle. In figure 6.4 measurements are shown, where f_{ceo} (which is proportional to ϕ_{ce}) is locked to values $f_{\text{rep}}/32$ apart. This ensures that the pulse-to-pulse phase shift seen by the atom is 0, $\pi/2$, π and $3\pi/2$, respectively, for each of the measurements shown. And indeed the observed interference

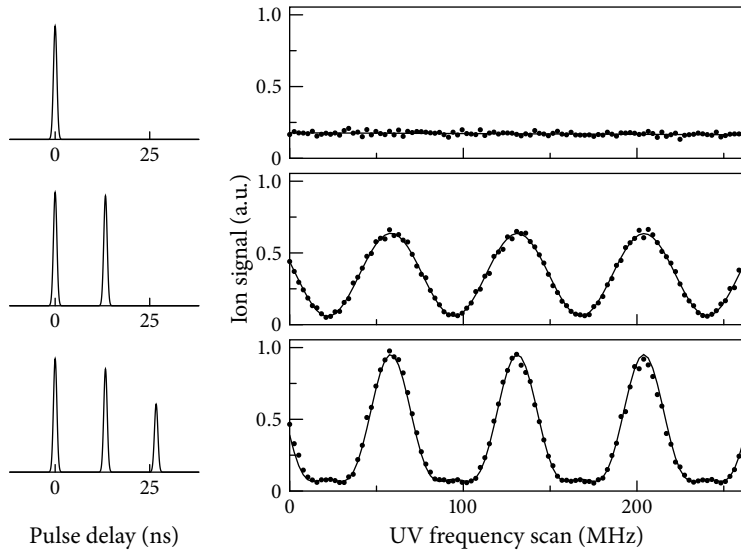


Figure 6.3: Demonstration of quantum-interference metrology. ^{84}Kr signal as a function of the repetition rate of the comb laser for one, two, and three pulses 13.3 ns apart. Relative pulse intensities and time delays are shown on the left of the graphs. The solid lines are fits to the theory (see text). The counter gate time is 10 s for each data point.

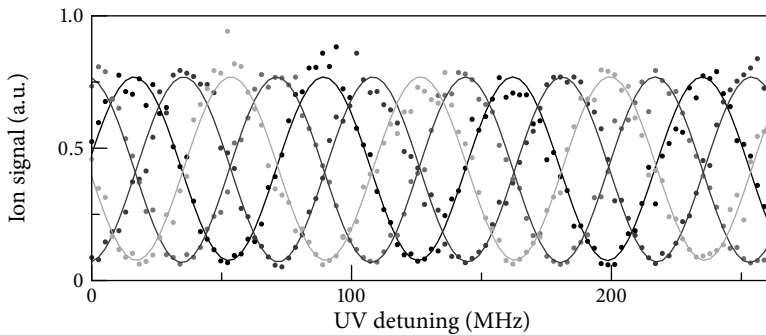


Figure 6.4: Measurement of the quantum-interference signal for various phase differences between two excitation pulses, with the pulse-to-pulse phase shift as seen by the atom set to 0 , $\pi/2$, π and $3\pi/2$, respectively.

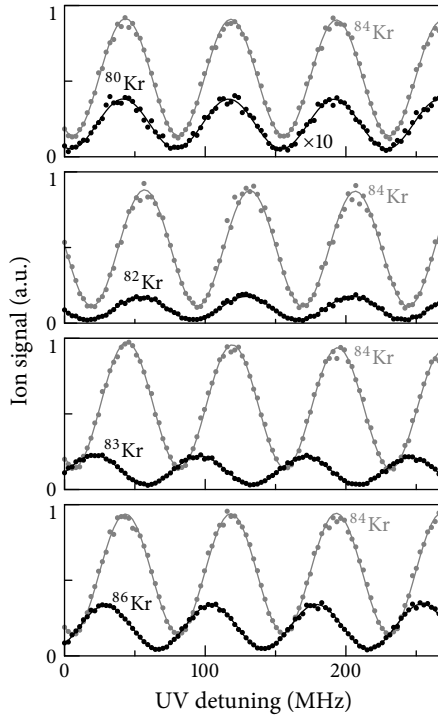


Figure 6.5: Quantum interference fringes recorded for the five observed Kr isotopes, with ^{84}Kr serving as reference. The ^{80}Kr trace has been scaled by a factor of ten for clarity. The isotope shift can be determined modulo 75 MHz from the phase shift between such simultaneously recorded scans. The counter gate time is 10 s for each data point.

fringes move by a quarter of a fringe for each measurement, completing a full cycle when f_{ceo} is scanned over $f_{\text{rep}}/8$, as expected.

6.6 Isotope shift measurements

Because the TOF-tube resolves the isotopes very well, isotope shifts can be measured straightforwardly. The broad spectrum of the pulses places a frequency ruler on all isotopes simultaneously, so spectra of ^{80}Kr through ^{86}Kr could be acquired at the same time. Examples are shown in figure 6.5 for each isotope. In order to determine the actual

Table 6.1: The determination of the isotope shifts from the measured phase shifts and literature data.

Isotope	Fringe shift (rad)	Lit. value (MHz)	Present value (MHz)
^{80}Kr	0.188	306 (6) [199]	302.02 (28)
^{82}Kr	0.211	150 (6) [199]	152.41 (15)
^{83}Kr	1.978	88 (17) [200]	98.54 (17)
^{86}Kr	1.165	-141 (6) [199]	-135.99 (17)

isotope shifts, the mode number and sign ambiguity must be overcome (see chapter 3): we used the measurements of Kaufman [199] and Brandi [200] for identification of the proper comb line for each isotope (table 6.1). The resulting shifts ($^{84}\text{Kr} - ^X\text{Kr}$), based on at least 6 measurements per isotope, are: 302.02 (28) MHz (^{80}Kr), 152.41 (15) MHz (^{82}Kr), 98.54 (17) MHz (^{83}Kr), and -135.99 (17) MHz (^{86}Kr). The stated uncertainties (1σ) are between 20 and 40 times smaller than the 6 MHz uncertainty reported by Kaufman [199].

6.7 Systematic shifts

Unlike the isotope shift measurements, which are relative measurements, the measurement of the absolute transition frequency is affected by systematic effects. Two of these dominate the determination of the resonance frequency: the amplifier phase shift measurement and the residual Doppler shift. The amplifier phase shift measurements show a ~ 12 mrad total statistical error and have an estimated 11 mrad total systematic error, corresponding to 1.2 MHz and 1.1 MHz in the UV, respectively. The residual Doppler shift due to a possible non-collinear alignment of the counter-propagating beams is estimated to be 2 MHz in the UV. Other effects include light shifts (0.47 ± 0.44 MHz), static field effects ($\ll 100$ kHz), the second-order Doppler shift (~ 1 kHz), and a recoil shift (209 kHz). The pulse-picker EOM does not introduce significant phase shifts, as verified experimentally (see chapter 3). The phase shift due to frequency doubling is negligible as well, being estimated of the order of 5 mrad in the UV (see also chapter 3). An overview of the error budget for our measurements is given in table 6.2.

Table 6.2: The error budget for the determination of the absolute transition frequency. All values are expressed in MHz.

Effect	Value	Syst. error	Stat. error	
Residual Doppler shift	29	2.0	-	
Amplifier phase shifts ^a	10-20	1.1	1.2	
AC Stark shift	0.47	-	0.44	
DC Stark shift	0	≪ 0.1	-	
SHG phase shift	0.48	-	0.19	
Pockels cell phase shift	0	-	< 0.5	
Recoil shift ^b	0.209	-	-	
2 nd order Doppler shift	~ 0.001	-	-	
Total		2.28	1.29	3.5

^a Measured for each individual measurement; typical value is quoted here.

^b Calculated value

6.8 Absolute frequency measurements

In the measurement of the absolute transition frequency, an additional issue is the determination of the mode that corresponds to the true position of the resonance, as explained in chapter 3. The most accurate measurement to date [200] has an uncertainty of 40 MHz, which is not sufficient to assign the mode with confidence. Therefore measurements were repeated at repetition rates near 60.9 MHz, 68.6 MHz and 75.0 MHz to find the point at which the measurements coincide. At each repetition rate, 4 to 9 measurements on ⁸⁴Kr are performed.

After correction of the data for the phase shifts and systematic effects, there were 3 sets of possible positions for the 5p resonance transition, shown in figure 6.6. The measurements have one clear coincidence (with an estimated probability of 98.5%, based on a statistical uncertainty of 2.5 MHz for each data point) near the literature value. Combining the three sets leads to an absolute frequency for ⁸⁴Kr of 2,820,833,097.7 MHz with a 1σ uncertainty of 3.5 MHz (statistical and systematic errors combined). This is an order of magnitude better than the best previous determination by Brandi et al., who obtained a value of 2,820,833,061 (40) MHz using single nanosecond laser pulses [200]. The older value of 2,820,835 (1.5) GHz, measured by Kaufman and Humphreys [201], is brought into agreement using the correction factor derived by Brandi, -1679 MHz. This factor deviates from that suggested by Trickl et al. [202], who arrive at -2031 MHz.

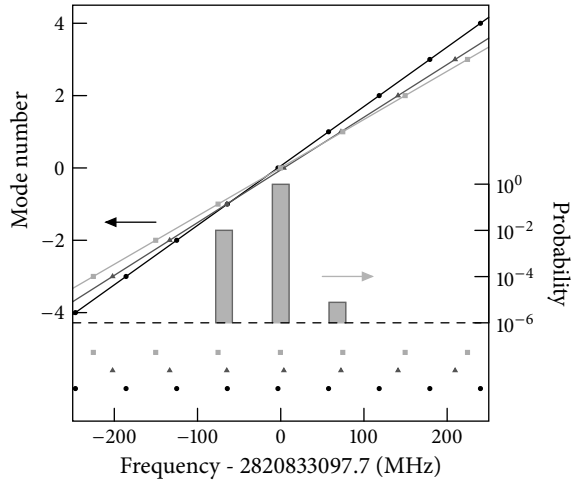


Figure 6.6: Absolute calibration of the $4p^6 \rightarrow 4p^5 5p[1/2]_o$ transition in krypton is performed by finding the coincidence of three separate measurement series with repetition rates of 60.9 MHz (circles), 68.6 MHz (triangles) and at 75.0 MHz (squares). The bars (logarithmic scale) show the normalized statistical probability per mode for each measured mode position, revealing the location of the most probable coincidence.

However, based on a recent re-evaluation of their results [203], Trickl has corrected their value to -1661 MHz, resolving the discrepancy.

6.9 Outlook

We envision several extensions of the above technique. One possibility is the use of a regenerative amplifier, to amplify pulses to the μJ level at a repetition rate of 100 kHz. For high frequency metrology, the resolution is ultimately limited by the comb laser and the interaction time of the atom with the pulses. This interaction time can be increased almost indefinitely if cooled ions in a trap are used instead of an atomic beam, opening the prospect of atomic optical clocks operating at vacuum ultraviolet or extreme ultraviolet frequencies. Outside frequency metrology, amplified frequency combs could be used to perform quantum-control experiments on a time scale much longer than is presently possible, as phase coherence can be maintained for many consecutive laser pulses.

Frequency comb laser spectroscopy in the vacuum ultraviolet region

It is demonstrated that the output of a frequency comb laser can be amplified and up-converted to the vacuum ultraviolet (VUV) in a gaseous medium while its phase coherence is maintained to a high degree ($< 1/30^{\text{th}}$ of a VUV cycle). The produced VUV pulses are well suited to perform frequency comb spectroscopy with sub-MHz accuracy, which is experimentally verified using a Ramsey-type quantum-interference scheme to excite a transition in xenon at 125 nm. The achieved resolution constitutes an improvement of six orders of magnitude compared to previous demonstrations of frequency domain quantum interference in this wavelength range.

7.1 Coherent pulsed excitation in the VUV

Frequency comb devices based on mode-locked lasers at infrared wavelengths have led to dramatic progress in fields such as ultra-high precision frequency metrology [38, 61], optical clocks [204, 205], and ultrafast laser science [180]. For precision spectroscopy, a frequency comb laser generally acts as a phase-coherent link between the radio frequency of an atomic clock and the optical frequency of a stabilized narrow-band continuous wave (cw) laser used for the actual spectroscopy. However, many atomic transitions (in e.g. helium and hydrogen-like ions) that are of interest for testing fundamental theories such as quantum-electrodynamics require excitation with vacuum ultraviolet (VUV) and extreme ultraviolet (XUV) radiation. Suitable narrow-bandwidth cw sources hardly exist at such short wavelengths [63].

New measurement schemes based on excitation of atomic transitions with phase-locked pulse sequences [69, 73, 78, 79, 206] may provide a solution. No cw laser is required anymore, while frequency up-conversion through harmonic generation is facilitated by the high peak intensity of the pulses. Such up-conversion has recently been demonstrated with un-amplified frequency comb lasers, using a gas jet inside an external enhancement cavity [110, 111]. Radiation down to a wavelength of 60 nm at 112 MHz repetition rate [110] was generated, albeit at relatively low power per pulse, and phase coherence was only confirmed at 266 nm through comparison with the third harmonic generated in crystals. In general, degradation of the pulse-to-pulse phase stability in the up-conversion process is a potential cause for concern, due to the interaction of the required gaseous nonlinear medium with such high-intensity laser pulses: the harmonic generation process itself [103] as well as competing ionization effects [94] will adversely affect the phase coherence. Previous experiments in the xuv spectral range have qualitatively shown a certain degree of temporal [102, 105] and spatial coherence [106], by up-converting two replicas of a single amplified pulse and recording the resulting interference patterns on a CCD camera. Similarly, frequency-domain studies of the phase coherence have also been reported, using pulse pairs created with an interferometer [108, 109] or a birefringent crystal [107]. However, in all these experiments the pulse delay could only be varied on a ~ 100 fs timescale, while the phase difference between the pulses could not be measured. As a result, the spectral resolution was limited in all cases to the THz range, which is still far below the requirements of precision spectroscopy.

In this chapter we demonstrate that frequency comb spectroscopy can be performed in the vuv with sub-MHz accuracy, through an experiment on xenon at 125 nm. The obtained resolution is six orders of magnitude better than demonstrated so far at vuv and shorter wavelengths [109]. This is accomplished using pulse pairs, which are selected from a frequency comb laser with a variable delay, then individually amplified, and finally frequency up-converted in a gaseous medium. This approach allows extension to much shorter wavelengths in the future, with an adjustable resolution by changing the pulse delay.

7.2 Design of the experiment

The measurement principle is based on quantum interference between the contributions of multiple excitation pulses, which gives rise to an oscillation in the atomic excitation probability as a function of time delay T and the phase difference $\Delta\varphi$ between consecu-

tive pulses [65, 70]. From the Ramsey-like interferogram that is obtained when scanning either T or $\Delta\phi$, the absolute transition frequency can in principle be retrieved. In the frequency domain, this corresponds to scanning the repetition frequency f_{rep} or the carrier-envelope offset frequency f_{ceo} , respectively, thus moving all the modes in the comb laser spectrum. A maximum in the excitation probability occurs when one of the comb modes coincides with the transition frequency. Using this approach, the resolution is no longer determined by the bandwidth of the individual laser pulses, but rather by the duration of the pulse train and the phase coherence between the constituent pulses.

The source of phase-coherent pulses for the experiments described in this chapter is an 11 fs Kerr-lens mode-locked frequency comb laser referenced to a GPS-disciplined Rb atomic clock (Stanford Research Systems PRS10). Two electro-optic pulse pickers are used to select either one pulse, two pulses separated by an integer number of oscillator round-trip times, or a pulse train consisting of up to six pulses. These are injected into a multi-pass Ti:sapphire amplifier that boosts the power to 25 μJ per pulse while clipping the spectrum to a width of about 0.7 nm centered around 750 nm, to ensure that the light is resonant with only one xenon transition. Subsequently, the pulses are frequency doubled in a BBO crystal, yielding about 10 μJ per pulse at 375 nm.

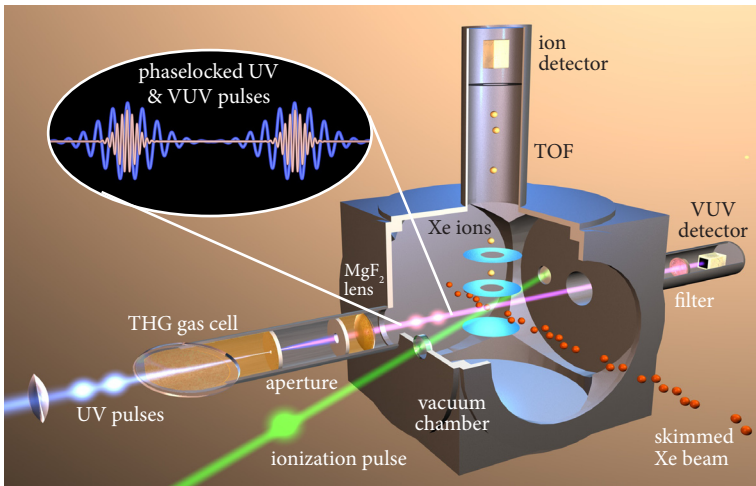


Figure 7.1: The setup used for vuv quantum-interference spectroscopy on xenon. TOF, time-of-flight mass spectrometer. THG, third-harmonic generation.

7.3 Third-harmonic generation

These 375 nm (UV) pulses are focused into a gas cell filled with either oxygen or acetylene, to generate the third harmonic at 125 nm (see Fig. 7.1). Since phase matching is not possible at this wavelength due to a positive phase mismatch in most gases, we focus the UV pulses through a 0.1 mm pinhole, and employ differential pumping to create a sudden pressure drop across the pinhole. This provides the asymmetry necessary for third-harmonic generation (THG), producing about 50 fJ per pulse at 125 nm. After the pinhole, the VUV radiation is collimated using a MgF₂ lens and perpendicularly intersects a beam of xenon atoms. The VUV intensity is monitored using a low-impedance channel electron multiplier (CEM, Dr. Sjuts Optotechnik GmbH) behind a Lyman- α VUV filter (Acton 122-XN). The CEM signal for a train of six pulses is shown in figure 7.2: the area under these peaks is proportional to the charge accumulated in the CEM, and thus to the energy of the VUV pulses. From these direct measurements of the CEM signal, the efficiency of the harmonic generation process can be estimated to be about 5×10^{-9} . This value was used to calculate the energy of the VUV pulses quoted above. It must be noted however that this is based on a very conservative value for the CEM gain, while saturation is not taken into account. A second differentially pumped gas cell in front of the MgF₂ lens ensures a steady gas flow away from the lens, to prevent contamination of its surface. The VUV pulses are used to excite the $5p^6 \ ^1S_0 \rightarrow 5p^5 \ (^2P_{3/2}) \ 5d[1/2]_1$ transition at 2.398×10^{15} Hz (125 nm) in xenon, which has a measured lifetime of 58.9 ns (see below). The xenon beam is collimated using two skimmers, limiting the Doppler

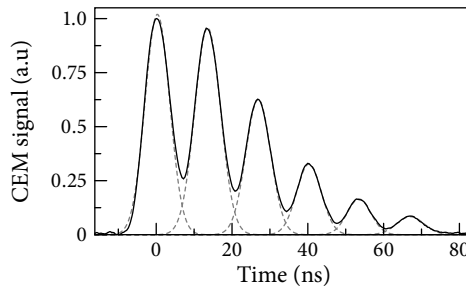


Figure 7.2: The signal from the channel electron multiplier as acquired using a 50 Ω -terminated oscilloscope. The solid black curve is the measured six pulse signal, the dashed gray curves show the individual peaks of a multiple Gaussian fit.

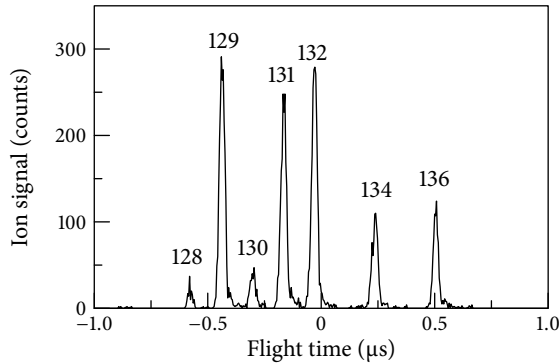


Figure 7.3: The measured time-of-flight mass spectrum of xenon ions. All isotopes except ^{124}Xe and ^{126}Xe are clearly resolved. The numbers indicate the atomic masses.

width to <10 MHz. Ionization of the excited xenon atoms is done with 1.5 mJ, 30 ps frequency-doubled pulses from a synchronized Nd:YAG laser/amplifier system. Ions are then detected with a time-of-flight mass spectrometer, capable of clearly resolving the various xenon isotopes, as can be seen in figure 7.3.

7.4 Lifetime measurement

The setup that is built for multi-pulse quantum-interference spectroscopy is very well suited for lifetime measurements, due to the tight synchronization between the comb pulses and the ionization pulse. For such a measurement, only a single excitation pulse is used, and the excited state population is probed some time later with an ionization pulse. The timing of these pulses can be varied on a ps timescale, so an accurate measurement of the lifetime can be made. The result of such a measurement is shown in figure 7.4. Fitting the data to a simple decaying exponential, a lifetime of 58.9 ± 1.3 ns is retrieved, in very good agreement with the theoretical prediction made by [207] of 60.5 ns.

7.5 Isotope shift measurements

Quantum interference in the excitation process is seen when two VUV pulses are used and the time delay between them is scanned on an attosecond timescale by varying the repetition frequency of the frequency comb oscillator, while keeping the phase

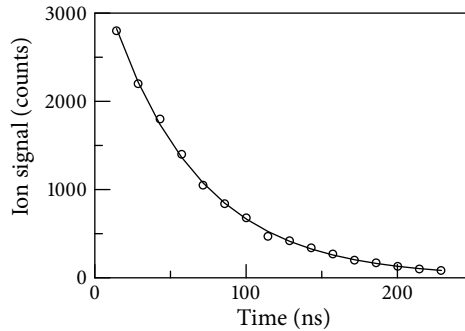


Figure 7.4: The excited state population probed at different delays after excitation with a single pulse (circles). From a fit to the decay curve (solid line), a lifetime of 58.9 ± 1.3 ns is determined.

difference between pulses fixed. The initial delay between consecutive pulses from the frequency comb oscillator is 13.3652 ns, leading to an oscillation period of 74.8212 MHz. This time delay is changed by 12.6 attoseconds per scan step, and every data point is averaged over 10 seconds (10,000 laser shots).

Similar to the measurements presented in the previous chapter, we have recorded quantum-interference signals for multiple isotopes simultaneously, in principle allowing the determination of the isotope shifts. Recordings for the various isotopes using ^{132}Xe as a reference are shown in figure 7.5. These measurements cannot be used directly for the determination of the isotope shifts, since an unknown Doppler shift is present in the measurement, which differs for the various isotopes on account of their different masses. As the experimental setup does not allow excitation from opposite sides, as was done in the krypton measurements of the previous chapter, it is not possible to correct the measurements for this isotope-dependent Doppler shift. However, when comparing the situation to the krypton experiment, the average velocity of the xenon atoms is 80% of the average velocity of the krypton atoms, and there the difference in isotope shifts was a few hundred kHz. As the geometry is comparable, it seems safe to estimate the isotope shift difference to be less than a MHz. A suitable measurement of the same transition that can be used to solve the mode ambiguity is not available. However, using the level isotope shifts tabulated by Jackson et al. [208], a determination of the transition isotope shifts can still be made. To this end, the level isotope shifts for the $6p[1/2]_0$ level are used in combination with a measurement of the transition isotope shifts from the ground state to this level performed by Plimmer et al. [209], to determine the ground

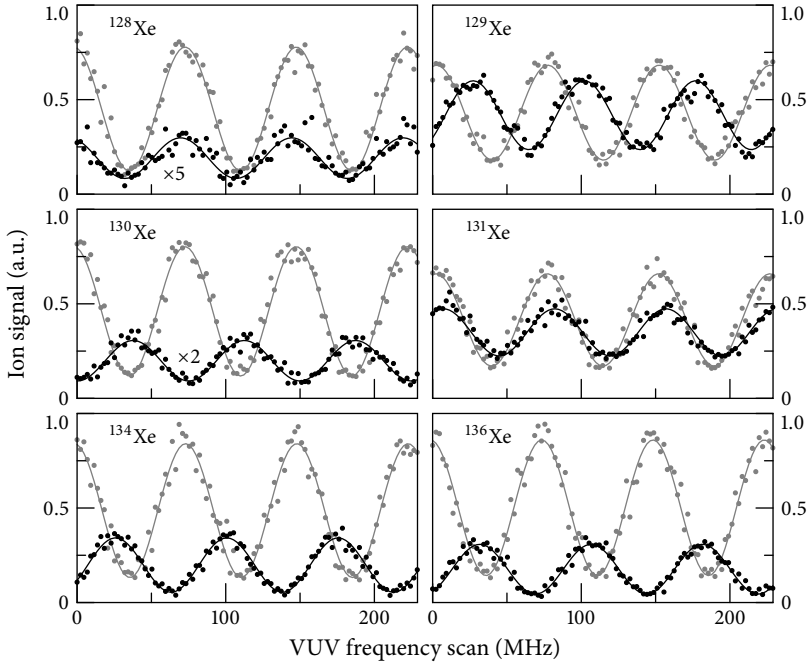


Figure 7.5: Isotope shift measurements using ^{132}Xe (gray traces) as a reference, the solid lines are fits. Each data point is a 10,000 shots average.

state isotope shifts (see figure 7.6). Together with the level shifts for the $5d[\frac{1}{2}]_1$ level from Jackson, this results in an estimate of the isotope shifts in the transition measured in this work. The results are gathered in table 7.1: the agreement is quite good. As the level isotope shifts of the upper states taken from [208] are rather small compared to the transition isotope shifts while the error in the level isotope shifts is just as large as their values, it seems safe to trust the values that are found for the transition isotope shifts of the $5p^6 \rightarrow 5p^5 5d[\frac{1}{2}]_1$ transition. The accuracy of these values is conservatively estimated to be about 1 MHz, mainly due to the residual Doppler shift.

7.6 Pulse train signals

By adding more pulses to the first two, the frequency resolution can be increased, as is shown in figure 7.7. In the limit of interaction with an infinite number of pulses and

	6p[$\frac{1}{2}$] _o [209]			5d[$\frac{1}{2}$] ₁ (this work)			
	Δf_{us}	Δf_{meas}	Δf_{gs}	Δf_{us}	Δf_{meas}	Δf_{lit}	Δf_{final}
128-132	0(16)	-292.9(0.9)	293(16)	-87(16)	-3 (mod 75)	-380(23)	-378
129-132	-	-259.8(1.3)	-	-	25 (mod 75)	-	-
130-132	12(9)	-139.9	152(9)	-42(9)	-35 (mod 75)	-194(13)	-185
131-132	-	-133.6(1.1)	-	-	5 (mod 75)	-	-
134-132	9(11)	137.3(0.5)	-128(11)	39(11)	28 (mod 75)	167(16)	178
136-132	6(6)	324.8(0.9)	-319(6)	81(6)	33 (mod 75)	400(8)	408

Table 7.1: A comparison of the measured isotopes with data available in the literature. The level isotopes shifts for the upper states Δf_{us} are taken from [208], and using the measured values of the transition isotope shifts Δf_{meas} from [209], the ground state isotope shifts Δf_{gs} are calculated. This ground state isotope shift is used together with the upper state isotope shift for the 5d[$\frac{1}{2}$]₁ level from [208] to calculate the isotope shift for the $5p^6 \rightarrow 5p^5 5d[\frac{1}{2}]_1$ transition Δf_{lit} . The values measured in this work Δf_{meas} are then transformed to the best matching value Δf_{final} by adding or subtracting an integer times f_{rep} . The odd isotopes were not included in [208]. All values are in MHz, the values in parentheses are standard deviations.

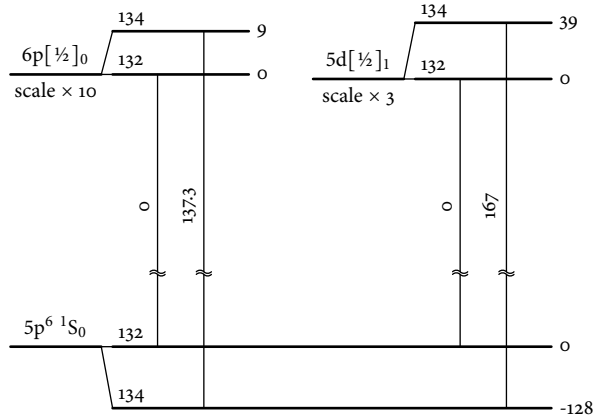


Figure 7.6: The determination of the isotope shift from the level isotope shift data from [208] combined with the data from [209] for the $6p[\frac{1}{2}]_o$ state (shown here on the left). Only ^{132}Xe and ^{134}Xe are included for clarity. From these numbers, the ground state isotope shift can be deduced, which can be used together with the level shifts for the $5d[\frac{1}{2}]_1$ level to estimate the transition isotope shift for the transition studied in this chapter (shown on the right side).

infinite transition lifetime, sharp modes would emerge, resembling the original frequency comb structure, possibly limited by transit time broadening. We have performed measurements with trains consisting of up to six pulses. The resonances retain the 74.8 MHz period, and narrow down as expected when more pulses are added. However, the amplifier introduces slightly different phase shifts within the pulse train, varying by a few hundred mrad. As a result, the excitation contributions of later pulses cause small shifts of the resonance position and an asymmetry in the resonance shape (see figure 7.7), which hampers an accurate determination of the transition frequency. To obtain maximum contrast, the intensity of the vuv pulses should be matched to the surviving amplitude in the excited state, which would require an independent control over the intensity of the individual vuv pulses. In the present situation the later pulses contribute less to the final excitation amplitude, which slows down the narrowing of the interference peaks: ideally, the six-pulse train for example should yield about 11.5 MHz wide resonances, while the measured width is 16.9 MHz. Furthermore, intensity variations in the pulse train are a cause for concern as the phase of harmonics generated in a gas might be influenced by processes such as ionization and dissociation that create a time dependent refractive index [107], see also chapter 2. Pulse intensity jitter can then lead to differences in the degree of ionization of the harmonic gas, possibly causing detrimental phase fluctuations that do not occur when crystals are used [206]. Although the presence of high-contrast interference signals in figure 7.7 demonstrates that such phase fluctuations are not very large in the third-harmonic generation (THG) process in a gas, these effects are difficult to measure quantitatively in longer pulse trains.

7.7 Pulse pair signals

A simple solution that enables the determination of such unknown phase shifts without loss of resolution is to use pulse pairs instead of longer pulse trains. The advantage of using two pulses is that phase shifts between the pulses caused by the amplifier system can be measured with high accuracy [206], as explained in section 4.4. Phase shifts in the THG process will be visible as a simple shift of the interference pattern. Note that the frequency resolution of a pulse pair spaced by e.g. 67 ns is similar to what can be obtained with a pulse train of six pulses spaced by 13.4 ns. This is demonstrated in figure 7.8, where a series of pulse pair measurements with delays ranging from 13.4 to 67 ns is shown. The narrowest resonance that is observed has a full width at half maximum (FWHM) of 7.5 MHz, which is a 13-fold improvement compared to any other measurement performed so far at such short wavelengths using nanosecond

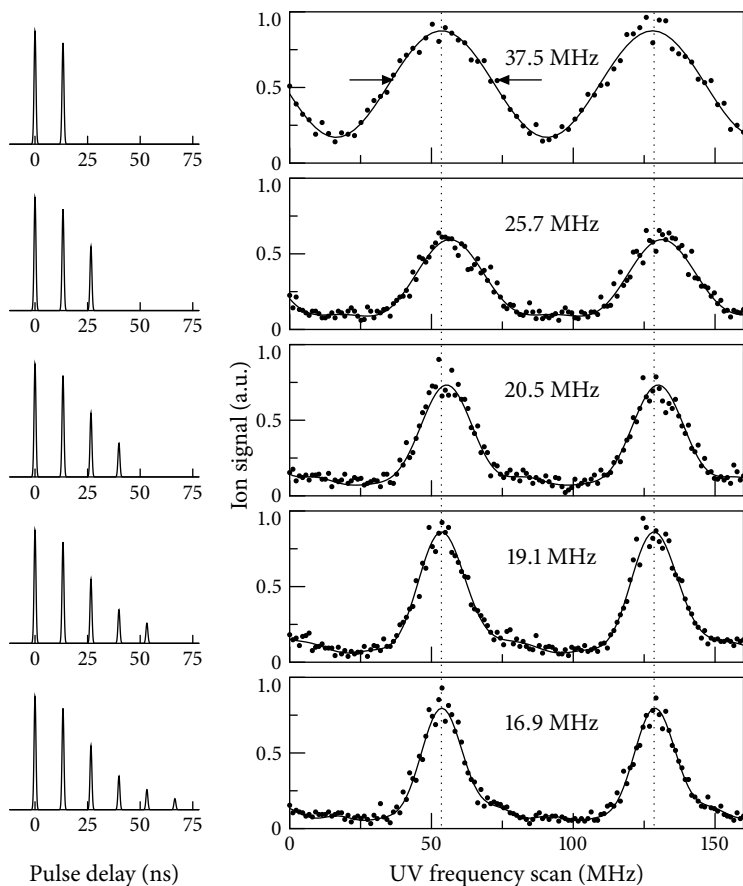


Figure 7.7: Quantum interference signals at 125 nm in ^{132}Xe using a vuv pulse train of increasing length. Relative pulse intensities and time delays are shown on the left of the graphs, and the width of the resonances (FWHM) is denoted in each panel. The solid lines represent fits to model interference pattern functions, allowing for an intensity difference between the excitation pulses, as well as a varying pulse-to-pulse phase shift $\Delta\varphi$ in graph due to the amplifier (see text).

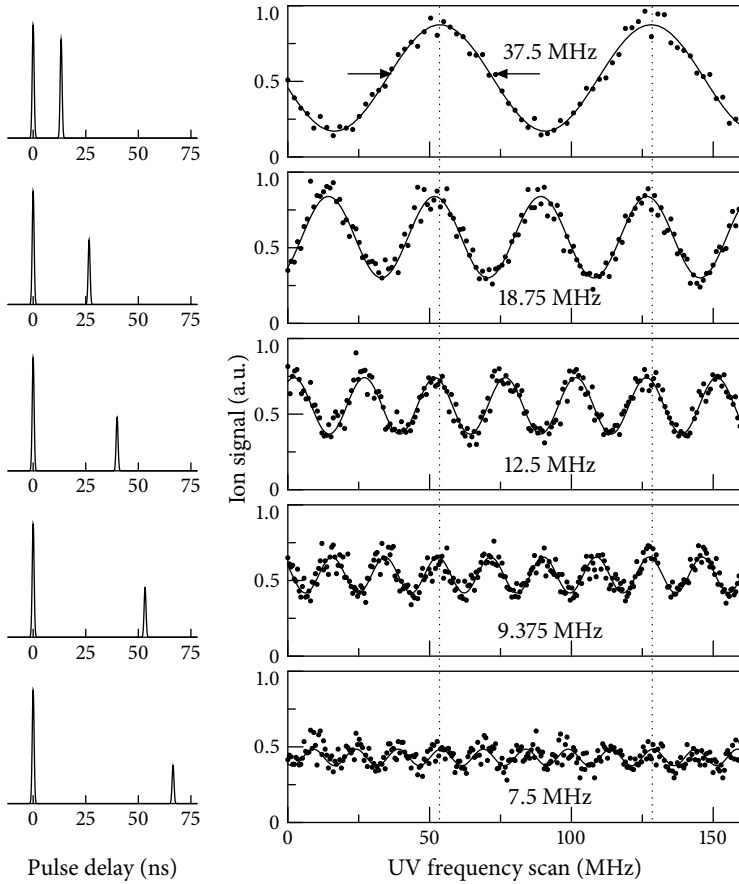


Figure 7.8: Quantum interference signals at 125 nm in ^{132}Xe using two vuv pulses with increasing delays. Relative pulse intensities and time delays are shown on the left of the graphs, and the width of the resonances (FWHM) is denoted in each panel. The solid lines represent fits to model interference pattern functions, allowing for an intensity difference between the excitation pulses. The upper panel is identical to that in figure 7.7, as all data was acquired during the same measurement run.

pulsed lasers [210] or cw lasers [63]. The frequency resolution demonstrated in this measurement is 3×10^{-9} , constituting an improvement of about six orders of magnitude compared to previous experiments in the vuv and xuv using Michelson interferometers and ultrashort pulses [108, 109]. The decrease in fringe contrast with increasing T as seen in figure 7.8 can be explained with a model that includes the measured pulse intensity ratios, the lifetime of the upper state, and the Doppler width. The differences between the observed signals presented here and the calculated signals of section 3.6 (figure 3.11) is completely explained by the fact that the calculations employ equal intensity pulses. By investigating transitions to longer-lived states, and reduction of the Doppler width through e.g. cooling techniques and confinement in an ion trap, much narrower resonances can in principle be recorded with high contrast using this method. But even from a relatively low-contrast signal as shown in the bottom panel of figure 7.8 the resonance position can be extracted reliably, since the rapid sine wave oscillation allows to fit many periods simultaneously.

7.8 Procedure for absolute frequency measurements with pulse pairs

The control over the measurement resolution by changing the pulse delay can be used to overcome the ambiguity in the determination of the right mode when absolute frequencies are to be measured [79, 206]. An initial measurement with sufficiently short time delay T allows identification of the mode by comparison with existing low-resolution data. Here we demonstrate (figure 7.8) that the measurement accuracy can be improved by increasing T to zoom in on the transition, while keeping track of the previously determined excitation mode. This is illustrated by the dotted lines in figure 7.8. Apart from the normal systematic effects in laser spectroscopy (e.g. Doppler shift and AC Stark shift) and the statistical fit uncertainty, the amplifier phase shift error (6×25 mrad) amounts to an error in the vuv of about 2 MHz for $T = 13.4$ ns. However, as the pulse delay increases, the influence of the amplifier phase shifts is progressively reduced inversely proportional to T . For example, at $T = 67$ ns the uncertainty due to phase shifts has improved to 360 kHz (1×10^{-10} accuracy). As in the measurements presented here the contrast of the signals deteriorates with increasing delay due to the finite lifetime of the transition, the accuracy in this case is limited by the statistical fit uncertainty. When this is included, a statistical error of about 2.3 MHz for the measurement at 13.4 ns delay and 1.0 MHz for the one at 67 ns delay is obtained for the current experiment. When a transition is studied that has a longer lifetime, this limitation will be lifted.

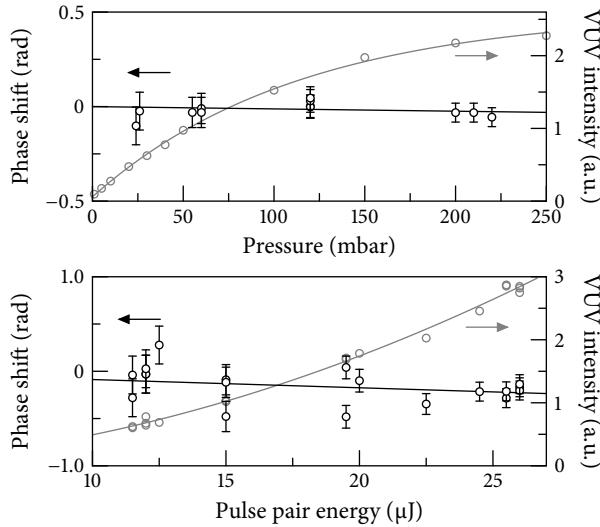


Figure 7.9: Dependence of the relative phase between the vuv pulses on the THG process in O_2 . Measurements of the phase shift of the quantum-interference signals in xenon (as shown in figure 7.8) using two vuv pulses. Upper panel: phase shift as a function of the O_2 pressure in the gas cell (incident pulse pair energy $23 \mu\text{J}$). Lower panel: phase shift as a function of incident laser pulse pair energy (O_2 pressure 190 mbar). The phase shift is set to zero at zero intensity and pressure. The grey curves indicate the generated vuv intensity.

The absolute transition frequency has not been calibrated here, as no spectroscopic data with sufficient accuracy for mode identification exists at present for the studied xenon transition (in contrast to our previous experiment on krypton at $2 \times 212 \text{ nm}$, see chapter 6). As this transition in itself is of no fundamental spectroscopic importance, no further efforts were undertaken to perform an initial calibration by traditional means.

However, if absolute frequency measurements are to be performed, the possibility of a systematic phase shift caused by the THG process needs to be investigated precisely. We have done this by systematically varying the parameters relevant to THG, in particular the gas pressure and laser intensity. The xenon atoms are now used as high-resolution vuv phase detectors, by recording two-pulse interferograms with 13.365 ns time delay at various gas pressures and laser intensities. Figure 7.9 shows the retrieved phases when using oxygen (O_2) for THG, while figure 7.10 shows the same for acetylene. The data have been fitted to straight lines, yielding the slopes presented in table 7.2. For O_2 , no

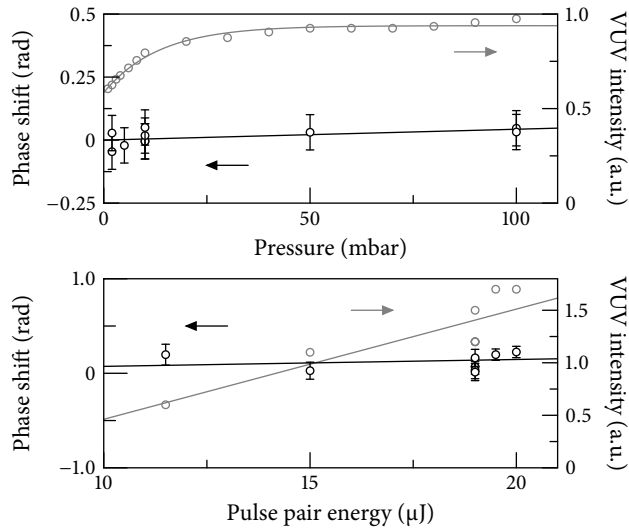


Figure 7.10: Dependence of the relative phase between the VUV pulses on the THG process in acetylene. Measurements of the phase shift of the quantum-interference signals in xenon (as shown in figure 7.8) using two VUV pulses. Upper panel: phase shift as a function of the acetylene pressure in the gas cell (incident pulse pair energy 23 μJ). Lower panel: phase shift as a function of incident laser pulse pair energy (acetylene pressure 100 mbar). The phase shift is set to zero at zero intensity and pressure. The gray curves indicate the generated VUV intensity.

real phase shifts are observed within $\frac{1}{30}$ th of a VUV cycle, even though the VUV intensity changes by an order of magnitude and shows signs of saturation. We repeated these measurements using acetylene as the nonlinear medium, which already saturates at a pressure below 1 mbar, but displays a maximum THG efficiency at 10 mbar, comparable to O_2 at about 200 mbar. Also with acetylene, no phase shift is observed within the measurement resolution. This ensures that when a sufficiently long time delay between the pulses is used, a sub-MHz resolution can indeed be achieved.

7.9 Conclusions

In conclusion, we have demonstrated that frequency combs can be transferred to the VUV by harmonic up-conversion in a gas while distortion of the phase coherence between subsequent comb pulses is well within $\frac{1}{30}$ th of a VUV cycle. We used these VUV pulses to

Table 7.2: Summary of the pressure and intensity dependence of the phase shift in harmonic generation. The numbers in parentheses are standard deviations.

	$\Delta\phi/\Delta P$	$\Delta\phi/\Delta I$
O ₂	-0.12(0.29) mrad/mbar	-8.7(5.8) mrad/ μ J
	-1.5(3.4) kHz/mbar	-104(70) kHz/ μ J
C ₂ H ₂	0.43(59) mrad/mbar	7.3(12) mrad/ μ J
	5.1(7.1) kHz/mbar	87(146) kHz/ μ J

excite a 125 nm transition in xenon, showing that quantum interference is a powerful tool for high-resolution spectroscopy at VUV and shorter wavelengths, possibly even down to the soft-X-ray regime when a more powerful amplifier is used. In addition, separate pump pulses could be used to increase the time delay between the VUV pulses, potentially improving the resolution to the kHz level. In the near future, we plan to perform measurements on the $1s^2 \rightarrow 1s2s$ two-photon transition at 2×120 nm in helium with a target accuracy of ~ 500 kHz, which would lead to two orders of magnitude improvement in the determination of the ground state Lamb shift [56]. Applying the technique of quantum-interference spectroscopy to trapped ions may lead to the emergence of a new generation of ultra-precise clocks, operating in the XUV domain.

A source of 2 terawatt, 2.7 cycle laser pulses based on non-collinear optical parametric chirped-pulse amplification

The method of direct frequency comb spectroscopy described in the previous chapter is hampered by the amplifier used to produce pulses that are intense enough for frequency conversion. The phase shifts that occur in the multi-pass amplifier due to population inversion changes and self-phase modulation are tedious to measure. At the same time, the delay between the pulses is limited by the duration of the pump pulse. In this chapter, another type of amplifier is discussed: a non-collinear optical parametric chirped-pulse amplifier (NOPCPA). It is a versatile amplifier, that although designed for high-power ultrashort pulse applications, can be adapted to quantum-interference metrology experiments. We demonstrate a NOPCPA system that produces 7.6 fs pulses with a peak power of 2 terawatt at 30 Hz repetition rate. Using an ultra-broadband Ti:sapphire seed oscillator and grating-based stretching and compression combined with an LCD phase-shaper, a 310 nm wide spectrum is amplified with a total gain of 3×10^7 , and is recompressed within 5% of its Fourier limit. The total integrated parametric fluorescence is kept below 0.2%, leading to a pre-pulse contrast of 2×10^{-8} on picosecond timescales.

8.1 Introduction

The generation of high-intensity few-cycle laser pulses is a subject of great interest [171], as experimental progress in fields such as attosecond science [211] and quantum control [212] is for a large part dependent on the availability of suitable laser sources. In recent years, optical parametric chirped-pulse amplification (OPCPA) [213, 214] has been

demonstrated to be a very promising technique for the production of ultrashort, high-intensity laser pulses [215, 216]. Especially the development of OPCPA in a non-collinear geometry (NOPCPA) has facilitated the amplification of ultra-broadband spectra both in the Ti:sapphire wavelength range [217–219] and at longer wavelengths [220, 221].

In this chapter we present an NOPCPA system that produces 2 terawatt peak intensity laser pulses with a duration of 2.7 optical cycles (7.6 fs). The system utilizes the full >300 nm gain bandwidth that has been theoretically predicted for a 532 nm pumped NOPCPA system [222, 223] based on BBO (β -barium borate) crystals, while maintaining spectral phase control over this entire bandwidth. State-of-the-art few-cycle laser sources can deliver sub-3-cycle pulses with an intensity reaching 0.2 TW [112, 224, 225]; therefore, our system represents an order of magnitude increase in peak intensity in sub-3-cycle pulse generation, with excellent prospects for further power scaling.

8.2 Principles of NOPCPA

First a brief overview of the theory of NOPCPA is presented; more extensive analyses can be found elsewhere [88, 222, 226]. For parametric amplification, we consider two waves $E_p = E_p(z)e^{-i(\omega_p t - k_p z)}$ and $E_s = E_s(z)e^{-i(\omega_s t - k_s z)}$, the pump and signal waves, traveling through a medium with a non-zero $\chi^{(2)}$, i.e. media without inversion symmetry. These waves will generate a polarization in the medium oscillating amongst others at the difference frequency, called the idler frequency, $\omega_i = \omega_p - \omega_s$:

$$P_i(z, t) = \chi^{(2)}(-\omega_s; \omega_1, -\omega_2)E_p(z, t)E_s^*(z, t). \quad (8.1)$$

Using this as a source term in the wave equation 2.8, the following coupled amplitude equations can be derived in the slowly-varying-envelope approximation:

$$\begin{aligned} \frac{\partial E_s}{\partial z} &= -\frac{i\omega_s \chi^{(2)}}{2cn_s} E_p E_i^* e^{-i\Delta k z} \\ \frac{\partial E_i}{\partial z} &= -\frac{i\omega_i \chi^{(2)}}{2cn_i} E_p E_s^* e^{-i\Delta k z} \\ \frac{\partial E_p}{\partial z} &= -\frac{i\omega_p \chi^{(2)}}{2cn_p} E_s E_i e^{i\Delta k z}, \end{aligned} \quad (8.2)$$

with $\Delta k = k_p - k_s - k_i$ once more denotes the phase mismatch. When there is no initial idler field, the initial pump field is much stronger than the initial signal field, and the depletion of the pump field is negligible, simple solutions can be found for these coupled

equations [226]:

$$\begin{aligned}
 I_s(z) &= I_s(0) \cosh^2(gz) \\
 I_i(z) &= I_i(0) \frac{\omega_i}{\omega_s} \sinh^2(gz) \\
 I_p(z) &= I_p(0),
 \end{aligned} \tag{8.3}$$

where the small signal gain coefficient is defined by

$$g = \sqrt{(\chi^{(2)})^2 \frac{\omega_s \omega_i I_p(0)}{2\epsilon_0 c^3 n_p n_s n_i} - \left(\frac{\Delta k}{2}\right)^2}. \tag{8.4}$$

The gain of the signal field is approximately exponential: when pumping BBO with a few GW/cm², a gain of the order of 10,000 can be realized in only a few mm of material. This allows for a very compact amplifier setup.

For the amplification of short pulses, the bandwidth of amplification is of great importance, which is determined mainly by the phase mismatch Δk . This Δk can be minimized over a wide bandwidth when birefringent crystals are used to tune the refractive index seen by participating waves with different polarizations, and by introducing a non-collinear angle between the waves. For type I interaction in the uni-axial crystal BBO pumped with 532 nm light and a small non-collinear angle ($\sim 2.4^\circ$ internal), the phase-matching curve can be minimized over a bandwidth extending from about 720 to over 1000 nm [222, 223]. This is enough bandwidth to amplify pulses as short as 5.7 fs [222].

Although the damage threshold of BBO is quite high, exceeding 100 GW/cm² for a 10 ps pulse [222], it is too low for direct amplification of ultrashort pulses to a TW-level peak power. This problem can be overcome by the application of chirped-pulse amplification [194]. In this method an ultrashort, broadband seed pulse is stretched to match its duration to a long, high-energy pump pulse from e.g. a Nd:YAG laser system. Energy transfer and subsequent recompression of the amplified seed pulse then lead to the production of ultrashort high-energy pulses. For BBO, the high damage threshold makes it possible to work with a stretched pulse duration of about 10-20 ps, much less than what is needed for Ti:sapphire systems. Therefore, the stretching and compression setups can be compact as well.

Finally, the fact that the interaction is instantaneous is beneficial as well. In contrast to Titanium:sapphire multi-pass amplifiers, there is virtually no energy deposited in the gain medium. This means that there are hardly any thermal effects, which are often detrimental in Ti:sapphire amplifiers and require complicated compensation schemes.

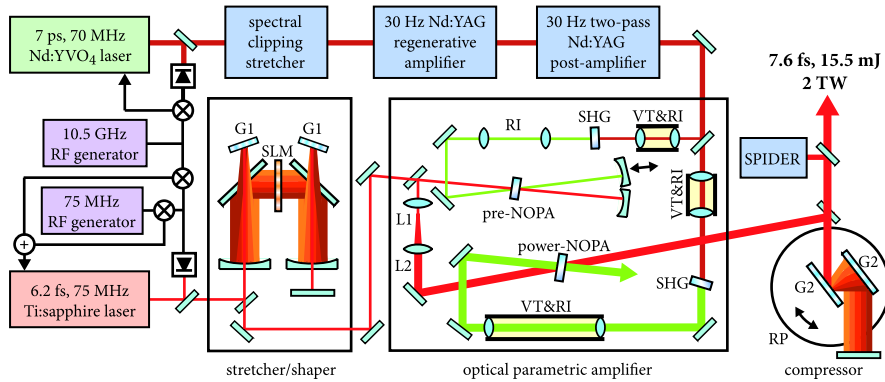


Figure 8.1: Schematic of the 2 TW, 7.6 fs NOPCPA system. G1: 600 l/mm grating, G2: 1200 l/mm grating, SLM: 640-element LCD spatial light modulator, VT: vacuum tube, RI: relay-imaging, RP: rotatable platform, SHG: crystal for second-harmonic generation. The lenses L1 and L2 are drawn for simplicity, in practice only reflective optics are used in the seed beam path. See text for further details.

8.3 Ultra-broadband two-terawatt NOPCPA system

We have designed a laser-amplifier system that exploits these benefits of NOPCPA to generate terawatt-level few-cycle pulses. Key elements of this system are: 1) a compact, three-pass amplifier with a gain of 3×10^7 ; 2) a stretcher-compressor combination including a programmable dispersion compensator capable of accurate spectral phase compensation over a >300 nm bandwidth; 3) a pump pulse duration in the 10-100 ps range and hence a moderate stretching ratio ($\sim 10^3$); 4) pump-seed synchronization with sub-picosecond accuracy. All these features are implemented in the setup shown in figure 8.1.

The seed laser is a home-built ultra-broadband Ti:sapphire oscillator, which produces 5.5 nJ pulses at 75 MHz repetition rate, with a spectrum that has a Fourier-limit of 6.2 fs. The repetition rate of this oscillator is locked to the signal of a 75 MHz RF generator using a piezo-mounted mirror in the laser cavity. For increased stability, we employ an additional lock at the 140th harmonic (10.5 GHz) of the repetition rate, which is generated in a fast photodiode. The seed pulses are stretched to about 13 ps using a grating-based pulse stretcher, in which a 640-element LCD phase-only spatial light modulator (Jenoptik) is incorporated for high-resolution spectral phase control. From the available seed light, 4 nJ pulses are sent into the stretcher, which has a transmission

of 30%. A more detailed discussion of pulse stretching and compression is given in section 8.4.

The pump laser source is based on amplification of pulses from a SESAM mode-locked 70 MHz Nd:YVO₄ oscillator (High-Q Laser). This laser is synchronized to the Ti:sapphire oscillator by locking the 150th harmonic of its repetition frequency to the same 10.5 GHz RF generator that is used for the Ti:sapphire laser stabilization. Such a locking scheme ensures that every 14th pulse from the Nd:YVO₄ laser (corresponding to a 200 ns delay) overlaps with every 15th Ti:sapphire laser pulse. At the lower repetition rate of an amplifier system (30 Hz in the present case) this then leads to properly synchronized pulses, provided the amplifier pulse repetition period is an integer multiple of the aforementioned 200 ns time delay.

The pulses from the Nd:YVO₄ oscillator are first stretched to 60 ps in time to allow amplification to higher energy without damaging optics. This is done by dispersing the spectrum of the pulses in a 4f-setup and cutting away a large part of the spectrum with a slit in the Fourier plane. The 60 ps pulses are then amplified to the mJ level in a diode-pumped Nd:YAG regenerative amplifier. The regenerative amplifier causes some reshaping of the pump pulse, as it operates at a power level where the effects of self-phase-modulation and self-compression start to become appreciable. To limit the influence of these effects the regenerative amplifier is not operated at full saturation. From an autocorrelation measurement, we confirmed that the pump pulse has a smooth shape without significant pre- or post-pulses. Further amplification up to 250 mJ per pulse at 30 Hz repetition rate is achieved with a double-pass post-amplifier containing two flashlamp-pumped Nd:YAG modules (EKSPLA Ltd.) in a ring geometry. After second-harmonic generation (SHG), up to 160 mJ per pulse is produced at 532 nm. The difference in pulse duration between pump and seed (60 ps vs. 13 ps) is chosen such that the pump intensity variation is relatively small across the entire chirped seed pulse. Consequently, all spectral components in the seed pulse experience similar gain, which improves the bandwidth of the amplified spectrum. As the wings of the seed spectrum extend considerably beyond the 13 ps FWHM duration of the stretched seed pulse, saturation in the last pass still ensures a good energy extraction efficiency [218].

The actual NOPCPA system consists of only three amplification passes: two in a pre-amplifier pumped by 10 mJ 532 nm pulses, and a final pass through a power-amplifier crystal pumped by 150 mJ of pump light. The pre-amplifier contains a 5.5 mm long BBO crystal ($\theta = 22.5^\circ$, $\phi = 0^\circ$, type I phase matching) as the gain medium. Both pump and seed beam are collimated to a 1.5 mm diameter, and intersect with a non-collinear angle of about 2.4° inside the crystal. The non-collinear angles in the two passes through the

pre-amplifier are aligned slightly differently to optimize the output spectral bandwidth. The pre-amplifier increases the energy of the seed pulses from 1 nJ to about 0.5 mJ.

After the pre-amplifier, the beam is expanded to 10 mm diameter by a telescope, and amplified to 30 mJ per pulse in a single pass through the power-amplifier stage. This power-amplifier has a 5 mm long, 14 mm × 14 mm BBO crystal (phase-matching angles identical to the pre-amplifier crystal) as the gain medium. Similar to the pre-amplifier, the non-collinear angle is near 2.4° , and optimized by maximizing the amplified bandwidth.

As the transverse beam profile of the pump laser has a top-hat distribution, relay-imaging is applied between the final Nd:YAG amplifier rod in the pump laser and the SHG crystals, as well as between the SHG crystals and the respective OPA amplifier stages. The relay-imaging ensures a good-quality pump beam profile in the OPA crystals. This is of paramount importance for proper NOPCPA operation as gain, pulse contrast and beam profile of the amplified seed beam are all strongly affected by the pump beam profile. Where needed, the focus that occurs in the Fourier plane of the relay-imaging systems has been placed in a vacuum tube to prevent optical breakdown and self-phase-modulation in air.

Figure 8.2 displays a typical spectrum of the oscillator output, and one of the amplified and recompressed pulses after the full NOPCPA system. The part of the oscillator

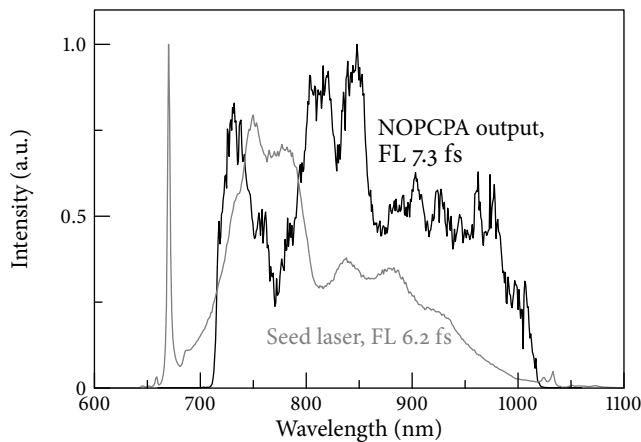


Figure 8.2: The oscillator spectrum (black curve), and the NOPCPA output after amplification to 30 mJ per pulse and subsequent pulse compression (gray curve). FL: Fourier limit.

spectrum below 700 nm is actually not transmitted by the stretcher; as the phase mismatch of the parametric amplification process becomes too high for wavelengths below 710 nm to have any significant gain, the stretcher has been designed for spectra between 700 nm and 1100 nm. Figure 8.2 clearly shows the rectangular spectral shape characteristic of a saturated NOPCPA, and the amplified spectrum extends from about 710 nm to 1020 nm. The width of the generated spectrum is very close to the theoretically predicted limit for an NOPCPA system based on 5 mm long BBO crystals and a pump wavelength of 532 nm [214, 222, 223]. The Fourier limit of the NOPCPA output is 7.3 fs FWHM, which corresponds to a 2.5 cycle pulse at a carrier wavelength of 850 nm. The intensity stability of the OPA output is measured to be 4% RMS, which is mainly the result of the 2.5% RMS fluctuations of the pump intensity.

While the initial beam profile of the Ti:sapphire oscillator output is Gaussian, the beam profile of the amplified NOPCPA output adopts the top-hat shape of the pump laser due to saturation (figures. 8.3a and 8.3b). To investigate the possibility of spatial chirp in the amplified beam, we measured the spectrum in various parts of the beam using a fiber-coupled spectrometer. Although some spectral variations across the beam have been observed, no systematic spatial chirp is detected. Additional information has been obtained by recording the beam profile with various interference filters in the beam (see

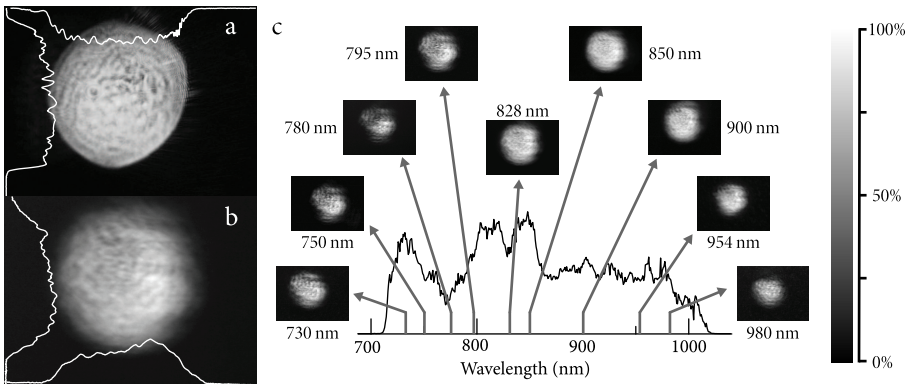


Figure 8.3: a) Beam profile of the pump laser in the power-amplifier stage; b) beam profile of the amplified OPA output beam in the power-amplifier stage; c) measured beam profile of the OPA output for various parts of the spectrum. All pictures were taken by relay-imaging the beam in the power-amplifier crystal onto a CCD camera. The white traces in a) and b) represent the beam profile across the center of the respective beams, averaged over 10 rows (or columns) of pixels.

figure 8.3c). These pictures show some variations, mostly in the regions of low spectral amplitude. This structure is attributed to the wavelength dependent phase matching and sensitivity to perturbations in the pump beam wavefront, leading to some differences in gain and saturation.

8.4 Spectral phase shaping and few-cycle pulse compression

The stretching and recompression needed for chirped pulse amplification can present serious problems when few-cycle pulses are involved, due to the large bandwidth over which the dispersion needs to be compensated with high accuracy. To date, mJ-level few-cycle pulse sources all employ the output pulses of a relatively narrow-band chirped-pulse amplifier, which are spectrally broadened in a nonlinear medium [112, 224, 225]. Such pulses require only a minor amount of chirp compensation that can readily be provided by chirped mirrors. Full chirped-pulse amplification and recompression for a broad bandwidth with a large stretching ratio has — to the best of our knowledge — not been demonstrated so far for sub-10-fs pulses, although Takada et al. have reported on a stretcher-compressor system for 8 fs pulses, which they employed in the compression of terawatt-level pulses to 12 fs [227].

The options for broadband stretching and compression are limited. For instance, prism compressors would become impractically large for such broad spectra, even when multiple prism sequences are used, as in [228], where the bandwidth is still relatively narrow. Negative-dispersion stretching and subsequent bulk-glass compression may be applicable to few-cycle pulses [219], and has the advantage of a high compressor efficiency. However, the extreme power densities of a terawatt-class amplifier can easily lead to self-phase-modulation in the bulk material, or distortion of the wavefront due to glass inhomogeneities when larger beam diameters are used. Instead, we have implemented a grating-based stretcher and compressor system. Although the throughput is typically limited to ~50% (after four grating bounces), such a system can be realized in a much smaller setup with only reflective optics.

For higher-order dispersion compensation, a 640 pixel LCD spatial light modulator (SLM) is included in our setup. As such a device requires an extra grating $4f$ -system, its inclusion would increase the complexity and the size of the setup and would introduce even more losses for the seed beam. To circumvent these drawbacks, the SLM has been incorporated in the stretcher setup. The fact that the stretcher is not built as a true $4f$ -system does not influence the shaping capabilities, as the individual colors are still focused on the central plane of the SLM. Only the angles at which the individual colors

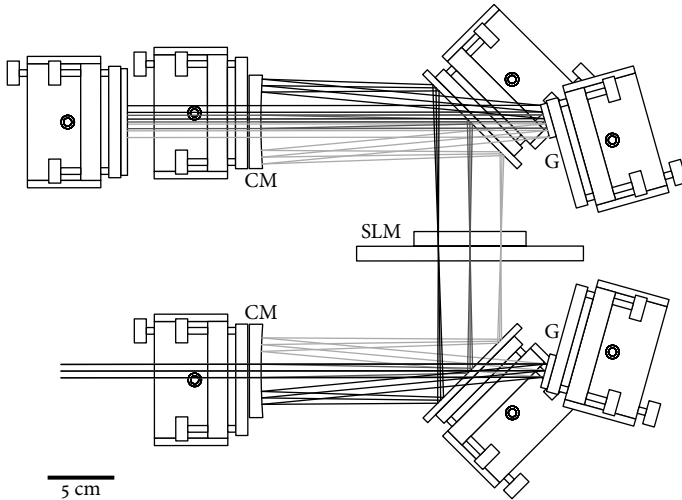


Figure 8.4: The design of the stretcher/shaper combination. The gratings are displaced from the $4f$ -configuration to introduce positive dispersion. This does not influence the focusing of the separate colors on the central SLM plane, only the angle at which the light traverses the SLM. CM: cylindrical mirror, G: grating, SLM: spatial light modulator.

cross the central plane may now deviate from the perpendicular, see figure 8.4. The double-pass geometry of the stretcher/shaper does not pose a problem either, as long as it is taken into consideration that any phase pattern that is put on the SLM is imprinted twice on the pulse spectrum. Therefore only half of the required phase shape is to be sent to the SLM.

The total stretcher/shaper setup has been built using a design that is similar to that of Präkelt et al. [229], which is compact and robust. Our setup (see figure 8.4) has a footprint of only 40×50 cm, and employs large, heavy mounts for all the optical components for added stability. Two 600 l/mm gold-coated gratings (Richardson) are used in combination with gold coated cylindrical mirrors with a radius-of-curvature (ROC) of 50 cm, and the stretcher is double-passed. The gratings are displaced from the $4f$ -configuration by about 3 cm to introduce a group velocity dispersion of about 6.4×10^4 fs². The total throughput of the stretcher/shaper combination exceeds 30%.

The compressor, at the other end of the amplifier, employs gold-coated gratings as well, but here a groove density of 1200 l/mm is used. Due to the small stretching

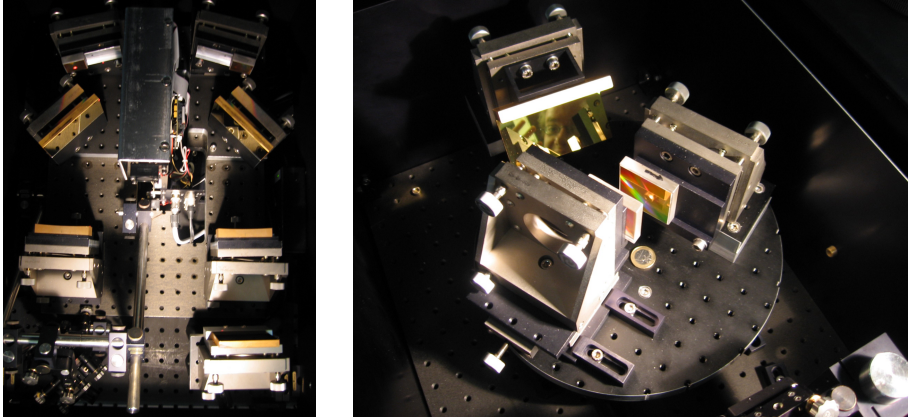


Figure 8.5: Photographs of the physical setup of the stretcher (left) and the compressor (right). In the compressor photo, a 1 euro coin is shown for size comparison.

ratio required for NOPCPA, the compressor design is compact as well, with a grating separation of only ~ 20 mm. The combination of the stretcher and compressor is designed to compensate dispersion up to third order over a bandwidth of about 400 nm. This is facilitated by the different groove densities and by putting the compressor grating pair on a rotatable platform, such that the input angle on the gratings can be tuned (thereby varying the ratio between the different dispersion orders) without affecting the overall alignment. Higher-order dispersion is counteracted by adaptive control over the spectral phase with the SLM. Pictures of both the stretcher/shaper and the compressor are shown in figure 8.5.

The stretcher and BBO crystals in the amplifier together yield a calculated dispersion of $6.3 \times 10^4 \text{ fs}^2$, $-9.54 \times 10^4 \text{ fs}^3$ and $1.88 \times 10^5 \text{ fs}^4$ for the second-, third- and fourth-order dispersion, respectively. Throughout the entire setup we have only used gold-coated mirrors, which have a negligible contribution to the dispersion. The dispersion of air is not taken into account, as the total beam path from oscillator to compressor output is only 13 meters. The compressor can be tuned to compensate the second- and third-order dispersion, so that a residual fourth-order dispersion of about $4.0 \times 10^4 \text{ fs}^4$ remains. Considering the spectral bandwidth of the pulses and the Nyquist limit of the SLM, we calculate that up to $5.34 \times 10^4 \text{ fs}^4$ can be compensated by adaptive phase-shaping. In practice, the requirements on the SLM are eased by partially canceling the excess higher-order phase deviations through over-compensation of the lower-order phase

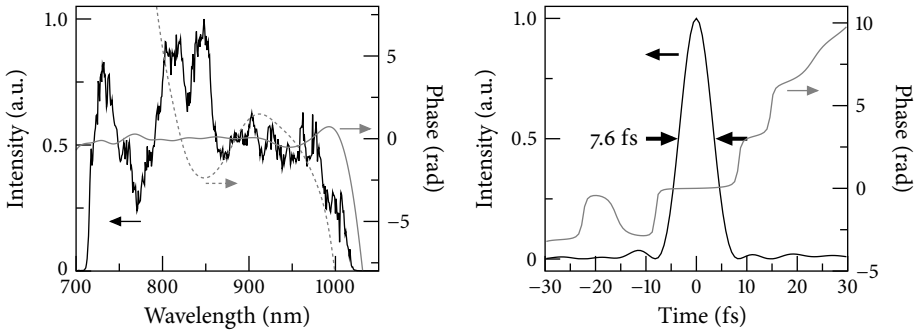


Figure 8.6: Left: the spectral intensity (black curve), and spectral phase before (dashed gray curve) and after (gray curve) adaptive pulse compression with the spatial light modulator. Right: the reconstructed pulse intensity (black curve) and phase (gray curve) in the time domain.

terms. This is done by aligning the compressor while monitoring the spectral phase in real-time using SPIDER [230] such that the residual phase excursions are well within the range of the SLM across the entire spectrum.

The results of the adaptive pulse compression are shown in the left panel of figure 8.6. Initially, the spectral phase after compression shows deviations ranging from 55 rad at 710 nm to -20 rad at 1020 nm. After adaptive phase shaping with the SLM, the residual spectral phase remains within 0.6 rad between 710 and 930 nm, while only above 1000 nm it exceeds 1 rad. The resulting intensity and phase in the time domain are depicted in the right panel of figure 8.6. The FWHM pulse duration is 7.6 fs, which is within 5% of the 7.3 fs Fourier limit. Due to the 52% compressor efficiency, the pulse energy after compression is reduced to 15.5 mJ. This corresponds to pulses with a duration of only 2.7 optical cycles and a peak intensity of 2 TW.

8.5 Pulse contrast measurements

An important issue in NOPCPA is the amount of parametric fluorescence that is generated in the various amplifier stages. Especially fluorescence from the first pass (where the gain is highest) can be amplified in subsequent passes to form a significant fraction of the total OPA output, limiting the attainable pulse contrast. In our present amplifier system, we made an initial measurement of the amplified fluorescence by blocking the seed light, in which case 0.3% of the total amplified pulse energy remains. However,

as the presence of the seed beam will decrease the gain for the fluorescence, the total integrated fluorescence will be less under normal operating conditions. This difference can be determined by cutting away part of the seed spectrum in the grating stretcher, and monitoring the idler wavelength that corresponds to this “missing” signal spectrum. An increase in the intensity of this particular idler wavelength is then observed when the seed beam is blocked. From these combined measurements, a total integrated fluorescence of 0.2% in the presence of seed light is deduced.

More detailed information on the parametric fluorescence background can be obtained from a high-dynamic-range autocorrelation measurement. However, such a measurement of the pulse contrast is not trivial when compressed few-cycle pulses are involved, due to the large spectral bandwidth and the sensitivity to chirp. Pulse characterization methods like second-order autocorrelation and SPIDER are not capable of measuring the pulse contrast properly: the SPIDER-technique can not cover such a large dynamic range and time delay, while second-order autocorrelators can not distinguish between pre- and post-pulses. Therefore, a high-dynamic-range pulse contrast measurement usually requires two cascaded second-order processes, such as SHG and subsequent sum-frequency generation to obtain the third harmonic. For a reliable measurement, these up-conversion processes should induce no spectral modulation or significant pulse stretching, as any such distortions would immediately appear as a reduced pulse contrast. Third-harmonic generation is very sensitive to a properly matched pulse duration of the fundamental and second harmonic in the process of sum-frequency generation, while the fluorescence background is hardly affected by such a chirp. For this reason, we constructed a high-dynamic-range autocorrelator based on optical parametric amplification [231], which allows for a larger spectral bandwidth than conventional third-order autocorrelation. In this scheme, the second harmonic of the input pulse is used to pump an OPA, seeded by another part of the input pulse. The contrast can then be measured by monitoring the intensity of the produced idler while scanning the pump-seed delay.

This type of pulse contrast measurement with an OPA correlator (OPAC) is described in detail in [231], although the characterization of few-cycle pulses requires some modifications, as discussed by Tavella et al. [232] for the case of third-harmonic autocorrelation. Firstly, attenuation of the seed pulse in the OPAC is done by taking reflections of wedged fused silica substrates ($R \sim 0.3\%$) instead of using (dispersive) neutral density filters. Only for the measurement scans with the highest attenuation, one additional thin gray filter (either $12\times$ or $88\times$ attenuation) has been used. Secondly, a thin crystal (0.2 mm) is used for SHG to minimize chirp and spectral narrowing. Finally, the non-collinear angle in

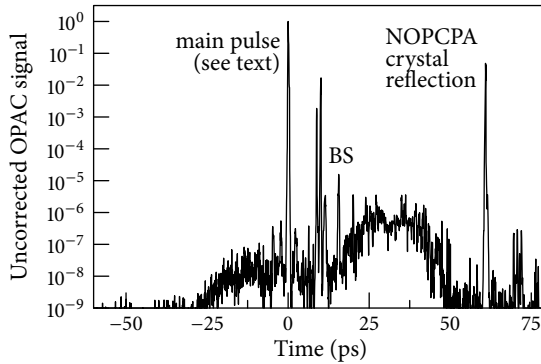


Figure 8.7: Uncorrected measurement (raw data) of the pulse contrast using an OPA correlator. A few spurious post-pulses can be seen (BS), caused by beamsplitters in the NOPCPA setup. The peak at 60 ps results from a double internal reflection in the first NOPCPA crystal. The fluorescence background peaks at the 10^{-6} level, but stays below 10^{-7} on the leading edge of the pulse. At times when there is no pump light present, the pulse contrast exceeds the detection limit. The height of the main pulse still needs to be corrected for the effects of pulse broadening in the OPAC: by taking this effect into account, the actual pre-pulse contrast is found to be better than 2×10^{-8} .

the 1 mm long OPAC crystal is set at 4° instead of 10° as used in [231] to keep the pulse front tilt small.

A typical pulse contrast measurement is shown in figure 8.7. Aside from the main pulse, several features can be readily identified: first, a fluorescence background is observed between -25 and +50 ps; second, several post-pulses are seen, most notably at 8.6 and 10 ps, which can be traced back to beamsplitters in the NOPCPA setup; third, two pre-pulses at the 10^{-7} level appear at 2.2 ps and 4.4 ps, corresponding to multiple internal reflections of the pump beam inside the 0.2 mm SHG crystal in the OPAC (note that a post-pulse in the pump beam will show up as an artificial pre-pulse in the measurement when scanning the pump-seed time delay); fourth, a significant post-pulse at 60 ps delay arises from a double internal reflection of the signal pulse in the first NOPCPA crystal.

Before attaching any significance to the relative intensities of these features, it should be realized that contrast measurements of few-cycle pulses are easily distorted by various systematic effects. For instance, the SHG used in the OPAC causes spectral narrowing and therefore a longer pulse. In our case, this SHG pulse is estimated to be ~ 40 fs. The effect of such a pulse duration mismatch on the measured OPAC signal is depicted in figure 8.8. A schematic of a contrast measurement with fundamental seed and SHG pump pulses of

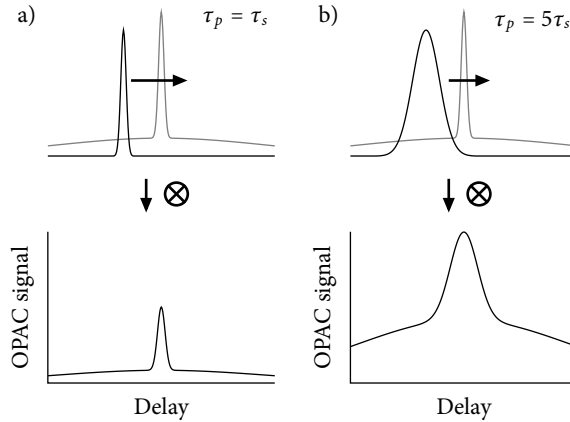


Figure 8.8: The influence of a pulse duration mismatch in the OPAC. Pump pulse duration τ_p is a) equal to the seed pulse duration τ_s ; b) longer than the seed pulse duration. In the upper panels, the gray trace represents a short seed pulse on top of a long fluorescence background, while the black trace represents the pump pulse. A comparison of a) and b) reveals that the use of a pump pulse which is longer than the seed pulse leads to a decrease of the measured contrast ratio between the main pulse and the fluorescence (note that all graphs have a linear scale).

equal duration is shown in figure 8.8a, while in figure 8.8b the pump pulse is significantly longer than the seed. Comparing these two figures, one can see that a stretched pump pulse not only leads to broader peaks, but also to a decrease of the measured contrast between main pulse and fluorescence background. A quantitative analysis of this effect is performed by calculating convolutions of model pulses with varying pulse duration mismatch. We find that the pulse contrast decreases by a factor approximately equal to the ratio of pump and seed pulse durations, assuming an unchirped seed pulse. A chirp in the seed pulse has negligible effect provided that the seed pulse remains shorter than the pump pulse. Therefore, to correct for the spectral narrowing of the SHG pulse in the present system, the measured pulse contrast from figure 8.7 needs to be increased by an estimated factor of about 5.

The peak at 60 ps requires careful analysis as well. This peak can be identified as a double internal reflection (DIR) in the 5.5 mm long NOPCPA crystal, which is amplified by the tail of the pump pulse. Since this pulse is chirped to a duration of 13 ps, its spectral content varies in time and only the longer wavelengths (which are ahead) will be amplified by the tail of the pump pulse. To estimate the spectrum of the DIR pulse

after the amplifier, we delayed the seed pulse by 60 ps with respect to the pump. The measured output spectrum has a FWHM of 32 nm centered at 965 nm, which corresponds to a Fourier limit of 43 fs. Because this pulse travels through an additional 11 mm of BBO compared to the main pulse, it will be chirped to about 55 fs when the main pulse is properly compressed. As this pulse is longer than the SHG pump pulse of the OPAC, the contrast of the DIR peak compared to the fluorescence background is realistic, i.e. no correction factor is required in this case. This implies that the present DIR pulse has a peak intensity of less than 1% of the main pulse. However, since it is longer than the main pulse, the total energy content of this DIR pulse is estimated to be about 5%. This DIR pulse energy can be decreased by delaying the seed pulse with respect to the pump, but the present configuration in which the seed pulse timing is set more towards the front of the pump pulse is highly beneficial for the pre-pulse contrast. In figure 8.7, a small pre-pulse might also be expected due to the cross-correlation of the SHG of this DIR pulse with the fundamental of the main peak. However, since the spectrum around 965 nm of the DIR pulse is not phase-matched for frequency doubling in the OPAC SHG crystal, such a pre-pulse is not detected.

Taking the aforementioned correction factor of 5 into account, the observed fluorescence background reaches a maximum value of about 4×10^{-7} , but only after the main pulse. The fluorescence level preceding the pulse reaches 2×10^{-8} , and stays below the detection limit of 2×10^{-10} until the onset of the pump pulse at -28 ps. As the shape of the amplified spectrum (see figure 8.2) displays the steep edges that are typical for a saturated NOPCPA system, the corresponding pulse in the time domain has some sidebands that rapidly decay in intensity [233]. Therefore, the measured pre-pulse contrast of 2×10^{-8} will only be reached at times >600 fs before the main pulse. Due to the measurement uncertainty and the required correction factor, the accuracy of the present pulse contrast determination is estimated to be about a factor of 2. The integrated fluorescence background from the measurement shown in figure 8.7 is found to be $\sim 0.1\%$ of the main pulse energy, which is in fair agreement with the measured value of 0.2% total integrated fluorescence deduced earlier. The presently achieved pulse contrast constitutes an improvement of more than three orders of magnitude over previously published results on the pulse contrast of a short-pulse NOPCPA system [232]. It is interesting to note that even though the measured contrast is comparable to typical Ti:sapphire multi-pass amplifiers, in an NOPCPA system the fluorescence is only present for the duration of the pump pulse, which is orders of magnitude shorter than the inversion lifetime of Ti:sapphire. Therefore, the total integrated fluorescence energy can be small in comparison.

The possibility of replica pulses produced by the SLM [234] has been investigated as well by repeating the contrast measurement with a large linear phase pattern applied to the pulse shaper. No additional peak structure related to the SLM could be observed within the measurement sensitivity. This can be explained by the large spectral bandwidth of the pulses, leading to a significant “nonlinear spectral dispersion” [234] as the frequency components are not linearly spread across the SLM pixels. Any replica pulse generated by pixelation and phase-wrapping errors of the SLM will therefore be chirped to a duration of several picoseconds, leading to a strong decrease in the replica pulse intensity. In addition, the SLM is used in a double-pass configuration. This means that the phase mask steps are halved compared to single-pass implementations, and also that subtle alignment variations between the two passes through the device induce smoothing of the diffracted spectrum, leading to a decrease in the intensity of possible replica pulses.

8.6 Conclusions and outlook

In conclusion, we have demonstrated the generation of 7.6 fs laser pulses (2.7 optical cycles) with a 2 terawatt peak intensity at 30 Hz repetition rate, based on non-collinear optical parametric chirped-pulse amplification. By using an ultra-broadband Ti:sapphire oscillator as the seed source, the full spectral gain bandwidth of the 532 nm pumped BBO-based NOPCPA could be utilized, leading to the direct amplification of 310 nm wide spectra to 30 mJ pulse energy. Stretching by a factor of $\sim 2 \times 10^3$ and near-Fourier-limited recompression of these ultra-broadband spectra is performed using a grating-based pulse stretcher with an LCD phase-shaper, and a grating-pair pulse compressor. Important system characteristics such as beam profile, intensity stability and pulse contrast have been investigated, and are found to be of good quality. The pre-pulse contrast reaches 2×10^{-8} on short timescales, and exceeds the 2×10^{-10} detection limit of our contrast measurement setup on timescales > 28 ps.

Due to the compactness of the setup, the absence of thermal effects, and the existing Nd:YAG laser technology, scaling of the intensity by orders of magnitude looks promising, which might allow the generation of sub-3-cycle pulses with an intensity approaching the 100 TW level.

For application to quantum-interference metrology in the VUV, the main subject of this thesis, the present system shows promising features as well. First of all, we [217] and other other groups [235, 236] have demonstrated carrier-envelope phase stability of NOPCPA systems. For the present TW system, such measurements have been per-

formed as well, showing a carrier-envelope phase stability better than $1/25^{\text{th}}$ of an optical cycle [237]. To amplify the pulse pairs that are required for direct frequency comb spectroscopy, two independently timed pump pulses are needed. These can be generated by splitting the pump pulse in two with a beamsplitter, sending one of the beams through a delay line and recombining both beams. Because the phase of the pump pulses is not transferred to the seed pulses but only to the idler pulses during the OPA interaction, this delay line does not need to be stabilized. Timing the pump pulses such that they coincide with two separate seed pulses will yield two high-power output pulses with a delay that can be varied with steps equal to the inverse of the seed pulse repetition rate. Such a double-pulse NOPCPA system has recently been realized in our lab, delivering pairs of TW pulses. The phase stability of these pulse pairs is under investigation, but it is expected to be better than that of the Ti:sapphire amplifier used in the experiments described in this thesis, as the OPA interaction is instantaneous.

With the NOPCPA system described in this chapter, a trial experiment on high-harmonic generation has already been performed. By focusing the TW pulses into an argon gas jet in vacuum, harmonics up to the 29^{th} order (30 nm) have been observed. Much higher harmonics were undoubtedly produced, but the normal-incidence monochromator used did not allow their detection. In principle, it should be possible to generate harmonics with wavelengths shorter than 1 nm with the pulses from our TW laser system.

The combination of the carrier-envelope stability of the NOPCPA system and its capability of efficient high-harmonic generation is very well suited for direct frequency comb spectroscopy. Thus in the near future the NOPCPA system will be put to use in experiments on helium, aimed at measuring one or more of the $1s^2 \ ^1S_0 \rightarrow 1snp \ ^1P_1$ transitions with an accuracy of about 500 kHz. Such a measurement will improve the accuracy of the ground state Lamb shift by a factor of a hundred, and will enable a stringent test of quantum electrodynamics once the theoretical calculations reach a similar precision. There is no direct need for TW peak power and sub-10 fs duration in such an experiment, but the bandwidth of the amplifier can easily be reduced by cutting away unwanted wavelengths in the stretcher. Minor adjustments of the stretching and compression can again ensure the right pulse length in the amplifier stages.

The next step would be the use of two separate regenerative amplifiers in the pump laser system that deliver independently timed pump pulses. With such an arrangement, delays longer than 10 μs will be possible, in principle allowing a resolution of the order of a kHz. This approach could be applied to perform spectroscopy on e.g. singly ionized helium.

Bibliography

- [1] *Comptes Rendus de la 13^e CGPM (1967/1968)* (1969).
- [2] *Comptes Rendus de la 17^e CGPM (1983)* (1984).
- [3] A. L. Schawlow and C. H. Townes. *Infrared and optical masers*. *Physical Review*, **112**, 1940 (1958). doi:10.1103/PhysRev.112.1940.
- [4] J. Hecht. *Beam: the race to make the laser*. *Optics and Photonics News*, **16**, 24 (2005).
- [5] T. H. Maiman. *Stimulated optical radiation in ruby*. *Nature*, **187**, 493 (1960). doi:10.1038/187493a0.
- [6] A. Javan, W. R. Bennett and D. R. Herriott. *Population inversion and continuous optical maser oscillation in a gas discharge containing a He-Ne mixture*. *Physical Review Letters*, **6**, 106 (1961). doi:10.1103/PhysRevLett.6.106.
- [7] A. Szöke and A. Javan. *Isotope shift and saturation behavior of the 1.15- μ transition of Ne*. *Physical Review Letters*, **10**, 521 (1963). doi:10.1103/PhysRevLett.10.521.
- [8] W. E. Lamb. *Theory of an optical maser*. *Physical Review*, **134**, A1429 (1964). doi:10.1103/PhysRev.134.A1429.
- [9] R. L. Barger and J. L. Hall. *Pressure shift and broadening of methane line at 3.39 μ studied by laser-saturated molecular absorption*. *Physical Review Letters*, **22**, 4 (1969). doi:10.1103/PhysRevLett.22.4.

BIBLIOGRAPHY

- [10] T. Hänsch, I. Shahin and A. Schawlow. *High-resolution saturation spectroscopy of the sodium D lines with a pulsed tunable dye laser*. Physical Review Letters, **27**, 707 (1971). doi:10.1103/PhysRevLett.27.707.
- [11] T. Hänsch and B. Couillaud. *Laser frequency stabilization by polarization spectroscopy of a reflecting reference cavity*. Optics Communications, **35**, 441 (1980).
- [12] R. Drever and J. Hall. *Laser phase and frequency stabilization using an optical resonator*. Applied Physics B, **31**, 97 (1983).
- [13] K. M. Evenson, J. S. Wells, F. R. Petersen, B. L. Danielson and G. W. Day. *Accurate frequencies of molecular transitions used in laser stabilization: the 3.39- μm transition in CH_4 and the 9.33- and 10.18- μm transitions in CO_2* . Applied Physics Letters, **22**, 192 (1973). doi:10.1063/1.1654607.
- [14] D. A. Jennings, C. R. Pollock, F. R. Petersen, R. E. Drullinger, K. M. Evenson, J. S. Wells, J. L. Hall and H. P. Layer. *Direct frequency measurement of the I_2 -stabilized He-Ne 473-THz (633-nm) laser*. Optics Letters, **8**, 136 (1983).
- [15] H. Schnatz, B. Lipphardt, J. Helmcke, F. Riehle and G. Zinner. *First phase-coherent frequency measurement of visible radiation*. Physical Review Letters, **76**, 18 (1996). doi:10.1103/PhysRevLett.76.18.
- [16] H. R. Telle, D. Meschede and T. W. Hänsch. *Realization of a new concept for visible frequency division: phase locking of harmonic and sum frequencies*. Optics Letters, **15**, 532 (1990).
- [17] T. Udem, A. Huber, B. Gross, J. Reichert, M. Prevedelli, M. Weitz and T. W. Hänsch. *Phase-coherent measurement of the hydrogen 1S-2S transition frequency with an optical frequency interval divider chain*. Physical Review Letters, **79**, 2646 (1997). doi:10.1103/PhysRevLett.79.2646.
- [18] J. E. Bernard, A. A. Madej, L. Marmet, B. G. Whitford, K. J. Siemsen and S. Cundy. *Cs-based frequency measurement of a single, trapped ion transition in the visible region of the spectrum*. Physical Review Letters, **82**, 3228 (1999). doi:10.1103/PhysRevLett.82.3228.
- [19] C. Schwob, L. Jozefowski, B. de Beauvoir, L. Hilico, F. Nez, L. Julien, F. Biraben, O. Acaf, J.-J. Zondy and A. Clairon. *Optical frequency measurement of the 2s-12d transitions in hydrogen and deuterium: Rydberg constant and Lamb shift determinations*. Physical Review Letters, **82**, 4960 (1999). doi:10.1103/PhysRevLett.82.4960.

- [20] D. Lee and N. Wong. *Tunable optical frequency division using a phase-locked optical parametric oscillator*. Optics Letters, **17**, 13 (1992).
- [21] R. DeVoe, C. Fabre, K. Jungmann, J. Hoffnagle and R. Brewer. *Precision optical-frequency-difference measurements*. Physical Review A, **37**, 1802 (1988).
- [22] M. Kourogi, K. Nakagawa and M. Ohtsu. *Wide-span optical frequency comb generator for accurate optical frequency difference measurement*. IEEE Journal of Quantum Electronics, **29**, 2693 (1993). doi:10.1109/3.250392.
- [23] L. R. Brothers, D. Lee and N. C. Wong. *Terahertz optical frequency comb generation and phase locking of an optical parametric oscillator at 665 GHz*. Optics Letters, **19**, 245 (1994).
- [24] A. Huber, T. Udem, B. Gross, J. Reichert, M. Kourogi, K. Pachucki, M. Weitz and T. Hänsch. *Hydrogen-deuterium 1S-2S isotope shift and the structure of the deuteron*. Physical Review Letters, **80**, 468 (1998). doi:10.1103/PhysRevLett.80.468.
- [25] T. Udem, J. Reichert, T. W. Hänsch and M. Kourogi. *Absolute optical frequency measurement of the cesium D_2 line*. Physical Review A, **62**, 031801 (2000). doi:10.1103/PhysRevA.62.031801.
- [26] T. Udem, J. Reichert, R. Holzwarth and T. W. Hänsch. *Absolute optical frequency measurement of the cesium D_1 line with a mode-locked laser*. Physical Review Letters, **82**, 3568 (1999). doi:10.1103/PhysRevLett.82.3568.
- [27] J. Reichert, R. Holzwarth, T. Udem and T. Hänsch. *Measuring the frequency of light with mode-locked lasers*. Optics Communications, **172**, 59 (1999).
- [28] S. A. Diddams, D. J. Jones, J. Ye, S. T. Cundiff, J. L. Hall, J. K. Ranka, R. S. Windeler, R. Holzwarth, T. Udem and T. W. Hänsch. *Direct link between microwave and optical frequencies with a 300 Thz femtosecond laser comb*. Physical Review Letters, **84**, 5102 (2000).
- [29] D. J. Jones, S. A. Diddams, J. K. Ranka, A. Stentz, R. S. Windeler, J. L. Hall and S. T. Cundiff. *Carrier-envelope phase control of femtosecond mode-locked lasers and direct optical frequency synthesis*. Science, **288**, 635 (2000).
- [30] R. Holzwarth, T. Udem, T. W. Hänsch, J. C. Knight, W. J. Wadsworth and P. S. J. Russell. *Optical frequency synthesizer for precision spectroscopy*. Physical Review Letters, **85**, 2264 (2000).

BIBLIOGRAPHY

- [31] D. E. Spence, P. N. Kean and W. Sibbett. *60-fsec pulse generation from a self-mode-locked Ti:sapphire laser*. *Optics Letters*, **16**, 42 (1991).
- [32] M. Niering, R. Holzwarth, J. Reichert, P. Pokasov, T. Udem, M. Weitz, T. W. Hänsch, P. Lemonde, G. Santarelli, M. Abgrall, P. Laurent, C. Salomon and A. Clairon. *Measurement of the hydrogen 1S-2S transition frequency by phase coherent comparison with a microwave cesium fountain clock*. *Physical Review Letters*, **84**, 5496 (2000).
- [33] S. Diddams, J. Ye and L. Hollberg. *Femtosecond Optical Frequency Comb: Principle, Operation, and Applications*, chapter Femtosecond Lasers for Optical Clocks and Low Noise Frequency Synthesis, pages 221–262. Springer US (2005). doi:10.1007/0-387-23791-7_9.
- [34] A. Bartels, C. W. Oates, L. Hollberg and S. A. Diddams. *Stabilization of femtosecond laser frequency combs with subhertz residual linewidths*. *Optics Letters*, **29**, 1081 (2004).
- [35] L.-S. Ma, Z. Bi, A. Bartels, L. Robertsson, M. Zucco, R. S. Windeler, G. Wilpers, C. Oates, L. Hollberg and S. A. Diddams. *Optical frequency synthesis and comparison with uncertainty at the 10^{-19} level*. *Science*, **303**, 1843 (2004). doi:10.1126/science.1095092.
- [36] L.-S. Ma, Z. Bi, A. Bartels, K. Kim, L. Robertsson, M. Zucco, R. S. Windeler, G. Wilpers, C. Oates, L. Hollberg and S. A. Diddams. *Frequency uncertainty for optically referenced femtosecond laser frequency combs*. *IEEE Journal of Quantum Electronics*, **43**, 139 (2007).
- [37] B. R. Washburn, S. A. Diddams, N. R. Newbury, J. W. Nicholson, M. F. Yan and C. G. Jorgensen. *Phase-locked, erbium-fiber-laser-based frequency comb in the near infrared*. *Optics Letters*, **29**, 250 (2004).
- [38] H. S. Margolis, G. P. Barwood, G. Huang, H. A. Klein, S. N. Lea, K. Szymaniec and P. Gill. *Hertz level measurement of the optical clock frequency in a single $^{88}\text{Sr}^+$ ion*. *Science*, **306**, 1355 (2004). doi:10.1126/science.1105497.
- [39] W. H. Oskay, S. A. Diddams, E. A. Donley, T. M. Fortier, T. P. Heavner, L. Hollberg, W. M. Itano, S. R. Jefferts, M. J. Delaney, K. Kim, F. Levi, T. E. Parker and J. C. Bergquist. *Single-atom optical clock with high accuracy*. *Physical Review Letters*, **97**, 020801 (2006).

- [40] R. L. Targat, X. Baillard, M. Fouche, A. Bruschi, O. Tcherbakoff, G. D. Rovera and P. Lemonde. *Accurate optical lattice clock with ^{87}Sr atoms*. Physical Review Letters, **97**, 130801 (2006).
- [41] J. von Zanthier, T. Becker, M. Eichenseer, A. Y. Nevsky, C. Schwedes, E. Peik, H. Walther, R. Holzwarth, J. Reichert, T. Udem, T. W. Hänsch, P. V. Pokasov, M. N. Skvortsov and S. N. Bagayev. *Absolute frequency measurement of the In^+ clock transition with a mode-locked laser*. Optics Letters, **25**, 1729 (2000).
- [42] P. Schmidt, T. Rosenband, C. Langer, W. Itano, J. Bergquist and D. Wineland. *Spectroscopy using quantum logic*. Science, **309**, 749 (2005). doi:10.1126/science.1114375.
- [43] T. Rosenband, P. Schmidt, D. Hume, W. Itano, T. Fortier, J. Stalnaker, K. Kim, S. Diddams, J. Koelemeij, J. Bergquist and D. Wineland. *Observation of the $^1\text{S}_0 \rightarrow ^3\text{P}_0$ clock transition in $^{27}\text{Al}^+$* . Physical Review Letters, **98**, 220801 (2007). doi:10.1103/PhysRevLett.98.220801.
- [44] P. A. M. Dirac. *The quantum theory of the electron*. Proceedings of the Royal Society of London. Series A, Containing Papers of a Mathematical and Physical Character, **117**, 610 (1928). ISSN 0950-1207.
- [45] P. A. M. Dirac. *The quantum theory of the electron. Part II*. Proceedings of the Royal Society of London. Series A, Containing Papers of a Mathematical and Physical Character, **118**, 351 (1928). ISSN 0950-1207.
- [46] W. E. Lamb and R. C. Retherford. *Fine structure of the hydrogen atom by a microwave method*. Physical Review, **72**, 241 (1947). doi:10.1103/PhysRev.72.241.
- [47] W. E. Lamb and R. C. Retherford. *Fine structure of the hydrogen atom. Part I*. Physical Review, **79**, 549 (1950). doi:10.1103/PhysRev.79.549.
- [48] S. G. Karshenboim. *Precision physics of simple atoms: QED tests, nuclear structure and fundamental constants*. Physics Reports, **422**, 1 (2005). doi:10.1016/j.physrep.2005.08.008.
- [49] R. Rosenfelder. *Coulomb corrections to elastic electron - proton scattering and the proton charge radius*. Physics Letters B, **479**, 381 (2000). doi:10.1016/S0370-2693(00)00316-6.

BIBLIOGRAPHY

- [50] F. Kottmann, W. Amir, F. Biraben, C. A. N. Conde, S. Dhawan, T. W. Hänsch, F. J. Hartmann, V. W. Hughes, O. Huot, P. Indelicato, L. Julien, P. Knowles, S. Kazamias, Y.-W. Liu, F. Mulhauser, F. Nez, R. Pohl, P. Rabinowitz, J. M. F. dos Santos, L. A. Schaller, H. Schneuwly, W. Schott, D. Taqqu and J. F. C. A. Veloso. *The muonic hydrogen Lamb shift experiment at PSI*. *Hyperfine Interactions*, **138**, 55 (2001). doi:10.1023/A:1020886314237.
- [51] K. Pachucki and U. D. Jentschura. *Two-loop Bethe-logarithm correction in hydrogenlike atoms*. *Physical Review Letters*, **91**, 113005 (2003). doi:10.1103/PhysRevLett.91.113005.
- [52] K. Pachucki. *$\alpha^4 R$ corrections to singlet states of helium*. *Physical Review A (Atomic, Molecular, and Optical Physics)*, **74**, 022512 (2006). doi:10.1103/PhysRevA.74.022512.
- [53] B. de Beauvoir, F. Nez, L. Julien, B. Cagnac, F. Biraben, D. Touahri, L. Hilico, O. Acef, A. Clairon and J. J. Zondy. *Absolute frequency measurement of the $2S$ - $8S/D$ transitions in hydrogen and deuterium: New determination of the Rydberg constant*. *Physical Review Letters*, **78**, 440 (1997). doi:10.1103/PhysRevLett.78.440.
- [54] B. de Beauvoir, C. Schwob, O. Acef, L. Jozefowski, L. Hilico, F. Nez, L. Julien, A. Clairon and F. Biraben. *Metrology of the hydrogen and deuterium atoms: Determination of the Rydberg constant and Lamb shifts*. *European Journal of Physics D*, **12**, 61 (2000). doi:10.1007/s100530070043.
- [55] S. D. Bergeson, A. Balakrishnan, K. G. H. Baldwin, T. B. Lucatorto, J. P. Marangos, T. J. McIlrath, T. R. O'Brian, S. L. Rolston, C. J. Sansonetti, J. Wen, N. Westbrook, C. H. Cheng and E. E. Eyler. *Measurement of the He ground state Lamb shift via the two-photon 1^1S - 2^1S transition*. *Physical Review Letters*, **80**, 3475 (1998). doi:10.1103/PhysRevLett.80.3475.
- [56] K. S. E. Eikema, W. Ubachs, W. Vassen and W. Hogervorst. *Lamb shift measurement in the 1^1S ground state of helium*. *Physical Review A (Atomic, Molecular, and Optical Physics)*, **55**, 1866 (1997). doi:10.1103/PhysRevA.55.1866.
- [57] S. Bourzeix, B. de Beauvoir, F. Nez, M. D. Plimmer, F. de Tomasi, L. Julien, F. Biraben and D. N. Stacey. *High resolution spectroscopy of the hydrogen atom: Determination of the $1S$ Lamb shift*. *Physical Review Letters*, **76**, 384 (1996). doi:10.1103/PhysRevLett.76.384.

- [58] M. Weitz, A. Huber, F. Schmidt-Kaler, D. Leibfried, W. Vassen, C. Zimmermann, K. Pachucki, T. W. Hänsch, L. Julien and F. Biraben. *Precision measurement of the 1S ground-state Lamb shift in atomic hydrogen and deuterium by frequency comparison*. Physical Review A, **52**, 2664 (1995). doi:10.1103/PhysRevA.52.2664.
- [59] X. Calmet and H. Fritzsch. *Symmetry breaking and time variation of gauge couplings*. Physics Letters B, **540**, 173 (2002). doi:10.1016/S0370-2693(02)02147-0.
- [60] J.-P. Uzan. *The fundamental constants and their variation: observational and theoretical status*. Reviews of Modern Physics, **75**, 403 (2003).
- [61] M. Fischer, N. Kolachevsky, M. Zimmermann, R. Holzwarth, T. Udem, T. W. Hänsch, M. Abgrall, J. Grunert, I. Maksimovic, S. Bize, H. Marion, F. P. D. Santos, P. Lemonde, G. Santarelli, P. Laurent, A. Clairon, C. Salomon, M. Haas, U. D. Jentschura and C. H. Keitel. *New limits on the drift of fundamental constants from laboratory measurements*. Physical Review Letters, **92**, 230802 (2004).
- [62] E. Peik, B. Lipphardt, H. Schnatz, T. Schneider, C. Tamm and S. G. Karshenboim. *Limit on the present temporal variation of the fine structure constant*. Physical Review Letters, **93**, 170801 (2004).
- [63] K. Eikema, J. Walz and T. Hänsch. *Continuous coherent Lyman- α excitation of atomic hydrogen*. Physical Review Letters, **86**, 5679 (2001). doi:10.1103/PhysRevLett.86.5679.
- [64] N. F. Ramsey. *A new molecular beam resonance method*. Physical Review, **76**, 996 (1949). doi:10.1103/PhysRev.76.996.
- [65] N. F. Ramsey. *A molecular beam resonance method with separated oscillating fields*. Physical Review, **78**, 695 (1950). doi:10.1103/PhysRev.78.695.
- [66] J. C. Bergquist, S. A. Lee and J. L. Hall. *Saturated absorption with spatially separated laser fields: Observation of optical "Ramsey" fringes*. Physical Review Letters, **38**, 159 (1977). doi:10.1103/PhysRevLett.38.159.
- [67] M. M. Salour and C. Cohen-Tannoudji. *Observation of Ramsey's interference fringes in the profile of Doppler-free two-photon resonances*. Physical Review Letters, **38**, 757 (1977). doi:10.1103/PhysRevLett.38.757.

BIBLIOGRAPHY

- [68] Y. V. Baklanov and V. P. Chebotaev. *Narrow resonances of two-photon absorption of super-narrow pulses in a gas*. Applied Physics A: Materials Science & Processing, **12**, 97 (1977).
- [69] R. Teets, J. Eckstein and T. W. Hänsch. *Coherent two-photon excitation by multiple light pulses*. Physical Review Letters, **38**, 760 (1977). doi:10.1103/PhysRevLett.38.760.
- [70] M. M. Salour. *Quantum interference effects in two-photon spectroscopy*. Reviews of Modern Physics, **50**, 667 (1978). doi:10.1103/RevModPhys.50.667.
- [71] J. N. Eckstein, A. I. Ferguson and T. W. Hänsch. *High-resolution two-photon spectroscopy with picosecond light pulses*. Physical Review Letters, **40**, 847 (1978). doi:10.1103/PhysRevLett.40.847.
- [72] M. J. Snadden, A. S. Bell, E. Riis and A. I. Ferguson. *Two-photon spectroscopy of laser-cooled Rb using a mode-locked laser*. Optics Communications, **125**, 70 (1996).
- [73] M. Bellini, A. Bartoli and T. W. Hänsch. *Two-photon fourier spectroscopy with femtosecond light pulses*. Optics Letters, **22**, 540 (1997).
- [74] T. H. Yoon, A. Marian, J. L. Hall and J. Ye. *Phase-coherent multilevel two-photon transitions in cold Rb atoms: Ultrahigh-resolution spectroscopy via frequency-stabilized femtosecond laser*. Physical Review A (Atomic, Molecular, and Optical Physics), **63**, 011402 (2001).
- [75] D. Felinto, C. A. C. Bosco, L. H. Acioli and S. S. Vianna. *Accumulative effects in temporal coherent control*. Physical Review A, **64**, 063413 (2001). doi:10.1103/PhysRevA.64.063413.
- [76] D. Felinto, C. A. C. Bosco, L. H. Acioli and S. S. Vianna. *Coherent accumulation in two-level atoms excited by a train of ultrashort pulses*. Optics Communications, **215**, 69 (2003). doi:10.1016/S0030-4018(02)02230-7.
- [77] D. Felinto, L. H. Acioli and S. S. Vianna. *Accumulative effects in the coherence of three-level atoms excited by femtosecond-laser frequency combs*. Physical Review A, **70**, 043403 (2004). doi:10.1103/PhysRevA.70.043403.
- [78] A. Marian, M. C. Stowe, J. R. Lawall, D. Felinto and J. Ye. *United time-frequency spectroscopy for dynamics and global structure*. Science, **306**, 2063 (2004).

- [79] A. Marian, M. C. Stowe, D. Felinto and J. Ye. *Direct frequency comb measurements of absolute optical frequencies and population transfer dynamics*. Physical Review Letters, **95**, 023001 (2005).
- [80] P. Fendel, S. Bergeson, T. Udem and T. Hänsch. *Two-photon frequency comb spectroscopy of the 6s-8s transition in cesium*. Optics Letters, **32**, 701 (2007).
- [81] N. Vujičić, S. Vdović, D. Aumiler, T. Ban, H. Skenderović and G. Pichler. *Femtosecond laser pulse train effect on Doppler profile of cesium resonance lines*. The European Physical Journal D, **41**, 447 (2007). doi:10.1140/epjd/e2006-00261-5.
- [82] T. M. Fortier, Y. L. Coq, J. E. Stalnaker, D. Ortega, S. A. Diddams, C. W. Oates and L. Hollberg. *Kilohertz-resolution spectroscopy of cold atoms with an optical frequency comb*. Physical Review Letters, **97**, 163905 (2006). doi:10.1103/PhysRevLett.97.163905.
- [83] J. E. Stalnaker, Y. L. Coq, T. M. Fortier, S. A. Diddams, C. W. Oates and L. Hollberg. *Measurement of excited-state transitions in cold calcium atoms by direct femtosecond frequency-comb spectroscopy*. Physical Review A (Atomic, Molecular, and Optical Physics), **75**, 040502 (2007). doi:10.1103/PhysRevA.75.040502.
- [84] P. Fendel. *Präzisionsspektroskopie an Wasserstoff und Deuterium*. Ph.D. thesis, Ludwig-Maximilians-Universität München (2005).
- [85] P. A. Franken, A. E. Hill, C. W. Peters and G. Weinreich. *Generation of optical harmonics*. Physical Review Letters, **7**, 118 (1961). doi:10.1103/PhysRevLett.7.118.
- [86] M. Bass, P. A. Franken, A. E. Hill, C. W. Peters and G. Weinreich. *Optical mixing*. Physical Review Letters, **8**, 18 (1962). doi:10.1103/PhysRevLett.8.18.
- [87] J. A. Giordmaine. *Mixing of light beams in crystals*. Physical Review Letters, **8**, 19 (1962). doi:10.1103/PhysRevLett.8.19.
- [88] J. A. Armstrong, N. Bloembergen, J. Ducuing and P. S. Pershan. *Interactions between light waves in a nonlinear dielectric*. Physical Review, **127**, 1918 (1962).
- [89] R. Boyd. *Nonlinear optics*. Academic Press, Inc. (1992).
- [90] G. H. C. New and J. F. Ward. *Optical third-harmonic generation in gases*. Physical Review Letters, **19**, 556 (1967). doi:10.1103/PhysRevLett.19.556.

BIBLIOGRAPHY

- [91] N. H. Burnett, H. A. Baldis, M. C. Richardson and G. D. Enright. *Harmonic generation in CO₂ laser target interaction*. Applied Physics Letters, **31**, 172 (1977). doi:10.1063/1.89628.
- [92] A. McPherson, G. Gibson, H. Jara, U. Johann, T. S. Luk, I. A. McIntyre, K. Boyer and C. K. Rhodes. *Studies of multiphoton production of vacuum-ultraviolet radiation in the rare gases*. Journal of the Optical Society of America B, **4**, 595 (1987).
- [93] M. Ferray, A. L'Huillier, X. F. Li, L. A. Lompre, G. Mainfray and C. Manus. *Multiple-harmonic conversion of 1064 nm radiation in rare gases*. Journal of Physics B, **21**, L31 (1988). doi:10.1088/0953-4075/21/3/001.
- [94] P. B. Corkum. *Plasma perspective on strong field multiphoton ionization*. Physical Review Letters, **71**, 1994 (1993).
- [95] M. Lewenstein, P. Balcou, M. Y. Ivanov, A. L'Huillier and P. B. Corkum. *Theory of high-harmonic generation by low-frequency laser fields*. Physical Review A (Atomic, Molecular, and Optical Physics), **49**, 2117 (1994).
- [96] J. Seres, E. Seres, A. J. Verhoef, G. Tempea, C. Strelitz, P. Wobrauschek, V. Yakovlev, A. Scrinzi, C. Spielmann and F. Krausz. *Source of coherent kiloelectronvolt X-rays*. Nature, **433**, 596 (2005).
- [97] G. I. Stegeman, M. Sheik-Bahae, E. V. Stryland and G. Assanto. *Large nonlinear phase shifts in second-order nonlinear-optical processes*. Optics Letters, **18**, 13 (1993).
- [98] S. Gangopadhyay, N. Melikechi and E. E. Eyler. *Optical phase perturbations in nanosecond pulsed amplification and second-harmonic generation*. Journal of the Optical Society of America B, **11**, 231 (1994).
- [99] A. V. Smith and M. S. Bowers. *Phase distortions in sum- and difference-frequency mixing in crystals*. Journal of the Optical Society of America B, **12**, 49 (1995).
- [100] D. J. Armstrong, W. J. Alford, T. D. Raymond, A. V. Smith and M. S. Bowers. *Parametric amplification and oscillation with walkoff-compensating crystals*. Journal of the Optical Society of America B, **14**, 460 (1997).

- [101] R. DeSalvo, D. J. Hagan, M. Sheik-Bahae, G. I. Stegeman, E. W. V. Stryland and H. Vanherzeele. *Self-focusing and self-defocusing by cascaded second-order effects in KTP*. Optics Letters, **17**, 28 (1992).
- [102] C. Lyngå, M. B. Gaarde, C. Delfin, M. Bellini, T. W. Hänsch, A. L'Huillier and C.-G. Wahlström. *Temporal coherence of high-order harmonics*. Physical Review A (Atomic, Molecular, and Optical Physics), **60**, 4823 (1999).
- [103] H. J. Shin, D. G. Lee, Y. H. Cha, J.-H. Kim, K. H. Hong and C. H. Nam. *Nonadiabatic blueshift of high-order harmonics from Ar and Ne atoms in an intense femtosecond laser field*. Physical Review A, **63**, 053407 (2001). doi:10.1103/PhysRevA.63.053407.
- [104] A. Pirri, C. Corsi, E. Sali, A. Tortora and M. Bellini. *Interferometric measurement of the atomic dipole phase for the two electronic quantum paths generating high-order harmonics*. Laser Physics, **17**, 138 (2007).
- [105] M. Bellini, C. Lyngå, A. Tozzi, M. B. Gaarde, T. W. Hänsch, A. L'Huillier and C.-G. Wahlström. *Temporal coherence of ultrashort high-order harmonic pulses*. Physical Review Letters, **81**, 297 (1998).
- [106] R. Zerne, C. Altucci, M. Bellini, M. B. Gaarde, T. W. Hänsch, A. L'Huillier, C. Lyngå and C.-G. Wahlström. *Phase-locked high-order harmonic sources*. Physical Review Letters, **79**, 1006 (1997).
- [107] P. Salières, L. L. Deroff, T. Auguste, P. Monot, P. d'Oliveira, D. Campo, J.-F. Hergott, H. Merdji and B. Carre. *Frequency-domain interferometry in the XUV with high-order harmonics*. Physical Review Letters, **83**, 5483 (1999).
- [108] S. Cavalieri, R. Eramo, M. Materazzi, C. Corsi and M. Bellini. *Ramsey-type spectroscopy with high-order harmonics*. Physical Review Letters, **89**, 133002 (2002).
- [109] M. Kovačev, S. V. Fomichev, E. Priori, Y. Mairesse, H. Merdji, P. Monchicourt, P. Breger, J. Norin, A. Persson, A. L'Huillier, C.-G. Wahlström, B. Carré and P. Salières. *Extreme ultraviolet Fourier-transform spectroscopy with high order harmonics*. Physical Review Letters, **95**, 223903 (2005).
- [110] C. Gohle, T. Udem, M. Herrmann, J. Rauschenberger, R. Holzwarth, H. A. Schuessler, F. Krausz and T. W. Hänsch. *A frequency comb in the extreme ultraviolet*. Nature, **436**, 234 (2005). doi:10.1038/nature03851.

BIBLIOGRAPHY

- [111] R. Jones, K. Moll, M. Thorpe and J. Ye. *Phase-coherent frequency combs in the vacuum ultraviolet via high-harmonic generation inside a femtosecond enhancement cavity*. Physical Review Letters, **94**, 193201 (2005). doi: 10.1103/PhysRevLett.94.193201.
- [112] A. J. Verhoeef, J. Seres, K. Schmid, Y. Nomura, G. Tempea, L. Veisz and F. Krausz. *Compression of the pulses of a Ti:Sapphire laser system to 5 femtoseconds at 0.2 terawatt level*. Applied Physics B: Lasers and Optics, **82**, 513 (2006).
- [113] G. C. Bjorklund. *Effects of focusing on third-order nonlinear processes in isotropic media*. IEEE Journal of Quantum Electronics, **11**, 287 (1975).
- [114] K. J. Schafer, B. Yang, L. F. DiMauro and K. C. Kulander. *Above threshold ionization beyond the high harmonic cutoff*. Physical Review Letters, **70**, 1599 (1993). doi: 10.1103/PhysRevLett.70.1599.
- [115] J. G. Eden. *High-order harmonic generation and other intense optical field-matter interactions: review of recent experimental and theoretical advances*. Progress in Quantum Electronics, **28**, 197 (2004). doi:10.1016/j.pquantelec.2004.06.002.
- [116] M. Lewenstein, P. Salières and A. L'Huillier. *Phase of the atomic polarization in high-order harmonic generation*. Physical Review A, **52**, 4747 (1995). doi: 10.1103/PhysRevA.52.4747.
- [117] C. Kan, C. E. Capjack, R. Rankin and N. H. Burnett. *Spectral and temporal structure in high harmonic emission from ionizing atomic gases*. Physical Review A, **52**, R4336 (1995). doi:10.1103/PhysRevA.52.R4336.
- [118] C. Corsi, A. Pirri, E. Sali, A. Tortora and M. Bellini. *Direct interferometric measurement of the atomic dipole phase in high-order harmonic generation*. Physical Review Letters, **97**, 023901 (2006). doi:10.1103/PhysRevLett.97.023901.
- [119] P. F. Moulton. *Spectroscopic and laser characteristics of Ti:Al₂O₃*. Journal of the Optical Society of America B: Optical Physics, **3**, 125 (1986).
- [120] A. E. Siegman. *Lasers*. University Science Books (1986).
- [121] R. Szipöcs, K. Ferencz, C. Spielmann and F. Krausz. *Chirped multilayer coatings for broad-band dispersion control in femtosecond lasers*. Optics Letters, **19**, 201 (1994).

- [122] F. X. Kärtner, U. Morgner, R. Ell, T. Schibli, J. G. Fujimoto, E. P. Ippen, V. Scheuer, G. Angelow and T. Tschudi. *Ultrabroadband double-chirped mirror pairs for generation of octave spectra*. Journal of the Optical Society of America B, **18**, 882 (2001).
- [123] H. Telle, G. Steinmeyer, A. Dunlop, J. Stenger, D. Sutter and U. Keller. *Carrier-envelope offset phase control: A novel concept for absolute optical frequency measurement and ultrashort pulse generation*. Applied Physics B: Lasers and Optics, **69**, 327 (1999). doi:10.1007/s003409900148.
- [124] T. M. Fortier, J. Ye, S. T. Cundiff and R. S. Windeler. *Nonlinear phase noise generated in air silica microstructure fiber and its effect on carrier-envelope phase*. Optics Letters, **27**, 445 (2002).
- [125] T. M. Fortier, D. J. Jones, J. Ye, S. T. Cundiff and R. S. Windeler. *Long-term carrier-envelope phase coherence*. Optics Letters, **27**, 1436 (2002).
- [126] T. M. Fortier, D. J. Jones and S. T. Cundiff. *Phase stabilization of an octave-spanning Ti:sapphire laser*. Optics Letters, **28**, 2198 (2003).
- [127] T. Fuji, J. Rauschenberger, A. Apolonski, V. S. Yakovlev, G. Tempea, T. Udem, C. Gohle, T. W. Hänsch, W. Lehnert, M. Scherer and F. Krausz. *Monolithic carrier-envelope phase-stabilization scheme*. Optics Letters, **30**, 332 (2005).
- [128] S. Hannemann, E. J. Salumbides, S. Witte, R. T. Zinkstok, E.-J. van Duijn, K. S. E. Eikema and W. Ubachs. *Frequency metrology on the Mg $3s_2 \ ^1S \rightarrow 3s4p \ ^1P$ line for comparison with quasar data*. Physical Review A, **74**, 012505 (2006).
- [129] R. J. Jones, I. Thomann and J. Ye. *Precision stabilization of femtosecond lasers to high-finesse optical cavities*. Physical Review A (Atomic, Molecular, and Optical Physics), **69**, 051803 (2004). doi:10.1103/PhysRevA.69.051803.
- [130] T. Hänsch, J. Alnis, P. Fendel, M. Fischer, C. Gohle, M. Herrmann, R. Holzwarth, N. Kolachevsky, T. Udem and M. Zimmermann. *Precision spectroscopy of hydrogen and femtosecond laser frequency combs*. Philosophical Transactions of the Royal Society A: Mathematical, Physical and Engineering Sciences, **363**, 2155 (2005). doi:10.1098/rsta.2005.1639.
- [131] K. S. E. Eikema, J. Walz and T. W. Hänsch. *Continuous wave coherent Lyman- α radiation*. Physical Review Letters, **83**, 3828 (1999). doi:10.1103/PhysRevLett.83.3828.

BIBLIOGRAPHY

- [132] J. K. Ranka, R. S. Windeler and A. J. Stentz. *Visible continuum generation in air silica microstructure optical fibers with anomalous dispersion at 800 nm*. Optics Letters, **25**, 25 (2000).
- [133] S. A. Diddams, L. Hollberg, L.-S. Ma and L. Robertsson. *Femtosecond-laser-based optical clockwork with instability $\leq 6.3 \times 10^{-16}$ in 1 s*. Optics Letters, **27**, 58 (2002).
- [134] N. F. Ramsey. *Experiments with separated oscillatory fields and hydrogen masers*. Reviews of Modern Physics, **62**, 541 (1990). doi:10.1103/RevModPhys.62.541.
- [135] M. A. Kasevich, E. Riis, S. Chu and R. G. DeVoe. *RF spectroscopy in an atomic fountain*. Physical Review Letters, **63**, 612 (1989). doi:10.1103/PhysRevLett.63.612.
- [136] R. Loudon. *The Quantum Theory of Light*. Oxford University Press (2000).
- [137] C. Cohen-Tannoudji, B. Diu and F. Laloë. *Quantum Mechanics*. Herman, Paris (1977).
- [138] W. H. Press, S. A. Teukolsky, W. T. Vetterling and B. P. Flannery. *Numerical Recipes in C, second edition*. Cambridge University Press (1992).
- [139] R. C. Hilborn. *Einstein coefficients, cross sections, f values, dipole moments, and all that*. American Journal of Physics, **50**, 982 (1982).
- [140] K. Yoshino and D. E. Freeman. *Absorption spectrum of xenon in the vacuum-ultraviolet region*. Journal of the Optical Society of America B, **2**, 1268 (1985).
- [141] F. Riehle. *Frequency Standards*. Wiley-VCH Verlag (2004).
- [142] S. Hannemann, E. J. Salumbides and W. Ubachs. *Reducing first order Doppler shifts in a Sagnac interferometer*. Optics Letters (2007).
- [143] L. S. Vasilenko, V. P. Chebotayev and A. V. Shishaev. JETP Letters, **12**, 161 (1970).
- [144] F. Biraben, B. Cagnac and G. Grynberg. *Experimental evidence of two-photon transition without Doppler broadening*. Physical Review Letters, **32**, 643 (1974). doi:10.1103/PhysRevLett.32.643.
- [145] M. D. Levenson and N. Bloembergen. *Observation of two-photon absorption without Doppler broadening on the $3S-5S$ transition in sodium vapor*. Physical Review Letters, **32**, 645 (1974). doi:10.1103/PhysRevLett.32.645.

- [146] D. Budker, D. F. Kimball and D. P. DeMille. *Atomic Physics, an exploration through problems and solutions*. Oxford University Press (2004).
- [147] A. Yariv and P. Yeh. *Optical waves in crystals*. John Wiley & Sons (1984).
- [148] E. T. J. Nibbering, G. Grillon, M. A. Franco, B. S. Prade and A. Mysyrowicz. *Determination of the inertial contribution to the nonlinear refractive index of air, N₂, and O₂ by use of unfocused high-intensity femtosecond laser pulses*. Journal of the Optical Society of America B, **14**, 620 (1997).
- [149] R. W. Hellwarth, D. M. Pennington and M. A. Henesian. *Indices governing optical self-focusing and self-induced changes in the state of polarization in N₂, O₂, H₂, and Ar gases*. Physical Review A, **41**, 2766 (1990). doi:10.1103/PhysRevA.41.2766.
- [150] S. Carusotto, E. Iacopini, E. Polacco, F. Scuri, G. Stefanini and E. Zavattini. *Measurement of the Kerr constant of He, Ar, O₂, N₂, H₂, and D₂*. Nuovo Cimento D, **5**, 328 (1985).
- [151] M. J. Shaw and C. J. Hooker. *Measurement of the nonlinear refractive index of air and other gases at 248 nm*. Optics Communications, **103**, 153 (1993). doi:10.1016/0030-4018(93)90657-Q.
- [152] A. L'Huillier, P. Balcou, S. Candel, K. J. Schafer and K. C. Kulander. *Calculations of high-order harmonic-generation processes in xenon at 1064 nm*. Phys. Rev. A, **46**, 2778 (1992). doi:10.1103/PhysRevA.46.2778.
- [153] Z. Mics, F. Kadlec, P. Kužel, P. Jungwirth, S. E. Bradforth and V. A. Apkarian. *Non-resonant ionization of oxygen molecules by femtosecond pulses: Plasma dynamics studied by time-resolved terahertz spectroscopy*. Journal of Chemical Physics, **123**, 104310 (2005).
- [154] L. Belostotski, T. L. Landecker and D. Routledge. *Distance measurement with phase-stable CW radio link using the chinese remainder theorem*. Electronics Letters, **37**, 521 (2001).
- [155] L. Matos, D. Kleppner, O. Kuzucu, T. R. Schibli, J. Kim, E. P. Ippen and F. X. Kärtner. *Direct frequency comb generation from an octave-spanning, prismless Ti:sapphire laser*. Optics Letters, **29**, 1683 (2004). doi:10.1364/OL.29.001683.

BIBLIOGRAPHY

- [156] R. Ell, U. Morgner, F. X. Kärtner, J. G. Fujimoto, E. P. Ippen, V. Scheuer, G. Angelow, T. Tschudi, M. J. Lederer, A. Boiko and B. Luther-Davies. *Generation of 5-fs pulses and octave-spanning spectra directly from a Ti:sapphire laser*. Optics Letters, **26**, 373 (2001).
- [157] J. C. Knight, T. A. Birks, P. S. J. Russell and D. M. Atkin. *All-silica single-mode optical fiber with photonic crystal cladding*. Optics Letters, **21**, 1547 (1996).
- [158] P. Russell. *Photonic crystal fibers*. Science, **299**, 358 (2003).
- [159] J. M. Dudley, G. Genty and S. Coen. *Supercontinuum generation in photonic crystal fiber*. Reviews of Modern Physics, **78**, 1135 (2006). doi:10.1103/RevModPhys.78.1135.
- [160] J. Stenger and H. R. Telle. *Intensity-induced mode shift in a femtosecond laser by a change in the nonlinear index of refraction*. Optics Letters, **25**, 1553 (2000).
- [161] F. Helbing, G. Steinmeyer, J. Stenger, H. Telle and U. Keller. *Carrier envelope-offset dynamics and stabilization of femtosecond pulses*. Applied Physics B: Lasers and Optics, **74**, S35 (2002). doi:10.1007/s00340-002-0898-4.
- [162] M. Prevedelli, T. Freearge and T. Hänsch. *Phase locking of grating tuned diode lasers*. Applied Physics B: Lasers and Optics, **60**, S241 (1995).
- [163] M. Takeda, H. Ina and S. Kobayashi. *Fourier-transform method of fringe-pattern analysis for computer-based topography and interferometry*. Journal of the Optical Society of America, **72**, 156 (1982).
- [164] W. Rooijackers, W. Hogervorst and W. Vassen. *An intense collimated beam of metastable helium atoms by two-dimensional laser cooling*. Optics Communications, **123**, 321 (1996).
- [165] R. J. Cotter. *Time-of-flight mass spectrometry: instrumentation and applications in biological research*. An American Chemical Society Publication (1997).
- [166] G. Scoles (editor). *Atomic and molecular beam methods*, volume 1. Oxford University Press (1988).
- [167] G. Steinmeyer, D. Sutter, L. Gallmann, N. Matuschek and U. Keller. *Frontiers in ultrashort pulse generation: Pushing the limits in linear and nonlinear optics*. Science, **286**, 1507 (1999). doi:10.1126/science.286.5444.1507.

- [168] A. Baltuška, Z. Wei, M. Pshenichnikov, D. Wiersma and R. Szipőcs. *All-solid-state cavity-dumped sub-5-fs laser*. Applied Physics B: Lasers and Optics, **65**, 175 (1997). doi:10.1007/s003400050262.
- [169] V. Yakovlev, P. Dombi, G. Tempea, C. Lemell, J. Burgdörfer, T. Udem and A. Apolonski. *Phase-stabilized 4-fs pulses at the full oscillator repetition rate for a photoemission experiment*. Applied Physics B: Lasers and Optics, **76**, 329 (2003). doi:10.1007/s00340-003-1103-0.
- [170] T. Kobayashi and A. Shirakawa. *Tunable visible and near-infrared pulse generator in a 5 fs regime*. Applied Physics B: Lasers and Optics, **70**, S239 (2000). doi:10.1007/s003400000325.
- [171] T. Brabec and F. Krausz. *Intense few-cycle laser fields: Frontiers of nonlinear optics*. Reviews of Modern Physics, **72**, 545 (2000). doi:10.1103/RevModPhys.72.545.
- [172] A. Apolonski, A. Poppe, G. Tempea, C. Spielmann, T. Udem, R. Holzwarth, T. W. Hänsch and F. Krausz. *Controlling the phase evolution of few-cycle light pulses*. Physical Review Letters, **85**, 740 (2000).
- [173] U. Morgner, R. Ell, G. Metzler, T. R. Schibli, F. X. Kärtner, J. G. Fujimoto, H. A. Haus and E. P. Ippen. *Nonlinear optics with phase-controlled pulses in the sub-two-cycle regime*. Physical Review Letters, **86**, 5462 (2001). doi:10.1103/PhysRevLett.86.5462.
- [174] A. Baltuška, T. Fuji and T. Kobayashi. *Controlling the carrier-envelope phase of ultrashort light pulses with optical parametric amplifiers*. Physical Review Letters, **88**, 133901 (2002). doi:10.1103/PhysRevLett.88.133901.
- [175] G. G. Paulus, F. Grasbon, H. Walther, P. Villoresi, M. Nisoli, S. Stagira, E. Priori and S. D. Silvestri. *Absolute-phase phenomena in photoionization with few-cycle laser pulses*. Nature, **414**, 182 (2001).
- [176] A. Baltuška, T. Udem, M. Uiberacker, M. Hentschel, E. Goulielmakis, C. Gohle, R. Holzwarth, V. S. Yakovlev, A. Scrinzi, T. W. Hänsch and F. Krausz. *Attosecond control of electronic processes by intense light fields*. Nature, **421**, 611 (2003).
- [177] R. Shelton, L. Ma, H. Kapteyn, M. Murnane, J. Hall and J. Ye. *Phase-coherent optical pulse synthesis from separate femtosecond lasers*. Science, **293**, 1286 (2001). doi:10.1126/science.1061754.

BIBLIOGRAPHY

- [178] J. Ye, S. Cundiff, S. Foreman, T. Fortier, J. Hall, K. Holman, D. Jones, J. Jost, H. Kapteyn, K. V. Leeuwen, L. Ma, M. Murnane, J. Peng and R. Shelton. *Phase-coherent synthesis of optical frequencies and waveforms*. Applied Physics B: Lasers and Optics, **74**, S27 (2002). doi:10.1007/s00340-002-0905-9.
- [179] M. Drescher, M. Hentschel, R. Kienberger, G. Tempea, C. Spielmann, G. A. Reider, P. B. Corkum and F. Krausz. *X-ray pulses approaching the attosecond frontier*. Science, **291**, 1923 (2001). doi:10.1126/science.1058561.
- [180] M. Hentschel, R. Kienberger, C. Spielmann, G. Reider, N. Milosevic, T. Brabec, P. Corkum, U. Heinzmann, M. Drescher and F. Krausz. *Attosecond metrology*. Nature, **414**, 509 (2001).
- [181] A. Poppe, R. Holzwarth, A. Apolonski, G. Tempea, C. Spielmann, T. Hänsch and F. Krausz. *Few-cycle optical waveform synthesis*. Applied Physics B: Lasers and Optics, **72**, 373 (2001). doi:10.1007/s003400000526.
- [182] L. Xu, C. Spielmann, A. Poppe, T. Brabec, F. Krausz and T. W. Hansch. *Route to phase control of ultrashort light pulses*. Optics Letters, **21**, 2008 (1996).
- [183] K. W. Holman, R. J. Jones, A. Marian, S. T. Cundiff and J. Ye. *Intensity-related dynamics of femtosecond frequency combs*. Optics Letters, **28**, 851 (2003).
- [184] K. W. Holman, R. J. Jones, A. Marian, S. T. Cundiff and J. Ye. *Detailed studies and control of intensity-related dynamics of femtosecond frequency combs from mode-locked Ti:Sapphire lasers*. IEEE Journal of Selected Topics in Quantum Electronics, **9**, 1018 (2003). doi:10.1109/JSTQE.2003.819098.
- [185] A. J. Taylor, G. Rodriguez and T. S. Clement. *Determination of n_2 by direct measurement of the optical phase*. Optics Letters, **21**, 1812 (1996).
- [186] T. M. Fortier, D. J. Jones, J. Ye and S. T. Cundiff. *Highly phase stable mode-locked lasers*. IEEE Journal of Selected Topics in Quantum Electronics, **9**, 1002 (2003).
- [187] R. J. Jones. Private communication (2003).
- [188] R. Scott, C. Langrock and B. Kolner. *High-dynamic-range laser amplitude and phase noise measurement techniques*. IEEE Journal of Selected Topics in Quantum Electronics, **7**, 641 (2001). doi:10.1109/2944.974236.

- [189] D. von der Linde. *Characterization of the noise in continuously operating mode-locked lasers*. Applied Physics B: Lasers and Optics, **39**, 201 (1986). doi:10.1007/BF00697487.
- [190] M. Aoyama and K. Yamakawa. *Noise characterization of an all-solid-state mirror-dispersion-controlled 10-fs Ti:sapphire laser*. Optics Communications, **140**, 255 (1997). doi:10.1016/S0030-4018(97)00200-9.
- [191] A. Poppe, L. Xu, F. Krausz and C. Spielmann. *Noise characterization of sub-10-fs Ti:sapphire oscillators*. IEEE Journal of Selected Topics in Quantum Electronics, **4**, 179 (1998). doi:10.1109/2944.686721.
- [192] D. W. Allan. *Statistics of atomic frequency standards*. Proceedings of the IEEE, **54**, 221 (1966).
- [193] A. G. Kostenbauder. *Ray-pulse matrices: a rational treatment for dispersive optical systems*. IEEE Journal of Quantum Electronics, **26**, 1148 (1990). doi:10.1109/3.108113.
- [194] D. Strickland and G. Mourou. *Compression of amplified chirped optical pulses*. Optics Communications, **56**, 219 (1985).
- [195] T. Udem, R. Holzwarth and T. W. Hänsch. *Optical frequency metrology*. Nature, **416**, 233 (2002).
- [196] T. Udem, S. A. Diddams, K. R. Vogel, C. W. Oates, E. A. Curtis, W. D. Lee, W. M. Itano, R. E. Drullinger, J. C. Bergquist and L. Hollberg. *Absolute frequency measurements of the Hg^+ and Ca optical clock transitions with a femtosecond laser*. Physical Review Letters, **86**, 4996 (2001).
- [197] A. Clairon, C. Salomon, S. Guellati and W. D. Phillips. *Ramsey resonance in a Zacharias fountain*. Europhysics Letters, **16**, 165 (1991).
- [198] S. Witte, R. T. Zinkstok, W. Hogervorst and K. S. E. Eikema. *Control and precise measurement of carrier-envelope phase dynamics*. Applied Physics B: Lasers and Optics, **78**, 5 (2004). doi:10.1007/s00340-003-1307-3.
- [199] V. Kaufman. *Wavelengths and energy-levels of neutral Kr-84 and level shifts in all Kr even isotopes*. Journal of Research of the National Institute of Standards and Technology, **98**, 717 (1993).

BIBLIOGRAPHY

- [200] F. Brandi, W. Hogervorst and W. Ubachs. *High-resolution vacuum-ultraviolet and ultraviolet photoionization spectroscopy of krypton*. Journal of Physics B: Atomic, Molecular and Optical Physics, **35**, 1071 (2002).
- [201] V. Kaufman and C. J. Humphreys. *Accurate energy levels and calculated wavelengths of ^{86}Kr I*. Journal of the Optical Society of America, **59**, 1614 (1969).
- [202] T. Trickl, M. J. J. Vrakking, E. Cromwell, Y. T. Lee and A. H. Kung. *Ultra-high-resolution (1+1) photoionization spectroscopy of Kr I: Hyperfine structures, isotope shifts, and lifetimes for the $n=5,6,7$ $4p^5$ ns Rydberg levels*. Physical Review A, **39**, 2948 (1989). doi:10.1103/PhysRevA.39.2948.
- [203] T. Trickl, A. H. Kung and Y. T. Lee. *Krypton atom and testing the limits of extreme-ultraviolet tunable-laser spectroscopy*. Physical Review A (Atomic, Molecular, and Optical Physics), **75**, 022501 (2007). doi:10.1103/PhysRevA.75.022501.
- [204] M. Takamoto, F.-L. Hong, R. Higashi and H. Katori. *An optical lattice clock*. Nature, **435**, 321 (2005). doi:10.1038/nature03541.
- [205] S. A. Diddams, J. C. Bergquist, S. R. Jefferts and C. W. Oates. *Standards of time and frequency at the outset of the 21st century*. Science, **306**, 1318 (2004).
- [206] S. Witte, R. T. Zinkstok, W. Ubachs, W. Hogervorst and K. S. E. Eikema. *Deep-ultraviolet quantum interference metrology with ultrashort laser pulses*. Science, **307**, 400 (2005). doi:10.1126/science.1106612.
- [207] A. V. Loginov and P. F. Gruzdev. *Radiation lifetimes of xenon levels*. Optical Spectroscopy, **41**, 104 (1976).
- [208] D. A. Jackson, M.-C. Coulombe and J. Bauche. *Interpretation of the isotope shifts in the arc spectrum of xenon*. Proceedings of the Royal Society of London. Series A, Mathematical and Physical Sciences, **343**, 443 (1975).
- [209] M. Plimmer, P. Baird, C. Foot, D. Stacey, J. Swan and G. Woodgate. *Isotope shift in xenon by Doppler-free two-photon laser spectroscopy*. Journal of Physics B, **22**, L241 (1989).
- [210] T. A. Paul and F. Merkt. *High-resolution spectroscopy of xenon using a tunable Fourier-transform-limited all-solid-state vacuum-ultraviolet laser system*. Journal of Physics B: Atomic, Molecular and Optical Physics, **38**, 4145 (2005). doi:10.1088/0953-4075/38/22/017.

- [211] A. Scrinzi, M. Y. Ivanov, R. Kienberger and D. M. Villeneuve. *Attosecond physics*. Journal of Physics B: Atomic, Molecular and Optical Physics, **39**, R1 (2006).
- [212] H. Niikura, D. M. Villeneuve and P. B. Corkum. *Controlling vibrational wave packets with intense, few-cycle laser pulses*. Physical Review A (Atomic, Molecular, and Optical Physics), **73**, 021402 (2006).
- [213] A. Dubietis, G. Jonušauskas and A. Piskarskas. *Powerful femtosecond pulse generation by chirped and stretched pulse parametric amplification in BBO crystal*. Optics Communications, **88**, 437 (1992). doi:10.1016/0030-4018(92)90070-8.
- [214] I. N. Ross, P. Matousek, M. Towrie, A. J. Langley and J. L. Collier. *The prospects for ultrashort pulse duration and ultrahigh intensity using optical parametric chirped pulse amplifiers*. Optics Communications, **144**, 125 (1997).
- [215] I. N. Ross, J. L. Collier, P. Matousek, C. N. Danson, D. Neely, R. M. Allott, D. A. Pepler, C. Hernandez-Gomez and K. Osvay. *Generation of terawatt pulses by use of optical parametric chirped pulse amplification*. Applied Optics, **39**, 2422 (2000).
- [216] V. V. Lozhkarev, G. I. Freidman, V. N. Ginzburg, E. V. Katin, E. A. Khazanov, A. V. Kirsanov, G. A. Luchinin, A. N. Mal'shakov, M. A. Martyanov, O. V. Palashov, A. K. Poteomkin, A. M. Sergeev, A. A. Shaykin, I. V. Yakovlev, S. G. Garanin, S. A. Sukharev, N. N. Rukavishnikov, A. V. Charukhchev, R. R. Gerke and V. E. Yashin. *200 TW 45 fs laser based on optical parametric chirped pulse amplification*. Optics Express, **14**, 446 (2006).
- [217] R. Zinkstok, S. Witte, W. Hogervorst and K. Eikema. *High-power parametric amplification of 11.8-fs laser pulses with carrier-envelope phase control*. Optics Letters, **30**, 78 (2005).
- [218] S. Witte, R. T. Zinkstok, W. Hogervorst and K. S. E. Eikema. *Generation of few-cycle terawatt light pulses using optical parametric chirped pulse amplification*. Optics Express, **13**, 4903 (2005).
- [219] N. Ishii, L. Turi, V. S. Yakovlev, T. Fuji, F. Krausz, A. Baltuška, R. Butkus, G. Veitas, V. Smilgevicius, R. Danielius and A. Piskarskas. *Multimillijoule chirped parametric amplification of few-cycle pulses*. Optics Letters, **30**, 567 (2005).
- [220] T. Fuji, N. Ishii, C. Y. Teisset, X. Gu, T. Metzger, A. Baltuška, N. Forget, D. Kaplan, A. Galvanauskas and F. Krausz. *Parametric amplification of few-cycle carrier-envelope phase-stable pulses at 2.1 μm* . Optics Letters, **31**, 1103 (2006).

BIBLIOGRAPHY

- [221] D. Kraemer, R. Hua, M. L. Cowan, K. Franjic and R. J. D. Miller. *Ultrafast noncollinear optical parametric chirped pulse amplification in KTiOAsO_4* . Optics Letters, **31**, 981 (2006).
- [222] I. Ross, P. Matousek, G. New and K. Osvay. *Analysis and optimization of optical parametric chirped pulse amplification*. Journal of the Optical Society of America B, **19**, 2945 (2002).
- [223] X. Yang, Z. Xu, Z. Zhang, Y. Leng, J. Peng, J. Wang, S. Jin, W. Zhang and R. Li. *Dependence of spectrum on pump-signal angle in BBO-I noncollinear optical-parametric chirped-pulse amplification*. Applied Physics B: Lasers and Optics, **73**, 219 (2001). doi:10.1007/s003400100630.
- [224] J. H. Sung, J. Y. Park, T. Imran, Y. S. Lee and C. H. Nam. *Generation of 0.2-TW 5.5-fs optical pulses at 1 kHz using a differentially pumped hollow-fiber chirped-mirror compressor*. Applied Physics B: Lasers and Optics, **82**, 5 (2006).
- [225] G. Stibenz, N. Zhavoronkov and G. Steinmeyer. *Self-compression of millijoule pulses to 7.8 fs duration in a white-light filament*. Optics Letters, **31**, 274 (2006).
- [226] R. A. Baumgartner and R. L. Byer. *Optical parametric amplification*. IEEE Journal of Quantum Electronics, **15**, 432 (1979).
- [227] H. Takada and K. Torizuka. *Design and construction of a TW-class 12-fs Ti:Sapphire chirped-pulse amplification system*. IEEE Journal of Selected Topics in Quantum Electronics, **12**, 201 (2006).
- [228] Z. Cheng, F. Krausz and C. Spielmann. *Compression of 2 mJ kilohertz laser pulses to 175 fs by pairing double-prism compressor: analysis and performance*. Optics Communications, **201**, 145 (2002).
- [229] A. Präkelt, M. Wollenhaupt, A. Assion, C. Horn, C. Sarpe-Tudoran, M. Winter and T. Baumert. *Compact, robust, and flexible setup for femtosecond pulse shaping*. Review of Scientific Instruments, **74**, 4950 (2003). doi:10.1063/1.1611998.
- [230] C. Iaconis and I. A. Walmsley. *Spectral phase interferometry for direct electric-field reconstruction of ultrashort optical pulses*. Optics Letters, **23**, 792 (1998).
- [231] E. J. Divall and I. N. Ross. *High dynamic range contrast measurements by use of an optical parametric amplifier correlator*. Optics Letters, **29**, 2273 (2004).

- [232] F. Tavella, K. Schmid, N. Ishii, A. Marcinkevičius, L. Veisz and F. Krausz. *High-dynamic range pulse-contrast measurements of a broadband optical parametric chirped-pulse amplifier*. Applied Physics B: Lasers and Optics, **81**, 753 (2005).
- [233] K. Osvay, M. Csatári, I. N. Ross, A. Persson and C.-G. Wahlström. *On the temporal contrast of high intensity femtosecond laser pulses*. Laser and Particle Beams, **23**, 327 (2005).
- [234] J. C. Vaughan, T. Feurer, K. W. Stone and K. A. Nelson. *Analysis of replica pulses in femtosecond pulse shaping with pixelated devices*. Optics Express, **14**, 1314 (2006).
- [235] I. Thomann, E. Gagnon, R. J. Jones, A. S. Sandhu, A. Lytle, R. Anderson, J. Ye, M. Murnane and H. Kapteyn. *Investigation of a grating-based stretcher/compressor for carrier-envelope phase stabilized fs pulses*. Optics Express, **12**, 3493 (2004).
- [236] M. Kakehata, H. Takada, Y. Kobayashi, K. Torizuka, H. Takamiya, K. Nishijima, T. Homma, H. Takahashi, K. Okubo, S. Nakamura and Y. Koyamada. *Carrier-envelope-phase stabilized chirped-pulse amplification system scalable to higher pulse energies*. Optics Express, **12**, 2070 (2004).
- [237] A. Renault, D. Z. Kandula, S. Witte, A. L. Wolf, R. T. Zinkstok, W. Hogervorst and K. S. E. Eikema. *Phase stability of terawatt-class ultrabroadband parametric amplification*. Optics Letters, **32** (2007).

List of publications

The work presented in this thesis is based on the following publications:

Chapter 5:

Control and precise measurement of carrier-envelope phase dynamics

R.Th. Zinkstok, S. Witte, W. Hogervorst, K.S.E. Eikema

Applied Physics B **78**, 5–12 (2004).

Chapter 6:

Deep-ultraviolet quantum interference metrology with ultrashort laser pulses

S. Witte, R.Th. Zinkstok, W. Ubachs, W. Hogervorst, K.S.E. Eikema

Science **307**, 400–403 (2005).

Chapter 7:

Frequency comb laser spectroscopy in the vacuum-ultraviolet region

R.Th. Zinkstok, S. Witte, W. Ubachs, W. Hogervorst, K.S.E. Eikema

Physical Review A **73**, 061801 (2006).

Chapter 8:

A source of 2 terawatt, 2.7 cycle laser pulses based on noncollinear optical parametric chirped pulse amplification

S. Witte, R.Th. Zinkstok, A.L. Wolff, W. Hogervorst, W. Ubachs, K.S.E. Eikema

Optics Express **14**, 8168–8177 (2006).

Other publications to which the author contributed:

Phase stability of terawatt-class ultrabroadband parametric amplification

A. Renault, D.Z. Kandula, S. Witte, A.L. Wolf, R.Th. Zinkstok, W. Hogervorst, K.S.E. Eikema
Optics Letters **32**, 2363–2365 (2007).

Numerical simulations for performance optimization of a few-cycle terawatt NOPCPA system

S. Witte, R.Th. Zinkstok, W. Hogervorst, K.S.E. Eikema
Applied Physics B **87**, 677–684 (2007).

Frequency metrology on the $EF\ ^1\Sigma_g^+ \leftarrow X\ ^1\Sigma_g^+(0,0)$ transition in H_2 , HD , and D_2

S. Hannemann, E.J. Salumbides, S. Witte, R.Th. Zinkstok, E.-J. van Duijn, K.S.E. Eikema, W. Ubachs
Physical Review A **74**, 062512 (2006).

Frequency metrology on the $Mg\ 3s^2\ ^1S \rightarrow 3s4p\ ^1P$ line for comparison with quasar data

S. Hannemann, E.J. Salumbides, S. Witte, R.Th. Zinkstok, K.S.E. Eikema, W. Ubachs
Physical Review A **74**, 012505 (2006).

Generation of few-cycle terawatt light pulses using optical parametric chirped pulse amplification

S. Witte, R.Th. Zinkstok, W. Hogervorst, K.S.E. Eikema
Optics Express **13**, 4903–4908 (2005).

High-power parametric amplification of 11.8-fs laser pulses with carrier-envelope phase control

R.Th. Zinkstok, S. Witte, W. Hogervorst, K.S.E. Eikema
Optics Letters **30**, 78–80 (2005).

Summary

The field of spectroscopy is concerned with the precise measurement of transition frequencies in a wide variety of e.g. atomic and molecular systems. Such frequency measurements are the most accurate measurements possible, and they give detailed insight into the structure of matter as well as into the interaction between matter and radiation. As such, it is hardly astonishing that they have been a driving force behind many advancements of the physical description of nature. And although the precision of measuring frequencies has progressed from the crude solar-oriented measurements of ancient times to modern atomic clock measurements of an astonishing 1-part-in-10-quadrillion accuracy, this is by no means the limit. Even currently available technology still allows for large improvements in accuracy, although the experiments in that direction are very complicated.

An important role in the emergence of modern frequency metrology experiments has been and still is being played by the laser, because such a device can be made to emit a very well-defined frequency. When stabilized, this narrow-band light can be used as a very pure source to probe the transition frequencies of e.g. atoms. Still, the laser frequency must be calibrated using a stable reference frequency, such as an atomic clock. Today's primary frequency standard is the cesium atomic clock, which produces a frequency of 9.2 GHz, in the radio frequency (RF) domain. This poses quite a problem, as the optical frequencies that are produced by lasers are some 100 000 times larger. For that reason, linking optical frequencies to the RF standard has always been a very difficult and inefficient endeavor, especially since these experiments could be used for only one frequency.

The invention of the frequency comb laser in 1999 caused a revolutionary simplification of these experiments. Such a laser does not emit continuous light, but produces very short pulses, lasting only about a millionth of a billionth of a second (10 fs). In contrast to single-mode lasers, the frequency spectrum of comb lasers consists of a large number of simultaneously oscillating modes which have a very regular spacing equal to the repetition frequency of the laser pulses, f_{rep} . This comb structure of modes can be stabilized when both the spacing of the teeth, f_{rep} , and the offset of the entire comb are carefully controlled. This second parameter is related to the pulse-to-pulse difference in the phase shift between the carrier wave and the envelope of the pulses, hence the name carrier-envelope offset frequency (f_{ceo}). As both these parameters are RF frequencies, they can be locked easily to a reference oscillator. The frequency comb then acts much like a ruler, to which unknown frequencies can be compared and thus measured. With this technique, the accuracy of a radio-frequency atomic clock could be transferred to the optical domain, simplifying absolute frequency measurements enormously.

Several important lines of research stand to gain from these developments. Theories of the structure of matter, like quantum-electrodynamics (QED), can be tested to unprecedented levels of accuracy, provided the precision of the experimental methods is comparable to that of theoretical calculations. As the latter are most accurate for the ground-state transitions in simple atoms and ions, such as hydrogen, helium and hydrogen-like ions, performing experiments on these transitions is especially attractive. However, these transitions invariably lie in the vacuum ultraviolet (VUV) or the extreme ultraviolet (XUV) wavelength regions, which are extremely arduous to cover using conventional laser technology.

The development of modern clock devices is similarly linked to progress in ultra-precise spectroscopy. Higher precision can be obtained by using a higher clock frequency: a clock that ticks faster, divides time in smaller chunks. Great experimental effort is expended in order to replace today's microwave atomic clocks with clocks that run on optical frequencies. Undoubtedly these will in turn be supplanted by clocks operating on UV, VUV or even XUV frequencies in the future.

Performing high-resolution laser spectroscopy at the high frequencies demanded in these and other applications is not an easy task. Narrow-band lasers at XUV or VUV wavelengths are almost impossible to construct, so the traditional methods of laser spectroscopy, with or without a frequency comb to calibrate the narrow-band laser, are not viable. The work presented in this dissertation, therefore, provides a new method to extend the high accuracy of a frequency comb laser to higher frequencies.

This method, of which the theoretical, conceptual and experimental details are presented in chapters 2–4, is based on two ideas. The first is to use the pulsed output of a frequency comb to excite the studied system (e.g. the atom) directly. The excitation contribution of consecutive phase-locked pulses will interfere, and by changing the phase difference between the pulses, the excitation can be modulated. From this modulation signal, the transition frequency can be determined. This approach is closely related to Ramsey’s method of separated oscillatory fields, which is routinely used for atomic clocks in the microwave region.

The other cornerstone of the method described in this thesis is the up-conversion of the comb pulses to the required wavelength range using frequency mixing in crystals or gases. If the phase coherence of the comb pulses survives this frequency-conversion process, the pulses can be used to perform direct frequency comb spectroscopy in the VUV or even XUV. Because such frequency-conversion processes are usually quite inefficient, it is necessary to amplify the comb pulses before up-conversion. Again, the phase coherence of the pulses must not be compromised by this amplification process.

Careful control of the two parameters of a frequency comb laser is required for such an experiment to work, and in chapter 5 detailed studies are presented on the carrier-envelope phase (ϕ_{ce}) dynamics of our comb laser system. Real-time measurements were performed on the influence of the feedback loops, the nonlinear interaction in the micro-structured fiber employed in the ϕ_{ce} detection system, the pump laser and environmental influences. The most important findings were that the effects of fiber nonlinearities are too small to be detected in our experiments, and that the use of a single-mode pump laser dramatically improves the stability of phase control compared to the use of a multi-mode pump laser.

The feasibility of the proposed method of direct frequency comb spectroscopy at high frequencies is demonstrated in chapter 6, where an experiment is described on a deep-UV transition in krypton at 2×212.5 nm. Short trains of comb pulses were amplified in a multi-pass non-saturating Ti:sapphire amplifier, and after two stages of frequency doubling in BBO crystals, the resulting deep-UV pulses were sent through a beam of krypton atoms, while any ions produced were detected. Careful measurement of the phase changes introduced by the amplifier ensured that the pulse-to-pulse phase difference was known. Changing the repetition rate of the frequency comb resulted in high-contrast modulation of the ion production, demonstrating that the deep-UV comb pulses retain the required phase coherence throughout the amplification and frequency-conversion processes. By recording modulation signals for different isotopes, the isotope shifts could be determined with a precision of a few hundred kHz. An

absolute frequency measurement could be performed by combining measurements at three sufficiently different repetition rates. In this way, the transition frequency could be determined with a precision of 3.5 MHz, which is an order of magnitude more accurate than earlier measurements using nanosecond-pulsed lasers.

Since this experiment used only frequency doubling in crystals, a new experiment was set up in order to test our method using harmonic generation in a gas. The interactions in gaseous media are much more likely to cause detrimental phase distortions than those occurring in crystals. Chapter 7 describes an experiment on the 125 nm transition in xenon, which is excited using amplified comb pulses which have been frequency doubled in a crystal and subsequently frequency tripled in a gas cell. Again high-quality interference signals were recorded. Extensive investigation of the effects of gas pressure and driving laser intensity have been performed using oxygen and acetylene for a medium. The xenon atoms were used as high-resolution phase detectors. No significant correlation was found between the harmonic-generation parameters and the recorded phases, from which the conclusion was drawn that direct frequency comb spectroscopy in the VUV using harmonic generation in a gas is indeed possible.

In this experiment, it was also demonstrated that an increase in resolution is possible not only by increasing the number of pulses, but also by increasing the delay between just two pulses. The latter method is preferred in our experiments, as measurements of the amplifier-induced phase shifts could only be performed on pulse pairs; apart from that, it is generally easier to amplify just two pulses.

The experiments of chapters 6 and 7 are complicated by the multi-pass amplifier used, which makes it necessary to track the phase changes it induces. A different amplification approach is presented in chapter 8. This approach concerns the use of a non-collinear optical parametric chirped-pulse amplifier (NOPCPA), which uses the instantaneous parametric interaction in a BBO crystal to transfer power from an intense pump laser beam to the frequency comb laser seed beam. As the interaction preserves the phase of the seed pulses, high-power phase-controlled frequency comb pulses can be produced.

To this end, a Nd:YAG pump laser system was built capable of delivering 160 mJ, 532 nm pulses at a 30 Hz repetition rate, which were synchronized to the frequency comb. This system was used to pump a three-stage NOPCPA system. Due to the high damage threshold of BBO, modest stretching could be applied to the seed pulses, leading to a very compact and stable setup. Adaptive pulse shaping was employed to fine-tune the dispersion compensation of the stretcher-compressor combination, yielding a compressed pulse duration of 7.5 fs. The complete NOPCPA system delivered 15.5 mJ pulses after compression, corresponding to 2 TW. Pulse contrast measurements showed a

2×10^{-8} pre-pulse contrast between the main pulse and the fluorescence background. An amplifier system like this is very useful in research on, for example, extreme-nonlinear optics, but can be put to very good use as well in direct frequency comb spectroscopy. To demonstrate this, the NOPCPA system described here will be employed in such experiments on helium in the near future.

Samenvatting

In de spectroscopie houdt men zich bezig met het zeer precies meten van overgangsfrequenties in allerlei atomaire en moleculaire systemen. Omdat frequentiemetingen nauwkeuriger kunnen worden uitgevoerd dan alle andere soorten metingen, geven ze een zeer gedetailleerd beeld van de structuur der materie en van de interactie tussen straling en materie. Het is dan ook niet verwonderlijk dat frequentiemetingen al meer dan een eeuw een drijvende kracht achter de voortdurende verbetering van de fysische beschrijving van de natuur vormen. Hoewel het overduidelijk is dat de nauwkeurigheid van frequentiemetingen enorm is toegenomen — vergelijk bijvoorbeeld de metingen op basis van de zonnestand uit de oudheid met de onvoorstelbaar precieze metingen met behulp van moderne atoomklokken — is het einde van deze ontwikkeling nog niet in zicht. Zelfs zonder rekening te houden met nog niet ontdekte methoden zijn er met behulp van de huidige technieken nog grote stappen te zetten, al zijn de experimenten die daarvoor nodig zijn niet makkelijk uit te voeren.

In de ontwikkeling van spectroscopie en frequentiemetrologie speelt de laser een belangrijke rol omdat laserlicht uiterst coherent is en omdat de frequentie van een smalbandige, continue laser zeer nauwkeurig is af te stemmen. Het smalbandige licht van een goed gestabiliseerde laser is dan ook bijzonder geschikt voor het verrichten van metingen aan atomaire overgangsfrequenties. Voor een absolute frequentiemeting moet de laserfrequentie uiteraard wel gekalibreerd worden met behulp van een goed gedefinieerde referentiefrequentie, zoals bijvoorbeeld een atoomklok. De huidige internationale frequentiestandaard is de cesiumatoomklok, die een frequentie afgeeft van ongeveer 9,2 GHz, een frequentie die in het radiofrequentiegebied (RF-gebied) ligt. In combinatie met lasers geeft deze standaard echter behoorlijke problemen, aangezien de optische

frequenties van lasers veel hoger liggen: het verschil is grofweg een factor 100.000. Het leggen van een link tussen optische frequenties en de RF-frequentiestandaard was hierdoor lange tijd een zeer complexe en inefficiënte aangelegenheid, zeker omdat een dergelijk experiment slechts bruikbaar was voor het meten van één enkele frequentie.

De uitvinding van de frequentiekamlaser in 1999 zorgde voor een drastische vereenvoudiging van deze experimenten. Een dergelijke laser zendt geen continue lichtbundel uit, maar juist zeer korte pulsen die ongeveer een miljoenste van een miljardste seconde (10 fs) duren. In tegenstelling tot het frequentiespectrum van smalbandige, continue lasers bestaat het spectrum van een frequentiekam uit zeer veel verschillende smalbandige frequenties, die allemaal tegelijkertijd oscilleren. Deze frequenties zijn zeer regelmatig verdeeld, waarbij de exact bepaalde onderlinge afstand gelijk is aan de herhalingsfrequentie van de pulsen uit de laser, f_{rep} . De kamstructuur die door deze 'frequentietanden' wordt gevormd kan volledig worden vastgelegd door het fixeren van deze f_{rep} en de verschuiving van de hele kam. Deze tweede parameter is gerelateerd aan het puls-tot-pulsverschil in de faseverschuiving tussen de draaggolf (*carrier*) en de omhullende (*envelope*) van de frequentiekam-pulsen, en wordt daarom de *carrier-envelope offset*-frequentie (f_{ceo}) genoemd. Aangezien deze beide parameters RF-frequenties zijn, kunnen zij zonder problemen vergeleken worden met de gangbare frequentiestandaard. De frequentiekam fungeert dan als een soort meetlat, waarmee onbekende optische frequenties vergeleken en dus gemeten kunnen worden. Op deze manier kan de nauwkeurigheid van RF-atoomklokken overgebracht worden naar het optische domein, waardoor de meting van absolute frequenties aanzienlijk wordt vereenvoudigd.

Verschuivingen onderzoeksgebieden profiteren van deze ontwikkelingen. Zo kunnen de theorieën over de structuur van de materie, zoals de quantumelektrodynamica (QED), zeer nauwkeurig getest worden, ervan uitgaande dat de theoretische berekeningen van een vergelijkbare precisie zijn als de experimentele metingen. Deze berekeningen zijn het beste uit te voeren voor eenvoudige atomen zoals waterstof, helium en waterstofachtige ionen. Met name de overgangen vanuit de grondtoestand het interessantst; vandaar dat deze overgangen het aantrekkelijkst zijn om nauwkeurig te meten. Helaas liggen deze allemaal in het vacuüm-ultraviolet (vuv) of het extreem-ultraviolet (xuv), en het is zeer moeilijk zo niet onmogelijk om smalbandige lasers te maken bij dergelijke frequenties.

Ook de ontwikkeling van moderne atoomklokken is afhankelijk van de vooruitgang in de nauwkeurigheid van spectroscopische experimenten. Betere, preciezere klokken kunnen worden geconstrueerd door gebruik te maken van een hogere klokfrequentie: de klok tikt dan sneller, zodat de tijd in kleinere stukjes wordt opgedeeld. Er wordt

dan ook zeer veel moeite gestoken in experimenten die erop uitzijn de tegenwoordige microgolfklokken te vervangen door klokken die werken met optische frequenties — en in de toekomst zullen deze zonder twijfel op hun beurt vervangen worden door UV-, VUV- en XUV-klokken.

Het voorgaande schetst de behoefte aan zeer nauwkeurige laserspectroscopie bij hoge frequenties; ook is duidelijk geworden dat dit geen eenvoudige kwestie is, aangezien het bijna onmogelijk is om smalbandige lasers te bouwen in het VUV of XUV. Hierdoor falen de traditionele spectroscopische methoden, ook al maken ze gebruik van een frequentiekam voor de kalibratie. In dit proefschrift wordt derhalve een methode voorgesteld en gedemonstreerd die het toch mogelijk maakt om de nauwkeurigheid van frequentiekamlasers over te brengen naar zeer hoge frequenties.

Deze methode, waarvan de theoretische, conceptuele en experimentele details behandeld worden in de hoofdstukken 2 tot en met 4, rust op twee belangrijke pijlers. De eerste is het idee om de korte pulsen van een frequentiekamlaser direct te gebruiken om atomen aan te slaan. De excitatie ten gevolge van opeenvolgende pulsen zal dan interfereren, en door bijvoorbeeld het faseverschil tussen de pulsen te variëren kan de excitatiewaarschijnlijkheid worden gemoduleerd. Uit dit modulatiesignaal kan dan de overgangsfrequentie in kwestie bepaald worden. Deze aanpak is nauw verwant aan Ramseys methode van gescheiden oscillerende velden, een standaardmethode voor atoomklokken in het RF-domein.

De tweede pijler van de beschreven methode is het gebruik van frequentieconversie van de frequentiekam-pulsen in kristallen of gassen om de gewenste hoge frequenties te bereiken. De geconverteerde pulsen kunnen dan worden gebruikt voor directe frequentiekamspectroscopie in het VUV of zelfs in het XUV, mits de fasecoherentie van de pulsen dit conversieproces overleeft. Omdat deze processen doorgaans weinig efficiënt zijn, is het nodig de kam-pulsen te versterken om ze bruikbaar te maken voor frequentieconversie. Ook hier geldt dat de fasecoherentie van de pulsen niet aangetast mag worden door het versterkingsproces.

Zoals gezegd is een goede controle over de twee bepalende parameters f_{rep} en f_{ceo} van een frequentiekam nodig om experimenten met dit instrument te doen slagen. In hoofdstuk 5 wordt dan ook een gedetailleerde studie naar de dynamica van de carrier-envelope-fase van onze frequentiekam beschreven. Om de invloed van de feedbackloops, de niet-lineaire interacties in de fotonische glasvezel die wordt gebruikt in het f_{ceo} -detectiesysteem, de pomplaser en omgevingsinvloeden te bepalen zijn reëltimemetingen verricht. De belangrijkste uitkomsten hiervan zijn dat de effecten

van de niet-lineariteiten in de fotonische glasvezel te klein zijn om door ons gemeten te kunnen worden, en dat het gebruik van een *single mode*-pomplaser de stabiliteit van de fasecontrole drastisch verbetert in vergelijking met een *multi mode*-pomplaser.

De praktische haalbaarheid van de voorgestelde methode van directe frequentiekam-spectroscopie bij hoge frequenties wordt vervolgens gedemonstreerd in hoofdstuk 6. In dit hoofdstuk wordt een experiment beschreven aan een diep-UV-overgang in het kryptonatoom bij 2×212.5 nm. Korte reeksen van kam-pulsen zijn hiertoe versterkt in een niet-verzadigende multipass titaan:saffier-versterker; na twee frequentieverdubbelingstrappen in BBO-kristallen werden de aldus gegenereerde diep-UV-pulsen door een kryptonatoombundel geschoten en de geproduceerde ionen gedetecteerd. Om de precieze faserelatie tussen opeenvolgende pulsen te weten te komen zijn zorgvuldige metingen van de door de versterker veroorzaakte faseveranderingen uitgevoerd. Een langzame verstemming van de herhalingsfrequentie van de pulsen resulteerde in het een zeer uitgesproken modulatie van de ionenproductie, waarmee is aangetoond dat de diep-UV-pulsen hun fasecoherentie niet verliezen gedurende de versterking en de frequentieconversie.

Door de modulatie in het ionensignaal voor verschillende isotopen tegelijkertijd te meten, waren we in staat de isotoopverschuiving te bepalen met een nauwkeurigheid van een paar honderd kilohertz. De absolute overgangsfrequentie kon worden bepaald uit drie sets metingen die elk met een andere f_{rep} gemeten waren. De nauwkeurigheid van deze meting was 3,5 MHz, ruim een factor 10 beter dan eerdere metingen die gebruik maakten van nanosecondegepulste lasers.

Aangezien dit experiment slechts gebruik maakte van frequentieverdubbeling in kristallen, is een tweede experiment opgezet om de methode te testen, ditmaal met gebruikmaking van de generatie van harmonische frequenties in een gas. Bij de interacties in een dergelijk gasvormig medium is het risico op faseverstoringen vele malen groter dan in kristallen. Hoofdstuk 7 beschrijft dit experiment, waarin de overgang bij 125 nm in xenon centraal staat. Deze overgang is aangeslagen met versterkte frequentiekam-pulsen waarvan de frequentie eerst verdubbeld is in een kristal en vervolgens is verdrievoudigd in een gascel. Ook in dit experiment werden zeer duidelijke modulatiesignalen gemeten. Uitgebreid onderzoek naar de effecten van de gasdruk en laserintensiteit is uitgevoerd met zuurstof en acetyleen als medium; de xenonatomen fungeerden hierbij als zeer precieze fasedetectoren. Er werd geen significant verband gevonden tussen de parameters van frequentieconversie en de gemeten faserelatie tussen de pulsen. Hieruit kan geconcludeerd worden dat het inderdaad mogelijk is

om directe frequentiekamspectroscopie uit te voeren in het vuv, gebruik makend van frequentieconversie in een gasvormig medium.

In dit tweede experiment is ook aangetoond dat een hogere resolutie niet alleen verkregen kan worden door reeksen met meer pulsen te gebruiken, maar ook door de tijdsduur tussen slechts twee pulsen te vergroten. Deze laatste aanpak is een stuk praktischer bij onze experimenten, aangezien het meten van de faseverschuiving van de versterker slechts mogelijk is voor twee pulsen. Daar komt nog bij dat het in het algemeen makkelijker is om slechts twee pulsen te versterken.

Vanwege het gebruik van een multi-pass titaan:saffier-versterker zijn de experimenten beschreven in de hoofdstukken 6 en 7 nodeloos complex, aangezien het nodig is de faseverschuiving die deze versterker veroorzaakt te meten. In hoofdstuk 8 wordt daarom een systeem gepresenteerd dat gebaseerd is op een andere versterkingsmethode, namelijk de niet-collineaire optische parametrische gechirpte-pulsversterking (in het Engels afgekort tot NOPCPA). Deze methode is gebaseerd op de instantane parametrische interactie in een BBO-kristal, waarbij het vermogen van een intense pompplaserpuls overgedragen wordt op de geïnjecteerde frequentiekam-puls. Aangezien de fase van de geïnjecteerde pulsen bij deze interactie behouden blijft, kunnen fasestabiele frequentiekam-pulsen met hoog vermogen gegenereerd worden.

Hiertoe is een Nd:YAG-pomplasersysteem gebouwd dat 160 mJ-pulsen bij 532 nm kan produceren met een herhalingsfrequentie van 30 Hz, gesynchroniseerd met de frequentiekam; deze pulsen pompen vervolgens een drietraps NOPCPA-systeem. Doordat BBO zeer hoge lichtintensiteiten kan weerstaan, hoeven de pulsen maar beperkt uitgerekt te worden in de tijd, waardoor de opstelling zeer compact kan blijven. Adaptieve *pulse shaping* is toegepast om de dispersiecompensatie van de stretcher en compressor zeer precies bij te kunnen stellen. De uiteindelijke outputpulsen van de versterker waren slechts 7.5 fs lang, terwijl ze een energie van 15.5 mJ bevatten: dit komt overeen met een piekvermogen van 2 terawatt. Pulscontrastmetingen resulteerden in een pre-pulscontrast van 2×10^{-8} tussen de hoofdpuls en de fluorescentieachtergrond. Een dergelijk systeem is zeer interessant voor velerlei onderzoek op het gebied van bijvoorbeeld extreem niet-lineaire optica, maar kan ook uitstekend gebruikt worden in directe frequentiekamspectroscopie. Het hier beschreven NOPCPA-versterkersysteem zal dan ook in de nabije toekomst worden toegepast bij dergelijke experimenten met helium.

Dankwoord

Na alle pagina's met wetenschappelijke schrijfsels dan ook een paar wat meer persoonlijke bladzijden: niet alleen voor velen de leukste om te lezen, ook voor mij om te schrijven. Want onderzoek doen is natuurlijk erg leuk en spannend, maar zonder collega's, vrienden en familie zou het niet gelukt zijn, en zou het sowieso niet half zo leuk zijn geweest.

Kjeld Eikema is dan uiteraard de eerste die ik wil bedanken. Kjeld, ik prijs mezelf gelukkig dat jij mijn begeleider bent geweest, en ik ben er trots op dat ik in jouw mooie lab heb mogen werken. Ik heb enorm veel geleerd van je uitzonderlijke kennis en veelzijdigheid, doorzettingsvermogen, kritische geest (*dat geloof je toch zeker zelf niet!*) en onverbeterlijk optimisme (*geweld lost alles op!*). Je hebt een aanstekelijke, jongensachtige kijk op onderzoek doen, waarbij nieuwsgierigheid, avontuur en prettig gestoord zijn een grote rol spelen: ik heb me daar altijd heel goed bij thuis gevoeld. Heel veel dank voor dit alles, en heel veel succes met het vervolg van je lab-avonturen!

Wim Hogervorst, achter de schermen heb jij ook heel veel gedaan voor mijn onderzoek. Het door jouw opgezette Lasercentrum is een uitstekende en inspirerende omgeving om in te kunnen werken. Maar ook je betrokkenheid bij mijn onderzoek heb ik erg gewaardeerd: feilloos wist je de momenten uit te zoeken om in het lab langs te komen, waar we dan net een mooie meting konden laten zien. Ook wil ik je bedanken voor je immer pijlsnelle correcties van manuscripten, de artikelen zijn er zeker beter op geworden!

Stefan Witte is degene met wie ik de afgelopen negen jaar verreweg het meeste gestudeerd en gewerkt heb. Stefan, ik ben heel blij dat we als studievrienden samen aan dit promotie-onderzoek konden beginnen. We hebben enorm veel bereikt, veel gelachen

DANKWOORD

maar ook gescholden op de setup. Zonder jouw experimenteerkunsten, creativiteit en goede ideeën waren we nooit zo ver gekomen, en bovendien: zonder jou was het niet zo leuk geweest. Niet alleen in het lab, maar ook daarbuiten hebben we heel wat beleefd, onder andere op de conferenties waar we vaak samen heen zijn gegaan. Bedankt voor alles, heel veel succes met je werk nu bij biofysica en alles wat je daarna nog gaat doen: ik hoop je nog vaak tegen te komen!

I would like to thank all members of the atomic physics group for the good atmosphere in the lab but also outside of it. Many of you have helped me with advice or lended me equipment, and my work would have been a lot harder without all of that: thank you all! Special thanks go to Stefan, John, Sandro, Edcel and Tom, who started their PhD-research around the same time I did. The coffee (or tea) breaks, movie nights, playing Worms-games, watching the soccer championship: we had a lot of fun, and I really needed that, especially when the experiments were ‘challenging’. The new femtolab crew (Anne-Lisa, Dominik, Amandine and Christoph), good luck with all the exciting but challenging experiments! Eric-Jan, enorm bedankt voor al je praktische hulp, je adviezen en de grote hoeveelheden spullen die we van je mochten gebruiken! Maarten Sneep, nog heel erg bedankt voor alle L^AT_EX-hulp die je me gegeven hebt. Wim Ubachs, bedankt voor al het werk dat je als groepsleider hebt verzet: ik heb met veel plezier in je groep gewerkt.

Jacques Bouma, ook jij verdient grote dank. Jouw vakkundige kennis, technisch inzicht en grote inzet zijn van onschatbare waarde geweest voor mijn onderzoek. Je hebt enorm geduld gehad met mijn vaak onbeholpen schetsjes van onderdelen die ik nodig had, en ik heb in de loop der jaren veel van je geleerd qua praktisch denken, technisch inzicht en vaardigheden met allerlei gereedschap.

Voor de technische ondersteuning vanuit de fijnmechanische en elektronische werkplaats ben ik ook erg dankbaar. Vanuit de eerste hebben met name Arie van Drimmelen en Pierre Noordeloos met grote vakkundigheid allerhande onderdelen van onze opstelling gemaakt.

Petra de Gijzel, jij ook enorm bedankt voor alle kleine en grote dingen die je geregeld hebt. En voor de opgewekte gezelligheid waar je altijd voor gezorgd hebt!

Naast alle mensen op de VU zijn er nog velen daarbuiten die mij in de afgelopen jaren hebben gesteund, mijn onderzoeksprikelen aan hebben gehoord en op allerlei manieren voor afleiding hebben gezorgd. Zonder deze mensen was mijn promotietijd (maar niet alleen die tijd!) lang niet zo leuk en waardevol geweest!

Bij het VU-Kamerkoor vind ik al jaren een ongelooflijk hechte groep geweldige vrienden. Elke week samen muziek maken is op zich al een feest, maar dat ik dat kan doen met zo veel lieve en mij erg dierbare mensen verbaast me nog altijd. Om met jullie allemaal wel en wee te kunnen delen, niet zelden met een goed glas wijn in de hand, is mij heel waardevol. Het vukk heeft me misschien soms wat meer tijd gekost dan goed was voor, noem eens wat, mijn onderzoek, maar het was het dubbel en dwars waard. Ik hoop nog lang samen met jullie te genieten van mooie muziek en alles wat daar bij komt kijken!

Marcel, ongelooflijk goede vriend! Wat er ook gebeurt, saai is het nooit met jou erbij. Ik ben heel erg blij met je interesse, je grappen, onze goede gesprekken, noem het maar op. Met grote interesse heb je mijn onderzoeksavonturen gevolgd, en meer dan eens heb je me door je vragen nog enthousiaster gemaakt voor mijn eigen werk dan ik al was. Heel erg bedankt ook voor het proeflezen van een paar hoofdstukken van dit boekje! Het verbaast me dan ook helemaal niet dat jij ook aan een promotie-onderzoek bent begonnen, je bent gelukkig een stuk wetenschappelijker ingesteld dan je zou verwachten van een medicus...

David, je bent een onmisbare en stabiele vriend! Met jou door het mooie Hollandse landschap wandelen, met de ontelbare verhalen die je daarbij wist te vertellen, waren de meest rustgevende momenten die ik heb meegemaakt, een welkome afwisseling met de soms lange dagen in het lab. Gaan we snel weer eens op pad?

Simone, vrienden zoals jij zijn met een lantaarntje te zoeken. Je bent enorm betrokken en nieuwsgierig naar hoe het gaat, altijd in voor leuke dingen, en je bemoedigende kaartjes waren geweldig!

Het vukk is niet het enige koor waar ik afleiding heb gevonden: mijn tijd in het Nederlands Studenten Kamerkoor, en vooral het jaar dat ik in het bestuur zat, was ronduit geweldig. Mede-NSK-bestuurders, en met name Tim, Maartje, Saskia en Rients: bedankt voor alles!

Job, mein lieber Bruder! Ik weet niet waar ik moet beginnen om jou te bedanken. De vele avonden die we met discussies, lekker eten, wijn, muziek en nog veel meer hebben gevuld zijn mij erg dierbaar en ik hoop dan ook dat er nog veel komen! Ook superbekant voor al je hulp tijdens het schrijven van dit proefschrift, van opmaakadviezen tot het redigeren van grote delen tekst. Ik ben er trots op dat ik zo'n bijzondere en veelzijdige broer en paranimf heb!

Lieve Janneke, grote zus! Bedankt voor je steun en de toffe dingen die we samen gedaan hebben! Bergwandelen in Zwitserland, samen stressen over promotie-onderzoek doen en wat daar zoal bij komt kijken, naar opera's luisteren, en nog veel meer. Je bent

DANKWOORD

een ongelooflijk lieve, avontuurlijke en slimme zus, en je hebt me misschien zonder het zelf te weten enorm gemotiveerd.

Jet, lieve zus van me! Ik ben superblij met jou en je heerlijke praktische kijk. Ik kan echt alles met je bespreken, en je staat altijd klaar om te helpen. Eindelijk heb ik dan ook eens ruimer de tijd om weer wat meer voor jou te betekenen. En voor het kleintje dat eraan komt natuurlijk!

Lieve pa en ma, bedankt voor jullie steun en betrokkenheid bij alles wat ik doe! Ook al kon ik niet altijd goed uitleggen wat ik nou precies deed in het lab (er zijn niet veel mensen bij wie dat wel is gelukt, wees niet bang), jullie belangstelling is nooit verflauwd. Bedankt voor alles!

Tenslotte natuurlijk mijn lief, Willemijn. Het begin van dit project heb je niet meegemaakt, maar juist alleen de moeilijkste laatste fase. Dat het schrijfwerk het laatste jaar grotendeels thuis in de avonden en weekends gebeurde maakte het niet makkelijker, en je enorme steun en vertrouwen in deze tijd had ik niet kunnen missen. Bij jou ben ik pas echt thuis!

This thesis was designed by Roel Zinkstok. It was typeset with pdf- \LaTeX , using the Memoir class. It was printed and bound by PrintPartners Ipskamp BV, Enschede.

The text face is Minion Pro, designed by Robert Slimbach. The captions are set in Linotype Finnegan, designed by Jürgen Weltin.

The figures were created by the author using METAPOST, Adobe Illustrator cs2 and Maxon Cinema 4D.

The image features a background of diagonal blue lines on a light blue gradient. A solid orange horizontal band is positioned in the center. The ISBN number is printed in white on this band.

ISBN 978-90-9022619-4